THESIS FOR THE DEGREE OF DOCTOR OF PHILOSOPHY

Spin and topological effects in 2D quantum material devices

LARS SJÖSTRÖM

Department of Microtechnology and Nanoscience (MC2)
Quantum Device Physics Laboratory
CHALMERS UNIVERSITY OF TECHNOLOGY

Göteborg, Sweden 2026

Spin and topological effects in 2D quantum material devices

LARS SJÖSTRÖM
Göteborg, Sweden 2026
ISBN 978-91-8103-504-9
DOI 10.63959/chalmers.dt/5961

COPYRIGHT ©LARS SJÖSTRÖM, 2026

Doktorsavhandlingar vid Chalmers tekniska högskola
Ny serie Nr 5961
ISSN 0346-718X

ISSN 1652-0769 Quantum Device Physics Laboratory
Department of Microtechnology and Nanoscience (MC2)
Chalmers University of Technology
SE-412 96 Göteborg, Sweden
Telephone: +46 (0)31-772 1000

Cover
Artistic illustration of a circuit with graphene and topological quantum materials, showcasing spin transport, spin sensing, charge-spin interconversion and nonlinear electronic transport.

Printed by Chalmers Reproservice
Göteborg, Sweden 2026

Spin and topological effects in 2D quantum material devices
LARS SJÖSTRÖM
Quantum Device Physics Laboratory
Department of Microtechnology and Nanoscience (MC2)
Chalmers University of Technology

Abstract

Topological quantum materials, such as topological insulators, Weyl semimetals and magnetic topological insulators, have electronic band structures with a nontrivial topology and protected surface or edge states that cannot be destroyed by disorder or small perturbations. These band structures contain characteristic spin textures where the electron's spin is locked to its momentum direction, thereby generating a spontaneous spin polarisation in response to an electric field. Additionally, the electronic states host fundamental quantum geometric features, which can give rise to nonlinear transport phenomena.

In this dissertation, spin and topological effects are explored in van der Waals quantum materials through spin and electronic transport in microscopic devices. First, spin textures in the ferromagnets cobalt and Fe_5GeTe_2 are sensed electrically through pure spin-polarised transport in lateral graphene spin-valve devices. Next, similar graphene heterostructure devices are employed to observe charge-spin interconversion in the topological bands of the topological insulator $Bi_{1.5}Sb_{0.5}Te_{1.7}Se_{1.3}$ and the Weyl semimetal $TaIrTe_4$. Finally, nonlinear electronic transport effects are utilised as a sensitive probe of the magnetic phases and the quantum geometry of the magnetic topological insulator $MnBi_2Te_4$. Together, these findings demonstrate the exciting physics of spin and topology in van der Waals topological quantum materials, which can lead towards new fundamental insights as well as novel spintronic and quantum devices for next-generation technologies.

Keywords: spintronics, topological insulators, Weyl semimetals, graphene spin valve, van der Waals heterostructure, spin sensing, charge-spin interconversion, nonlinear transport

'*The important thing is not to stop questioning. Curiosity has its own reason for existence. One cannot help but be in awe when he contemplates the mysteries of eternity, of life, of the marvelous structure of reality. It is enough if one tries merely to comprehend a little of this mystery each day.*'

— Albert Einstein

'*It was a strange universe. The more she learned, the stranger it seemed, and she doubted she would ever find the answers to all her questions.*'

— Christopher Paolini
To Sleep in a Sea of Stars

Acknowledgements

When I first arrived at Chalmers as a new bachelor student all the way back in August of 2016, it never crossed my mind that I might still be around more than ten years later. Even as I was beginning my master's studies in the autumn of 2019, I had no plans to take on a PhD. Yet, here I am. While I do admit to a love for physics and learning, it is nevertheless safe to say that I could never have made it on my own, and there is a long list of people who have not only made this journey possible to begin with, but who have also made it a rewarding and, more often than not, enjoyable experience.

First and foremost, I would like to thank my supervisor Professor Saroj Prasad Dash. Thank you for giving me the chance to pursue a PhD in the first place, and for your academic guidance along the way. There is no doubt that your never-ending supply of innovative ideas, suggestions and insightful feedback have had an enormous impact on the quality and novelty of my work.

I would also like to thank my assistant supervisor Associate professor Alexei Kalaboukhov and my examiner Professor Tomas Löfwander for their continuous assistance and engagement.

I have been fortunate enough to work alongside the excellent colleagues and researchers of the Spin and Quantum Technology group. My heartfelt gratitude to Dr Bing Zhao, Dr Md Anamul Hoque, Dr Roselle Ngaloy and Dr Richa Mitra for showing me the ropes in the beginning of my PhD. A special thank you also to Dr Prasanna Rout, Dr Bing Zhao and Dr Lalit Pandey for our many fruitful scientific discussions. Thank you to Dr Sameer Kumar Mallik, Dr Divya Prakash Dubey, Dr Himanshu Bangar, Dr Khadiza Ali, Dr Lakhan Bainsla, Ankit Khola, Dr Ivo Cools, Dr Dmitrii Khokhriakov and Dr Bogdan Karpiak for fostering such a collaborative and friendly working environment.

One part of my research and teaching duties that have been especially enjoyable is supervising master's students during their thesis projects. Thank

you to Marcus Göransson, Elias Rasmussen and Alexander Pinto for placing your trust in me and for your contributions to the results in this thesis.

A special thank you to Maha Khademi, Alessia Garibaldi, Núria Alcade-Herraiz and Klinti Sinojmeri for the good times, for always having my back and for sticking with me through it all. My mental health would have suffered without you guys.

A big thank you to everyone in the Quantum Device Physics laboratory: Assoc prof Thilo Bauch, Assoc prof Samuel Lara Avila, Prof Dag Winkler, Prof August Yurgens, Prof Floriana Lombardi, Prof Sergey Kubatkin, Dr Andrey Danilov, Prof Elsebeth Schröder, Prof Per Hyldgaard and Prof Tord Claeson, as well as Dr Kiryl Niherysh, Dr Aditya Jayaraman, Dr Naveen Shetty, Johanna Udén, Dr Ananthu Surendran, Dr Munis Khan, Karn Rongrueangkul, Joyal Palakulam, Vittorio Buccheri, Dr Nermin Trnjanin, Dr Federico Chianese and all other previous and current members. Thank you for the laughs, for making me feel included and for always showing a genuine interest in my work.

Also to those outside of QDP, thank you Na Liu, Dr Adithi Udupa and Prof Maria Abrahamsson for your support and encouragement.

All device fabrication in this thesis was performed at the Nanofabrication laboratory, Myfab, and I would like to thank Henrik Frederiksen, Irina Zubritskaya, Petra Johansson, Mattias Fredriksson, Niclas Lindvall and Mats Hagberg for their excellent support and assistance.

Thank you to Lars Jönsson for the help with maintaining and upgrading our lab. A big thank you also to Annika Holtringer, Louise Kvarefelt and Emma Wikfeldt for help with all administrative issues.

I would like to extend my gratitude to my collaborators in Sweden and abroad: Dr Shahid Sattar and Prof Carlo M Canali at Linnaeus University in Kalmar, Dr Alexander Tyner at Nordita in Stockholm, Dr Maurice E Bal and Prof Uli Zeitler at Radboud University in the Netherlands and Fereshteh Masoudinia at the Institute of Materials Science of Barcelona in Spain.

I would like to acknowledge financial support from the Swedish Research Council, which has made my PhD studies possible. I would also like to acknowledge funding from the European Magnetic Field Laboratory, the Adlerbertska Research Foundation and the Royal Swedish Academy of Sciences, which enabled my travels to the Netherlands, Germany and Japan, respectively.

To my friends beyond the nano area – Adis, Björn, Markus, Alexander, Alina and Pontus, thank you so much for helping me to keep my spirits up

and for luring me away from the office every once in a while. It was sorely needed!

Finally, I would like to give a very special thank you to my parents and to my sister Helena for all of your endless love and unyielding support and encouragement, right from the very beginning. *Tack!*

Lars Sjöström
Gothenburg, October 2026

List of publications

This thesis is based on the work contained in the following appended papers:

[I] L. Sjöström, B. Zhao, M. Khademi, R. Ngaloy, A. Kalaboukhov, J. Åkerman, and S. P. Dash, "Electrical Detection of Magnetic Spin Textures Using Pure Spin Currents in Graphene", Nano Letters **26**, 158–165 (2026).

[II] B. Zhao, R. Ngaloy, L. Sjöström, and S. P. Dash, "A Spin-Texture Spin-Valves With Van Der Waals Magnets", Advanced Science **13**, e00041 (2026).

[III] A. M. Hoque*, L. Sjöström*, D. Khokhriakov, B. Zhao, and S. P. Dash, "Room temperature nonlocal detection of charge-spin interconversion in a topological insulator", npj 2D Materials and Applications **8**, 10 (2024).

[IV] L. Sjöström, L. Pandey, R. Ngaloy, B. Zhao, and S. P. Dash, "Nonlocal electrical detection of charge-spin interconversion in Weyl semimetal $TaIrTe_4$", under review in Nano Letters (2026).

[V] L. Sjöström, P. Rout, M. E. Bal, K. Ali, A. Khola, M. Leandersson, F. Schiller, F. Choueikani, A. Thamizhavel, U. Zeitler, and S. P. Dash, "Quantum-metric-driven nonlinear transport for sensitive phase detection in magnetic topological insulator $MnBi_2Te_4$", submitted to Advanced Materials (2026).

[VI] L. Sjöström, P. Rout, S. Sattar, A. Tyner, M. E. Bal, A. Khola, E. Rasmussen, K. Ali, A. Thamizhavel, U. Zeitler, C. M. Canali, and S. P. Dash, "Revealing quantum metric multipoles in magnetic topological insulator $MnBi_2Te_4$", arXiv preprint, 2605.29595 (2026), under review in Physical Review Letters (2026).

Other publications not included in this thesis

[1] R. Ngaloy, B. Zhao, S. Ershadrad, R. Gupta, M. Davoudiniya, L. Bainsla, L. Sjöström, M. A. Hoque, A. Kalaboukhov, P. Svedlindh, B. Sanyal, and S. P. Dash, "Strong In-Plane Magnetization and Spin Polarization in $(Co_{0.15}Fe_{0.85})_5GeTe_2$/Graphene van der Waals Heterostructure Spin-Valve at Room Temperature", ACS Nano **18**, 5240–5248 (2024).

[2] L. Bainsla, B. Zhao, N. Behera, A. M. Hoque, L. Sjöström, A. Martinelli, M. Abdel-Hafiez, J. Åkerman, and S. P. Dash, "Large out-of-plane spin-orbit torque in topological Weyl semimetal $TaIrTe_4$", Nature Communications **15**, 4649 (2024).

[3] L. Pandey, B. Zhao, K. Tenzin, R. Ngaloy, V. Lamparská, H. Bangar, A. Ali, M. Abdel-Hafiez, G. Zhang, H. Wu, H. Chang, L. Sjöström, P. Rout, J. Sławińska, and S. P. Dash, "Tunable unconventional spin orbit torque magnetization dynamics in van der Waals heterostructures", Nature Communications **16**, 8722 (2025).

List of figures

1.1 Timeline of key advances towards the present day and the contents of this thesis 2

2.1 Timeline of key discoveries in topological quantum materials . . 8
2.2 Symmetries and the quantum geometry 9
2.3 Topological insulators 11
2.4 Experimental TI demonstrations 13
2.5 Charge-spin interconversion in TIs 14
2.6 Weyl semimetals 18
2.7 Experimental WSM demonstrations 19
2.8 Magnetic topological insulators 23
2.9 Experimental magnetic TI demonstrations 25
2.10 Nonlinear transport in $MnBi_2Te_4$ 27

3.1 Techniques for detection of magnetic spin textures 30
3.2 Graphene 33
3.3 Nonlocal spin transport measurements in graphene 35
3.4 Hanle-signal asymmetry under canted spin angles 37
3.5 Long-distance spin transport and spin logic operations in graphene 40
3.6 Graphene spin-valve device for electrical detection of magnetic spin textures in Co 43
3.7 Detection of multi-domain magnetic textures 44
3.8 Micromagnetic simulations of multi-domain magnetic textures . 45
3.9 Magnetic force microscopy of multi-domain magnetic textures . 46
3.10 Detection of magnetic vortex textures in a circular microstructure 47
3.11 Detection of magnetic vortex textures in a square microstructure 49
3.12 Minor-loop and Hanle spin precession measurements of magnetic vortex textures 51
3.13 Graphene spin-valve device for electrical detection of magnetic spin textures in Fe_5GeTe_2 53
3.14 Detection of spin textures in constricted FGT 55
3.15 Additional measurements of the spin-texture spin-valve signals in constricted FGT 56
3.16 Detection of spin textures in notched FGT 58

3.17 Hanle spin precession measurement of spin textures in constricted FGT 59
3.18 Hanle spin precession measurement of spin textures in notched FGT 61

4.1 Graphene/BSTS heterostructure device for nonlocal detection of charge-spin interconversion at room temperature 66
4.2 Raw and asymmetric Hanle spin precession signals from charge-to-spin conversion in BSTS 68
4.3 Geometry and bias current dependence of charge-to-spin conversion signals in graphene/BSTS heterostructure 70
4.4 Gate dependence of charge-to-spin conversion signals in graphene/BSTS heterostructure 72
4.5 Spin-to-charge conversion in graphene/BSTS heterostructure . . 74
4.6 Charge-spin interconversion effects in $TaIrTe_4$ 76
4.7 Spin transport in a graphene spin-valve device without TIT . . 77
4.8 Spin-to-charge conversion in a graphene/TIT spin-valve device . 78
4.9 Charge-to-spin conversion in a graphene/TIT spin-valve device . 79
4.10 Characterisation of the graphene/TIT interface and its impact on the spin signals 81

5.1 The magnetic landscape of $MnBi_2Te_4$ 88
5.2 Spectroscopic characterisation of MBT 89
5.3 Electronic transport and magnetic phase transitions in MBT . . 92
5.4 Magnetic phase diagram of MBT for out-of-plane magnetic fields 94
5.5 Magnetic phase diagram of MBT for in-plane magnetic fields . . 95
5.6 Magnetic phase diagram of MBT for oblique magnetic fields . . 96
5.7 Higher-harmonic nonlinear transport in multilayer MBT 99
5.8 Even-odd behaviour and current scaling of nonlinear transport in MBT 100
5.9 Control measurements to rule out spurious effects 102
5.10 Temperature-dependent higher-harmonic nonlinear transport and conductivity scaling analysis 105
5.11 Magnetic-field-dependent higher-order nonlinear transport . . . 107
5.12 Theoretical calculations of higher-order Drude and quantum metric contributions 109

Abbreviations and symbols

Abbreviations

2D	Two-dimensional
3D	Three-dimensional
AFM	Antiferromagnet; antiferromagnetic
AFM	Atomic force microscopy
ARPES	Angle-resolved photoemission spectroscopy
BSTS	$Bi_{1.5}Sb_{0.5}Te_{1.7}Se_{1.3}$
cAFM	Canted antiferromagnetic
CSC	Charge-to-spin conversion
CVD	Chemical vapour deposition
EBL	Electron beam lithography
FGT	Fe_5GeTe_2
FM	Ferromagnet; ferromagnetic
IP	In-plane
IREE	Inverse Rashba-Edelstein effect
ISHE	Inverse spin Hall effect
MBT	$MnBi_2Te_4$
MFM	Magnetic force microscopy
OOP	Out-of-plane
PM	Paramagnetic
REE	Rashba-Edelstein effect
SCC	Spin-to-charge conversion
SD	Single-domain
SHE	Spin Hall effect
SML	Spin-momentum locking
SL	Septuple layer
SOC	Spin-orbit coupling
SOT	Spin-orbit torque
ST	Spin-texture
TI	Topological insulator
TIT	$TaIrTe_4$
TRS	Time-reversal symmetry
TSML	Topological spin-momentum locking

TSS	Topological surface states
vdW	van der Waals
WSM	Weyl semimetal
XAS	X-ray absorption spectroscopy
XMCD	X-ray magnetic circular dichroism

Symbols

A	Area
B	Magnetic field
D_s	Spin diffusion coefficient
E	Electric field
E, ϵ	Energy
E_F	Fermi energy
G_{ab}	The band-energy normalized quantum metric tensor
g	Landé g factor
H_c	Coercive field
H_r	Recover field
I, I_c	Charge current
I_s	Spin current
I^ω	Alternating charge current with frequency ω
k	Wave vector
L, l	Channel length
M, m	Magnetisation
P	Spin polarisation
p	Momentum
$\mathcal{P}$	Inversion
p_F	Current polarisation
P_J	Interfacial current polarisation
R	Resistance
$R_{abs/tot}$	Relative contribution to the spin relaxation from spin absorption
R_i	Interface resistance
R_{NL}	Nonlocal resistance
$R_{NL,CSC}$	Averaged nonlocal resistance from charge-to-spin conversion
R_s	Spin resistance
R^ω	First-harmonic resistance
$R_\square$	Sheet resistance
S, s	Spin orientation

T	Temperature
t	Thickness
$\mathcal{T}$	Time-reversal
T_N	Néel temperature
V	Bias voltage
V_D	Dirac voltage
V_g	Gate voltage
V_{NL}	Nonlocal voltage
$V_{NL,\parallel/\perp}$	Symmetric/antisymmetric component of nonlocal voltage signal
$V^{n\omega}$	n^{th}-harmonic voltage
w	Channel width; flake width
Γ	Spin absorption rate
ΔV_{NL}	Spin signal amplitude
$\Delta V_{NL,\parallel/\perp}$	Amplitude of symmetric/antisymmetric nonlocal voltage signal component
λ_s	Spin diffusion length
μ	Charge carrier mobility
μ	Electrochemical potential
ρ	Resistivity
σ	Conductivity
τ	Scattering time
τ_s	Spin lifetime
$\tau_{s,abs}$	Spin lifetime contribution from spin absorption
$\tau_{s,SOC}$	Spin lifetime contribution from spin-orbit coupling
φ	Spin canting angle
ω_L	Larmor spin precession frequency
$\uparrow, \downarrow$	Indices to indicate FM contact magnetisation

Constants

e	Elementary charge $e = 1.602 \cdot 10^{-19}\,\text{C}$
h	Planck's constant $h = 6.626 \cdot 10^{-34}\,\text{Js}$
$\hbar$	Planck's reduced constant $\hbar = h/2\pi = 1.055 \cdot 10^{-34}\,\text{Js}$
μ_B	Bohr magneton $\mu_B = 9.274 \cdot 10^{-24}\,\text{J/T}$

Contents

Abstract iii

Acknowledgements vii

List of publications xi

List of figures xiii

Abbreviations and symbols xv

Contents xix

1 Introduction 1

2 Background 7
2.1 Topological insulators 10
2.2 Weyl semimetals 17
2.3 Magnetic topological insulators 22

3 Graphene spin-valve devices for spin sensing 29
3.1 Graphene spintronics 32
3.1.1 Spin transport measurements in graphene 33
3.1.2 Long-distance spin transport and spin logic operations in graphene 38
3.2 Electrical detection of spin textures in ferromagnet Co . . . 42
3.2.1 Detection of multi-domain magnetic textures 42
3.2.2 Detection of magnetic vortex textures in a circular microstructure 45
3.2.3 Detection of magnetic vortex textures in a square microstructure 48
3.3 Electrical detection of spin textures in van der Waals ferromagnet Fe_5GeTe_2 52
3.3.1 Spin-texture spin-valve device with a constriction in Fe_5GeTe_2 52

3.3.2 Spin-texture spin-valve device with a notch in Fe_5GeTe_2 57
3.3.3 Hanle spin precession measurements in spin-texture spin-valve devices 57

4 Charge-spin interconversion in topological quantum materials 63
4.1 Charge-spin interconversion in topological insulator $Bi_{1.5}Sb_{0.5}Te_{1.7}Se_{1.3}$ 65
4.1.1 Charge-to-spin conversion in $Bi_{1.5}Sb_{0.5}Te_{1.7}Se_{1.3}$ . . . 65
4.1.2 Geometry and bias dependence of the charge-to-spin conversion in $Bi_{1.5}Sb_{0.5}Te_{1.7}Se_{1.3}$ 69
4.1.3 Gate voltage dependence of the charge-to-spin conversion in $Bi_{1.5}Sb_{0.5}Te_{1.7}Se_{1.3}$ 71
4.1.4 Spin-to-charge conversion in $Bi_{1.5}Sb_{0.5}Te_{1.7}Se_{1.3}$ . . . 73
4.2 Charge-spin interconversion in Weyl semimetal $TaIrTe_4$ . . . 75
4.2.1 Spin transport in graphene 75
4.2.2 Spin-to-charge conversion in $TaIrTe_4$ 76
4.2.3 Charge-to-spin conversion in $TaIrTe_4$ 78
4.2.4 Impact from the graphene/$TaIrTe_4$ interface on the spin signals 80

5 Magnetic phases and nonlinear transport in a magnetic topological insulator 85
5.1 Magnetic phase characterisation in magnetic topological insulator $MnBi_2Te_4$ 87
5.1.1 Spectroscopic characterisation of $MnBi_2Te_4$ 87
5.1.2 Electronic transport and magnetic phase transitions in $MnBi_2Te_4$ 91
5.1.3 Out-of-plane magnetic phase diagram of $MnBi_2Te_4$. 92
5.1.4 In-plane magnetic phase diagram of $MnBi_2Te_4$ 93
5.1.5 Oblique magnetic phase diagram of $MnBi_2Te_4$ 95
5.2 Higher-order nonlinear transport in magnetic topological insulator $MnBi_2Te_4$ 98
5.2.1 Observation of higher-harmonic transport signals in $MnBi_2Te_4$ 98
5.2.2 Spurious effects and control measurements 101
5.2.3 Temperature dependence and conductivity scaling analysis in $MnBi_2Te_4$ 104
5.2.4 Magnetic field dependence and magnetic phase correlation in $MnBi_2Te_4$ 106

5.2.5 Theoretical calculations of the higher-order nonlinear transport in $MnBi_2Te_4$ 108

6 Summary and outlook **111**
6.1 Summary 111
6.2 Outlook 112

References **117**

Appended papers **177**

Paper I **179**

Paper II **189**

Paper III **201**

Paper IV **211**

Paper V **227**

Paper VI **245**

1 Introduction

Precisely 100 years ago, the new mathematical frameworks of Werner Heisenberg [1] and Erwin Schrödinger [2] marked the starting point of quantum mechanics. In the century since, an incredible number of scientific and technological breakthroughs have been made in the field, including the uncertainty principle [3], relativistic quantum mechanics [4], quantum entanglement [5–7], quantum electrodynamics [8], the theory of superconductivity [9], the integrated circuit [10], the laser [11], quantum computing [12, 13] and many others. This has enabled a staggering progress in technology that has completely transformed our society, letting us take for granted today what would have been impossible not too long ago. Equally important, if not even more so, the exploration of quantum mechanics has led to a better and more detailed understanding of the world around us than humanity has ever had before, along with the clarity that so much still remains to be discovered.

At the same time, our society is facing enormous challenges in terms of rising energy consumption and climate change. A substantial portion of the global energy demand comes from information and communication technology, and the emergence of the internet of things and artificial intelligence in recent years has made this increasingly apparent [14–19]. While predictions of the future energy consumption vary significantly, it remains clear that the development of more energy-efficient technologies is a necessity to manage the continued increase in computing and memory usage worldwide [20–22]. One reason for the large energy consumption of computing technologies is the mainstream use of volatile memory devices, which require a continuous power supply to retain the stored information. Another challenge is the inherent limitations in speed and energy-efficiency of the von Neumann architecture, where logic and memory are spatially separated in a device and information must be transferred between them. Nonvolatile, fast and energy-efficient electronics with integrated logic and memory can therefore become instrumental in the realisation of next-generation computing technologies.

With these perspectives in mind, this PhD thesis attempts to contribute

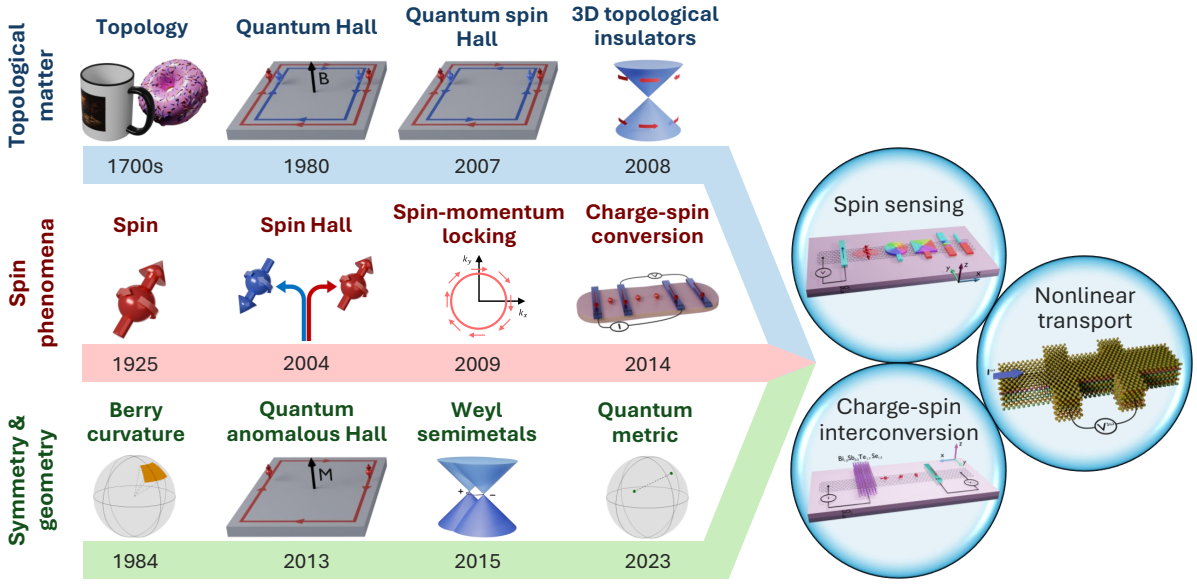


Figure 1.1: Timeline of key advances towards the present day and the contents of this thesis. The timeline has been separated into three topical branches: *topological matter*, *spin phenomena* and *symmetry and (quantum) geometry*. The highlighted key discoveries are elaborated upon below and in Chapter 2.

to both of these broader endeavours, striving towards a more detailed understanding of quantum mechanical properties and effects in materials, as well as towards technological utilisation for faster and more energy-efficient computing applications. An overview of the historical and scientific context of the included works is illustrated with a timeline in Figure 1.1. Two key quantum mechanical concepts stand out as especially important: spin and topology.

The electron spin was originally theorised in 1925 by George Uhlenbeck and Samuel Goudsmit as a 'self-rotation of the electron' [23]. While this semiclassical description has some intuitive merit, spin is a purely quantum mechanical property and an intrinsic angular momentum of the electron [24]. As the popular saying goes: imagine a ball that is spinning around its own axis, except it is not a ball and it is not actually spinning. Regardless, the spin of an electron gives rise to a magnetic moment, which allows it to interact with magnetic fields [25]. As a quantum mechanical property, the electron spin is quantised as $S = \pm 1/2$, which is known as spin-up and spin-down, respectively [26].

Topology is originally a branch of mathematics with roots from the 18$^{\text{th}}$ century [27] that considers properties of objects that are invariant under

smooth deformations. A famous example of this is that a cup and a doughnut are topologically equivalent, since they both have one hole and can be continuously transformed into each other. Beyond this illustrative macroscopic example, the topology of the electronic band structure in materials has important consequences for electronic transport and spin behaviour, and is the origin of many quantum mechanical effects [28]. Among these are charge-spin interconversion effects, which allow efficient conversion between charge currents and spin polarisation.

With spin and topology introduced as key concepts, topological quantum materials arise as an ideal platform for studying spin and topological effects. In essence, quantum materials are a class of materials where quantum mechanical effects are significant even on macroscopic length scales and cannot be properly described by classical mechanics [29]. The additional designation as topological indicates that the quantum material in question also has a nontrivial topology of its electronic band structure. In many of these materials, the prevalent quantum mechanical properties stem from the geometrical confinement of the charge carriers in one or two dimensions. In the case of so-called van der Waals materials, such confinement appears naturally from their layered crystal structure, which consists of atomically thin layers stacked on top of each other and held together by weak van der Waals forces. Additionally, the internal symmetries and inherent quantum mechanical geometry of these materials also have a major impact on many arising phenomena.

Spintronics (*i.e.* spin electronics) utilises the spin degree of freedom of electrons, rather than their charge, to write, store and read information for computing applications [30]. Among the main advantages of spintronics are the fast dynamics and nonvolatility of spin and magnetic states, as well as the possibility of integrated logic and memory [31–33]. The first commercial application of spintronics came already in 1997 through the implementation of giant magnetoresistance in the read-out of hard disk drives [34]. In more recent years, however, many promising novel spintronics technologies have appeared, including magnetic random access memories [35, 36], magnetic racetrack [37, 38] and magnetic tunnel junction [39] memories, spin logic [40, 41] and magnetologic [42] devices as well as probabilistic [43] and neuromorphic [44, 45] computing. Here, the unique properties of topological quantum materials can be very beneficial, such as for efficient spin generation and sensing. Integrating spintronics and topological quantum materials can therefore become an important route towards next-generation fast and energy-efficient nonvolatile computing technologies.

This thesis investigates spin and topological effects in topological van der Waals quantum materials in the context of spintronics. This is mainly done by integrating the topological quantum materials in microfabricated graphene spin-valve devices and Hall-bar devices, where their properties can be studied in detail through spin transport and magnetotransport measurements. The thesis is structured as follows.

Chapter 2 provides a comprehensive overview of the three categories of topological quantum materials that are studied in this thesis: topological insulators, Weyl semimetals and magnetic topological insulators. The general physics, historical backgrounds and important related phenomena are covered to contextualise the contributions of the works in this thesis.

In Chapter 3, graphene spin-valve devices are utilised for sensing polarised spin. Section 3.1 introduces spin transport measurements in graphene spin-valve devices, where pure spin-polarised currents are injected into the graphene and then detected electrically in a nonlocal measurement configuration. Section 3.2 demonstrates the versatility of such spin-valve measurements by detecting magnetic spin textures (*Paper I*). Ferromagnetic Co electrodes with engineered magnetic domain patterns are used to inject nonuniform spin textures, which are measured as distinct multilevel switching patterns. In Section 3.3, the same technique is used for detecting complex spin textures in the van der Waals ferromagnet Fe_5GeTe_2 with geometrical constrictions (*Paper II*).

Chapter 4 probes charge-spin interconversion effects in topological quantum materials. Nonlocal detection of charge-to-spin and spin-to-charge conversion in the topological insulator $Bi_{1.5}Sb_{0.5}Te_{1.7}Se_{1.3}$ at room temperature is presented in Section 4.1 (*Paper III*). Here, the robust interconversion is observed using spin transport measurements in graphene spin-valve devices with van der Waals heterostructures. Section 4.2 shows charge-spin interconversion in the low-symmetry Weyl semimetal $TaIrTe_4$ at room temperature, using similar heterostructure spin-valve devices (*Paper IV*).

Chapter 5 investigates the magnetisation and nonlinear electronic transport in the magnetic topological insulator $MnBi_2Te_4$. First, the magnetic phases of $MnBi_2Te_4$ are characterised in Section 5.1 (*Paper V*). Magnetic phase transitions are probed using nonlinear magnetotransport measurements and detailed magnetic phase diagrams are constructed. Next, Section 5.2 presents the observation of higher-order nonlinear transport due to quantum metric multipoles in Hall-bar devices at cryogenic temperatures (*Paper VI*). The odd-order nonlinear transport components are found to dominate over the even-order ones, and they correlate strongly with the

magnetic phase of the magnetic topological insulator.

Finally, Chapter 6 summarises the thesis and gives an outlook towards future perspectives and further studies.

2 Background

A century after the conceptualisation of the electron spin [23] and nearly two decades after the experimental discovery of the first topological insulators [46, 47], tremendous progress has been made in the fields of spintronics and topological quantum materials. Due to the unique quantum mechanical properties that stem from the nontrivial topology of their electronic band structures, topological quantum materials possess an incredible potential for integration with spintronics (as well as other technologies) for applications towards energy-efficient spin generation and sensing, nonvolatile memories, dissipationless transport, nonreciprocal effects *etc.* In light of recent estimates that more than half of all stoichiometric materials are topological at the Fermi level [48–50], and considering the 2016 Nobel prize in physics award to David J. Thouless, F. Duncan M. Haldane and J. Michael Kosterlitz for their incorporation of topology in the theory of condensed matter physics [51], it appears evident that topological materials and effects are not merely curious fringe-cases but instead central concepts with a clear importance for novel solid state physics.

This chapter attempts to provide a context and an overview to the current state of topological quantum materials and their place in spintronics as well as in the broader field of solid state physics. This is done by reviewing three of the most important classes of topological quantum materials: topological insulators, Weyl semimetals and magnetic topological insulators. The general physics, historical background as well as important theoretical and experimental findings are covered for each of these material classes, and current challenges and future research directions are outlined. Figure 2.1 gives a visual summary of this story, as a timeline with selected key discoveries leading up to the current state of topological insulators, Weyl semimetals and magnetic topological insulators.

However, before going into the details of the three classes of topological quantum materials, two important topics should be covered briefly. The first of these is inversion ($\mathcal{P}$; also known as parity) and time-reversal ($\mathcal{T}$) symmetry. Inversion symmetry means that a system is invariant under reversal of its spatial coordinates, so that $\psi(\boldsymbol{r}) = \psi(-\boldsymbol{r})$ for any wavefunction ψ, while

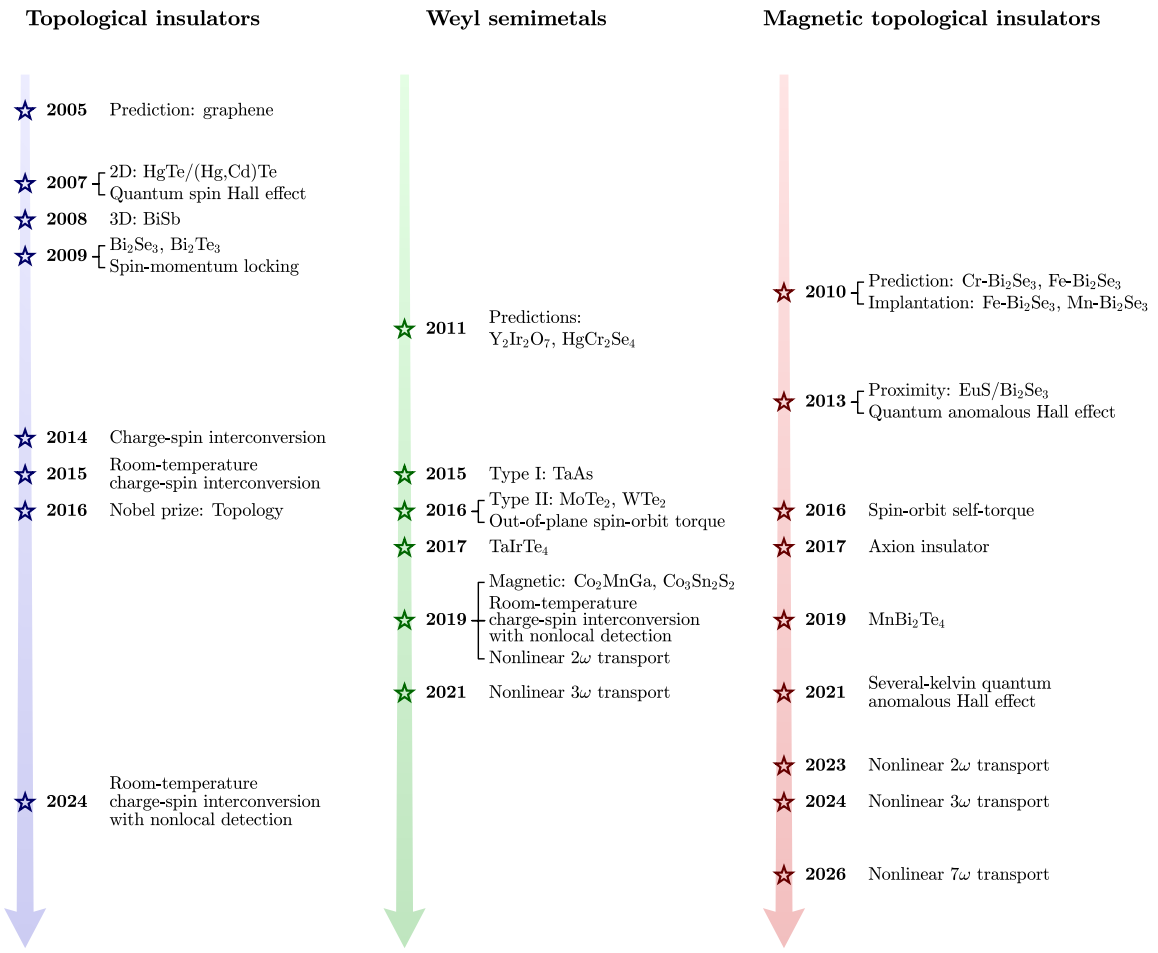


Figure 2.1: Timeline of key discoveries in topological quantum materials. A visual summary of the development of topological insulators, Weyl semimetals and magnetic topological insulators, respectively, including initial theoretical predictions, material realisations and observed phenomena.

time-reversal symmetry (TRS) means that the system is invariant under reversal of time (*i.e.* $\psi(t) = \psi(-t)$; to be noted, this includes spin flipping [52]) [24], as illustrated in Figure 2.2a. As will be seen in the following, the preservation or breaking of $\mathcal{P}$ and $\mathcal{T}$ symmetries are essential for the physical features and effects of topological quantum materials. Noncentrosymmetry and magnetism, which break $\mathcal{P}$ and $\mathcal{T}$ symmetries, respectively, are therefore good examples of material properties that are important to consider.

The other important topic that should be mentioned is quantum geometry. In essence, the quantum geometry is the geometry of the set of Bloch wavefunction eigenstates in Hilbert space [53–55]. It is described by the quantum geometric tensor, which in turn can be decomposed into its real

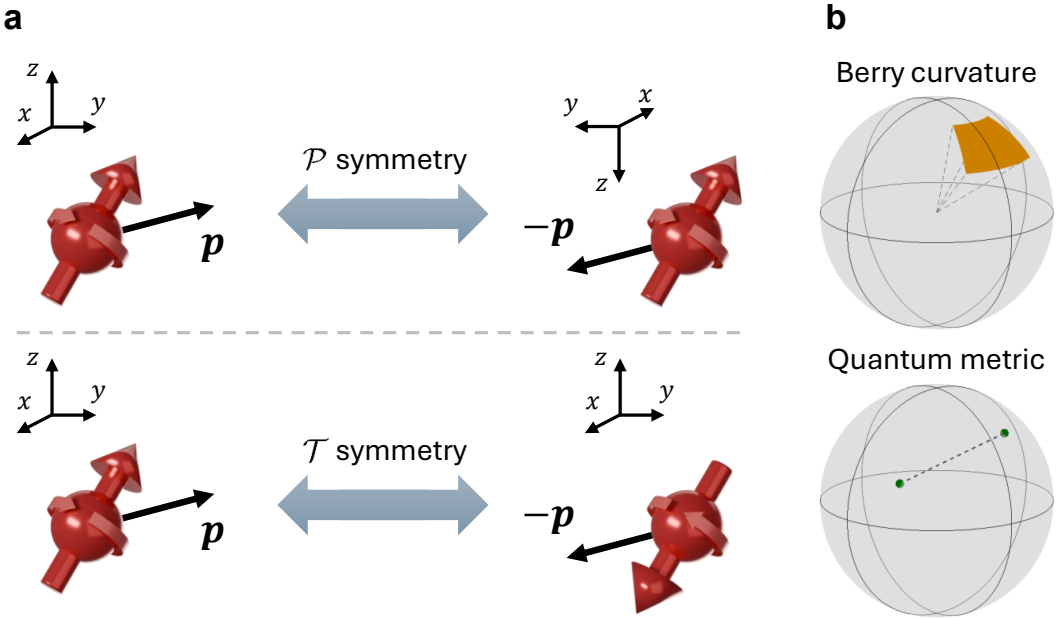


Figure 2.2: Symmetries and the quantum geometry. **(a)** Illustration of inversion ($\mathcal{P}$) and time-reversal ($\mathcal{T}$) symmetry for an electron with momentum $\boldsymbol{p}$. **(b)** Visualisation of the Berry curvature (top) and the quantum metric (bottom) as the curvature and distance, respectively, on a Bloch sphere.

and imaginary components as [56]

$$\boldsymbol{T_{ij}} = \boldsymbol{g_{ij}} + \frac{i}{2}\boldsymbol{\Omega_{ij}}. \tag{2.1}$$

Here, the imaginary part $\boldsymbol{\Omega_{ij}}$ is the Berry curvature, which correlates to the curvature of the wavefunction eigenstates in Hilbert space [57, 58] (visualised in the top panel of Figure 2.2b). It can have an effect similar to an effective magnetic field in a material [59], and has a well-established importance for electronic transport effects (including the anomalous Hall, quantum Hall, spin Hall and nonlinear transport effects), polarisation, orbital magnetism and topological spintronics [53, 60–64]. The real component of the quantum geometry is the quantum metric $\boldsymbol{g_{ij}}$, which measures distances between eigenstates in Hilbert space [56, 65] (as indicated in the bottom panel of Figure 2.2b). Comparatively, it is significantly less studied than the Berry curvature, but the quantum metric has in recent years begun to gain more attention [64, 66–69] as it has been found to have an important influence on electronic transport, including nonlinear transport effects, superconductivity, flat-band physics and other topological effects [53, 70–76].

2.1 Topological insulators

Topological insulators (TIs) are a class of topological quantum materials that have an insulating bulk and conducting surfaces. This is made possible by their unique inverted electronic band structure, where strong spin-orbit coupling (SOC; a relativistic effect that couples the spin and momentum of electrons [25]) pushes the valence and conduction bands together until the top of the valence band overlaps with the bottom of the conduction band [48, 77]. The resulting crossing points are forbidden by symmetry, and a bulk band gap is formed through band hybridisation [78, 79] (illustrated in Figure 2.3a). Because of the band inversion, a transition between two different topological invariants appears at the interface between the TI and an ordinary insulator or vacuum [80]. Continuity of the electronic wave-function demands that the band gap is closed at this interface, and metallic surface states are thus formed [77, 81], as shown in blue in Figure 2.3b. Importantly, since these surface states arise as a consequence of topology, they are topologically protected and robust to disorder as long as the topology of the bulk TI remains [80, 82].

The electronic band structure of the topological surface states (TSS) form so-called Dirac cones, where the linear dispersion relation following the Dirac equation corresponds to massless fermions [4, 83]. The focal point of these cones is the Dirac point with a fourfold Kramers' degeneracy, which is the topologically protected crossing point of the two (twofold degenerate) bands [29]. Figure 2.3c shows a schematic Dirac cone of a TI, where $k_{x,y}$ and E are the wave vector and electron energy, respectively. The strong SOC of the TSS manifests as spin-momentum locking (SML), where the spin and momentum of electrons are locked orthogonally to each other [83]. The resulting spin polarization of the Dirac cones is represented by red arrows in Figure 2.3c. Because of the round shape of the Dirac cones, the SML results in helical spin textures on a Fermi surface in the bulk band gap, similar to the illustration in Figure 2.3d. Notably, this helicity is opposite for electrons and holes above and below the Dirac point, respectively, as indicated by the arrows in Figure 2.3c.

It should be mentioned that the discussion so far, concerning TIs with an insulating bulk and conducting TSS, has mainly regarded so-called strong three-dimensional (3D) TIs. In the two-dimensional (2D) limit, the inverted band structure instead gives rise to topological edge states around the circumference of the 2D TI sheet [84]. Furthermore, weak 3D TIs resemble stacks of 2D TIs in the manner that they have topological edge states but

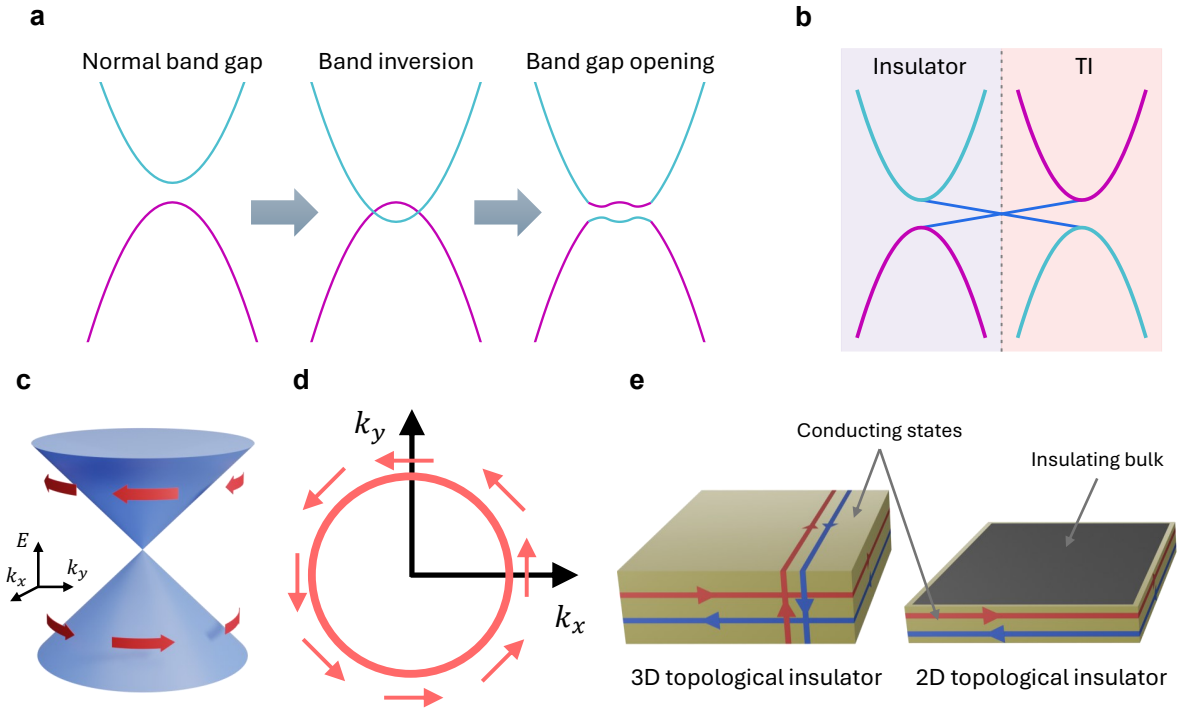


Figure 2.3: Topological insulators. **(a)** Schematic illustration of the band inversion and bulk band gap opening in a TI, resulting in an inverted bulk band gap. **(b)** Illustration of the formation of metallic surface states at the interface between an ordinary insulator and a TI, where the TSS (blue) maintain continuity of the electronic wavefunction between the direct and inverted bulk band gaps of the ordinary insulator and the TI, respectively. **(c)** Schematic band structure of the TSS in a TI. The spin polarization of the TSS is indicated with red arrows. **(d)** Schematic of a helical spin texture of the TSS on the Fermi surface of a TI. The spin polarisation of the TSS is indicated with arrows. **(e)** Schematic illustration of the surface conduction of a strong 3D TI and the edge conduction of a 2D TI (or a weak 3D TI).

remain insulating on their top and bottom surfaces [85, 86]. This distinction is illustrated in Figure 2.3e, where the spin-polarised conduction of topological edge and surface states is shown.

The first theoretical prediction of a TI was in 2D graphene in 2005 [84, 87], although this was never experimentally realised due to the weak SOC of graphene [80, 88, 89]. The first experimental demonstration of a TI came instead in 2D HgTe/(Hg,Cd)Te quantum wells in 2007 *via* the observation of the quantum spin Hall effect [46], after a theoretical prediction in the year prior [90]. In the quantum spin Hall effect (which is the spin counterpart to the quantum Hall effect [91]), the topological edge states host quantised dissipationless spin transport channels, since backscattering is only allowed

during a spin-flipping event due to the SML, which in turn is forbidden under the preservation of TRS [84, 92]. As is illustrated in Figure 2.4a, the counterpropagating spins of opposite polarisation generate a spin current I_s transverse to the applied charge current. Resistance values near the quantised value $h/2e^2$ (where h is Planck's constant and e is the elementary charge) measured in the HgTe/(Hg,Cd)Te quantum wells, are shown in Figure 2.4b, indicating ballistic helical edge transport through the quantum spin Hall effect [46].

Following the prediction of the 2D TI, several theoretical predictions were made of its 3D counterpart [59, 85, 97–100], including specific predictions of the alloy $Bi_{1-x}Sb_x$ [59, 98]. In 2008, $Bi_{1-x}Sb_x$ was indeed found as the first 3D TI through a direct observation of the Dirac cones of the TSS using angle-resolved photoemission spectroscopy (ARPES) [47], as shown in Figure 2.4c. In the same material, the spin polarisation of the TSS could be resolved using Mott polarimetry [101]. Soon after, this was followed by the theoretical predictions and experimental discoveries of the TIs Bi_2Se_3 [95, 96, 102], Bi_2Te_3 [94, 96, 102, 103] and Sb_2Te_3 [102, 103], which are layered van der Waals (vdW) materials and have a more idealised TI structure with larger bulk band gaps and simpler surface states than $Bi_{1-x}Sb_x$ [80, 82]. The vdW crystal structure with layered quintuple layers of Bi_2Te_3 is shown as an example in Figure 2.4d, and a representative ARPES image of the band structure of Bi_2Se_3 in Figure 2.4e demonstrates a large bulk bandgap and well-resolved TSS [95, 96]. Additionally, Figure 2.4f verifies the spin polarisation of the SML in the helical Fermi surface of Bi_2Te_3, as measured through spin-resolved ARPES [96]. A whole family of related TI compounds following the $Bi_{2-x}Sb_xTe_{3-y}Se_y$ formula has since been developed, where the stoichiometry has been optimised to tune the Fermi level towards the Dirac point in order to minimise bulk conductance and maximise the contributions from the TSS [104–110].

The most central application of TIs for spintronics is arguably charge-spin interconversion, where the strong SOC of TIs promotes efficient generation and sensing of spin polarisation. This conversion between charge currents and spin polarisation can originate from three possible microscopic mechanisms in a TI: the SML of the TSS, the Rashba-Edelstein effect (REE) and the spin Hall effect (SHE). Charge-to-spin conversion (CSC) through the SML of the TSS (also known as the Edelstein effect or topological spin momentum locking [TSML]) is facilitated by the spin polarisation of the Dirac cone of a TI. Under the application of an electric field E, the helical spin texture on the Fermi surface is shifted from its equilibrium state

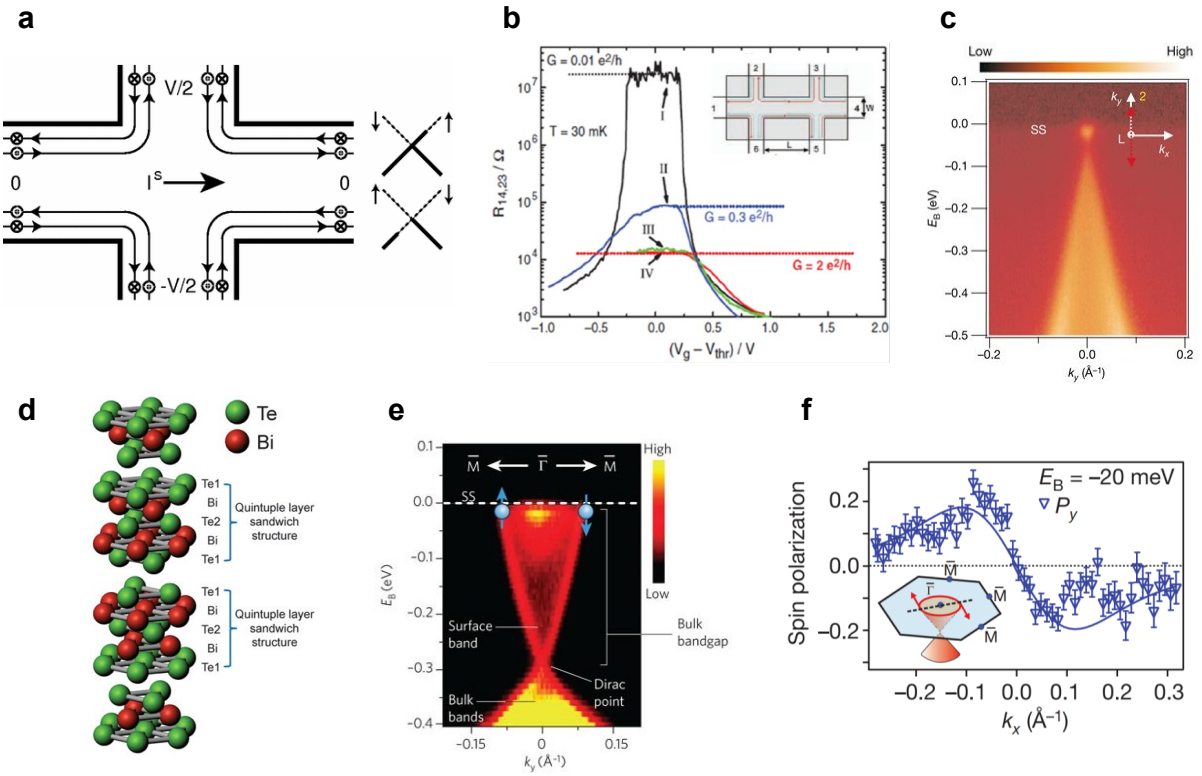


Figure 2.4: Experimental TI demonstrations. **(a)** Schematic diagram of the quantum spin Hall effect with counterpropagating spins along the edges of a 2D TI under the application of a bias voltage V. Insets: Indications of the respective population of the topological edge states. Adapted from [84]. **(b)** Four-terminal resistances of HgTe/(Hg,Cd)Te quantum-well Hall bars of different dimensions (samples I-IV). Samples II-IV have an inverted band structure and near-quantised resistance values. Inset: Schematic of a Hall bar sample. Adapted from [46, 93]. **(c)** ARPES spectrum showcasing Dirac cones of the TSS in the electronic band structure of $Bi_{1-x}Sb_x$. Adapted from [47]. **(d)** Schematic of the crystal structure of Bi_2Te_3. Adapted from [94]. **(e)** ARPES spectrum showcasing the electronic band structure of Bi_2Se_3. The spin polarization of the TSS is indicated schematically. Adapted from [80, 95, 96]. **(f)** Spin y polarisation of the TSS in Bi_2Te_3, measured using spin-resolved ARPES. Inset: Schematic of the cut direction of the measurement. Adapted from [96].

by a crystal momentum change Δk, as visualised in Figure 2.5a, and the occupation change on the Dirac cone causes a corresponding net spin polarisation through the SML with the polarised spins perpendicular to the momentum of the charge carriers [111, 112]. During the inverse effect (*i.e.* spin-to-charge conversion [SCC]), the spin texture is analogously shifted by the injection of a spin polarisation, which generates a perpendicular net momentum of the charge carriers and hence a charge current, following Onsager

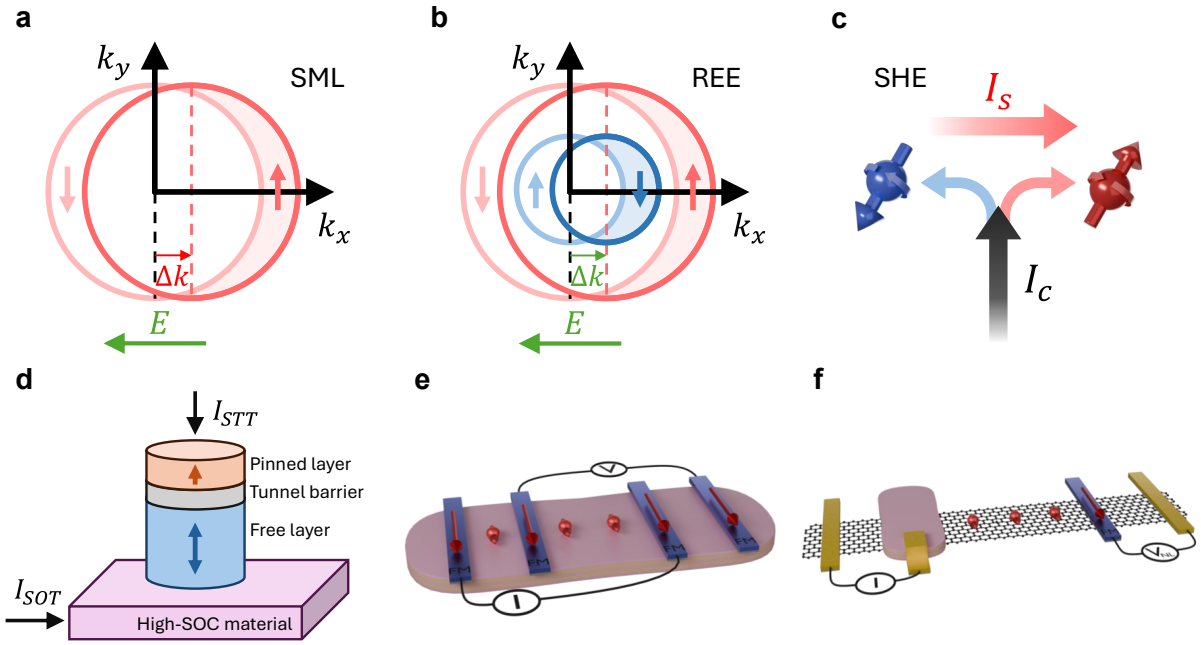


Figure 2.5: Charge-spin interconversion in TIs. **(a,b)** Schematics of CSC through the SML of the TSS (a) and the REE (b), respectively, showing net spin polarisation as the helical spin texture of the Fermi surface is shifted by an electric field. **(c)** Schematic of CSC through the SHE, showing the generation of a transverse spin current I_s from an applied charge current I_c. **(d)** Schematic of spin-transfer torque (STT) and SOT magnetisation switching of the free layer in a magnetic tunnel junction. **(e-f)** Schematic of a local (e) and a nonlocal (f) spin-valve device, respectively, for detection of charge-spin interconversion in TIs.

reciprocity [113–115]. It should be noted that the spin polarisation that is generated by the SML of the TSS in a TI is unchanged as the Fermi level is tuned across the Dirac point, since the opposite momenta of electrons and holes are counteracted by the opposite chirality of the spin textures above and below the Dirac point [116] (as shown in Figure 2.3c).

The REE functions under a similar principle to the CSC from the SML of the TSS but with a fundamental difference: here, the helical spin texture comes from the bulk states of the TI. Under broken inversion symmetry, the bulk bands are spin-split and shifted in momentum space by the Rashba effect, which causes a double-helical spin texture on a Fermi level outside the bulk band gap [117–119], as illustrated in Figure 2.5b. Notably, the inner helix has an opposite helicity compared to the outer one [111]. In this way, the two helices partly cancel each other's impact, but a net spin accumulation is still generated perpendicular to the charge carrier momentum.

Analogously, polarised spins can alternatively be converted into a charge current through the inverse REE (IREE). Since the Rashba effect requires $\mathcal{P}$ symmetry to be broken, the REE and IREE are interface effects where both the charge current and the spin polarisation are parallel to the surface of a TI [117, 120].

Finally, the SHE is the spin analogue of the ordinary Hall effect [121, 122]. When a charge current is applied through a material with strong SOC, the charge carriers are diverted in opposite directions based on their spin, either through extrinsic skew-scattering [123–125] or through an intrinsic spin-orbit field [126–129]. In this way, a transverse pure spin current is generated, which is shown in Figure 2.5c. In the reciprocal effect (the inverse SHE [ISHE]), a polarised spin current can in the same way give rise to a transverse charge current [130]. Importantly, the charge current I_c, the spin current I_s and the spin polarisation S are all required to be orthogonal to each other under the inversion symmetry of a TI [122, 130]. The case with broken inversion symmetry in Weyl semimetals is discussed in Section 2.2.

Importantly, these charge-spin interconversion mechanisms can be utilised for spin logic as well as for magnetic memory applications. In the latter case, the polarised spin currents can, for example, be used for efficient switching of magnets in magnetic tunnel junction devices through spin-orbit torque (SOT). A magnetic tunnel junction consists of two ferromagnetic (FM) layers separated by an insulator [30, 131], as shown in Figure 2.5d. While one FM layer has a fixed magnetisation, the magnetic state of the other, so-called free layer, can be switched as a nonvolatile way of storing information. This information can then be read out electrically *via* tunnelling magnetoresistance, in which the resistance through the magnetic tunnel junction is low (high) when the two FM layers are magnetised in parallel (antiparallel) [132–134]. In conventional electronics, switching of the free layer is done using spin-transfer torque, where a current is passed through the magnetic tunnel junction and the polarised spins of the fixed magnetic layer is used to switch the free one [135–137]. On the other hand, in SOT-based devices, a polarised spin current is instead generated through charge-spin interconversion in a nonmagnetic material, which can then be used to switch the free layer [138–140], as indicated in Figure 2.5d. Compared to spin-transfer torque, SOT can realise more energy-efficient and faster magnetisation switching as well as a higher device durability, since the writing current is not passed through the magnetic tunnel junction itself [141–144]. To be noted, SOT can also be very useful for other promising spintronics applications such as magnetic racetrack memories [37, 145], nano-oscillators [146, 147], neuromorphic com-

puting devices [148, 149], spin sensors [150, 151] *etc.* Thanks to their strong SOC and efficient charge-spin interconversion, TIs are excellent SOT materials [143, 152–155] and have been demonstrated to dramatically outperform the SOT efficiency of conventional heavy metals [139, 156–163]. This can make them vital components in next-generation SOT technologies.

In order to properly study the charge-spin interconversion and spin polarisation in detail, however, spin transport measurements in spin-valve devices have important advantages. Instead of probing the charge-spin interconversion indirectly through the torques in SOT devices, spin-valve devices allow direct sensing of the polarised spins. Such spin transport sensing, including spin-valve and Hanle spin precession measurements, are elaborated upon in detail in Chapters 3-4. Typically, TI charge-spin interconversion experiments with spin transport in spin-valve devices have been performed using local device geometries, where the spin is probed inside of the charge current loop (exemplified in Figure 2.5e), and at cryogenic temperatures, where the TI bulk states are (at least partially) passivated through freeze-out so that the TSS have a larger transport contribution [164–170]. In contrast, nonlocal device geometries function by detecting pure spin currents outside of the charge current loop (illustrated in Figure 2.5f) to achieve more reliable measurements with minimal signal contributions from charge-related effects. Until now, charge-spin interconversion in TI spin-valve devices has been demonstrated at room temperature in a local device geometry [171] (as well as in nonlocal geometries where the charge-spin interconversion was generated by proximity-induced SOC in graphene [172, 173]), but nonlocal measurements with charge-spin interconversion in the TI have been limited to cryogenic temperatures around 15 K [174]. The realisation of reliable nonlocal detection of charge-spin interconversion in a TI at room temperature would therefore constitute an important next step towards all-electrical room-temperature spintronic devices and applications.

2.2 Weyl semimetals

Weyl semimetals (WSMs) constitute another class of topological quantum materials. Although they bear similarities with TIs, a key difference is that WSMs have Weyl nodes (also known as Weyl points) in their bulk instead of Dirac points on their surfaces [78]. A Weyl node is a topologically protected crossing point where the linear dispersion relation is described by the Weyl equation [175, 176]. Because of their location in the bulk, as opposed to at the surface, the linear dispersion at the Weyl nodes persists in all directions in 3D momentum space [177], and WSMs are semimetallic and fully conducting in the bulk.

Importantly, the Weyl equation considers a 'handedness' of the massless Weyl fermions [29, 176], and a Weyl node can essentially be understood as the chiral twofold degenerate half of a split-up (achiral and fourfold degenerate) Dirac point [178], as illustrated in Figure 2.6a. A requirement for the existence of Weyl nodes is therefore that the material is noncentrosymmetric with broken parity symmetry (or has a broken TRS in the case of magnetic materials) in order to lift the spin degeneracy [77, 78, 179]. Since this so-called Chern chirality must total to zero overall in the Brillouin zone, Weyl nodes always appear in pairs with opposite chirality [178, 180]. Depending on their chiral charge, Weyl nodes act as either sources or sinks of Berry curvature, which gives them topological protection since they can only be destroyed by annihilating with another Weyl node of opposite chirality [61, 181].

A consequence of the Weyl nodes being Berry curvature sources and sinks, is the formation of unique TSS in WSMs [183, 184]. In contrast to the helical Fermi surface of a TI, WSMs exhibit open Fermi arcs. These Fermi arcs connect the projection of two Weyl nodes onto the surface of the WSM [175, 177], as visualised in Figure 2.6b. Alternatively, the two Fermi arcs on the top and bottom surface of a WSM can be imagined as two halves of a helical Fermi surface that are connected through the bulk *via* the two Weyl nodes, and the top and bottom Fermi arcs would in fact form a closed Fermi surface in the 2D limit [184]. Despite their topologically different origin as compared to the Dirac cones on the surfaces of TIs, SML has been observed also in WSM Fermi arcs [185–187].

To be noted, WSMs can be divided into two categories: type I and type II, both of which are illustrated in Figure 2.6c. The former has upright Weyl cones with a vanishing density of states for a Fermi surface at the Weyl node [188]. Meanwhile, type II WSMs with broken Lorentz symmetry

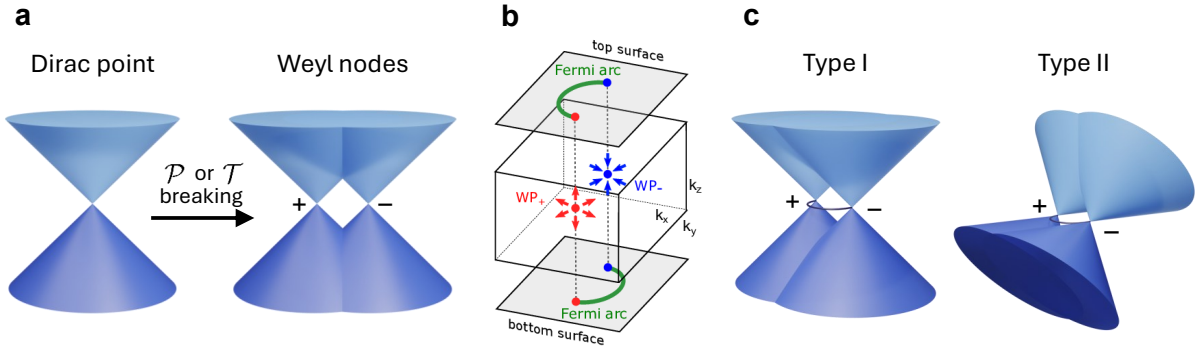


Figure 2.6: Weyl semimetals. (a) Schematic visualisation of a Dirac point being split into two Weyl nodes with opposite chirality through the breaking of parity ($\mathcal{P}$) or time-reversal ($\mathcal{T}$) symmetry. **(b)** Schematic of Fermi arcs and Weyl nodes on the top and bottom surfaces and in the bulk, respectively, of a WSM. Adapted from [182]. **(c)** Schematics of type I and type II WSMs, with upright and tilted Weyl cones, respectively.

instead have band structures with heavily tilted Weyl cones [189]. This leads to electron and hole pockets on the Fermi surface, with the Weyl node as a contact point between them [181]. The Weyl nodes of type II WSMs are still topologically protected, but the tilted nature of the Weyl nodes can give rise to unique electronic properties [188, 190], as will be mentioned below.

The initial theoretical predictions of WSMs were made for pyrochlore iridates such as $Y_2Ir_2O_7$ [183], $HgCr_2Se_4$ [191] and TI multilayers [192]. The first experimental demonstrations were, however, made in the noncentrosymmetric 3D material TaAs in 2015 through a direct observation of Fermi arcs and linear bulk band dispersion using ARPES [193–195] (shown in Figure 2.7a), following theoretical predictions made earlier in the same year [196, 197]. Similar observations were soon after made in other compounds of the same family, including TaP [198], NbAs [194] and NbP [199]. Also in 2015, the existence of type II WSMs was predicted for the vdW transition metal dichalcogenides WTe_2 [189] and $MoTe_2$ [200], which was verified experimentally with ARPES, where Fermi arcs could be observed between electron and hole pockets [201–205]. Not long after, the type II WSM $TaIrTe_4$ was predicted [206] and experimentally confirmed [207], which is especially attractive due to its relatively simple band structure with a minimal number of four well-separated Weyl nodes. Finally, despite initial experimental challenges relating to spectroscopic resolution and complex band structures [208], the magnetic WSM Co_2MnGa [209] and $Co_3Sn_2S_2$ [210,

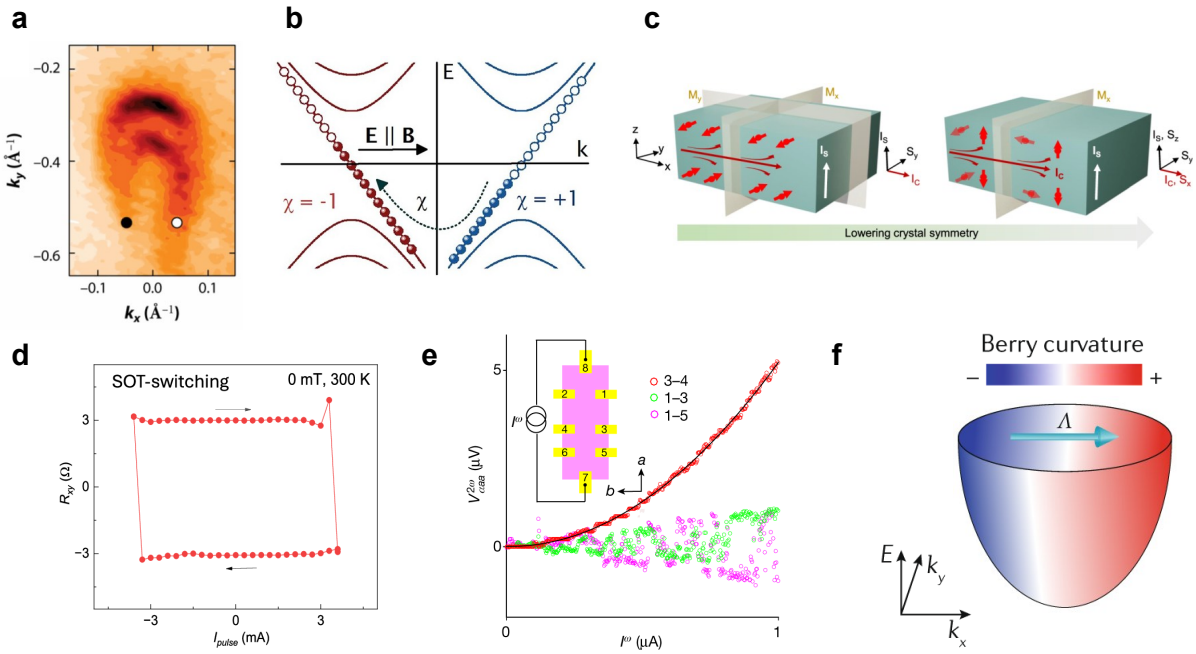


Figure 2.7: Experimental WSM demonstrations. **(a)** ARPES Fermi surface map of two Fermi arcs in TaAs. The projection of two Weyl nodes with opposite chirality are indicated with black and white dots. Adapted from [194, 212]. **(b)** Schematic of the chiral anomaly in a WSM under the application of parallel electric and magnetic fields, where charge carriers are pumped from one chirality to the other. Adapted from [213]. **(c)** Schematics of conventional and unconventional charge-spin interconversion in high-SOC materials with higher and lower crystal symmetries, where the former follows an orthogonality between the charge current, the spin current and the spin polarisation whereas the latter does not. Adapted from [214]. **(d)** Field-free SOT switching of in a $TaIrTe_4/Fe_3GaTe_2$ heterostructure device at room temperature. Adapted from [215]. **(e)** Nonlinear Hall effect signal (red) in WTe_2, following a quadratic IV characteristic. Longitudinal voltages (green and pink) in the same device show no nonlinear transport behaviour. Inset: Schematic of the Hall bar device. Adapted from [216]. **(f)** Schematic of a dipole Λ in the Berry curvature, corresponding to the second-order nonlinear Hall effect. Adapted from [216, 217].

211] with broken TRS were unambiguously identified in 2019.

The broken symmetries and unique band structure of WSMs with chiral Weyl nodes allows the rise of a chiral anomaly (*i.e.* breaking of the conservation of charge chirality) under the application of parallel electric and magnetic fields [179, 218]. As a side note, a single Weyl node breaks even the conservation of charge, but this is cancelled by the presence of multiple Weyl nodes with opposite chirality in real materials [29, 184]. However,

even though the total charge is conserved, the chiral anomaly is generated as a valley polarisation through a charge flow between Weyl nodes [184, 219, 220] as illustrated in Figure 2.7b. This can lead to exotic electronic transport effects such as a negative magnetoresistance [213, 219, 221–225], a giant anomalous Hall effect [226, 227] and the planar Hall effect [228, 229]. Interestingly, the chiral anomaly differs significantly between type I and type II WSMs, and manifests with an anisotropy with respect to the crystal orientation in the latter type [188, 230].

Another important feature of WSMs is their applicability for charge-spin interconversion. Similarly to TIs, WSMs have strong SOC and can facilitate charge-spin interconversion through the SHE and the REE, as well as *via* the SML of their Fermi arcs [111, 186, 231–235]. Differently from TIs, however, the low crystal symmetries of WSMs open up the possibility of unconventional charge-spin interconversion where the charge current, the spin current and the spin polarisation are not orthogonal to each other [236–244], as is imaged schematically in Figure 2.7c. Especially important, this can allow for CSC where in-plane (IP) charge currents can generate out-of-plane (OOP) spin currents and polarisations, which is beneficial for field-free SOT switching of magnets with a perpendicular magnetic anisotropy [139, 143]. The combination of strong SOC and unconventional spin polarisations thus make WSMs very attractive for energy-efficient SOT memory and logic devices [33, 140, 245, 246]. Recently, highly energy-efficient OOP SOTs and field-free magnetisation switching have been observed using $TaIrTe_4$ [214, 215, 247] (shown in Figure 2.7d), but the unconventional charge-spin interconversion has so far only been probed indirectly through SOT measurements in bilayer devices and a direct detection of the spin polarisation is still missing.

Finally, yet another consequence of the low symmetries of WSMs is the appearance of nonlinear electronic transport in noncentrosymmetric WSMs with broken $\mathcal{P}$ symmetry [217, 248]. Here, the current-voltage characteristics take on a power-law shape $V \sim I^n$, extending beyond Ohm's law [249]. The second-order nonlinear Hall effect was theoretically predicted in 2015 [250] and was first observed experimentally in WTe_2 in 2019 using lock-in amplifiers at low temperatures [251]. As can be seen in Figure 2.7e, the transverse Hall voltage depends quadratically on the applied current. The nonlinear Hall effect has since been demonstrated in various WSMs up to room temperature [215, 216, 252–257], and its third-order equivalent has been found as well [258–260]. Physically, the nonlinear transport originates from features in the Berry curvature, specifically from Berry curvature

dipoles (illustrated in Figure 2.7f) and from the Berry curvature polarisability for second- and third-order nonlinear Hall effects, respectively, under the application of an electric field [217, 250, 258, 261]. This makes nonlinear transport a powerful tool for probing the quantum geometry of materials, as is discussed further in the next section. Additionally, nonlinear transport is also promising for technical applications such as rectification and energy harvesting [252, 256].

2.3 Magnetic topological insulators

A magnetic TI is, as the name suggests, a TI where magnetism has been introduced into the material. The inclusion of magnetism breaks TRS and opens up a gap in the TSS near the Dirac point on the top and bottom surfaces of the TI, leaving only ungapped edge states at the sides or edges of the magnetic TI that are parallel with the TI magnetisation [82, 262]. This exchange gap opening in the surface-state Dirac cone with the introduction of magnetism is illustrated in Figure 2.8a, where the remaining one-dimensional edge states are also visualised. As will be seen in the following, the integration of topology and magnetism in the same material and breaking of $\mathcal{T}$ symmetry enable an abundance of novel physical phenomena.

Although the combination of topological physics and magnetism in a single material makes for a tantalising platform for studying exotic physics, the experimental realisation of magnetic TIs is not entirely straightforward and different methods have emerged. The earliest works were based on nonmagnetic TIs with magnetic dopants added through ion implantation [263–265]. While this approach has been successful in achieving magnetic TIs, the inevitable defects and dopant inhomogeneity from the ion implantation process are nevertheless considerable drawbacks that are detrimental to novel physical effects [266]. An alternative is modulation doping, where highly doped TIs and pristine TIs are stacked on top of each other [267]. This reduces disorder while maintaining magnetism in the TI structure, but too high doping levels can destroy the TI phase by significantly weakening the SOC [268]. A third method consists of magnetism in TIs through the proximity effect in heterostructures with magnetic insulators, which allows a low defect density in the TI [269–271]. However, the reliance on high-quality (ideally atomically sharp) interfaces for a maximum proximity-induced exchange coupling in the TI remains a practical limitation [268]. Finally, TIs can be intrinsically magnetic by a stoichiometric inclusion of magnetic atoms [272, 273]. Such intrinsically magnetic TIs have recently gathered enormous attention due to their promise as high-quality and robust magnetic TI materials with minimal disorder [274, 275].

One of the main motivators in the search for magnetic TIs was the realisation of the quantum anomalous Hall effect. Completing the set of the Hall [121], spin Hall [125] and anomalous Hall [276] effects and their quantised counterparts [46, 91, 277], the quantum anomalous Hall effect can best be seen as the magnetic-field-free analogue of the quantum Hall effect and the single-spin version of the quantum spin Hall effect. Namely, the chiral edge

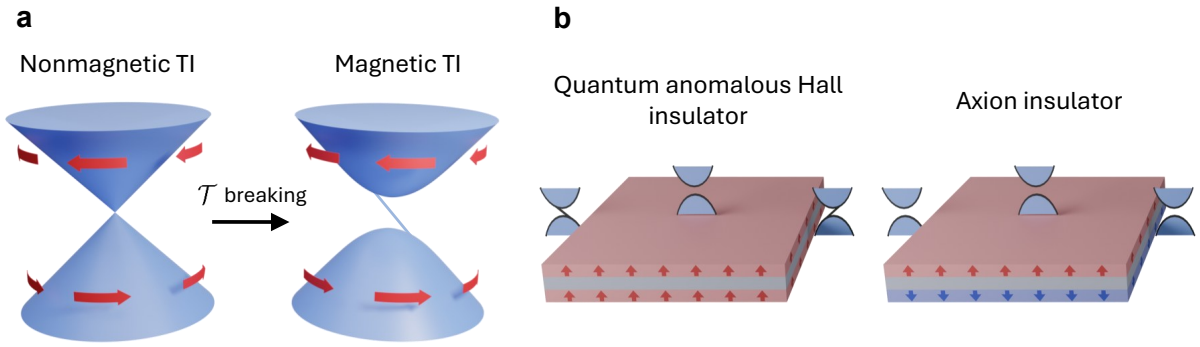


Figure 2.8: Magnetic topological insulators. (a) Schematic of the band-gap opening in the Dirac cones of a TI as $\mathcal{T}$ symmetry is broken by the introduction of magnetism. Ungapped edge states are indicated in the exchange gap of the TSS in the magnetic TI. The red arrows indicate the SML of the TSS. **(b)** Schematics of a quantum anomalous Hall insulator with FM coupling and dissipationless conduction through the ungapped edge states (left) and an axion insulator with AFM coupling and gapped edge states (right).

states of a magnetic TI can carry a dissipationless and spin-polarised charge current to generate a quantised transverse resistance of h/e^2 and a vanishing longitudinal resistance, even in the absence of an external magnetic field [278], which is illustrated to the left in Figure 2.8b. Such a quantised resistance in the absence of magnetic fields can be of critical use for metrology applications, since it can be implemented together with superconducting Josephson junctions for voltage and current quantisation in a single device [279]. The dissipationless transport of the quantum anomalous Hall effect can also become revolutionary for energy-efficient electronics and communication, especially if it can be realised at room temperature [266, 274]. Interestingly, layered magnetic TI structures can host quantum anomalous Hall states with higher Chern numbers, essentially connecting multiple quantum anomalous Hall channels in parallel, if the magnetic layers are coupled ferromagnetically [280, 281]. On the other hand, antiferromagnetic (AFM) layered structures lead to a cancellation of the quantum anomalous Hall conductivities with opposite chirality, which results in a fully gapped axion insulator state for a fully compensated AFM TI [282, 283], as shown to the right in Figure 2.8b, and can be a platform for studying exotic axion electrodynamics [99, 282, 284, 285].

An initial theoretical model for magnetic TIs was made already in 1988 [286], but the first practical material prediction (which was based on magnetically doped TIs) was not made until over twenty years later [263]. The first experimental demonstration came in 2010, where magnetic Fe and Mn

dopants were added to Bi_2Se_3 through ion implantation, and small exchange gap openings could be observed through ARPES measurements [264], which is shown in Figure 2.9a and can be compared to the nonmagnetic TI ARPES spectrum in Figure 2.4e. Soon thereafter, multiple other magnetic TIs, including Mn-, Cr- and V-doped $Bi_2Se_{3-x}Te_x$ and $Bi_{2-x}Sb_xTe_3$ compounds, were realised using the same ion-implantation method [287–290]. In 2013, both the prediction [269] and the realisation [270] of TIs with proximity-induced magnetism appeared, where the experimental demonstration was done in a EuS/Bi_2Se_3 heterostructure. Later works included heterostructures with *e.g.* $Y_3Fe_5O_{12}$, $Cr_2Ge_2Te_6$ and $MnBi_2Se_4$ [291–295]. Importantly, 2013 also saw the first experimental demonstration of the quantum anomalous Hall effect in a thin film of Cr-doped $Bi_{2-x}Sb_xTe_3$ [277] with the highly quantised Hall resistivity shown in Figure 2.9b. Four years later, this was followed by the first clear demonstration of the axion insulator state in a modulation-doped variant of the same material [285]. However, despite extensive research activity with many demonstrations of the quantum anomalous Hall effect in magnetic TIs based on ion implantation [296–311], modulation doping [267, 312, 313] and proximity effects [314] as well as higher-Chern-number quantum anomalous Hall effects in layered magnetic TIs [281, 315, 316], the material challenges mentioned above limited experiments to low temperatures in the millikelvin to $\sim 2\,\mathrm{K}$ range [268, 283].

For this reason, among others, the first intrinsic magnetic TI $MnBi_2Te_4$ (MBT) has attracted considerable attention since its theoretical prediction and experimental observation in 2019 [272, 273, 275, 318]. It is a vdW material consisting of stacked septuple layers (SLs) as illustrated in Figure 2.9c, with a nontrivial topology similar to Bi_2Te_3 and naturally incorporated magnetism *via* its stoichiometrically included Mn atoms [274, 318, 319]. While ARPES results in MBT have been controversial due to variations between samples due to differing defect concentrations [273, 275, 320–325], spectra with gap openings in the TSS have nevertheless been observed, as in Figure 2.9d. Interestingly, MBT is an A-type antiferromagnet (AFM), where the intralayer magnetic ordering of each SL is FM while adjacent SLs are antiferromagnetically ordered [273, 326]. This leads to a layer-dependent magnetisation of the material where monolayer MBT is fully FM while thicker flakes consisting of an even (odd) number of SLs are fully compensated (uncompensated) AFMs [317, 327–329]. Hence, MBT with odd and even number of SLs can host the quantum anomalous Hall effect [317, 330] (shown in Figure 2.9e) and the axion insulator state [331, 332], respectively. Indeed, due to its ordered crystal structure, high-quality samples have shown the

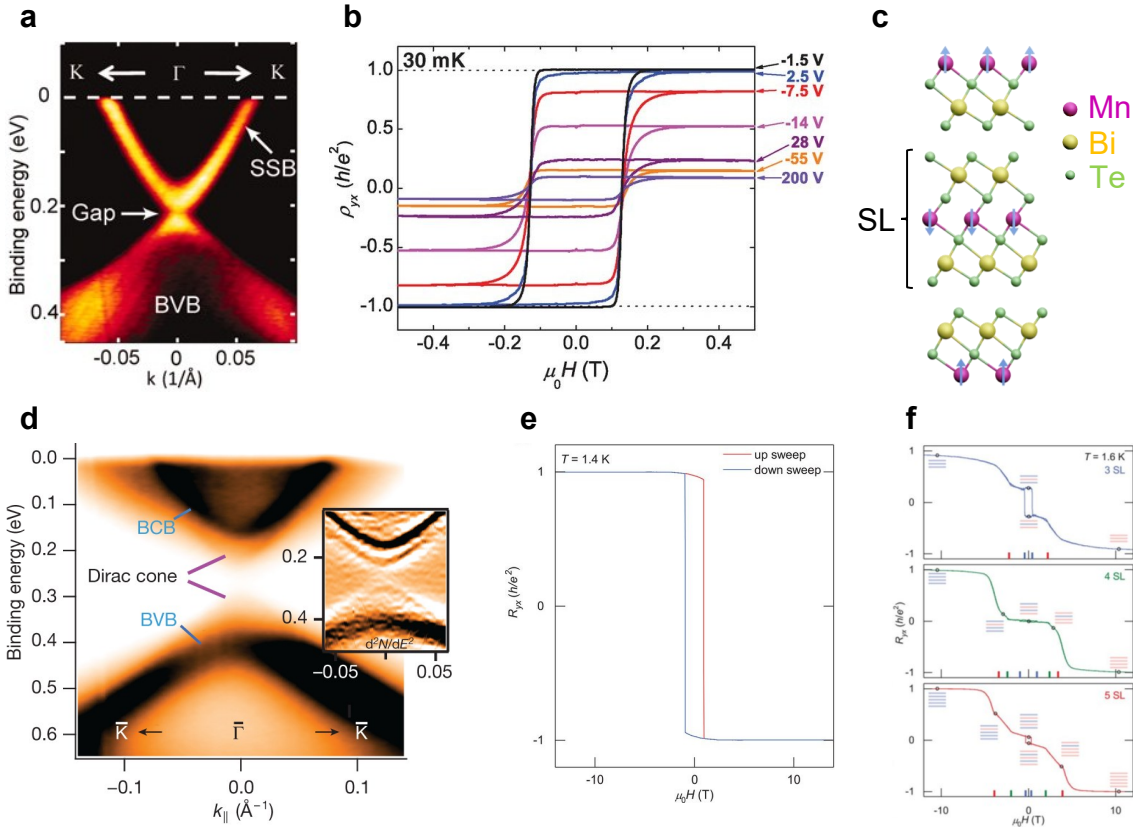


Figure 2.9: Experimental magnetic TI demonstrations. **(a)** ARPES spectrum showcasing the electronic band structure of Fe-doped Bi_2Se_3. A small exchange gap is visible at the Dirac point. Adapted from [264]. **(b)** Quantised Hall resistivities of Cr-doped $Bi_{2-x}Sb_xTe_3$ as a function of external magnetic field under different gate voltages. Adapted from [277]. **(c)** Side-view schematic of $MnBi_2Te_4$ crystal structure with magnetisation indicated by blue arrows. Adapted from *Paper V*. **(d)** ARPES spectrum showcasing the electronic band structure of MBT. Dirac cones with an exchange gap are visible in the bulk band gap. Inset: The second derivative for visual clarity. Adapted from [273]. **(e)** Quantised Hall resistivity of MBT as a function of external magnetic field. Adapted from [317]. **(f)** Anomalous Hall loops for three, four and five SLs of MBT, respectively. Insets: Schematics of the magnetic states of MBT at representative magnetic fields. Adapted from [317].

quantum anomalous Hall effect up to several kelvins [333], and significantly higher temperatures have been proposed for designed heterostructures with MBT [334, 335]. Figure 2.9f clearly demonstrates the even-odd layer dependence of the magnetisation in MBT, where a net magnetisation generates an open anomalous Hall loop at zero magnetic field whereas a fully AFM state causes a closed loop [317]. To be noted, however, the net magnetisation

of odd-layer flakes is only distinguishable in transport measurements in the few-layer limit.

Another key discovery in MBT is the observation of nonlinear electronic transport. As mentioned in Section 2.2, nonlinear transport has previously been reported in WSMs and other materials with broken inversion symmetry due to features in the Berry curvature [63, 248, 336]. However, nonlinear transport generated by the quantum metric were found for the first time thin even-layer MBT in 2023 [70, 71], where the measured longitudinal and transverse nonlinear voltages scale quadratically with the applied bias current, as shown in Figure 2.10a. These second-order nonlinear transport characteristics arise from dipoles in the quantum metric that are enabled by the preserved combined $\mathcal{PT}$ symmetry, which in turn is resulted from the separately broken $\mathcal{P}$ and $\mathcal{T}$ symmetries (visualised in Figure 2.10b) [337–340]. In the following year, longitudinal third-order nonlinear transport generated by quantum metric quadrupoles was demonstrated in bulk MBT [72]. Here, in contrast to in the thin even-layer MBT situation, the second-order nonlinear transport is suppressed by the preserved inversion symmetry of the bulk sample. In both systems, however, the nonlinear transport was found to relate closely to the magnetisation of MBT, increasing dramatically below the Néel temperature of $T_N \approx 24\,\mathrm{K}$ and shifting dramatically with applied magnetic fields [70–72]. Very recently, transverse third-, fifth- and seventh-order nonlinear transport was reported in thin even- and odd-layer $MnBi_{0.7}Sb_{0.3}Te_4$, whereas all even-order nonlinear transport components were suppressed [341]. Differently from the quantum-metric-induced nonlinear transport above, this higher-order transport was instead attributed to Berry curvature multipoles [341, 342]. From these experimental observations, as well as a series of theoretical works [342–351], it stands clear that nonlinear electronic transport is a powerful probe of features in the quantum geometry and can be a pathway to fundamental insights. Additionally, it has also been shown to be an indicator of magnetic and topological phase transitions, which can lead to both new physical understandings and technological applications such as nonvolatile-memory read-outs [70, 71, 76, 339, 352–357]. Yet, further investigation of nonlinear transport in MBT is warranted, especially regarding higher-order transport, where *e.g.* experimental correlation with magnetic phases and a detailed theoretical analysis are still lacking.

Notably, magnetic TIs are also very promising for spintronics applications. Highly efficient magnetic switching through SOT has been demonstrated in heterostructures of magnetic and nonmagnetic TIs, where the SOT is fa-

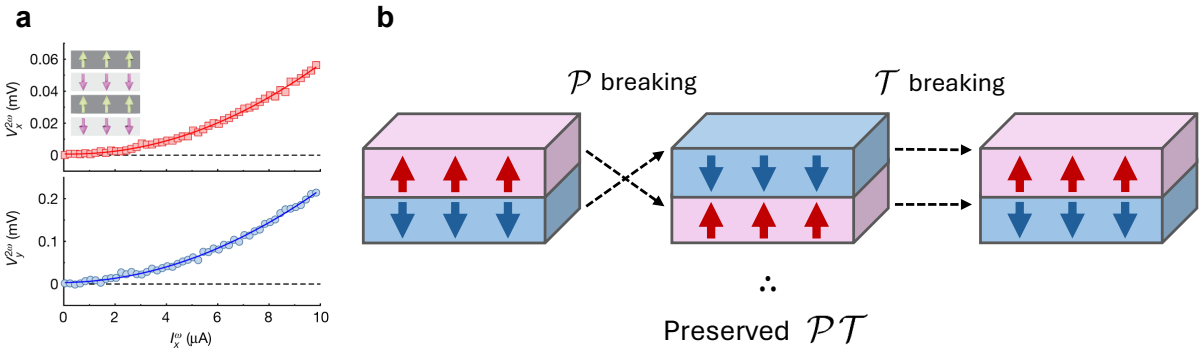


Figure 2.10: Nonlinear transport in $MnBi_2Te_4$. **(a)** Longitudinal and transverse second-order nonlinear IV characteristics due to the quantum metric dipole in MBT. Inset: Schematic of the AFM ordering in MBT. Adapted from [71]. **(b)** Illustration of how broken $\mathcal{P}$ and $\mathcal{T}$ symmetries lead to a preserved combined $\mathcal{PT}$ symmetry in thin MBT.

cilitated by the strong SOC of both TIs [152, 157, 358–360]. However, the combined magnetic ordering and strong SOC in a single material can enable magnetic switching in a magnetic TI through spin-orbit self-torque, eliminating the need for heterostructure devices, as has been realised in the FM TIs Cr-doped $Bi_{2-x}Sb_xTe_3$ [361, 362] and $MnSb_2Te_4$ [363]. Similar dynamics would be especially interesting in AFM TIs such as MBT, considering the proposed advantages of AFM spintronics, such as fast switching dynamics, robustness against magnetic perturbations and the absence of stray magnetic fields [364–368].

Beyond the quantum anomalous Hall effect, axion physics and nonlinear transport, a range of exotic phenomena and applications have been demonstrated and predicted in magnetic TIs thanks to their unique integration of magnetism and nontrivial topology, including nonreciprocal transport [369–372], the layer Hall [373] and diode [374] effects, orbital magnetisation [375] and superconducting physics [376, 377]. There is also a whole family of MBT-related compounds that are intrinsically magnetic TIs with rich physics [378–389]. This is to say that magnetic TIs (just like nonmagnetic TIs and WSMs) constitute a highly interesting class of materials that provides a platform for new and exciting physics in a broad scientific context.

3 Graphene spin-valve devices for spin sensing

Spin sensing is the vital read-out process in spintronics applications, and generally concerns the detection of polarised spin accumulations, spin textures or magnetic states. This is closely tied to the material characterisation of exotic topological [169, 171–173, 214, 215, 233–235, 241] and magnetic [390–396] materials, which brings a broader and deeper understanding of solid state physics. Additionally, spin sensing is also critical for many technological computing applications such as magnetic racetrack [37, 38, 397, 398], magnetic tunnel junction [39, 399] and magnetic domain-wall [400, 401] memories, spin-based probabilistic [43] and neuromorphic [44, 45, 402, 403] computing, as well as magnetologic [42, 404, 405] and spin logic [40, 41, 406–408] devices. The main appeal of utilising spins and magnetic states for the storage and processing of data lies in their nonvolatility and fast dynamics, opening pathways towards next-generation fast and energy-efficient computing.

So far, a variety of microscopic techniques have been established for the detection of spins and magnetic textures in different materials, including magnetooptical Kerr effect microscopy [38, 42, 401, 409], magnetic force microscopy [37, 42, 410, 411], spin-polarised scanning tunnelling microscopy [412], Lorentz transmission electron microscopy [413] and nitrogen-vacancy magnetometry [414]. However, for practical utilisation in technological devices, all-electrical spin sensing techniques are especially tantalising due to their easier integration with conventional electronic circuits. Such all-electrical spin and magnetic sensing has indeed been experimentally demonstrated using magnetoresistance [415, 416], SHE [417], anomalous Hall effect [145, 416], magnetic tunnel junction [39, 398, 418, 419] and metallic spin-valve [420–423] measurements. Spin-valve measurements, in particular, have the important benefit that they can be performed in nonlocal geometries where pure spin currents can be detected separately from the applied charge current, thereby minimising charge-current effects on the measured spin signal.

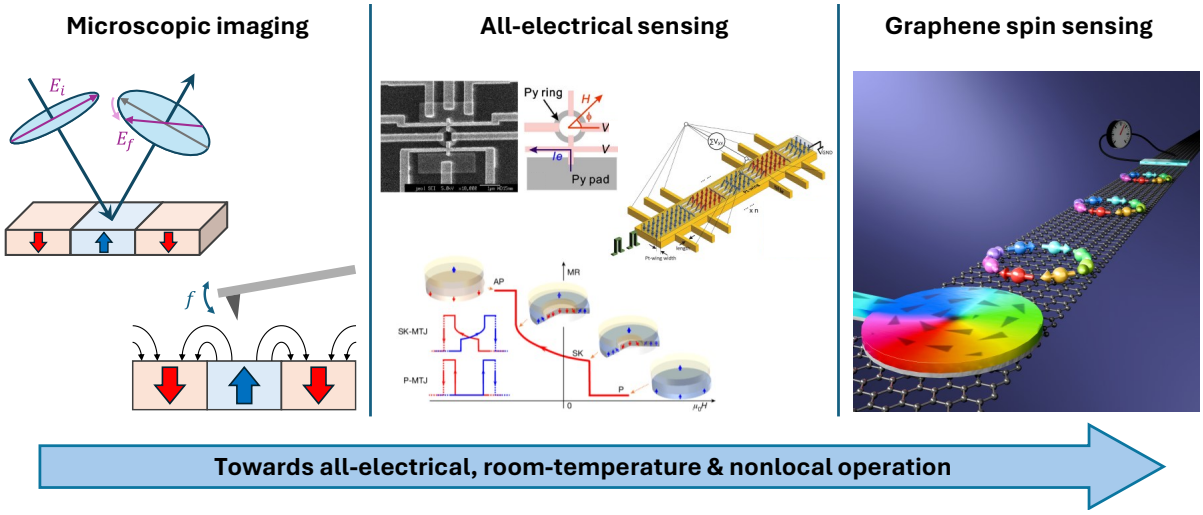


Figure 3.1: Techniques for detection of magnetic spin textures. Overview of spin sensing techniques and the progress towards all-electrical, room-temperature and nonlocal sensing operation. The illustrated techniques are magnetooptical Kerr effect and magnetic force microscopy (left), metallic spin-valve, anomalous Hall and magnetic tunnel junction measurements (centre) as well as spin texture sensing in a graphene spin-valve device (right). Adapted from [39, 145, 421].

Until now, detection of magnetic states using this kind of all-electrical spin-valve measurements has predominantly been performed in devices with metals such as copper as the spin transport material [420–423]. Because of the short spin diffusion lengths in metals at room temperature, these measurements have unfortunately been limited to cryogenic temperatures up to 77 K [420–423]. Graphene, on the other hand, is an excellent spin transport material with long spin diffusion lengths and robust spin transport even at room temperature [424–431]. As such, it is an ideal material for all-electrical room-temperature spin sensing in reliable nonlocal spin-valve devices. An overview of various spin sensing techniques and the overall progress towards all-electrical and nonlocal detection at room temperature is visualised in Figure 3.1.

Here, lateral graphene spin-valve devices and nonlocal spin transport measurements, including spin-valve and Hanle spin precession measurements, are established. Then, electrical detection of magnetic spin textures in the FM cobalt (*Paper I*) and the vdW FM Fe_5GeTe_2 (FGT) (*Paper II*) is demonstrated through pure spin-polarised transport in graphene spin-valve devices at room temperature. Multi-domain and vortex magnetic textures are engineered through geometrical constrictions of Co and FGT, enabling

the injection of complex spin textures into the graphene channel and resulting in distinct multi-level spin signals. An artistic preview of the detection method is given in the right panel of Figure 3.1. These advancements provide insights into all-electrical sensing of magnetic domains and spin textures using pure spin currents in graphene heterostructures and spin circuits.

3.1 Graphene spintronics

Graphene is the archetypical vdW quantum material, consisting of a single layer of carbon atoms in a 2D honeycomb lattice structure (illustrated in Figure 3.2a). It was discovered as the first vdW material by Andre Geim and Konstantin Novoselov in 2004 through mechanical exfoliation from graphite [432], which was rewarded with the Nobel prize in physics in 2010 [433]. The carbon atoms in graphene are sp^2-hybridised, which facilitates strong covalent bonds between the atoms in-plane as well as a sea of delocalised electrons (from the remaining p_z orbitals) throughout the graphene sheet. This, combined with its atomic thinness, gives graphene a unique set of material properties, showcasing very large mechanical strength and elasticity [434], high transparency [435] as well as excellent electrical properties.

As can be seen in Figure 3.2b, the band structure of graphene hosts Dirac cones at the K and K' points [436–438], where the linear dispersion relation enables massless fermions with uniquely high charge carrier mobilities [439–442]. However, an important difference to the Dirac cones of TIs is that graphene has a very low SOC due to its flat shape and its constituent light carbon atoms, and therefore lacks a band inversion as well as topological protection [443]. Moreover, the Dirac points in pristine graphene always lie at the Fermi level E_F, which enables ready access to both the conduction and the valence bands through chemical or electrostatic doping. This is demonstrated in Figure 3.2c, where the sheet resistance $R_\square = R \cdot w/l$ (where R, w and l are the resistance, width and length of the graphene channel, respectively) of graphene is tuned by electrostatic back-gating on a Si/SiO_2 chip. In Figure 3.2c, the so-called Dirac curve is offset to the right due to chemical p-doping with excess holes [444], which have most likely been introduced to the graphene channel by residues from microfabrication processing. The charge-neutrality point, where the Fermi level touches the Dirac point, therefore appears as a resistance maximum at the Dirac voltage $V_D = 33\,\mathrm{V}$. By tuning the gate voltage V_g, the charge carrier type and concentration can thus be modulated, with electrons (holes) as the majority charge carrier for $V_g > V_D$ ($V_g < V_D$), as schematically indicated by the insets in Figure 3.2c.

In a broader context, graphene has proven useful for a range of applications, including metrology through the quantum Hall effect [446–448], thermal management due to its high thermal conductivity [449] as well as flexible and wearable electronics because of its excellent electronic and mechanical properties [450, 451]. Its sensitivity and versatility for chemical

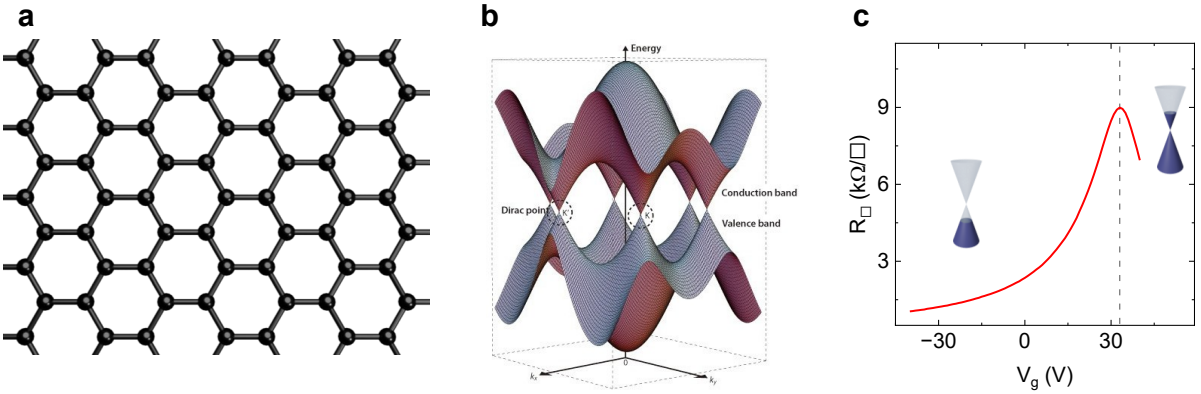


Figure 3.2: Graphene. **(a)** Schematic crystal structure of graphene. **(b)** Electronic band structure of graphene with Dirac cones at the K and K' points. Adapted from [445]. **(c)** Dirac curve of graphene with the sheet resistance as a function of gate voltage. The charge neutrality point is indicated with a dashed line. The measurement was performed in a CVD graphene channel with dimensions $w = 2.0\,\mu$m and $l = 1.0\,\mu$m, and bias current $I = 1\,\mu$A. Insets: Schematic Dirac cones with occupied states indicated by colour, signifying electron- and hole-doping, respectively.

functionalisation has made it a promising candidate for chemical and biological sensing applications [452–455]. Even flat-band superconductivity has been achieved through stacking and careful twisting of bilayer graphene [456].

3.1.1 Spin transport measurements in graphene

Importantly for this thesis, graphene is an excellent material for spin transport due to its high electrical mobility and low SOC. This is utilised in spin transport measurements in lateral graphene spin-valve devices. A graphene spin-valve device, which is illustrated in Figure 3.3a, consists of a graphene spin transport channel as well as FM and nonmagnetic electrodes or contacts. When a charge current I is passed between a FM contact and a nonmagnetic reference contact (left in Figure 3.3a), polarised spin is injected from the ferromagnet (FM) to the graphene channel due to the spin majority population of the FM. Microscopically, this spin injection takes place through a flow of spin-polarised electrons either from the FM to graphene or *vice versa*, and therefore results in a spin polarisation in graphene that is either parallel or antiparallel with respect to the magnetisation of the FM, depending on the polarity of the applied charge current. In contrast to the charge current, which is driven by the electrical potential between

the FM injector contact and the nonmagnetic reference, the spin polarisation diffuses in both directions through the graphene channel and thus generates a pure spin current outside of the charge-current loop. When the spin polarisation reaches a second FM contact (right in Figure 3.3a), a nonlocal voltage V_{NL} can be detected with respect to a nonmagnetic reference. This nonlocal voltage can be intuitively understood in comparison to a magnetic tunnel junction, where the tunnel magnetoresistance effect causes a low or a high resistance state in the device depending on whether the two FM layers have parallel or antiparallel magnetisations [457], although it should be noted that there is no charge transfer between the graphene and the detector contact in the graphene spin-valve case. In a more detailed approach, the electrochemical potential for spin-up and spin-down charge carriers can be drawn as in Figure 3.3b, where the potential has a maximum μ_0 by the injector FM electrode and then decays in both directions along the graphene channel as the propagating spins dephase [458, 459]. To be noted, the purely electrical potential has a gradient only inside the charge current loop and is constant everywhere else, as indicated by the black dotted line. The detected nonlocal voltage correlates to the difference in electrochemical potential between the spin-sensitive FM detector contact and the spin-insensitive nonmagnetic reference contact (indicated by black dots in the diagram) as $\Delta\mu = eV_{NL}$ [460]. The same process is illustrated with schematic band diagrams in Figure 3.3c.

Importantly, the sign of $\Delta\mu$ and V_{NL} depends on whether the net polarisation of the propagating spin is parallel or antiparallel to the magnetisation of the FM detector contact, in accordance with the magnetic tunnel junction analogue above. This is utilised in spin-valve measurements, where a magnetic field B_y is swept along the IP y axis (which is along the easy axis of the FM electrodes) to switch the magnetisation of the FM injector and detector electrodes. The FM contacts are designed with different widths to have slightly different coercive fields and therefore switch in sequence with increasing B_y, giving rise to a spin-valve signal as in Figure 3.3d with peaks in V_{NL} when the injector and detector contacts have opposite magnetisations. The sharp transition between parallel and antiparallel magnetisations of the two FM contacts gives a clear spin signal amplitude ΔV_{NL}, which corresponds to the potential difference between spin-up and spin-down charge carriers.

During Hanle spin precession measurements, a magnetic field B_z is instead applied OOP. Rather than switching the magnetisation of the FM contacts, this causes the propagating spins to precess IP around the magnetic field

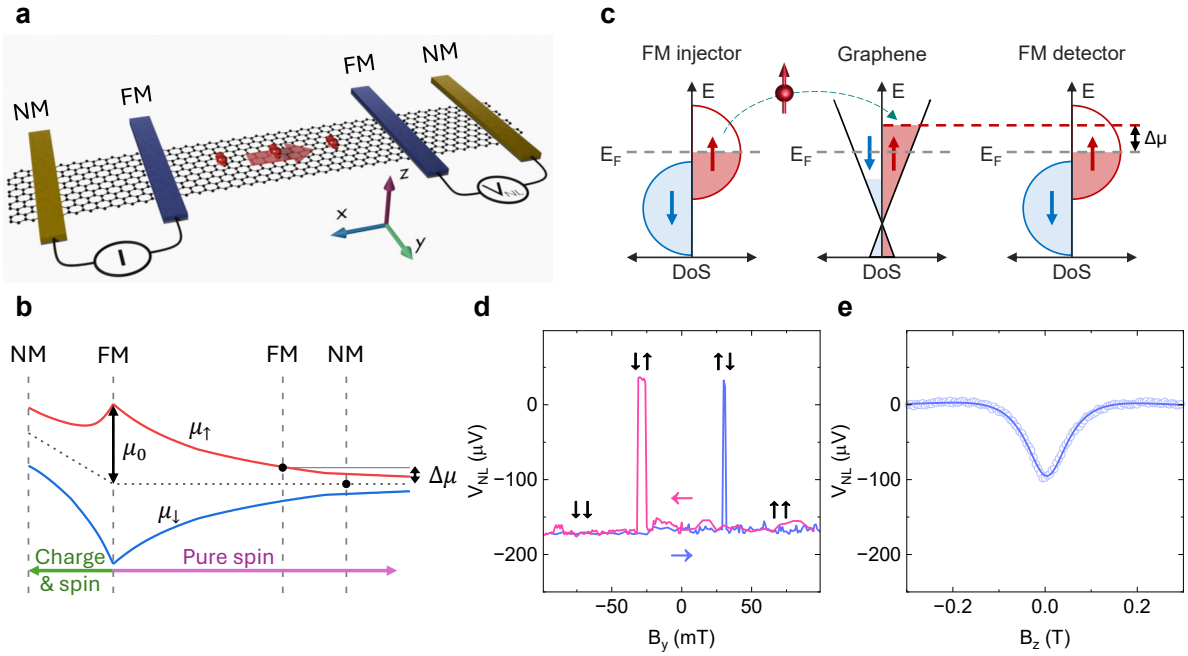


Figure 3.3: Nonlocal spin transport measurements in graphene. **(a)** Schematic of a graphene spin-valve device. **(b)** Schematic drawing of the electrochemical potential (red and blue for spin-up and spin-down, respectively) in a spin-valve device during spin injection from the leftmost FM electrode. The purely electrical potential is indicated by a dotted black line, and the electrochemical potential difference that corresponds to the nonlocal voltage that is measured by the rightmost electrodes is indicated as $\Delta\mu$. The combined charge and spin current and the pure spin current in the device are visualised with green and purple arrows. **(c)** Schematic illustration of spin injection and detection with band diagrams in a graphene spin-valve device, with spin polarisation and density of states (DoS) indicated. **(d)** Spin-valve signal. The blue and pink arrows indicate the B_y sweep directions for the measurement, and the black arrows indicate the magnetisation orientation of the FM injector and detector electrodes. **(e)** Hanle spin precession signal. The solid line is a fit to the signal using Equation (3.1). A linear background was subtracted from the measured signal. The measurements were performed in a graphene spin-valve device with $I = -100\,\mu$A and $V_g = -40\,$V.

and to dephase. Because of the precession, the net spin polarisation that arrives to the FM detector contact has an magnetic-field-dependent angle with respect to the magnetisation of the contact. At the same time, spin dephasing generally increases with the applied magnetic field. This results in a wave-shaped Hanle spin precession signal as in Figure 3.3e, where the measured V_{NL} corresponds to the projection of the net spin polarisation on

the easy axis of the FM (here, the y axis). The Hanle signal can be fitted by the spin diffusion and precession equation

$$V_{\mathrm{NL}} \propto \int_0^\infty \frac{1}{\sqrt{4D_s t}} \mathrm{e}^{-L^2/4D_s t} \cos(\omega_L t) \mathrm{e}^{-t/\tau_s} \, \mathrm{d}t, \tag{3.1}$$

where τ_s and D_s are the spin lifetime and the spin diffusion coefficient in graphene, L is the length of the graphene channel and $\omega_L = g\mu_B B_z/\hbar$ is the Larmor spin precession frequency (where g is the Landé g factor, μ_B is the Bohr magneton and $\hbar$ is Planck's reduced constant) [30, 458, 461] (shown as a solid line in Figure 3.3e). From this fitting, the important spin transport parameters τ_s and the spin diffusion length $\lambda_s = \sqrt{D_s \tau_s}$ of the graphene channel can be extracted.

Importantly, since the measured V_{NL} signal corresponds to the spin projection onto the easy axis of the FM detector contact, the symmetry of Hanle spin precession signals is sensitive to the initial spin orientation before the start of the precession. If the injected spin has a canted angle with respect to the detector contact (such as through a canted magnetism or a geometric misalignment of the injector contact, as illustrated in the inset of Figure 3.4a), the measured Hanle signal gains a corresponding antisymmetric component with respect to the magnetic field [429]. This is shown in Figure 3.4a with numerically generated Hanle signals for different canting angles. Consequently, the polarisation of the injected spin can be identified through a detailed analysis of the Hanle-signal asymmetry, as is detailed in the following.

First, to carefully eliminate any non-spin-related signal background, Hanle spin precession measurements can be performed with parallel (↑↑) and antiparallel (↑↓) magnetisation orientations of the injector and detector electrodes, which results in two signals with the same background but opposite spin components, as shown in the bottom of Figure 3.4b. The pure spin component of the measured signals (shown in the centre of Figure 3.4b) can therefore be obtained by averaging the two signals as

$$V_{NL,avg} = \frac{V_{NL,\uparrow\uparrow} - V_{NL,\uparrow\downarrow}}{2}, \tag{3.2}$$

where $V_{NL,\uparrow\uparrow}$ and $V_{NL,\uparrow\downarrow}$ are the nonlocal voltage of the parallel and antiparallel magnetization configurations, respectively [234, 239, 391]. Next, the averaged signal can be decomposed into its symmetric ($V_{NL,\parallel}$) and antisym-

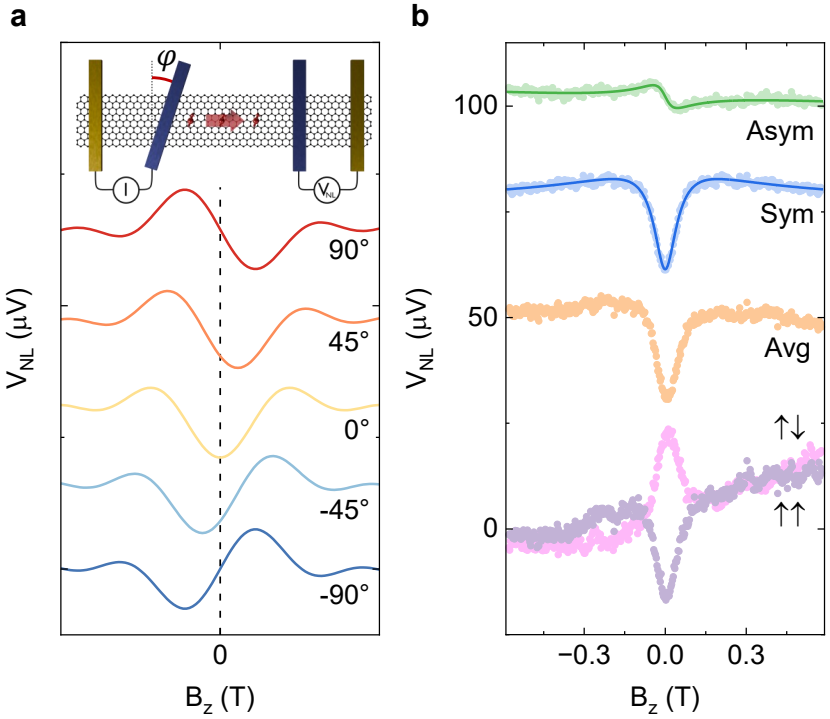


Figure 3.4: Hanle-signal asymmetry under canted spin angles. (a) Hanle spin precession signals for different canting angles of the injected spin, generated from Equation (3.4) and Equation (3.5). Inset: Schematic top view of a spin-valve device where the injector contact is misaligned by an angle φ. Adapted from *Paper III*. **(b)** Hanle spin precession signals for parallel (↑↑) and antiparallel (↑↓) magnetisations of the FM injector and detector contacts, respectively, as well as the averaged signal (Avg; from Equation (3.2)) and the symmetric (Sym) and antisymmetric (Asym) components of the averaged signal (from Equation (3.3)). The solid lines are fits of Equation (3.4) to the respective signal components. The data has been shifted vertically for clarity. The measurements were performed with $I = -200\,\mu$A and $V_g = -70\,$V.

metric ($V_{NL,\perp}$) components according to

$$\begin{cases} V_{NL,\parallel} = \frac{V_{NL}(B)+V_{NL}(-B)}{2} \\ V_{NL,\perp} = \frac{V_{NL}(B)-V_{NL}(-B)}{2} \end{cases} \tag{3.3}$$

[234, 391, 429], with the resulting signal components shown in the top of Figure 3.4b. The equations

$$\begin{cases} V_{NL,\parallel} \propto \int_0^\infty \frac{1}{\sqrt{4D_s t}} \mathrm{e}^{-L^2/4D_s t} \cos(\omega_L t) \mathrm{e}^{-t/\tau_s}\,\mathrm{d}t \\ V_{NL,\perp} \propto \int_0^\infty \frac{1}{\sqrt{4D_s t}} \mathrm{e}^{-L^2/4D_s t} \sin(\omega_L t) \mathrm{e}^{-t/\tau_s}\,\mathrm{d}t \end{cases} \tag{3.4}$$

can then be fitted to the respective signal components (shown as solid lines in Figure 3.4b), where the top equation is Equation (3.1) and the bottom equation has been adapted to be antisymmetric with respect to B [429]. Finally, the spin orientation can be calculated from

$$\varphi = \tan^{-1}\left(\frac{\Delta V_{NL,\perp}}{\Delta V_{NL,\parallel}}\right), \tag{3.5}$$

where $\Delta V_{NL,\parallel}$ and $\Delta V_{NL,\perp}$ are the respective signal component amplitudes gained from Equation (3.4) [429]. For the Hanle spin precession signals in Figure 3.4b, the signal asymmetry corresponds to an IP canting angle $\varphi = 14 \pm 1\,^{\circ}$.

To be noted, Hanle spin precession measurements can alternatively be performed with a magnetic field B_x applied IP along the graphene channel (*i.e.* along the x axis). To differentiate, this is known as xHanle spin precession measurements (with the situation above denoted as zHanle spin precession). xHanle measurements work similarly to zHanle, but with an OOP spin precession in the yz plane instead of in the xy plane. A combination of zHanle and xHanle spin precession measurements therefore enables the investigation of both IP and OOP spin precession in the graphene spin-valve device, including the determination of IP and OOP spin transport parameters and spin canting angles.

3.1.2 Long-distance spin transport and spin logic operations in graphene

Whereas the first demonstrations of spin transport in graphene around 2007 were performed using spin-valve devices based on exfoliated graphene flakes [427, 462], the quality of scalable chemical vapour deposition (CVD) graphene has since improved considerably, which enables long-distance spin transport in high-quality CVD graphene spin-valve devices [463]. One such device is presented in Figure 3.5a, where spin transport was successfully demonstrated over a 21 μm distance. The graphene channel was patterned by electron beam lithography (EBL) followed by oxygen plasma etching, and the nonmagnetic (Ti/Au) and FM (TiO_2/Co) electrodes were patterned by EBL followed by electron-beam evaporation deposition and lift-off processes. Importantly, the thin layer ($\sim$ 1 nm) of TiO_2 in the FM contacts acts as a tunnel barrier between the graphene and the FM Co. This is done to mitigate the so-called conductivity mismatch problem, where the low conductivity of graphene compared to the metallic FM can cause a low

spin injection efficiency through spin back-scattering and reabsorption in transparent FM contacts [464, 465]. Spin-valve and zHanle signals for the 21 μm spin transport are shown in Figure 3.5b,c, where the latter yields $\tau_s = 126 \pm 27$ ps and $\lambda_s = 2.2 \pm 0.5\,\mu$m after fitting with Equation (3.1). Indeed, long-distance spin transport up to 45 μm with spin lifetimes exceeding 3 ns has been reported in high-quality CVD graphene using similar spin-valve devices [428–431, 466].

Spin transport over long distances in good-quality scalable graphene can enable new and innovative spintronic applications, such as graphene spin logic circuits. Here, branched graphene channels are utilised to allow simultaneous spin injection from multiple FM contacts. Where the branches converge, the propagating spins from each branch are mixed together, yielding a combined net spin polarisation which can be detected with a single FM contact. Importantly, since positive and negative bias currents can be used for spin injection with opposite polarisations, the spin population of each branch can be controlled electrically without a need for external magnetic fields. This kind of graphene spin circuits with two or three branches has previously been used to demonstrate reconfigurable Boolean logic operations [41], which is a step towards integrated logic and memory in a single spin-based device.

For real spin logic applications, however, cascading logic with multiple Boolean gates applied in series is necessary. One such graphene circuit is shown in Figure 3.5d, where four spin inputs (left) are combined sequentially towards a single read-out (right), resulting in two layers of cascading spin logic operations. Figure 3.5e demonstrates the functionality of the two-branch top-left section of the circuit, where the top panel shows the measured nonlocal voltage in response to two applied bias currents (I_A and I_B; bottom panels). Here, the amplitudes of the two bias currents have been selected to compensate differences in spin injection efficiency between the two injector contacts, so that both spin inputs have similar weights in the spin mixing. As can be seen, the measured spin signal is proportional to the sum of the two injected spin polarisations, and varies between three distinct states with a high (for $I_A, I_B > 0$), a low (for $I_A, I_B < 0$) and a medium (for $I_A > 0$, $I_B < 0$ or $I_A < 0$, $I_B > 0$) voltage level. By assigning a threshold voltage ($V_{NL} = 0$ V in Figure 3.5e), this can be interpreted as the logical output of an AND Boolean gate, which gives a 1 (True) reading only when both bias currents are positive and a 0 (False) reading otherwise. Alternatively, by adjusting the threshold voltage (*e.g.* to $V_{NL} = -4$ V), OR logic operations (which return a 1 reading when either bias current is positive)

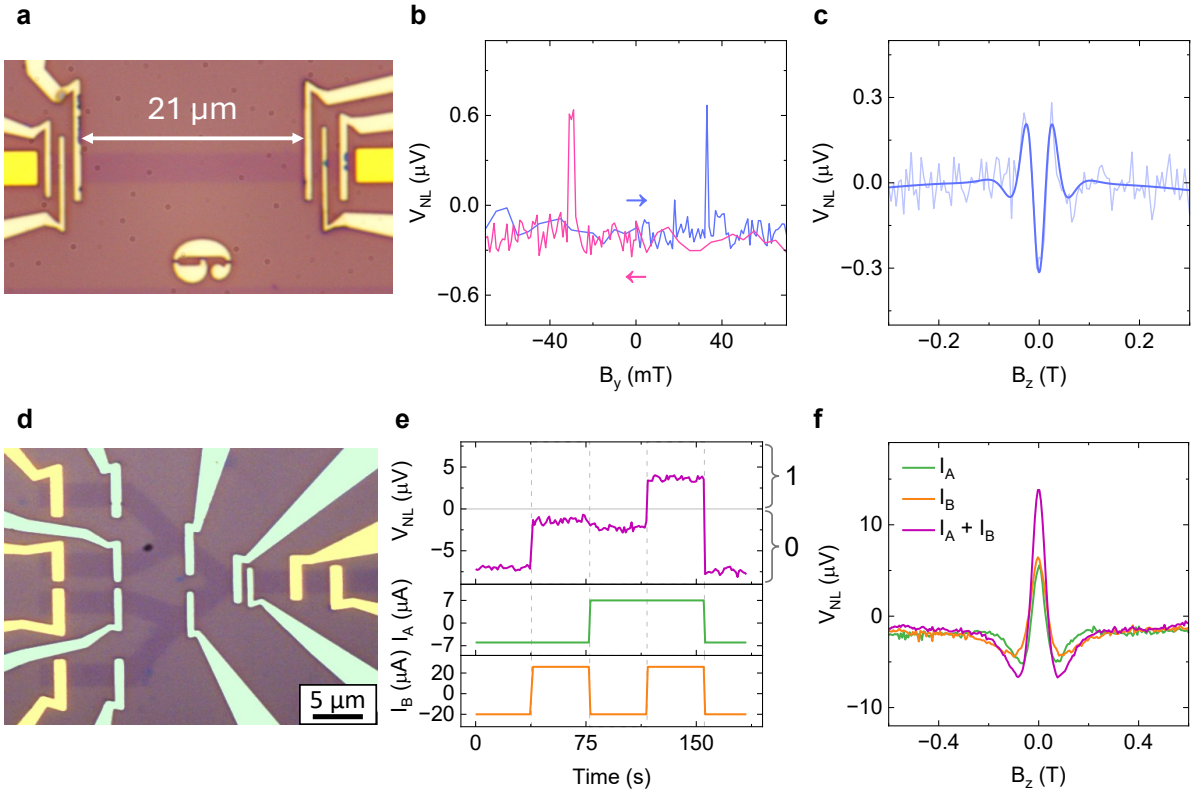


Figure 3.5: Long-distance spin transport and spin logic operations in graphene. **(a)** Microscopy image of a graphene spin-valve device with FM TiO_2/Co and nonmagnetic Ti/Au contacts. The distance of 21 μm between two of the FM contacts is indicated with white arrows. **(b,c)** Spin-valve and zHanle spin precession signals for long-distance spin transport in the device in (a). The green arrows in (b) indicate the B_y sweep directions for the spin-valve measurement, and the solid line in (c) is a fit to the Hanle signal. A linear background was subtracted from the Hanle signal. The measurements in (b,c) were performed with $I = -450\,\mu$A and $V_g = -40\,$V. **(d)** Microscopy image of a cascading spin logic graphene circuit, containing two layers of Boolean gates. **(e)** Measured spin-signal output (top panel) from a two-branch graphene circuit (top-left section of the circuit in (d)) in response to an applied sequence of two bias currents (bottom panels), as a function of time. The labels 1 and 0 indicate the logic read-outs of an AND gate, for an applied threshold voltage $V_{NL} = 0\,$V. **(f)** zHanle spin signals in a branched graphene circuit, obtained using individual bias currents I_A and I_B as well as through spin addition while applying both bias currents simultaneously. The measurements in (f) were performed with $I_A = 32\,\mu$A and $I_B = 100\,\mu$A.

can be achieved instead. Ideally, the outputs of two such logic gates can be passed on as the inputs to a third gate. The full circuit in Figure 3.5d could then generate, for example, (A AND B) OR (C AND D) logic operations

for four logical inputs A, B, C and D.

Interestingly, similar spin addition was observed also during spin precession under OOP magnetic fields in the same device. As can be seen in Figure 3.5f, the amplitude of the Hanle spin precession signal is doubled when both bias currents are applied simultaneously, signifying the combined contribution of precessing spins from both branches of the graphene circuit.

In order to extend this kind of graphene spin logic circuits to fully-functional cascading logic devices and other complex architectures [45, 402, 429], certain optimisation challenges must be overcome. Specifically, high-yield fabrication of good-quality graphene and FM contacts with efficient spin injection and detection is necessary, which can be achieved through hBN encapsulation of the graphene [467–471]. At the same time, narrower graphene channels and a smaller device footprint are needed for implementing more complex functionalities with a larger number of logic operations.

3.2 Electrical detection of spin textures in ferromagnet Co

Graphene spin-valve devices were designed with specially shaped FM cobalt electrodes, as shown with a schematic illustration in Figure 3.6a and with a representative device in Figure 3.6b. The geometric shapes of the FMs affect their magnetisation dynamics under the application of external magnetic fields, which can be traced with spin transport measurements. In a spin-valve measurement with a magnetic field B_y being swept in the y direction, the detected spin signal traces the changing magnetisation of the FM injector and detector contacts, with a low (high) nonlocal voltage corresponding to a parallel (antiparallel) magnetisation configuration of the two contacts. As established in Section 3.1.1, two elongated FM contacts with quasi-single magnetic domains generate a typical spin-valve signal with single steps in V_{NL}. However, the specially shaped contacts are designed with more complex magnetisation dynamics and give rise to anomalous multi-level spin-valve signals, as illustrated in Figure 3.6c. The relationship between the nonuniformly evolving magnetisation of a specially shaped FM contact and the corresponding multi-level spin signal is visualised in Figure 3.6d.

3.2.1 Detection of multi-domain magnetic textures

A spin-valve signal for two standard quasi-single-domain FM contacts (as in Figure 3.7a) is shown for reference in Figure 3.7b, with singular steps in the spin signal as the magnetisations of the FM contacts are switched between parallel and antiparallel alignments by the applied field. In contrast, 'single-notch' and 'double-notch' FM contacts (visualised in Figure 3.7c,e) have geometric notches that pin magnetic domain walls [37, 411, 415, 472], which separates the contacts into two decoupled magnetic domains that switch in sequence during a B_y sweep. Similarly, the wider and the narrower sections of a 'stepped' FM contact (in Figure 3.7g) are decoupled by a pinned magnetic domain wall at the sharp geometry of the constriction [401, 473]. The resulting multi-domain magnetisation dynamics of the specially shaped FM contacts are seen as sequential steps of increasing nonlocal voltages in the respective spin-valve signals in Figure 3.7d,f,h. Here, the relative amplitude of the spin signal is indicative of the proportion of the shaped contact that has been switched. Similar multi-domain contact designs can be extended to realise any number of magnetic domains and cor-

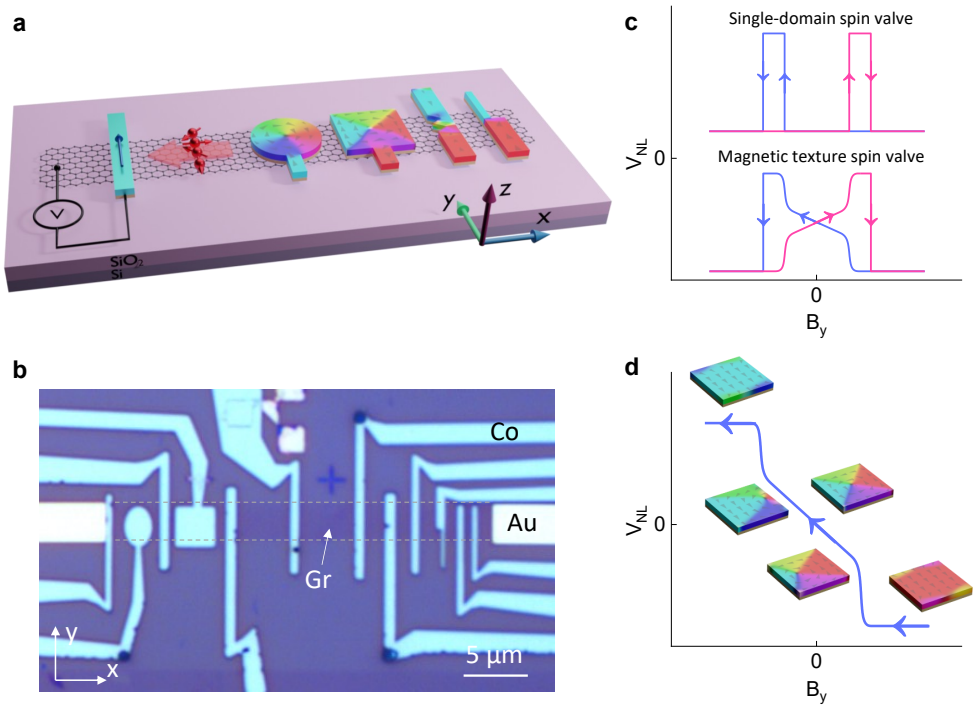


Figure 3.6: Graphene spin-valve device for electrical detection of magnetic spin textures in Co. (a,b) Schematic (a) and microscope picture (b) of a representative spin-valve device with different magnetic spin textures in specially shaped cobalt. The dashed lines in (b) indicate the borders of the graphene spin transport channel. **(c)** Schematics of expected spin signals for spin-valve devices with single-domain (top) and magnetic-texture (bottom) FM electrodes. **(d)** Schematic of the expected spin signal contribution from a vortex spin texture and corresponding magnetic textures of a square electrode at different stages of the magnetic field sweep. Adapted from *Paper I*.

responding intermediate magnetic states, which would be distinguishable in such a graphene spin-valve device. Based on the noise level of the present proof-of-principle devices, it is estimated that net magnetisation changes as small as $\sim 7\,\%$ can reliably be detected, which can be dramatically enhanced through fabrication and device optimisation [467, 469, 474].

Micromagnetic simulations using MuMax3 [475–477] of the notched and stepped contacts were performed to correlate the measured spin signals with magnetisation dynamics. Distinct magnetic textures for different points along the B_y sweeps are shown as insets in Figure 3.7b,d,f,h. Simulated magnetic hysteresis loops also show good qualitative agreement between the experimental spin signals and the simulated y magnetisation m_y of the FM contacts, as exemplified in Figure 3.8.

The multi-domain magnetisation of the specially shaped FM electrodes

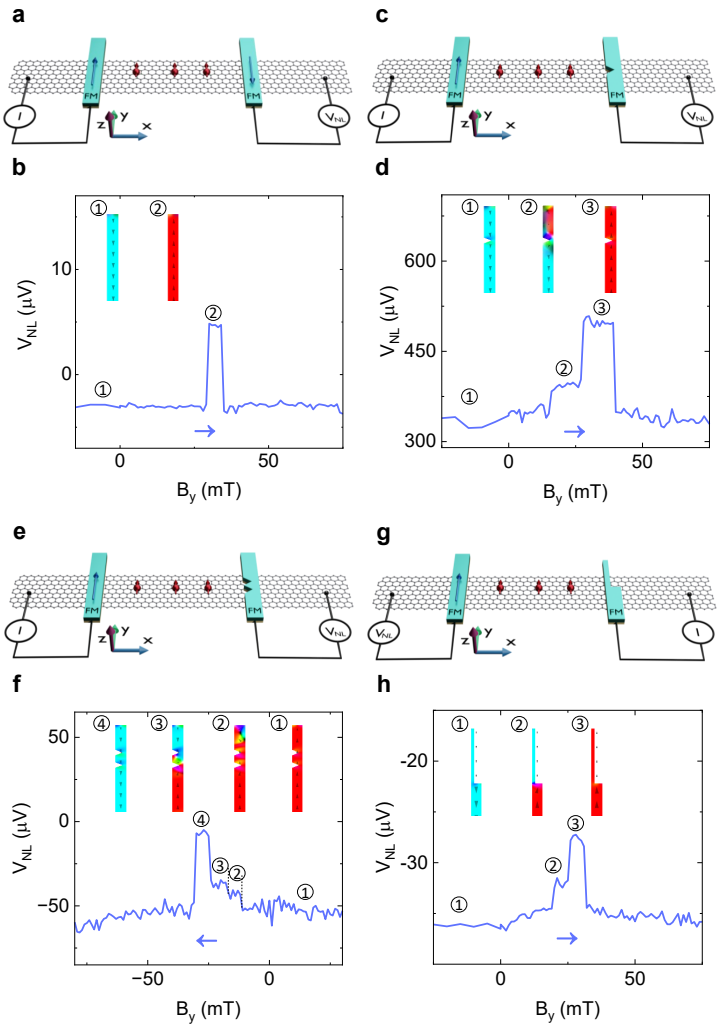


Figure 3.7: Detection of multi-domain magnetic textures. (a,c,e,g) Schematics of a standard spin-valve device (a) and spin-valve devices with a single-notch (c), a double-notch (e) and a stepped (g) FM contact, respectively. **(b,d,f,h)** Spin-valve signals from the devices in (a,c,e,g), respectively. The blue arrows indicate the B_y sweep directions. Insets: Simulated magnetic textures illustrating the magnetisation dynamics of the specially shaped FM contacts. The circled numbers indicate the correlation between the magnetic textures and the spin-valve signals. Adapted from *Paper I*.

was verified using magnetic force microscopy (MFM). Figure 3.9a,c show the atomic force microscopy (AFM) topology of a notched, a regular and a notched FM contact, respectively, and the corresponding MFM images are included in Figure 3.9b,d. Here, the MFM frequency contrast in the MFM images correlates with the second gradient of the magnetic force on the MFM tip, and can be related to the orientation of the sample magnetisation. The

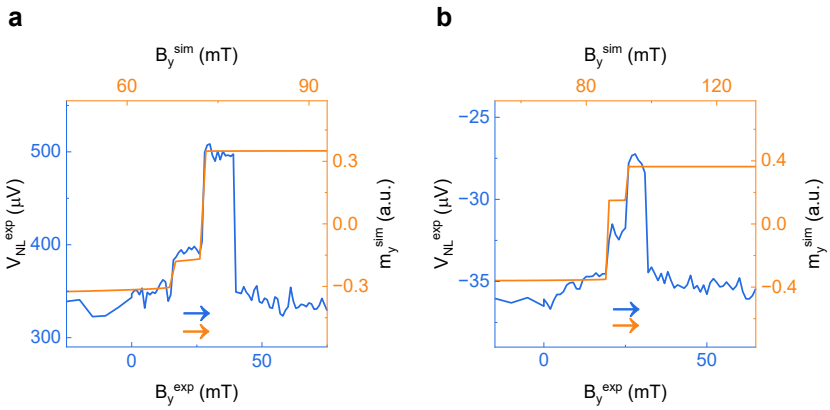


Figure 3.8: Micromagnetic simulations of multi-domain magnetic textures. (a,b) Experimental spin-valve signals (blue) and simulated y magnetization (orange) as a function of B_y for a single-notch (a) and a stepped (b) contact, showing qualitative agreement. The experimental signals are the same data as in Figure 3.7d,h. The arrows indicate the B_y sweep directions. Adapted from *Paper I*.

measured MFM signals are mainly homogeneous along the length of the contacts. However, the adjacent dark and bright areas at the notch in Figure 3.9b and the bright area at the sharp step in Figure 3.9d are clear indications of pinned magnetic domain walls at the respective geometrical constrictions. To correlate the experimental MFM results with magnetic textures in the FM electrodes, simulated MFM images were calculated from the simulated magnetic textures (Figure 3.9e,g). As can be seen in Figure 3.9f,h, the simulated MFM images follow the experimental results closely, confirming the multi-domain magnetic behaviour.

3.2.2 Detection of magnetic vortex textures in a circular microstructure

Magnetic vortex textures were studied in a spin-valve device with an engineered circular FM electrode, as illustrated in Figure 3.10a. The circular shape of the FM causes an ill-defined magnetic easy axis so that its magnetisation is not expected to be contained purely along the y axis. This leads to more complex magnetic textures in the FM contact and differently shaped spin-valve signals compared to the ones in Section 3.2.1. The spin signal in Figure 3.10b contains not only sharp steps in V_{NL}, but also a gradual slope. The corresponding magnetisation dynamics can be understood according to the following. Under large positive magnetic fields, the magnetisation of the

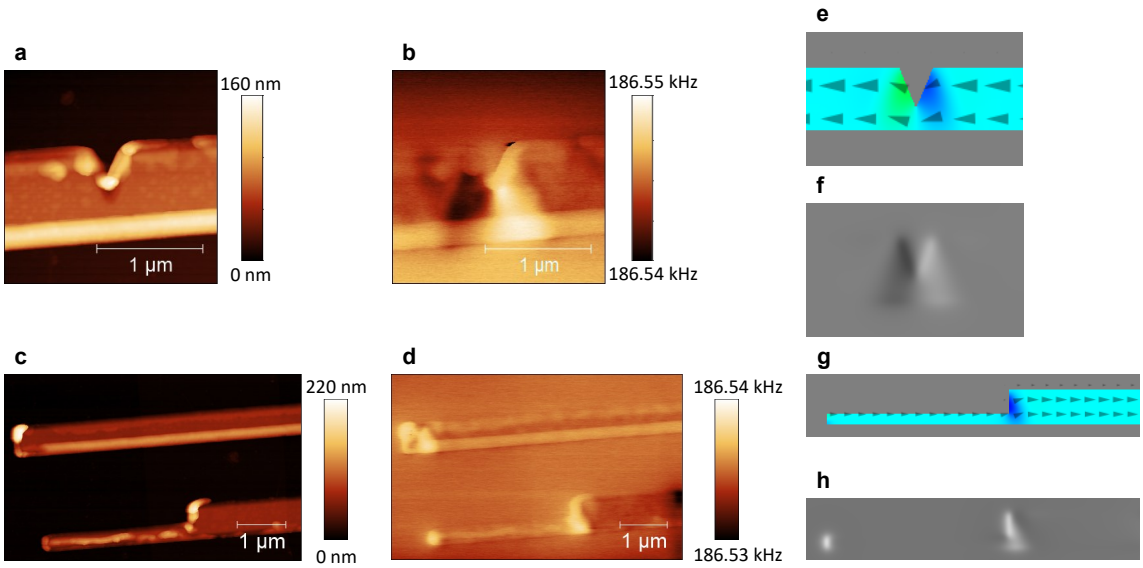


Figure 3.9: Magnetic force microscopy of multi-domain magnetic textures. **(a,b)** Atomic force microscopy (AFM) topography (a) and magnetic force microscopy (MFM) frequency contrast image (b) of a notched FM contact. **(c,d)** AFM topography (c) and MFM frequency contrast image (d) of a regular (top) and a stepped (bottom) FM contact. **(e,f)** Simulated magnetic texture of a notched contact (e) and the corresponding simulated MFM image (f). **(g,h)** Simulated magnetic texture of a stepped contact (g) and the corresponding simulated MFM image (h). Adapted from *Paper I*.

circular contact is saturated in the $+y$ orientation. As B_y is reduced below a certain level, a magnetic vortex is created close to the left edge of the circular electrode. This reduces the net magnetisation of the contact and leads to a sharp step in V_{NL}, since the spin-valve measurements are only sensitive to spins along the easy axis of the FM detector (*i.e.* the y direction). Interestingly, this vortex creation event happens before B_y reaches zero, indicating that the magnetic vortex texture is the ground state of the circular contact [413, 478, 479]. When the magnetic field is subsequently swept towards the $-y$ direction, the vortex moves continuously towards the right edge of the circular contact, leading to an increasing magnetisation in the $-y$ direction and a gradual increase in the nonlocal voltage signal. Here, the small spikes during this gradual slope in the measured signal can come from pinning of the magnetic vortex, in addition to electrical noise. It should additionally be noted that only the presence and movement of the magnetic vortex can be discerned in the spin-valve measurements, and not its chirality. Finally, as a sufficiently large negative magnetic field is applied, the vortex is annihilated and the contact magnetisation is saturated in the $-y$ direction, causing a

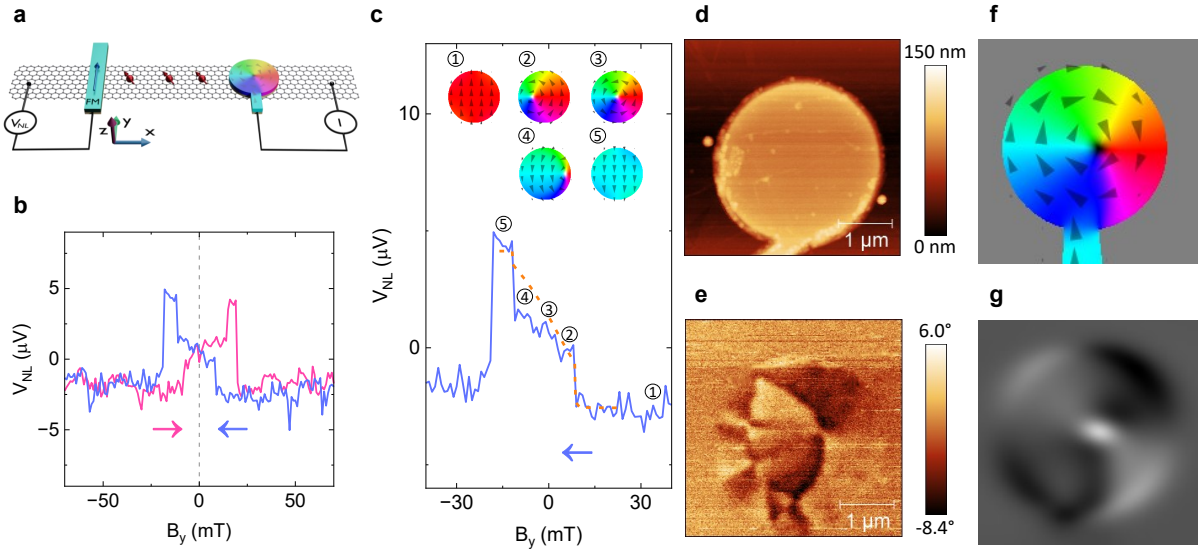


Figure 3.10: Detection of magnetic vortex textures in a circular microstructure. **(a)** Schematic of a spin-valve device with a circular FM contact. **(b)** Spin-valve signal from the device in (a). The arrows indicate the B_y sweep directions. **(c)** Backward sweep of the spin-valve signal in (b). The simulated $-y$ magnetisation is indicated by a dotted line. Inset: Simulated magnetic textures illustrating the magnetisation dynamics of the circular contact. The circled numbers 1-5 indicate the correlation between the magnetic textures and the spin-valve signal, where 3 is an intermediate point in the gradual shift between 2 and 4. **(d,e)** AFM topography (d) and MFM phase shift image (e) of a circular FM contact. **(f,g)** Simulated magnetic texture of a circular contact (f) and the corresponding simulated MFM image (g). Adapted from *Paper I*.

second sharp step in V_{NL}. These magnetisation dynamics were qualitatively replicated by the micromagnetic simulations. The insets in Figure 3.10c present representative simulated spin textures along the B_y sweep, and the dotted line in Figure 3.10c indicates the simulated $-y$ magnetisation of the circular contact with a similar shape to the experimental spin-valve signal.

The magnetic vortex texture in the circular contact was further corroborated with MFM measurements. Figure 3.10d,e contain AFM topography and MFM images, where the phase shift in the latter originates from the sample magnetisation. The main features of the MFM image are bright and dark arcs that extend outwards from a point close to the centre of the circular contact, which can be interpreted as a radial vortex texture with a changing magnetisation orientation around that centre point. A similar MFM image was replicated from the simulated magnetic texture in Figure 3.10f, with bright and dark arcs as can be seen in Figure 3.10g. The offset

of the vortex core from the centre of the circular contact (which appears both in the experiments and in the simulations) can be understood as a remanent magnetisation from the B_y sweep. On the other hand, the smaller vortex-like pattern on the left side of Figure 3.10e could not be captured by the micromagnetic simulations, and most likely originates from inhomogeneities in the magnetic texture because of defects in the cobalt thin film or because of frustrations in the magnetic domains due to their relatively large size [410].

3.2.3 Detection of magnetic vortex textures in a square microstructure

Finally, magnetic vortex textures were also investigated in a square FM contact, which is illustrated in Figure 3.11a. Unlike the circular contact, the square contact is not fully symmetric, but it still has an ill-defined magnetic easy axis due to its fourfold geometrical symmetry [409]. Figure 3.11b showcases a complicated spin-valve signal with sharp steps and gradual slopes of both increasing and decreasing V_{NL}. The added complexity originates from the regular and specially shaped FM contacts (left and right in Figure 3.11a, respectively) having overlapping contributions to the measured spin signal. By comparing the spin signal in Figure 3.11b with reference measurements without any specially shaped electrodes, the contribution from the left contact in Figure 3.11a could be identified as singular sharp steps at $B_y \approx \pm 20\,\mathrm{mT}$, and was subsequently removed in order to alleviate the analysis of the magnetisation dynamics of the square contact. The backward sweep of the resulting corrected spin signal with contributions only from the square FM contact is shown in Figure 3.11c.

The spin-valve signal from the square FM has a sharp step followed by a gradual slope and a second smaller step. As a magnetic field is swept from a large positive value towards zero, the saturated $+y$ magnetisation of the square contact transitions into its vortex ground state. Interestingly, the key difference compared to circular contact above is that the magnetic vortex of the square electrode is nonuniform and consists of four distinct triangular domains, in contrast to the continuously changing magnetisation in Figure 3.10 [410, 480]. The geometrical shape of the square contact causes this special type of vortex to be energetically favourable since it encompasses both a flux-closing magnetic configuration and an alignment of the cobalt spins with the straight edges of the contact [478]. When the external magnetic field is swept towards negative values, the core of the magnetic

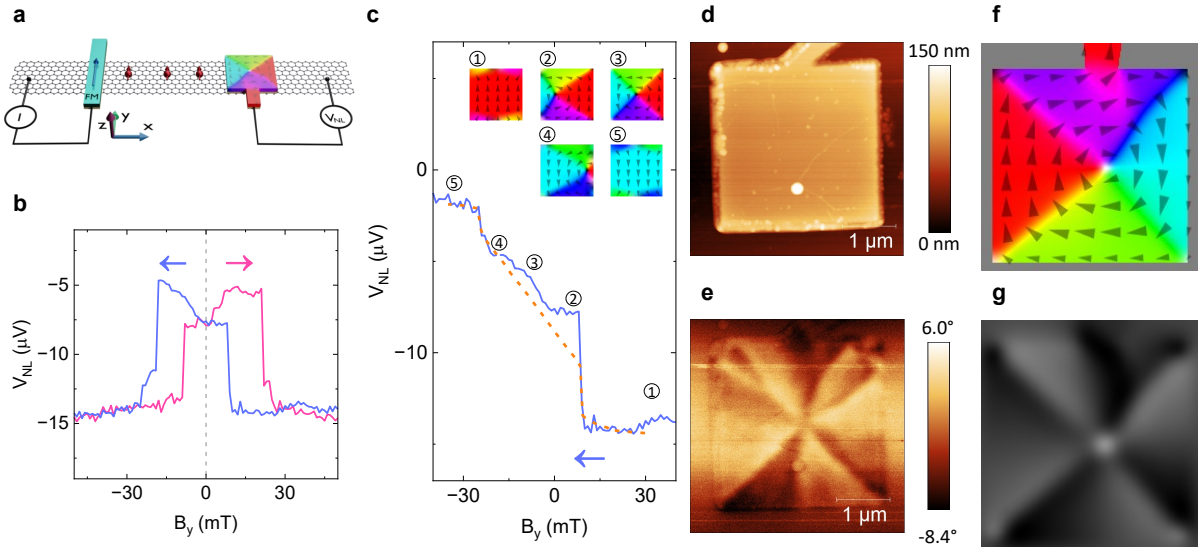


Figure 3.11: Detection of magnetic vortex textures in a square microstructure. **(a)** Schematic of a spin-valve device with a square FM contact. **(b)** Spin-valve signal from the device in (a). The arrows indicate the B_y sweep directions. **(c)** Corrected backward sweep of the spin-valve signal in (b), without the contribution from the regular FM contact. The simulated $-y$ magnetisation is indicated by a dotted line. Inset: Simulated magnetic textures illustrating the magnetisation dynamics of the square contact. The circled numbers 1-5 indicate the correlation between the magnetic textures and the spin-valve signal, where 3 is an intermediate point in the gradual shift between 2 and 4. **(d,e)** AFM topography (d) and MFM phase shift image (e) of a square FM contact. **(f,g)** Simulated magnetic texture of a square contact (f) and the corresponding simulated MFM image (g). Adapted from *Paper I*.

vortex moves continuously towards the right edge of the square contact and is eventually annihilated so that the magnetisation becomes saturated in the $-y$ direction. The slightly uneven slope of the measured spin signal may arise due to pinning of the magnetic vortex by defects in the cobalt thin film. These magnetisation dynamics were qualitatively reproduced by the micromagnetic simulations, and representative magnetic textures and the simulated y magnetisation of the square contact are shown in Figure 3.11c.

AFM and MFM measurements were performed for the square contact, with the results shown in Figure 3.11d,e. The triangular pattern with straight borders between bright and dark areas is noticeably different from the arcs observed in the circular FM contact. As can be seen in Figure 3.11f,g, a simulated magnetic vortex texture with distinct triangular domains generates an MFM image that is nearly identical to the experimental

results.

To further verify the vortex character of the magnetisation of the square contact, additional spin transport measurements were performed. The spin signal from a minor-loop measurement is shown in the top of Figure 3.12a, where the B_y sweep was reversed before the second sharp step in the spin signal to prevent the annihilation of the magnetic vortex. As can be seen, the gradual slope in the spin-valve signal is reversible whereas the sharp step is hysteretic, which agrees well with the expected behaviour of the reversible movement and the hysteretic creation/annihilation of a magnetic vortex, respectively [420, 478, 480]. Hanle spin precession measurements were also performed, and the spin-valve and Hanle signals are shown with the same scaling in Figure 3.12b,c for a stepped and a square FM contact, respectively. Both the spin-valve and the Hanle signal from the stepped contact have similar amplitudes, as expected for a large net magnetisation at zero in-plane magnetic field for the elongated contact with a well-defined magnetic easy axis. In contrast, the Hanle signal that was measured with the square contact has a significantly reduced amplitude, which indicates a small net magnetisation. These results thus provide further confirmation of the square FM contact having a vortex magnetic texture.

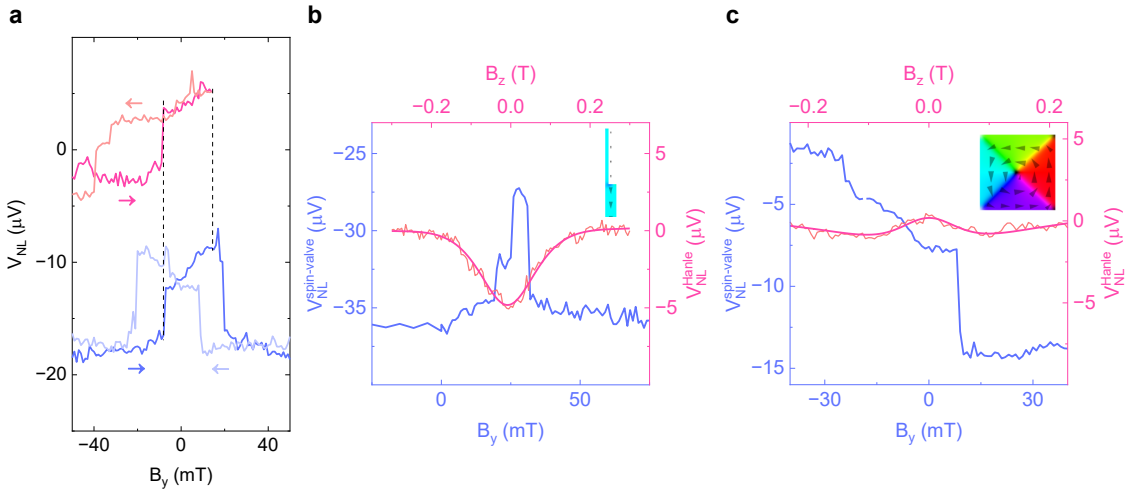


Figure 3.12: Minor-loop and Hanle spin precession measurements of magnetic vortex textures. (a) Minor-loop (top) and full-sweep (bottom) spin-valve measurements of a spin-valve device with a square FM contact. The arrows indicate the B_y sweep directions. The data has been shifted vertically for clarity. The field range of the reversible slope in V_{NL} is indicated by black dashed lines. **(b,c)** Spin-valve (blue) and Hanle spin precession (pink) signals from spin-valve devices with a stepped (b) and a square (c) FM contact, respectively, with the same scaling between the spin-valve and the Hanle signals. The spin-valve signals are the same data as in Figure 3.7h and in Figure 3.11c, respectively. Linear backgrounds were subtracted from the Hanle signals and the solid lines are fits to the signals, using Equation (3.1). Insets: Simulated magnetic textures of a stepped (b) and a square (c) FM contact, respectively, for $B_y = 0\,\mathrm{T}$. Adapted from *Paper I*.

3.3 Electrical detection of spin textures in van der Waals ferromagnet Fe_5GeTe_2

Beyond conventional 3D magnets such as cobalt, vdW magnets have the potential for magnetism and spin dynamics down to the atomically thin 2D limit [481, 482] and can host exotic magnetic domains and spin textures [483–487]. The vdW magnet Fe_5GeTe_2 (FGT) is noncentrosymmetric [391, 488] and can host chiral stripe and skyrmionic spin textures due to its Dzyaloshinskii-Moriya interactions [485, 489], although geometrical constrictions or other nucleation sites can be necessary for deterministic generation of such chiral spin textures [490–493]. FGT flakes with constrictions or notches, where the geometric shapes can cause formation and pinning of chiral spin textures at room temperature, were used to fabricate graphene spin-valve devices with van der Waals heterostructures, as shown schematically in Figure 3.13a and with a microscope picture in Figure 3.13b.

By injecting spin from FGT into the graphene channel, spin textures can be detected by a reference quasi-single-domain cobalt contact, and the evolution of the spin texture in FGT can be probed by spin transport measurements. Schematic spin-valve signals for single magnetic domains and chiral spin textures are visualised in Figure 3.13c,d. Here, the nonlocal resistance is defined as $R_{NL} = V_{NL}/I$. Different from spin-valve signals with two Co contacts (*e.g.* in Figure 3.3d), the single-domain (SD) spin-valve signal in Figure 3.13c has one sharp and one slightly more gradual step in R_{NL}. The sharp step is associated with the magnetisation switching of Co, whereas the more gradual step originates from the switching of FGT due to its canted magnetic domain realignment to the y axis [391]. Meanwhile, the spin-texture (ST) signal is expected to have broader peaks with switching before zero magnetic fields due to the reduced energy state of the spin texture compared to a saturated magnetisation along the y axis (which can be compared to the circular and square Co contacts in Section 3.2).

3.3.1 Spin-texture spin-valve device with a constriction in Fe_5GeTe_2

The measured spin-valve signal in a device with a constriction in the FGT flake is presented in Figure 3.14a. Multi-step switching is observed due to overlapping SD and ST contributions to the spin-valve signal from the narrower and the wider sections of the FGT flake, respectively, which are decoupled by the geometric constriction. To alleviate the analysis, the spin

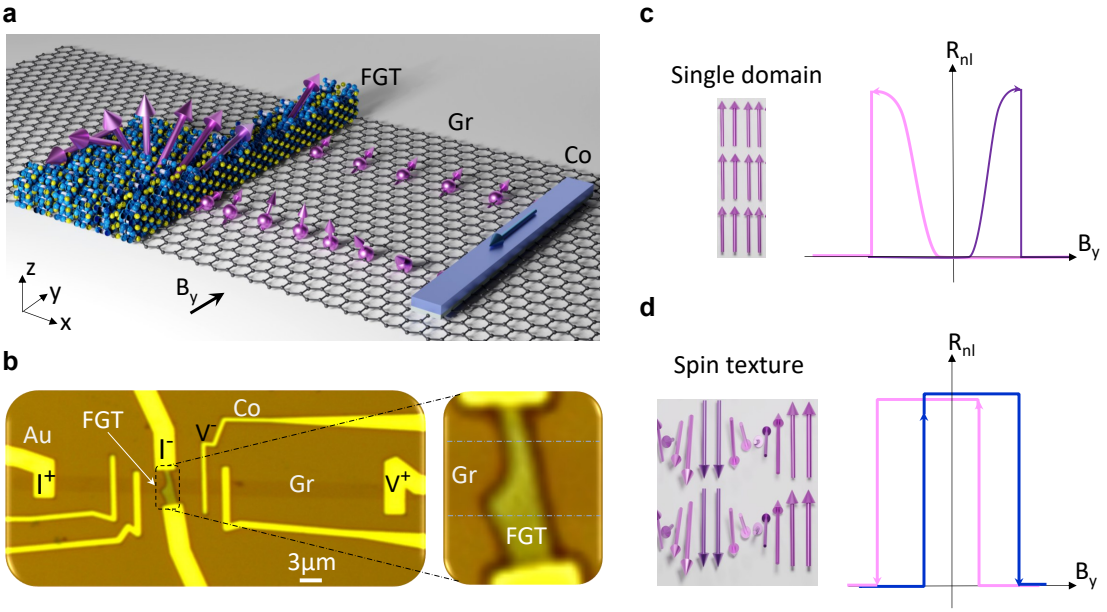


Figure 3.13: Graphene spin-valve device for electrical detection of magnetic spin textures in Fe_5GeTe_2. (a,b) Schematic (a) and microscope picture (b) of a spin-valve device with an Fe_5GeTe_2 (FGT) flake with a constriction that can host chiral magnetic spin textures. The right panel in (b) shows a magnified microscope picture of the constricted FGT flake, where the dashed lines indicate the borders of the graphene spin transport channel. The used current and voltage connections for the nonlocal spin transport measurements are indicated as $I^{+/-}$ and $V^{+/-}$, respectively. **(c,d)** Illustrations of a single magnetic domain and a chiral spin texture, respectively, in FGT, and the associated expected spin-valve signals. Adapted from *Paper II*.

signal is decomposed to separate the SD and ST components in Figure 3.14b. The magnetisation dynamics of the FGT flake and the reference Co electrode can be understood as follows. For large negative magnetic fields, all magnetic domains are aligned in the $-y$ direction (stage I in Figure 3.14a). As B_y approaches zero, the wider section of the FGT flake transitions to a chiral spin texture state with a small net magnetisation (stage II), which is seen as a sharp step in R_{NL}. Similarly to the vortex states in the circular and square Co contacts in Section 3.2, the onset of the spin texture before the magnetic field reaches zero indicates that this is the ground state of the wider section of the FGT flake. At small positive magnetic fields, the slightly gradual step in the spin signal is caused by the switching of the narrower section of the FGT flake from a $-y$ to a $+y$ SD magnetisation (stage III). This is followed by a sharper step of decreasing R_{NL} due to the switching of the reference Co contact (stage IV). Stage III and stage IV therefore

correspond to the same magnetic state of the FGT flake, whereas stage II and stage IV correspond to different states despite having similar spin signal magnitudes. Finally, when a strong positive magnetic field is applied, the spin texture is destroyed so that all magnetic domains are aligned in the $+y$ direction (stage V), which is seen as another step of decreasing R_{NL}. The respective magnetisations of the SD and ST sections of the FGT flake and the reference Co contact are illustrated with arrows in Figure 3.14b. The backward sweep from positive to negative magnetic fields produces analogous magnetisation dynamics and a similar spin signal. The robust spin signals with multi-level switching clearly indicates the coexistence of spin textures and canted single magnetic domains in the constricted FGT flake at room temperature.

Additional experiments were conducted to properly probe the spin texture in FGT. First, spin-valve measurements were performed with two standard Co contacts, one of which was the same FM contact as was used for the measurement in Figure 3.14 (see Figure 3.15a). The Co-Co and FGT-Co spin-valve signals are compared in Figure 3.15b, where both signals contain a sharp step at the same coercive field due to the contribution from the same quasi-single-domain Co contact. This hence confirms the identification of the Co magnetisation switching above, and that stage III and stage IV in Figure 3.14a indeed represent the same magnetic configuration of FGT. The small gradual shift in stage III-IV comes from the continuous realignment of the FGT SD towards the $+y$ orientation [391].

Next, spin-valve measurements were performed in a heterostructure device with an FGT flake without a geometric constriction, as shown schematically in Figure 3.15c. The resulting spin-valve signal in Figure 3.15d without any multi-level switching demonstrates that the constriction in FGT above pins the spin textures and decouples them into different magnetic domains.

Low-temperature measurements of the constricted FGT were also performed. Figure 3.15e shows the spin-valve signal at a temperature of $T = 60\,\mathrm{K}$ in comparison to the the room-temperature signal. The amplitude of the spin signal is significantly enhanced at low temperatures. The low-temperature signal also shows more detailed switching features, which can be attributed to the presence of more subtle spin textures in FGT at low temperatures [494]. The coercive fields of both SD FGT (H_{c1}) and Co increases due to the enhanced magnetic anisotropies of both materials at decreased temperatures. Interestingly, however, the ST FGT gains an increased coercive field (H_{c2}), where the ST is destroyed, but the 'recover field' (H_r), where the ST is created, remains unchanged between 300 K and

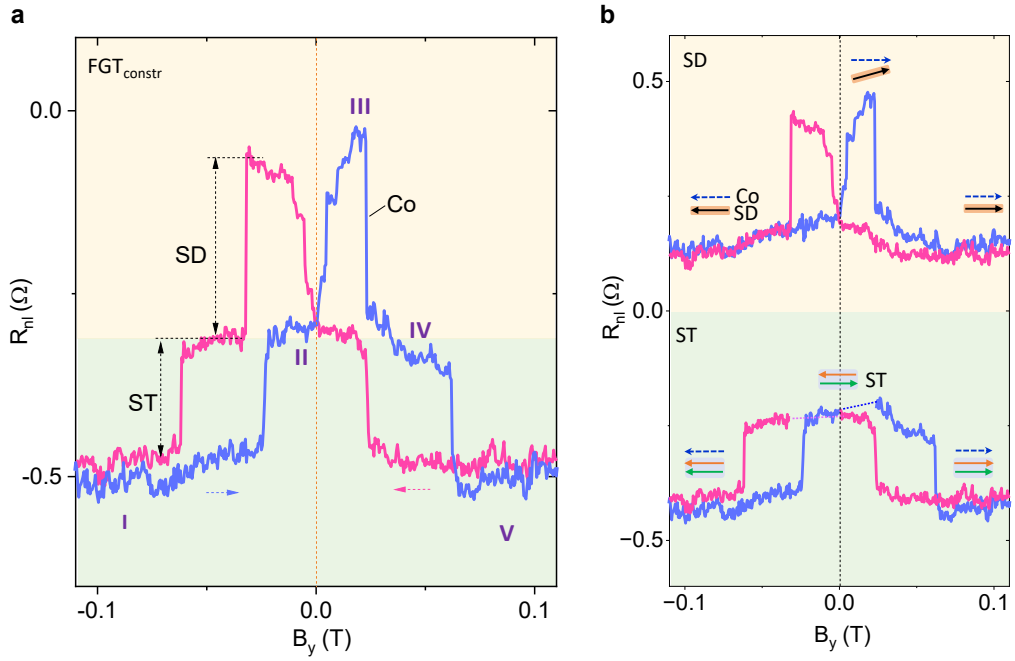


Figure 3.14: Detection of spin textures in constricted FGT. (a) Spin-valve signal from a van der Waals heterostructure device with FGT with a constriction (FGT$_{\text{constr}}$) at room temperature. The stages I-V correspond to different magnetisation states of FGT and the reference Co contact. The single-domain and spin-texture components of the spin signal are indicated as SD and ST, respectively. **(b)** The decomposed SD (top) and and ST (bottom) components of the signal in (a). The blue and black arrows indicate the magnetisations of the Co contact and the SD section of FGT, respectively, and the green and orange arrows indicate y projections of the effective subdomain structures of the ST section of FGT. The dashed blue and pink arrows indicate the B_y sweep directions. The data in (b) has been shifted vertically for clarity. Adapted from *Paper II*.

60 K, as indicated with dashed lines in Figure 3.15e. This nonuniform shift highlights the fundamental difference between the ST in FGT compared to conventional SDs, and may appear due to pinning effects of the spin textures by the geometrical constriction.

Finally, the bias-current dependency of the spin-valve signals from FGT with a constriction is shown in Figure 3.15f. As can be seen, the multi-level spin signal gains an opposite sign but retains a similar amplitude when the polarity of the bias current is reversed.

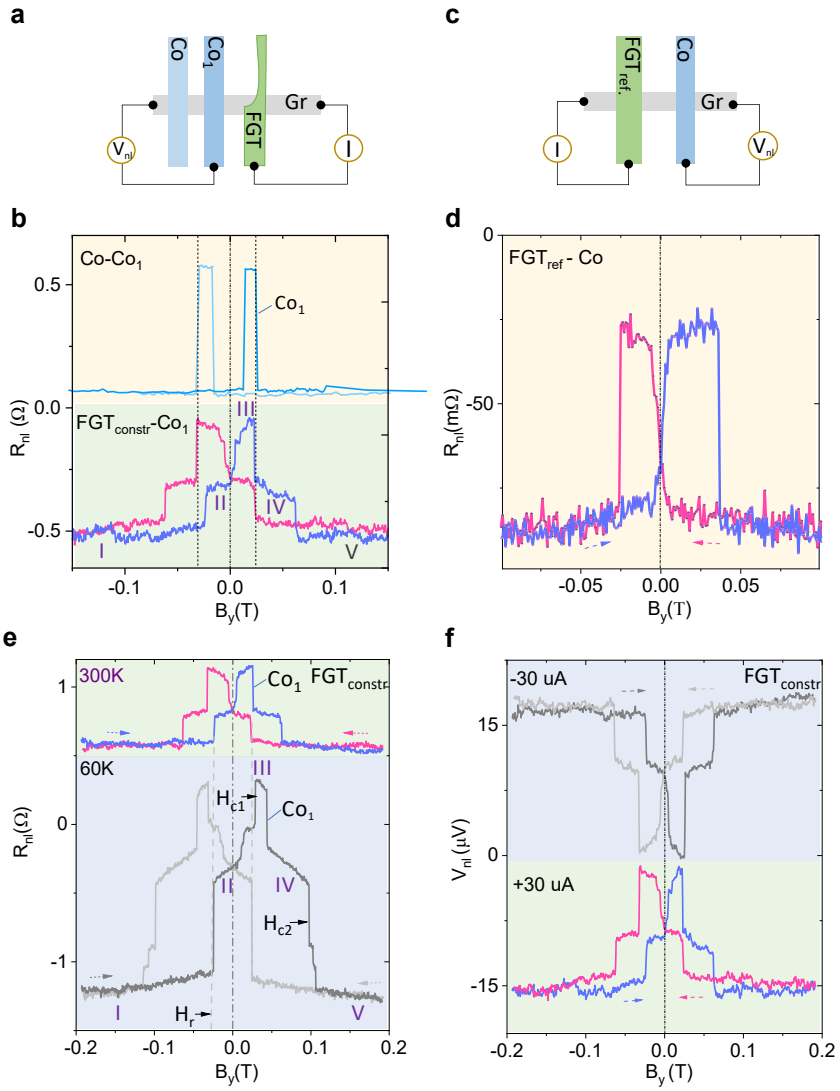


Figure 3.15: Additional measurements of the spin-texture spin-valve signals in constricted FGT. (a) Schematic of a spin-valve device with constricted FGT and two standard Co contacts. **(b)** Spin-valve signals from the device in (a) with two Co contacts (top) and with one Co contact and constricted FGT (bottom). The same Co contact (Co_1) was used in both measurements. **(c)** Schematic of a reference spin-valve device with FGT without a constriction. **(d)** Spin-valve signal of the reference device in (c). **(e)** Spin-valve signals from the device in (a) at room- ($T = 300\,\mathrm{K}$; top) and low temperature ($T = 60\,\mathrm{K}$; bottom). The coercive fields $H_{c1,2}$ and recover field H_r are indicated by arrows. **(f)** Spin-valve signals from the device in (a) for positive (bottom) and negative (top) bias currents ($I = \pm 30\,\mu\mathrm{A}$). The dashed arrows indicate the B_y sweep directions. The data has been shifted vertically for clarity. The bottom signals in (b,f) is the same data as in Figure 3.14a. Adapted from *Paper II*.

3.3.2 Spin-texture spin-valve device with a notch in Fe_5GeTe_2

A van der Waals heterostructure spin-valve device with an FGT flake with a notch instead of a constriction is shown schematically and with a microscope picture in Figure 3.16a,b, which was studied to investigate the pinning effects of exotic spin textures in FGT with different geometries. The measured spin-valve signal can be seen in Figure 3.16c, and has a similar multi-level shape to the signals from the constricted FGT above. This indicates a coexistence of a chiral spin texture and a single magnetic domain in FGT, with an evolution across the stages I-V similar to the description above.

The magnetic hysteresis of the ST and SD components of the spin signal were investigated in detail through minor-loop measurements [427], as shown in Figure 3.16d. A large hysteresis effect of the ST signal component is observed in the top panel of Figure 3.16d, where the creation and annihilation of the spin texture happen at significantly different magnetic fields (the recover and coercive fields H_r and H_c, respectively). It is noticed that H_r and H_c are independent of the field sweeping history throughout the minor-loop measurements, as indicated with dashed lines. The hysteresis of both the ST and the SD components of the spin signal is shown in the middle and bottom panels of Figure 3.16d. In the middle panel, the switching and hysteresis of the SD FGT results in a triangular loop in addition to the square hysteresis loop of the ST FGT. Meanwhile, the butterfly pattern in the bottom panel contains the switching and hysteresis effects of both the SD FGT and the reference Co contact.

3.3.3 Hanle spin precession measurements in spin-texture spin-valve devices

Hanle spin precession measurements were performed in both devices with constricted and notched FGT to further probe their spin polarisations, as described in detail in Section 3.1.1. Figure 3.17a visualises the zHanle measurements of the spin-valve device with constricted FGT, and Figure 3.17b contains the measured zHanle spin signal in comparison to the spin-valve signal. Interestingly, the amplitude of the zHanle signal is similar to the amplitude of the SD component of the spin-valve signal, indicating that the main contribution to the zHanle signal is the SD section of the FGT flake, whereas the contribution from the ST section is minor due to its small net magnetisation in the absence of an IP magnetic field. The asymmetric

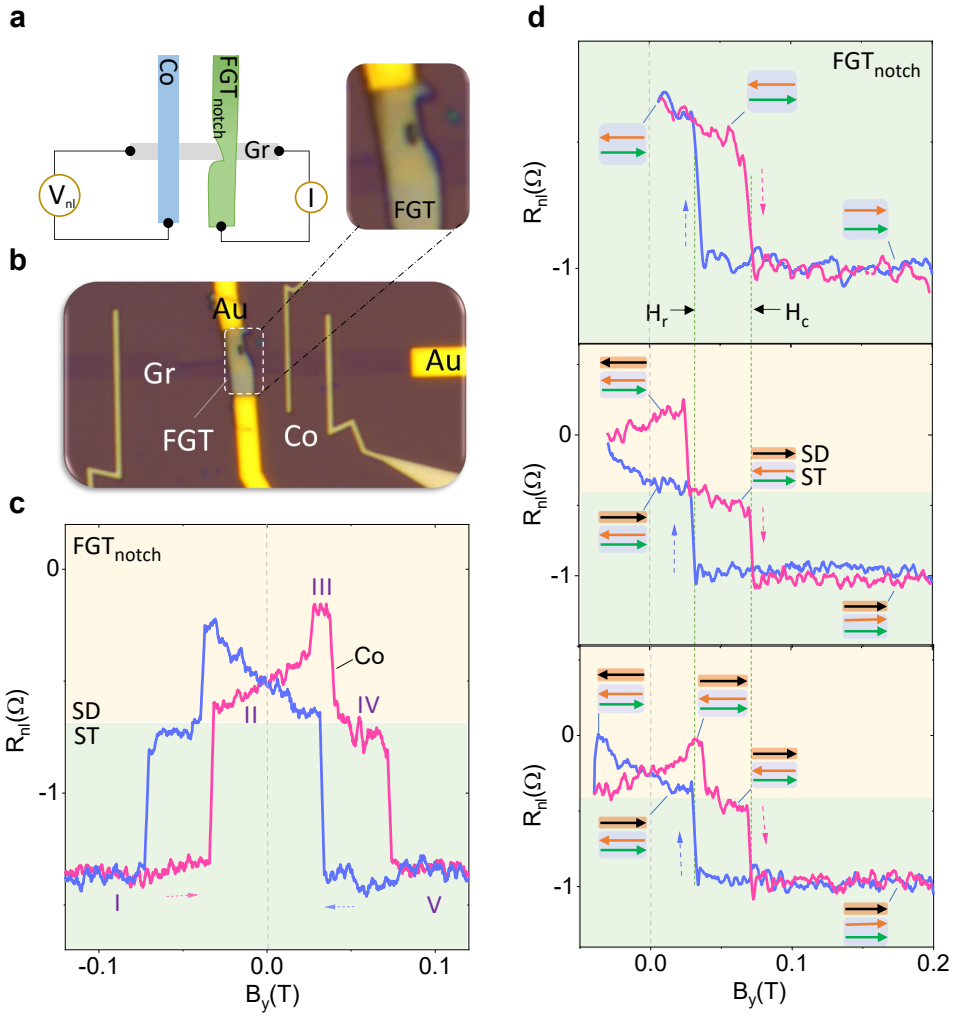


Figure 3.16: Detection of spin textures in notched FGT. (a,b) Schematic (a) and microscope picture (b) of a spin-valve device with an FGT flake with a notch. The top-right panel in (b) shows a magnified microscope picture of the notched FGT. **(c)** Spin-valve signal from the device in (a,b) with notched FGT (FGT_{notch}). The stages I-V correspond to different magnetisation states of FGT and the reference Co contact. The single-domain and spin-texture components of the spin signal are indicated as SD and ST, respectively. **(d)** Minor-loop measurements of the device in (a,b). The black arrows indicate the magnetisation of the SD section of FGT, and the green and orange arrows indicate y projections of the effective subdomain structures of the ST section of FGT. The recover H_r and coercive H_c fields of the ST section are indicated by arrows and dashed lines. The dashed pink and blue arrows indicate the B_y sweep directions. Adapted from *Paper II*.

shape of the zHanle spin signal with nonzero antisymmetric and symmetric components (as shown in Figure 3.17c) signifies the presence of both x and

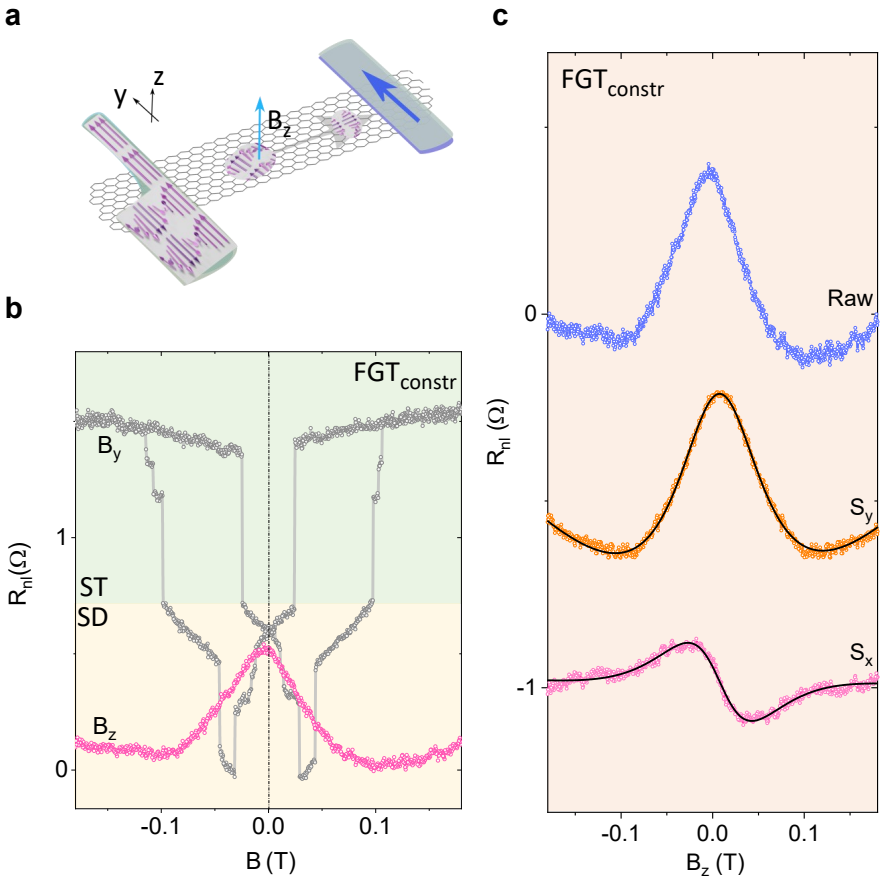


Figure 3.17: Hanle spin precession measurement of spin textures in constricted FGT. (a) Schematic of zHanle spin precession in a spin-valve device with constricted FGT. **(b)** Comparison of zHanle (B_z) and spin-valve (B_y) signals from the device in (a). **(c)** The raw zHanle signal from (b) as well as its symmetric and antisymmetric components, which correspond to y and x spin polarisations, respectively. The solid lines are fits to the signal components. The data has been shifted vertically for clarity. Adapted from *Paper II*.

y components of the IP spin polarisation. The larger amplitude of the symmetric component, compared to the antisymmetric one, indicates that the net spin polarisation is closer to the y direction than the x direction, which aligns with the typical canted magnetisation of SD FGT [394].

Detailed zHanle and xHanle spin precession measurements were conducted for the notched FGT (illustrated in Figure 3.18a,d) with parallel and antiparallel magnetisation of the reference Co contact and the SD section of the FGT flake. Similar to the zHanle signal from the constricted FGT, the amplitudes of the zHanle signals in Figure 3.18b compared to the corresponding spin-valve signal indicate that the spin contribution from the

SD FGT dominates also in the notched case. The two zHanle signals for opposite magnetisation configurations were averaged using Equation (3.2), and the symmetric and antisymmetric components of the pure spin signal in Figure 3.18c could be extracted. As for the constricted FGT, the two signal components indicate a similarly canted IP magnetism in the SD section of the notched FGT.

Interestingly, the xHanle signal in Figure 3.18e has an amplitude that is similar to the SD part of the spin-valve signal for small magnetic fields, but gains a different behaviour and a significantly larger magnitude in the high-field range. This can be understood as a dominant SD contribution to the xHanle spin precession for smaller fields, followed by a realignment of the magnetisation of the entire notched FGT flake as well as the Co detector contact for larger IP magnetic fields. By averaging the two spin signals for parallel and antiparallel magnetisation configurations, the non-spin-precession contributions can be removed (including the effects of the magnetisation realignment at large B_x values [391]), resulting in the symmetric and antisymmetric signal components in Figure 3.18f without such anomalous behaviour. Here, the symmetric component of the xHanle signal dominates, which corresponds to the y spin polarisation, while the smaller antisymmetric signal component indicates an out-of-plane canting. Together with the results in Figure 3.18c, the SD notched FGT magnetisation can therefore be concluded to point mainly along the y direction but with a canting in the x and z directions.

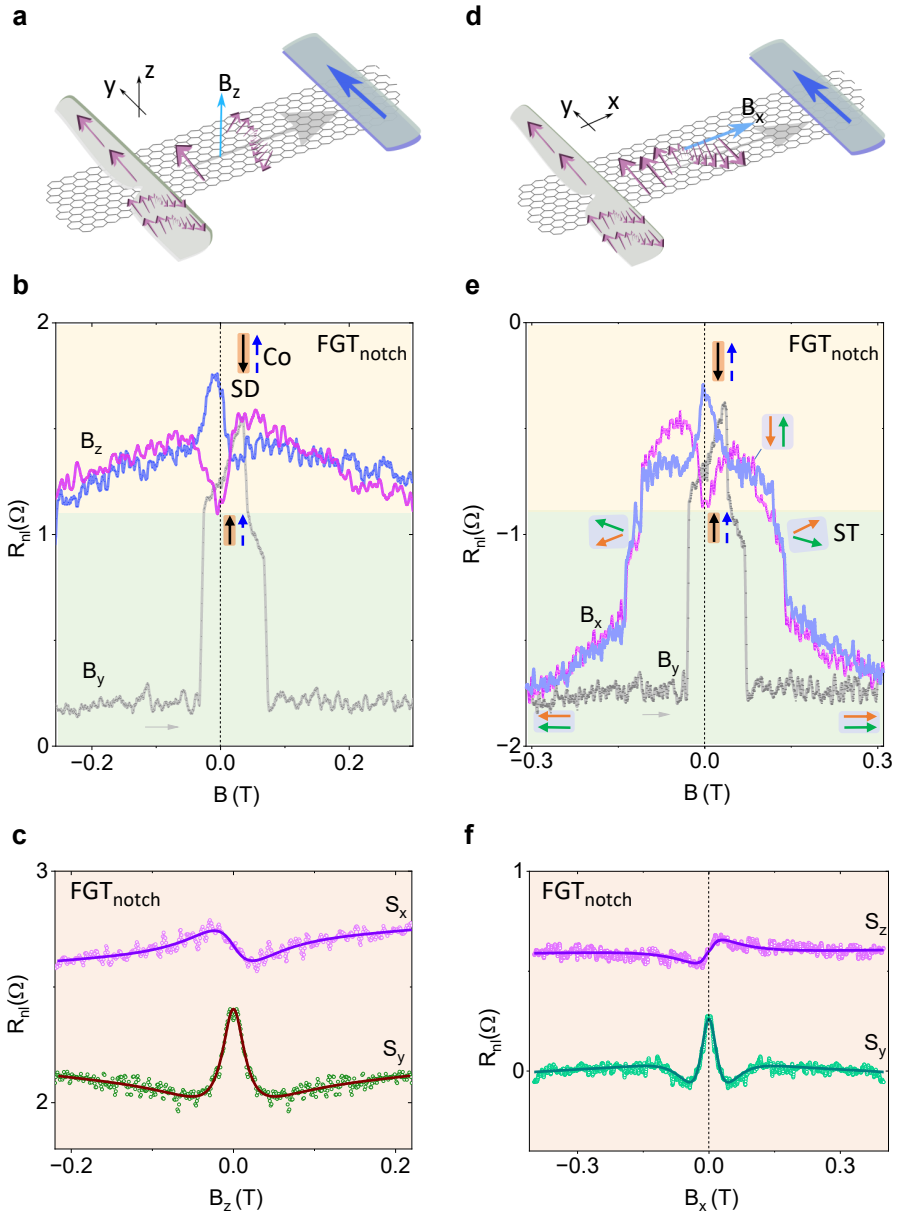


Figure 3.18: Hanle spin precession measurement of spin textures in notched FGT. (a,d) Schematics of zHanle (a) and xHanle (d) spin precession, respectively, in a spin-valve device with notched FGT. **(b,e)** Comparison of zHanle (B_z) and spin-valve (B_y) signals (b) and of xHanle (B_x) and spin-valve signals (e), respectively, from the device in (a,d). The blue and black arrows indicate the magnetisations of the Co contact and the SD section of FGT, respectively, and the green and orange arrows indicate the effective subdomain structures of the ST section of FGT. The grey arrows indicate the B_y sweep direction. **(c,f)** The symmetric and antisymmetric components of the Hanle signals in (b,e), which correspond to y and x (c) and y and z (f) spin polarisations, respectively. The solid lines are fits to the signal components. The data has been shifted vertically for clarity. Adapted from *Paper II*.

4 Charge-spin interconversion in topological quantum materials

Charge-spin interconversion effects encompass current-induced polarisation of spin, *i.e.* the generation of spin accumulations or spin currents from electronic charge currents, as well as the inverse effect where a net spin polarisation generates a charge current or voltage. Naturally, such effects are of central importance for spintronics applications, where charge-spin interconversion can allow nonmagnetic materials with strong SOC to act as efficient spin sources and sensors in the absence of magnetic fields. Reliable demonstrations of robust charge-spin interconversion at room temperature are therefore important steps towards next-generation fast and energy-efficient spin-based nonvolatile computing technologies.

Topological quantum materials such as TIs and WSMs stand out as an especially promising material platform for robust and energy-efficient charge-spin interconversion effects due to their topologically nontrivial band structures with strong SOC and SML [**Sierra2021VanOpto-spintronics**, 495, 496], which is elaborated upon in detail in Chapter 2. TIs exhibit bulk bands with strong SOC and topologically protected surface states with SML. As such, TIs can facilitate efficient CSC and large spin polarisations through the SHE and the REE as well as *via* the SML of the TSS [83, 156, 158, 159, 162, 497–500]. Charge-spin interconversion effects in TIs have previously been investigated up to room temperature using potentiometric measurements in local geometries with FM electrodes placed on the TI, which results in competing charge and spin contributions to the measured signal [164–166, 168, 169, 171, 501–503]. In contrast, nonlocal spin-switch and Hanle spin precession measurements with pure spin currents can unambiguously confirm the generation of polarised spin, which can be realised in lateral graphene/TI vdW hybrid spin-valve devices [424, 461, 504]. However, detection of charge-spin interconversion using this kind of reliable nonlocal spin-transport measurements in spin-valve devices has so far been limited to cryogenic temperatures up to $T = 15\,\mathrm{K}$ [170, 174], which is a detrimental limitation for real applications.

WSMs can similarly host efficient charge-spin interconversion effects owing to their semimetallic bulk states with strong SOC and their topologically protected Fermi-arc surface states with SML [77, 179]. Spin polarisation can be generated efficiently through the SHE, the REE as well as the SML of the Fermi arcs, and charge-spin interconversion in WSMs has been experimentally observed up to room temperature [186, 236–238, 240, 242–244], including using nonlocal measurements in graphene heterostructure spin-valve devices [233–235, 239, 241]. The type-II WSM $TaIrTe_4$ (TIT) is of particular interest, however, since its topological band structure has the smallest allowed number of four Weyl nodes for a time-reversal-symmetric WSM [206, 207, 505] as well as topological spin textures on its Weyl nodes and Fermi arcs [207]. Whereas CSC in TIT has recently been demonstrated indirectly through SOT measurements [214, 215, 247], direct detection of charge-spin interconversion is so far still missing.

Here, charge-spin interconversion in the TI $Bi_{1.5}Sb_{0.5}Te_{1.7}Se_{1.3}$ (BSTS) (*Paper III*) and in the WSM TIT (*Paper IV*) is detected using reliable nonlocal spin transport measurements in graphene heterostructure spin-valve devices at room temperature. Spin-switch and Hanle spin precession signals for both CSC and SCC unequivocally confirms the spin origin of the measured signals and demonstrate the robustness of the charge-spin interconversion effects. These results show reliable spin generation and sensing using topological states in TIs and WSMs, and pave the way towards energy-efficient all-electrical spin technologies with topological quantum materials at room temperature.

4.1 Charge-spin interconversion in topological insulator $Bi_{1.5}Sb_{0.5}Te_{1.7}Se_{1.3}$

BSTS is a TI with an optimised chemical composition to tune its Fermi level into the bulk band gap and maximise the electrical transport contribution from its TSS [104–110, 169]. To study its charge-spin interconversion properties, vdW heterostructure spin-valve devices were fabricated from BSTS and graphene, as shown schematically and with a scanning electron microscopy image in Figure 4.1a,b. The heterostructure devices were fabricated through mechanical exfoliation and transfer of BSTS onto a patterned CVD graphene channel, followed by evaporation deposition of nonmagnetic Cr/Au and FM TiO_2/Co contacts as described in Section 3.1.

CSC in TIs at room temperature can originate from the SHE or the REE due to the strong SOC of the TI bulk band states, or from the SML of the TSS [122, 506], all of which are described in more detail in Section 2.1. The REE and the TSML are visualised in Figure 4.1c, where BSTS hosts winding spin textures both in the bulk bands and in the Dirac cones. Under the application of an electric field, the spin textures are offset from their equilibrium positions so that a net spin polarisation is generated. To be noted, the TSML dominates the CSC in BSTS at low temperatures under 100 K [169], but can have a nonzero contribution even at room temperature. In the graphene/BSTS hybrid spin-valve devices, the generated spin from the CSC effects in BSTS is injected across a vdW gap to the graphene channel, and a pure spin current can be detected nonlocally by a FM electrode outside of the charge-current loop.

4.1.1 Charge-to-spin conversion in $Bi_{1.5}Sb_{0.5}Te_{1.7}Se_{1.3}$

First, spin-switch measurements were conducted with an IP magnetic field B_y along the easy axis of the FM contact. In the same way as during spin-valve measurements, the magnetisation reversal of the FM contact is seen as a sharp step in the spin signal, whereas the generated spin polarisation from the CSC of BSTS is unaffected by the applied magnetic field. The resulting spin-switch signal in Figure 4.1d therefore clearly indicates the presence of CSC in the TI at room temperature.

Next, zHanle and xHanle spin precession measurements were performed, where the generated spin from the CSC precesses and dephases while propagating along the graphene channel. The characteristic spin signals in Figure 4.1e,f therefore unambiguously verify the spin origin of the observed sig-

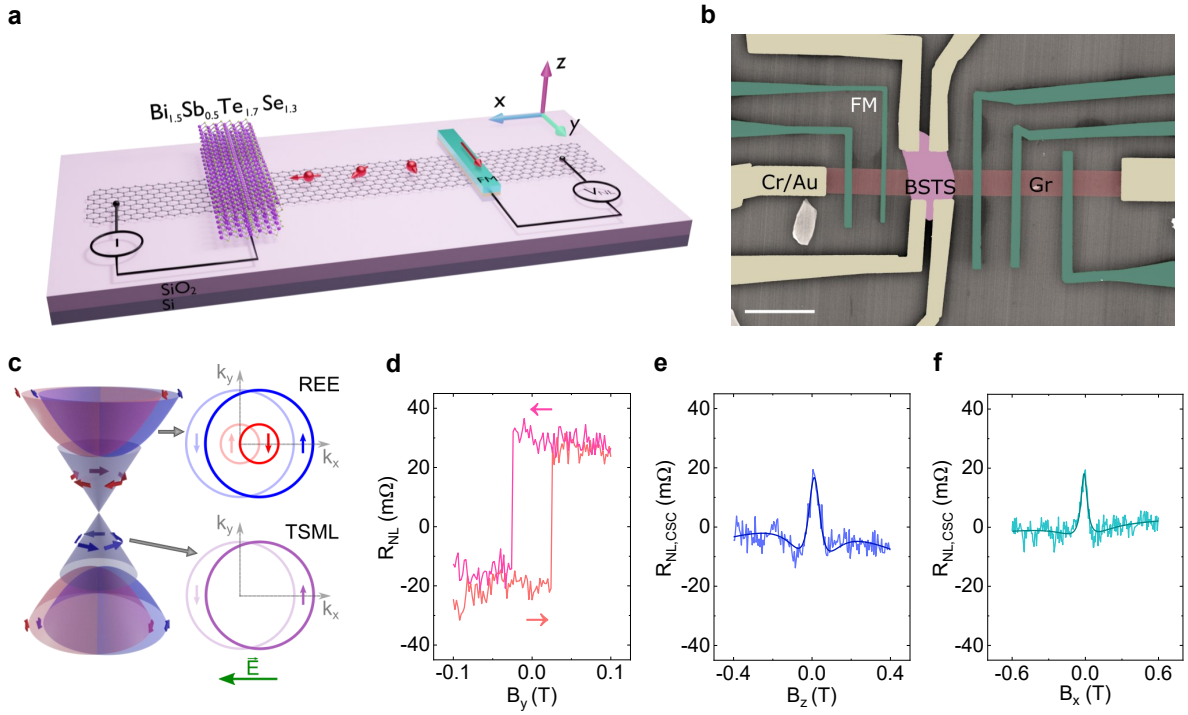


Figure 4.1: Graphene/BSTS heterostructure device for nonlocal detection of charge-spin interconversion at room temperature. (a,b) Schematic (a) and coloured SEM image (b) of a representative graphene/BSTS heterostructure spin-valve device. The scale bar in the SEM image is 5 μm. **(c)** Simplified band structure of BSTS and schematics of CSC through the REE and the TSML, respectively. **(d-f)** Spin-switch (d), zHanle spin precession (e) and xHanle spin precession (f) signals from CSC in BSTS. The Hanle signals ($R_{NL,CSC}$) were obtained by averaging the measured signals for $\pm y$ magnetisations of the detector contact using Equation (4.1). The pink arrows in (d) indicate the B_y sweep directions, and the solid lines in (e,f) are fits to the Hanle signals. The measurements were performed in Device BSTS-1. Adapted from *Paper III*.

nal. In order to remove non-spin-related contributions from the measured signals, the Hanle signals in Figure 4.1e,f were obtained by averaging spin signals for $+y$ and $-y$ magnetisations of the FM detector contact ($R_{NL,\uparrow}$ and $R_{NL,\downarrow}$, respectively) as

$$R_{NL,CSC} = \frac{R_{NL,\uparrow} - R_{NL,\downarrow}}{2}, \tag{4.1}$$

in analogue to Equation (3.2). The raw Hanle signals are shown in Figure 4.2a,b. By fitting the spin diffusion and precession equation in Equation (3.1) to the data in Figure 4.1e,f, a spin lifetime $\tau_s \approx 130$ ps and a spin

diffusion length $\lambda_s \approx 0.7\,\mu$m in the graphene channel could be extracted from the zHanle measurement ($\tau_s \approx 210\,$ps and $\lambda_s \approx 1.6\,\mu$m for xHanle).

The symmetric shape of the zHanle and xHanle signals in Figure 4.1e,f indicates that the injected spin from the BSTS flake has a polarisation along the y axis (as explained in detail in Section 3.1.1). Interestingly, however, CSC measurements in a second device (Device BSTS-2) yields zHanle spin precession signals with a clear asymmetry. Figure 4.2c includes measured zHanle signals for opposite magnetisations of the detector contact, as well as the corresponding averaged signal from Equation (4.1). The averaged zHanle signal was decomposed into its symmetric and antisymmetric components using Equation (3.3) (shown in the top of Figure 4.2c), and Equation (3.5) yields a significant IP canting angle of 67 °. The most probable reason for this canted spin polarisation with sizeable x and y components is that the charge current distribution through the BSTS flake is similarly diagonal in the xy plane, as the bias current is passed between a nonmagnetic electrode on the TI and the graphene channel (indicated in Figure 4.3a,c), since the charge current and the spin polarisation are expected to be mutually perpendicular under charge-spin interconversion [234, 507]. Meanwhile, the symmetric Hanle signals and y-polarised spin in the first device (Device BSTS-1) signifies a dominant x component of the charge current, which is further confirmed in the next section.

In order to quantify the CSC in BSTS, the polarisation of the injected spin current from the TI was estimated. First, the polarisation P_{FM} of the FM Co contacts was estimated from the equation

$$\Delta R_{NL} = \frac{{P_{FM}}^2 R_{\square} \lambda_s}{w} \exp\left(\frac{-L}{\lambda_s}\right), \tag{4.2}$$

where ΔR_{NL} is the amplitude of the spin signal between two similar FM electrodes in the absence of BSTS, and w and L are the dimensions of the graphene channel [427, 465, 508]. For simplicity, Equation (4.2) assumes that both FM electrodes have identical polarisations. In this way, a FM polarisation of 17 % could be estimated in Device BSTS-1 and 4 % in Device BSTS-2. Next, the spin polarisation from the CSC of BSTS could be estimated from

$$\Delta R_{NL} = \frac{P_{CSC} P_{FM} R_{\square} \lambda_s}{w} \exp\left(\frac{-L}{\lambda_s}\right), \tag{4.3}$$

where ΔR_{NL} is now the amplitude of the CSC spin signal, and one of the P_{FM} factors in Equation (4.2) has been replaced by the polarisation P_{CSC}

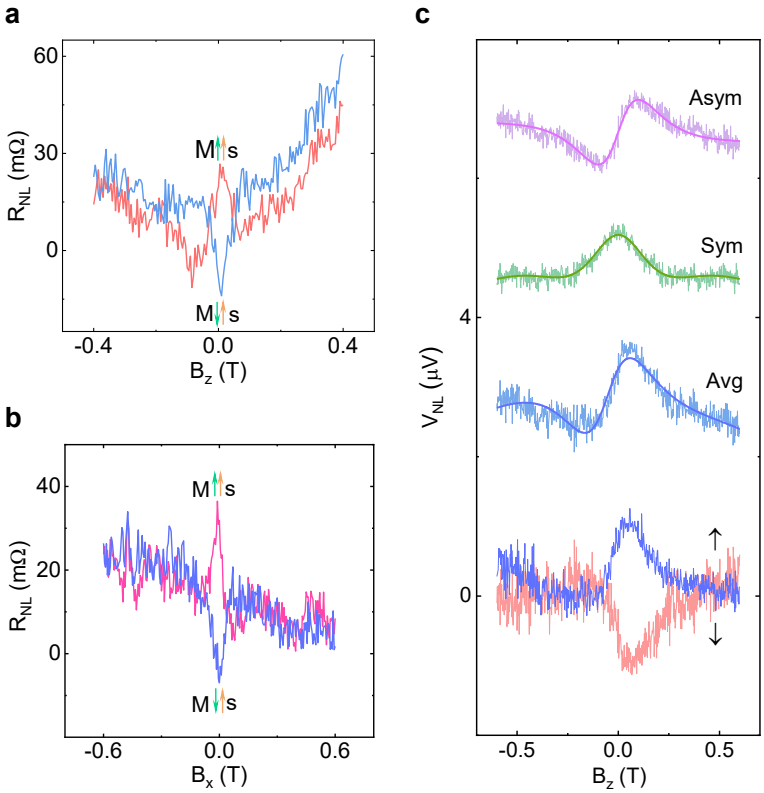


Figure 4.2: Raw and asymmetric Hanle spin precession signals from charge-to-spin conversion in BSTS. (a,b) Raw zHanle (a) and xHanle (b) spin precession signals from CSC in BSTS for $\pm y$ magnetisations of the FM detector contact, corresponding to the averaged signals in Figure 4.1e,f. The magnetisation of the FM contact (M) and the generated spin polarisation from the CSC (s) are indicated with green and orange arrows, respectively. **(c)** zHanle spin precession signals from CSC in BSTS for $\pm y$ magnetisations of the detector contact ($\uparrow$ and $\downarrow$, respectively), as well as the averaged signal (Avg) and the symmetric (Sym) and antisymmetric (Asym) components of the averaged signal. The solid lines are fits to the symmetric and antisymmetric signal components, and a guide to the eye for the averaged signal. The data in (c) has been shifted vertically for clarity. The measurements were performed in Device BSTS-1 (a,b) and in Device BSTS-2 (c), respectively. Adapted from *Paper III*.

of the injected spin current from the CSC. This yields $P_{CSC} \approx 1.5\,\%$ in Device BSTS-1 and $0.1\,\%$ in Device BSTS-2 at room temperature. For comparison, a spin polarisation of $10\,\%$ has previously been reported in a graphene/Bi_2Te_2Se spin-valve device at very low temperatures, but the corresponding spin signal could not be resolved above $T \approx 15\,\mathrm{K}$ [174]. Further-

more, the estimated spin polarisation values in the BSTS devices are likely to be affected by the spin injection efficiency across the vdW gap between BSTS and graphene, and may be underestimated by the relatively simplistic one-dimensional spin-diffusion model in Equation (4.2) and Equation (4.3).

4.1.2 Geometry and bias dependence of the charge-to-spin conversion in $Bi_{1.5}Sb_{0.5}Te_{1.7}Se_{1.3}$

The CSC effect in BSTS was examined further using different measurement geometries with respect to the BSTS flake, as illustrated in Figure 4.3a. In the first measurement geometry, a bias current I_1 is passed to the BSTS flake from the $+x$ direction and the nonlocal voltage $V_{NL,1}$ is measured on the $-x$ side of the flake, whereas the second geometry is mirrored with a bias current I_2 coming from the $-x$ direction and the nonlocal voltage $V_{NL,2}$ being detected on the $+x$ side of the flake. Interestingly, the observed spin-switch signals in the two measurement geometries have opposite polarities, as shown in Figure 4.3b. Since the two geometries are identical in the yz plane but mirrored along the x axis, this means that the CSC effect is odd with the x component of the applied charge current. These results, where a charge current in the x direction leads to a y spin polarisation, is compatible with conventional charge-spin interconversion effects, where the charge current, spin current and spin polarisation are required to be mutually perpendicular ($I \perp I_s \perp S$) [122, 173, 506]. Certain unconventional CSC mechanisms, on the other hand, where broken symmetries allow the charge current and spin polarisation to be parallel [509], can accordingly be ruled out in the present devices.

The bias current dependence of the CSC effect was probed by passing positive and negative bias charge currents through the BSTS flake as shown in Figure 4.3c. When the polarity of the bias current is reversed, the measured spin signals gain a sign change but retain a similar amplitude, which is presented with both spin-switch and zHanle signals in Figure 4.3d,e. Detailed bias dependencies following a linear trend are shown in Figure 4.3f. Reversal of the bias current polarity can be interpreted as a change between injection and extraction of polarised spin, or, equivalently, as a full reversal of the charge current direction in the TI, and both cases agree well with the observed sign change of the spin signals. Furthermore, it is also expected that a larger charge current can lead to the generation of a proportionally larger spin polarisation through the CSC.

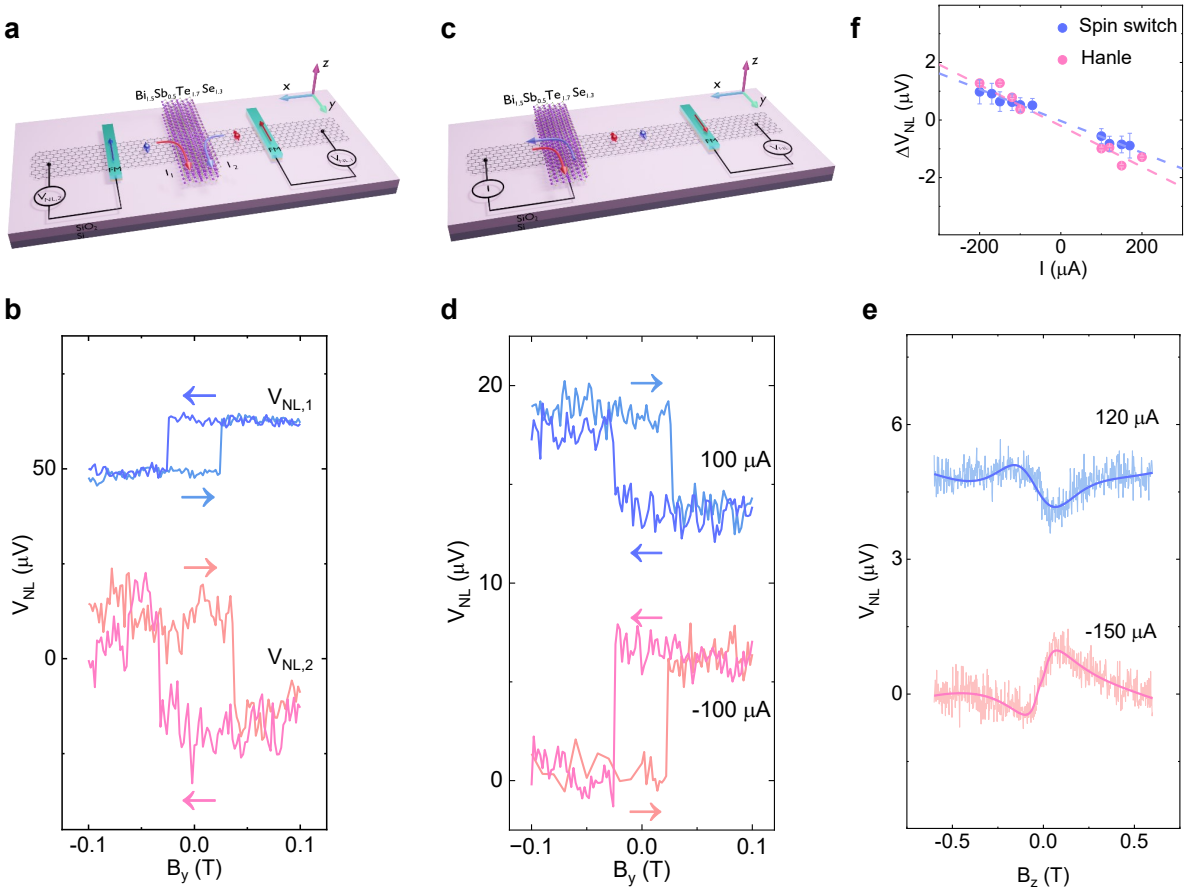


Figure 4.3: Geometry and bias current dependence of charge-to-spin conversion signals in graphene/BSTS heterostructure. **(a)** Schematic of CSC measurements in two different geometries in a graphene/BSTS spin-valve device. **(b)** Spin-switch signals from CSC in BSTS for the two measurement geometries in (a). **(c)** Schematic of CSC measurements with arrows indicating positive and negative bias currents, respectively. **(d,e)** Spin-switch (d) and zHanle (e) signals from CSC in BSTS with positive and negative bias currents. The blue and pink arrows in (b,d) indicate the B_y sweep directions and the solid lines in (e) are guides to the eye for the Hanle signals. The data has been shifted vertically for clarity. **(f)** The amplitude of the measured spin-switch and zHanle signals as a function of bias current with linear fits as guides to the eye. Some error bars are smaller than the data points. The measurements were performed in Device BSTS-1 (b,d) and in Device BSTS-2 (e,f), respectively. Adapted from *Paper III*.

4.1.3 Gate voltage dependence of the charge-to-spin conversion in $Bi_{1.5}Sb_{0.5}Te_{1.7}Se_{1.3}$

Next, the gate voltage modulation of the CSC was studied in the vdW heterostructure device. Here, the gating is applied as a back-gate voltage across the Si/SiO_2 substrate, as visualised in Figure 4.4a. First, Dirac curves showing the gate response of the resistance in graphene were measured across the graphene/TI heterostructure and in pristine graphene outside of the heterostructure area in the same device, using local four-terminal measurement geometries. As can be seen in Figure 4.4b, both the heterostructure and the pristine graphene have very similar doping levels with Dirac voltages of $V_D = 43\,\mathrm{V}$ and $41\,\mathrm{V}$, respectively. This indicates a negligible contribution to the doping of graphene from the TI and/or band misalignment between graphene and BSTS, which could otherwise have offset the charge carrier concentration. To be noted, the resistance difference between the two curves in Figure 4.4b comes from the different channel lengths of the two graphene areas ($6.7\,\mu\mathrm{m}$ and $2.5\,\mu\mathrm{m}$, respectively), and is unrelated to the doping level. The charge carrier mobility was calculated [510] to be $\mu = 1200\,\mathrm{cm^2V^{-1}s^{-1}}$ for graphene in the heterostructure and $\mu = 1000\,\mathrm{cm^2V^{-1}s^{-1}}$ for the pristine graphene, which are expected values for CVD graphene [172, 173, 235, 511, 512].

Spin-switch signals from the CSC in the TI are shown in Figure 4.4c for gate voltages corresponding to the electron- ($V_g = 70\,\mathrm{V}$) and hole-doped ($V_g = -70\,\mathrm{V}$) regimes of the graphene channel. It is found that the spin signals are insensitive to changes in the charge carrier type in graphene, retaining the same sign and similar amplitudes. Meanwhile, the electrochemical potential of the TI flake is largely unaffected by the applied gate voltage due to its thickness as well as electrostatic shielding from the graphene. A detailed gate-dependence of the zHanle spin precession signal amplitude and the corresponding spin transport parameters in graphene are summarised in Figure 4.4d. The top panel contains the Dirac curve of the graphene channel in the heterostructure area for reference. The amplitude of the CSC signals is mainly constant with gate voltage, but has a clear minimum around the charge-neutrality point of graphene. As can be seen, the spin lifetime and spin diffusion length in graphene have similar minima, and increase approximately linearly further away from V_D. The observed disappearance of the spin signal around the charge-neutrality point of graphene is likely caused by a reduced spin injection efficiency due to a conductivity mismatch between the graphene and the TI [428, 465, 467], and/or impaired spin transport in

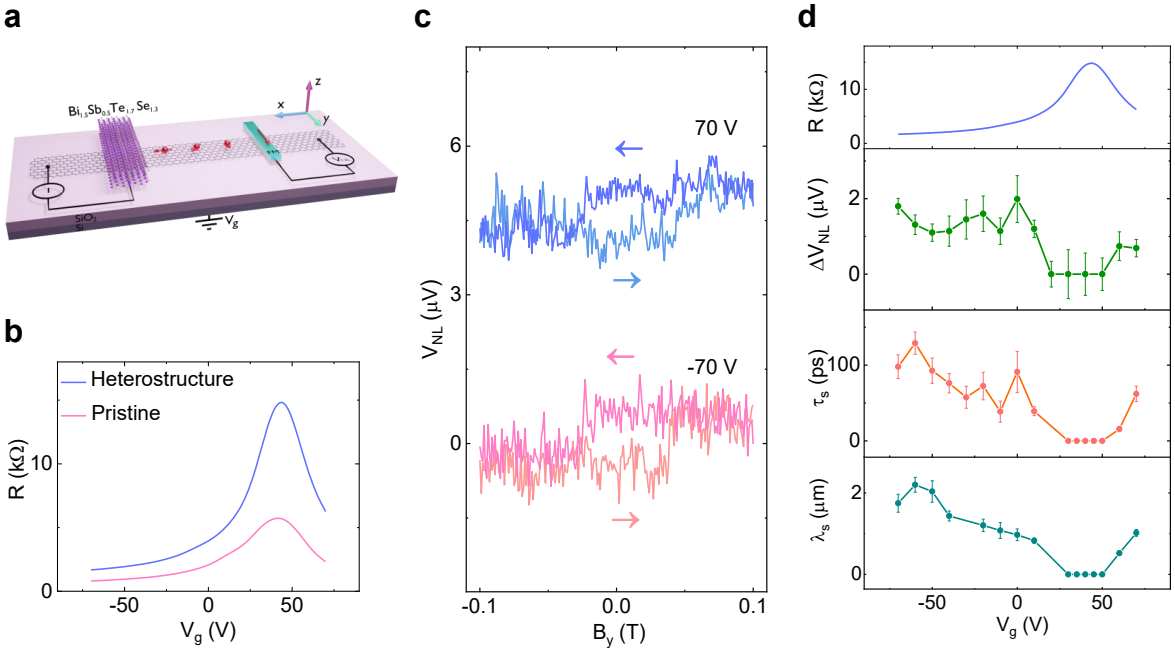


Figure 4.4: Gate dependence of charge-to-spin conversion signals in graphene/BSTS heterostructure. **(a)** Schematic of CSC measurements in a graphene/BSTS spin-valve device with an applied back-gate voltage across the Si/SiO_2 substrate. **(b)** Dirac curves, showing the gate response of the graphene resistance across the vdW heterostructure and in pristine graphene. **(c)** Spin-switch signals from CSC in BSTS for gate voltages corresponding to electron- and hole-doped graphene, respectively. The blue and pink arrows indicate the B_y sweep directions. The data has been shifted vertically for clarity. **(d)** Top panel: Dirac curve for the graphene channel across the vdW heterostructure. This is the same data as the blue curve in (b). Bottom three panels: Gate dependence of the zHanle signal amplitude from the CSC measurements, as well as of the spin lifetime and spin diffusion length in graphene. The measurements were performed in Device BSTS-2. Adapted from *Paper III*.

graphene as the resistivity of the spin transport channel rises.

Notably, the unchanged polarity of the spin signals in Figure 4.4c,d confirms that the CSC originates from the TI itself and not from proximity-induced SOC or stray magnetic fields in graphene. This is because both the proximity-induced SHE and the proximity-induced REE generate CSC with opposite spin polarisations for electron- and hole-dominated transport in graphene [172, 173, 513–515], and stray-field-induced artifacts exhibit a similar sign change between p- and n-doped graphene [516]. The used measurement geometry is furthermore not optimal for observing proximity-induced CSC effects in graphene, since the applied bias current flows mainly

through the TI flake and likely only through graphene in a part of the heterostructure area. In contrast, CSC in the TI through the SHE or the REE is only expected to show a similar sign change if the Fermi level is tuned across the bulk band gap, which is inaccessible through electrical gating in the present devices [173, 235]. CSC through the TSML in the TI is not expected to gain a sign change at any Fermi level because of the opposite spin texture chiralities of the upper and lower TI Dirac cones, respectively [169, 173]. It is, however, not possible to further discern which of these three microscopic mechanisms gives a dominant contribution to the CSC in the present devices, due to their similar dependencies on geometry, charge current and gate voltage.

4.1.4 Spin-to-charge conversion in $Bi_{1.5}Sb_{0.5}Te_{1.7}Se_{1.3}$

The inverse effect with SSC in BSTS was also measured, which demonstrates detection of spin polarisation in the graphene channel with the TI. As illustrated in Figure 4.5a, a spin current is injected from a FM electrode to the graphene channel, which propagates and can be absorbed by the TI to generate a nonlocal voltage with respect to a nonmagnetic reference contact. In accordance with the Onsager reciprocity [113], the SCC can arise through the ISHE, the IREE and the TSML. The latter two are visualised in the inset of Figure 4.5a, where a spin polarisation offsets the spin texture in a bulk band (for the IREE) or on the Dirac cone (for the TSML) to produce a net charge current. Spin-switch and zHanle spin precession signals from SCC in BSTS at room temperature are shown in Figure 4.5b,c.

The extracted spin lifetime and spin diffusion length in graphene from the SCC measurements are $\tau_s \approx 80\,\mathrm{ps}$ and $\lambda_s \approx 1.3\,\mu\mathrm{m}$, respectively, similar to the spin transport parameters of the CSC measurements. The spin polarisation was estimated using Equation (4.3), which yields 0.2 % for the SCC in Device BSTS-2 (slightly larger than for the CSC in the same device). It is also noted that the Hanle signal in Figure 4.5c is symmetric with respect to the magnetic field, whereas the corresponding CSC signal in Figure 4.2c has an asymmetric character. The electric field that is applied across the graphene/TI interface during the CSC may influence this by inducing a canted charge current in the xy plane, as discussed above, whereas such an electric field across the graphene/TI interface is absent in the SCC measurement geometry.

As can be seen in Figure 4.5d, the SCC is insensitive to the charge carrier type in graphene, and the spin-switch signals have the same sign and similar

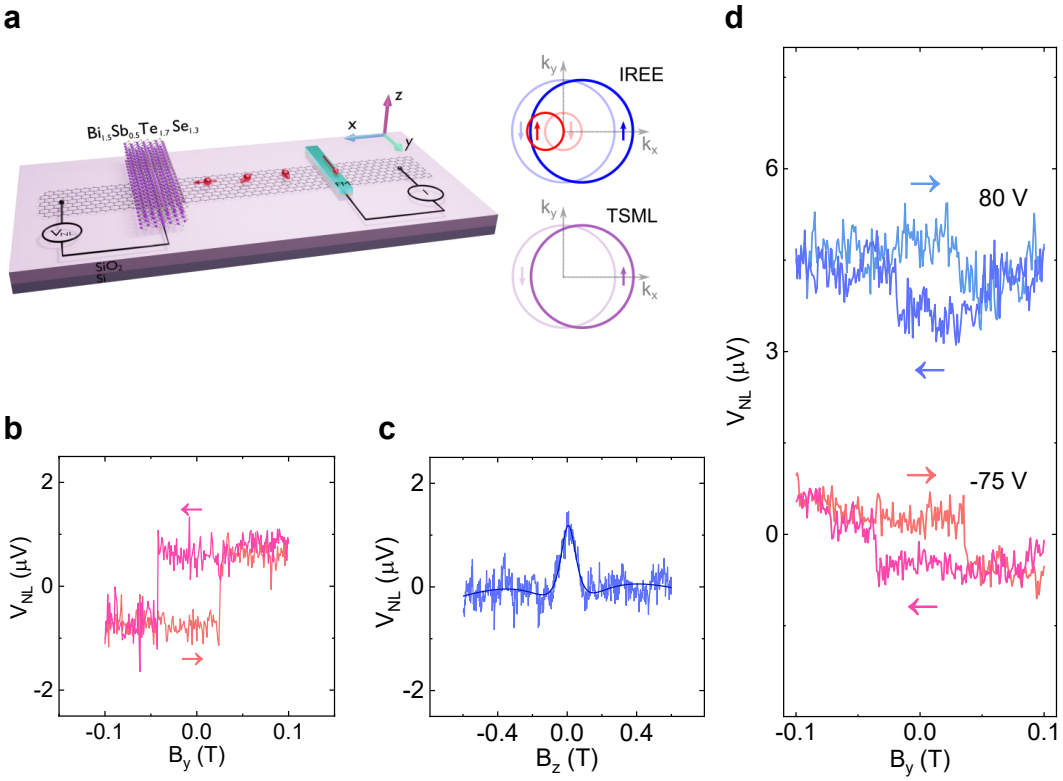


Figure 4.5: Spin-to-charge conversion in graphene/BSTS heterostructure. **(a)** Schematic of SCC measurements in a graphene/BSTS spin-valve device. Inset: Schematics of SCC through the IREE and the TSML, respectively. **(b,c)** Spin-switch (b) and zHanle spin precession (c) signals from SCC in BSTS. The Hanle signal was obtained by averaging the measured signals for $\pm y$ magnetisations of the injector contact using Equation (4.1). **(d)** Spin-switch signals from SCC in BSTS for gate voltages corresponding to electron- and hole-doped graphene. The data has been shifted vertically for clarity. The pink and blue arrows in (b,d) indicate the B_y sweep directions, and the solid line in (c) is a fit to the Hanle signal. The measurements were performed in Device BSTS-2. Adapted from *Paper III*.

magnitude for n- and p-doped graphene. Analogously to the discussion in Section 4.1.3, this excludes proximity-induced SOC and stray magnetic field effects in graphene as the microscopic origin of the SCC. The SCC effect is therefore concluded to originate from the ISHE, the IREE or the TSML in the TI.

4.2 Charge-spin interconversion in Weyl semimetal $TaIrTe_4$

The charge-spin interconversion in TIT was measured at room temperature using spin transport measurements in graphene/TIT vdW heterostructure spin-valve devices, as illustrated in the schematic in Figure 4.6a and with a microscopy image in Figure 4.6b. Similar to the BSTS devices in Section 4.1, the TIT spin-valve devices were fabricated from patterned CVD graphene and exfoliated TIT flakes with FM TiO_2/Co and nonmagnetic Ti/Au contacts. The crystal structure of TIT with broken inversion symmetry is shown in Figure 4.6c, and the tilted Weyl cones of the type-II WSM are visualised in Figure 4.6d with a Fermi arc drawn as a connection between the two Weyl nodes with opposite chirality.

Due to the strong SOC of the bulk bands and the SML of the surface Fermi arcs in TIT, CSC can originate in the WSM through the SHE, the REE and the Fermi-arc SML [122, 207, 506]. In analogue to Figure 4.1c, CSC through the REE and the SML is illustrated in Figure 4.6e with Fermi surfaces being shifted and gaining a spin accumulation under an applied electric field. In contrast to the TSS in a TI, however, the topologically protected surface states in a WSM form an open Fermi arc rather than a closed circle [184].

4.2.1 Spin transport in graphene

Before probing the charge-spin interconversion effects, the spin transport was studied in graphene channel areas without TIT, as illustrated in Figure 4.7a. As described in Section 3.1.1, polarised spin diffuses between the two FM electrodes and can be detected nonlocally outside of the charge-current loop. Figure 4.7b,c show the measured spin-valve and Hanle spin precession signals for magnetic fields along the y and z directions, respectively. The Hanle signal was fitted by Equation (3.1), which yields a spin lifetime $\tau_s \approx 120\,\mathrm{ps}$ and a spin diffusion length $\lambda_s \approx 2.3\,\mu\mathrm{m}$ in CVD graphene in Device Gr-1. Next, the spin transport measurements were repeated with an oblique magnetic field B_β oriented along different angles β in the yz plane. As is presented in Figure 4.7d, the spin signal evolves smoothly from a Hanle to a spin-valve shape as the orientation of the magnetic field is tuned from the OOP z ($\beta = 90\,^\circ$) to the IP y ($\beta = 0\,^\circ$) direction.

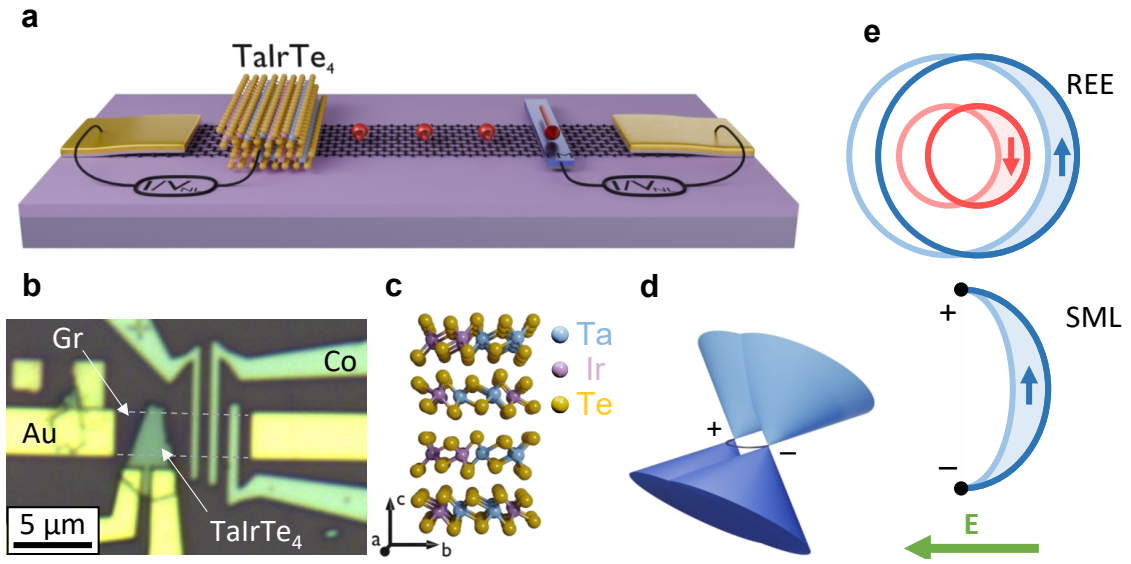


Figure 4.6: Charge-spin interconversion effects in $TaIrTe_4$. **(a,b)** Schematic (a) and microscopy image (b) of a representative graphene/TIT vdW heterostructure spin-valve device. **(c)** Schematic side view of the crystal structure of TIT. **(d)** Simplified band structure of TIT with two Weyl nodes connected by a Fermi arc. **(e)** Schematics of CSC through the REE and the SML of the Fermi arc states, respectively. Adapted from *Paper IV*.

4.2.2 Spin-to-charge conversion in $TaIrTe_4$

Charge-spin interconversion effects in TIT were first measured in terms of SCC using nonlocal electronic detection in Device TIT-1, as illustrated in Figure 4.8a. Polarised spin is here injected to the graphene channel from a FM contact and detected as a nonlocal voltage through the SCC effect in TIT, similar to the SCC measurements in BSTS as described in Section 4.1.4. First, spin-switch measurements were performed, with the spin signal in Figure 4.8b demonstrating SCC in TIT.

Next, Hanle spin precession measurements were performed, with Figure 4.8c clearly demonstrating the spin origin and IP precession character of the measured signals. Notably, the FM contact injects opposite spin polarisations to the graphene depending on its $\pm y$ magnetisation, and correspondingly yields spin signals with opposite polarity ($\uparrow$ and $\downarrow$ in Figure 4.8c). By fitting Equation (3.1), a spin lifetime $\tau_s \approx 80\,\text{ps}$ and a spin diffusion length $\lambda_s \approx 1.3\,\mu\text{m}$ could be extracted. Following the detection of SCC in spin-valve and Hanle measurements, spin signals due to the SCC were also detected using oblique magnetic fields. The systematic signals for varying field orientations in Figure 4.8d evolve continuously between spin-switch

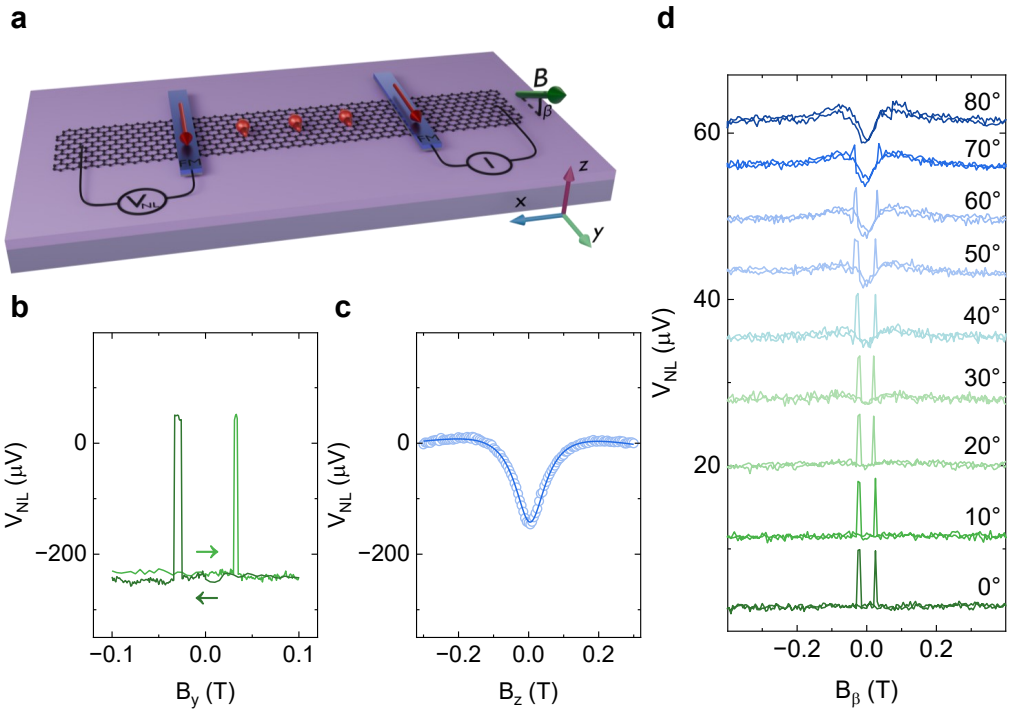


Figure 4.7: Spin transport in a graphene spin-valve device without TIT. (a) Schematic of spin transport measurements in a graphene spin-valve channel without TIT. A magnetic field in the yz plane is indicated by a green arrow. **(b,c)** Spin-valve (b) and Hanle spin precession (c) signals for spin transport in graphene. The green arrows in (b) indicate the B_y sweep directions, and the solid line in (c) is a fit to the Hanle signal. **(d)** Spin transport signals for oblique magnetic fields oriented along different angles β in the yz plane. Linear backgrounds were subtracted from the Hanle signals and the data in (d) has been shifted vertically for clarity. The measurements were performed in Device Gr-1 (b,c) and in Device Gr-2 (d), respectively. Adapted from *Paper IV*.

and Hanle characters, analogously to the spin transport signals in Figure 4.7d. This smooth transition between spin-switch and Hanle signals clearly demonstrates their common origin in the SCC in TIT.

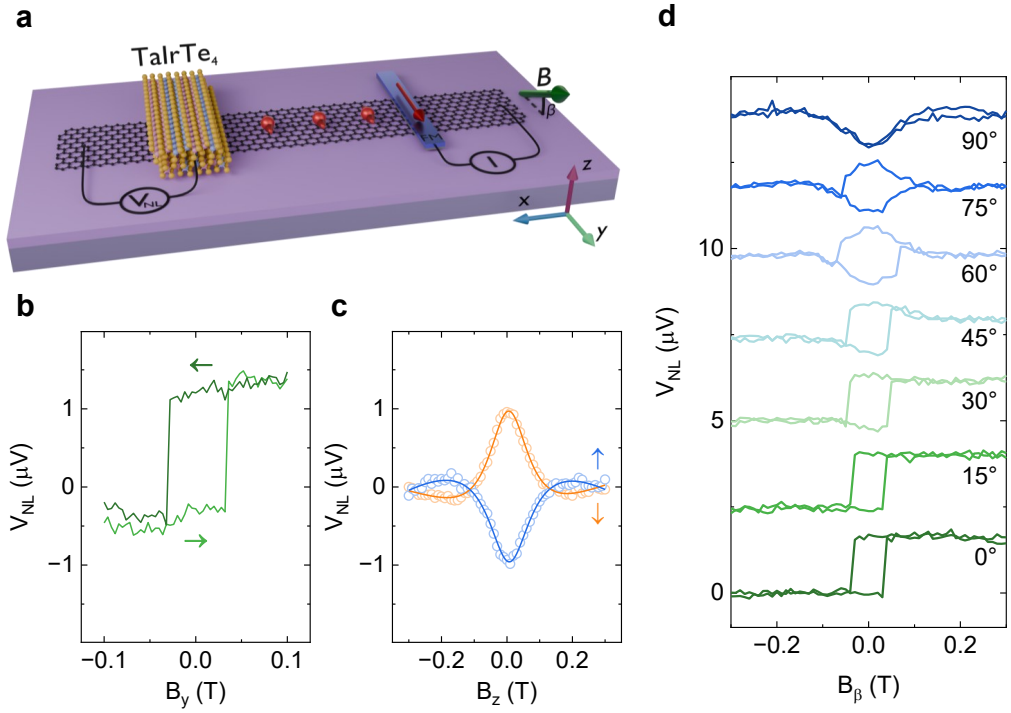


Figure 4.8: Spin-to-charge conversion in a graphene/TIT spin-valve device. **(a)** Schematic of SCC measurements in a graphene/TIT spin-valve device. A magnetic field in the yz plane is indicated by a green arrow. **(b,c)** Spin-switch (b) and Hanle spin precession (c) signals from SCC in TIT. The green arrows in (b) indicate the B_y sweep directions, and the solid lines in (c) are fits to the Hanle signals. The blue and orange Hanle signals in (c) were measured with opposite $\pm y$ magnetisations of the FM injector contact. **(d)** Spin signals from SCC in TIT for oblique magnetic fields oriented along different angles β in the yz plane. Linear backgrounds were subtracted from the Hanle signals and the data in (d) has been shifted vertically for clarity. The measurements were performed in Device TIT-1. Adapted from *Paper IV*.

4.2.3 Charge-to-spin conversion in $TaIrTe_4$

Generation of polarised spin through CSC in TIT and nonlocal detection with a FM electrode, as visualised in Figure 4.9a, was similarly achieved, which confirms Onsager reciprocity of the charge-spin conversion effects in TIT [113]. Figure 4.9b,c shows spin-switch as well as Hanle spin precession signals from polarised spin that is generated by CSC in TIT and injected to the graphene channel.

The charge current dependence of the CSC effect in TIT was studied by passing positive and negative bias charge currents through TIT in the heterostructure device, with opposite current polarities illustrated by green and

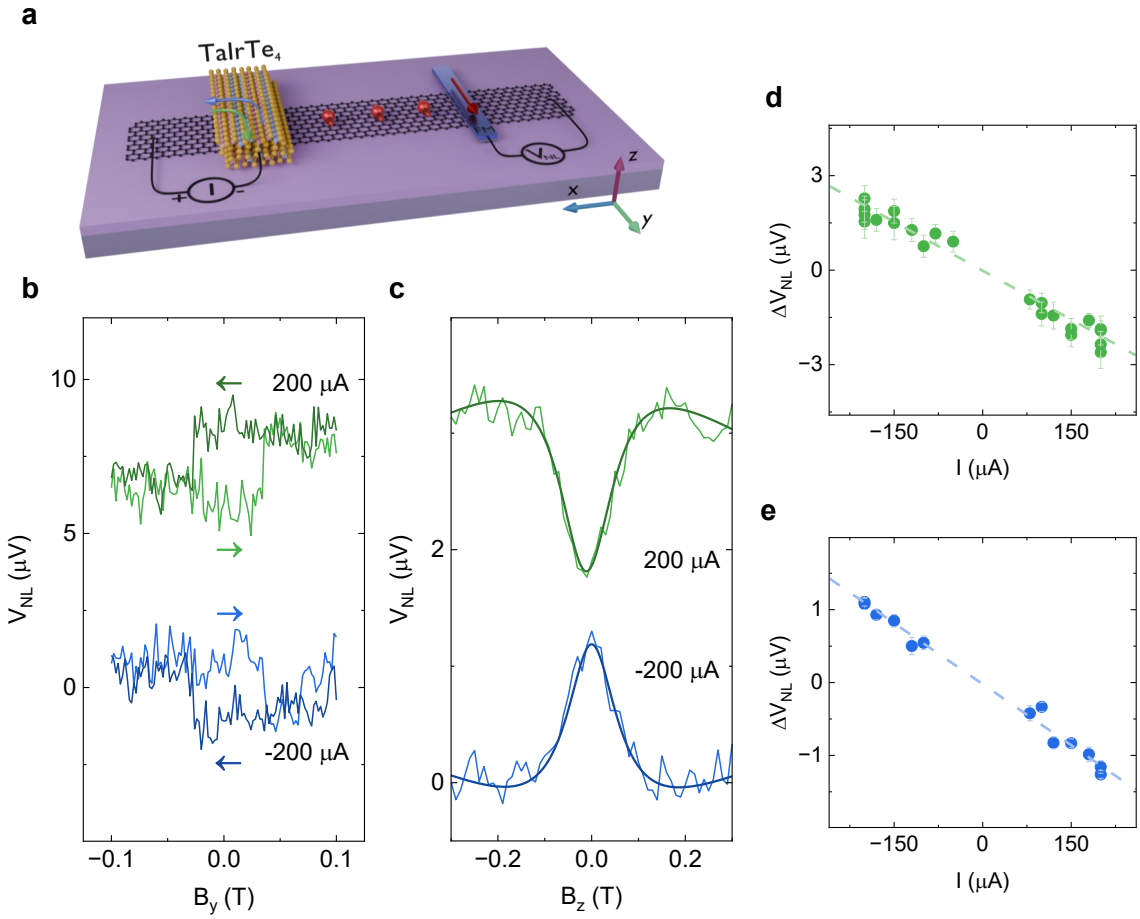


Figure 4.9: Charge-to-spin conversion in a graphene/TIT spin-valve device. **(a)** Schematic of CSC measurements in a graphene/TIT spin-valve device with positive (green) and negative (blue) bias charge currents. **(b,c)** Spin-switch (b) and Hanle spin precession (c) signals from CSC in TIT for positive and negative bias currents. The arrows in (b) indicate the B_y sweep directions. Linear backgrounds were subtracted from the Hanle signals in (c) and the solid lines are fits to the signals. The data has been shifted vertically for clarity. **(d,e)** Full bias dependencies of the spin-switch and Hanle signals from CSC in TIT, with linear fits to the data as guides to the eye. The measurements were performed in Device TIT-1. Adapted from *Paper IV*.

blue arrows in Figure 4.9a. As can be seen in Figure 4.9b,c, both spin-switch and Hanle CSC signals are measured with opposite sign when the charge current is reversed, signifying a sensitivity of the CSC effect on the direction of the charge current in TIT. Further, the full bias dependencies of the CSC signals are summarised in Figure 4.9d,e. As indicated by the observed linear bias dependence, increasing charge currents are reproducibly converted to proportionally larger spin polarisations within the probed current range.

In order to get a quantitative measure of the CSC in TIT, the generated spin polarisation was estimated. Using the same methodology as in Section 4.1.1, the polarisation of the FM contact in Device TIT-1 was estimated as $P_{FM} = 1.8\,\%$ from Equation (4.2). The spin polarisation from TIT through the CSC could subsequently be estimated from Equation (4.3) to $P_{CSC} = 0.07\,\%$. Analogously, the spin polarisation of the SCC yielded a nearly identical $P_{SCC} = 0.06\,\%$ in the same device, in accordance with Onsager reciprocity. Similar spin polarisations of the FM contact and the CSC ($P_{FM} = 8.1\,\%$ and $P_{CSC} = 0.13\,\%$, respectively) were estimated for Device TIT-2, which is also comparable to the estimated values for BSTS in Section 4.1.1. Notably, these estimated spin polarisations are relatively low despite the clear CSC signals in Figure 4.1, Figure 4.8, Figure 4.9 *etc.* Importantly, however, this should not be interpreted as inefficient charge-spin interconversion in TIT (and BSTS). Multiple parameters have an influence on the injection and detection of polarised spin in the graphene channel and the estimated spin polarisation values. It is especially probable that the spin injection efficiency across the vdW gap between the TIT flake and the graphene channel is lowered due to a conductivity mismatch between the two materials, which is discussed in Section 4.2.4 below. Meanwhile, the observation of clear spin signals despite the low spin polarisation in graphene demonstrates the sensitivity of the nonlocal electrical detection method in the graphene spin-valve devices.

4.2.4 Impact from the graphene/$TaIrTe_4$ interface on the spin signals

The graphene/TIT interface has an important impact on the spin injection and detection efficiency. The mismatch of the relatively low conductivity of graphene, compared to the semimetallic TIT, can give rise to a low spin injection efficiency due to spin back-scattering and reabsorption at the TIT/graphene interface [464, 465]. Here, the naturally occurring vdW gap between graphene and TIT acts as an analogue to the TiO_2 tunnel barriers of the FM contacts (mentioned in Section 3.1.2). The vdW gap in the graphene/TIT interface was characterised with IV characteristics in a three-terminal measurement geometry, which is illustrated in the inset of Figure 4.10a. By using the three-terminal geometry, the measured resistance is dominated by the graphene/TIT interface resistance, while the resistance of the graphene channel is avoided. The resulting IV characteristics in the low-bias range in Figure 4.10a indicate relatively transparent

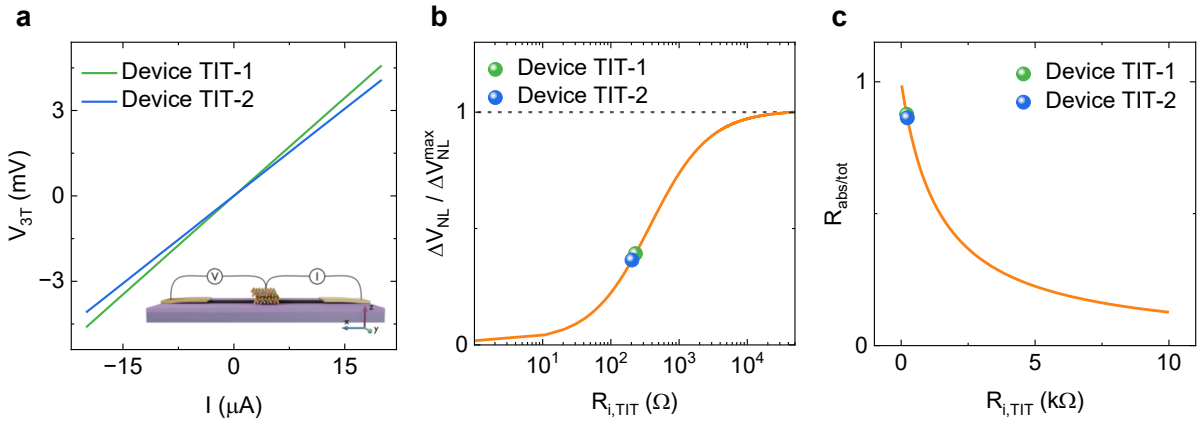


Figure 4.10: Characterisation of the graphene/TIT interface and its impact on the spin signals. **(a)** *IV* characteristics from three-terminal measurements of graphene/TIT interfaces. The measurements were performed in Device TIT-1 and in Device TIT-2. Inset: Schematic of a three-terminal measurement of a graphene/TIT interface in a spin-valve device. **(b)** Normalised spin signal amplitude from charge-spin interconversion in TIT as calculated from Equation (4.5), as a function of the graphene/TIT interface resistance $R_{i,TIT}$. **(c)** Relative contribution to the spin relaxation in the graphene/TIT heterostructure from spin absorption as calculated from Equation (4.7) and Equation (4.8), as a function of the graphene/TIT interface resistance. The green and blue dots in (b,c) indicate where the measured devices fall on the respective lines, based on their interface resistances. Adapted from *Paper IV*.

vdW gaps with interface resistances $R_{i,TIT} \approx 200\,\Omega$ both in Device TIT-1 and in Device TIT-2.

The spin resistances of TIT and graphene ($R_{s,TIT}$ and $R_{s,Gr}$, respectively) can be calculated as important material parameters for estimating the conductivity mismatch, according to

$$\begin{cases} R_{s,TIT} = \frac{\rho_{TIT}\lambda_{s,TIT}}{t_{TIT}w_{TIT}} \\ R_{s,Gr} = \frac{R_{\square}\lambda_{s,Gr}}{w_{Gr}}, \end{cases} \tag{4.4}$$

where ρ_{TIT} is the resistivity of TIT, $R_{\square}$ is the sheet resistance of graphene, $\lambda_{s,TIT}$ ($\lambda_{s,Gr}$) is the spin diffusion length in TIT (graphene), t_{TIT} is the thickness of the TIT flake and w_{TIT} (w_{Gr}) is the width of the TIT flake (graphene channel) [391, 517]. The resistivity of TIT $\rho_{TIT} \approx 8\,\mathrm{m\Omega cm}$ and the sheet resistance of the graphene $R_{\square} \approx 1 - 4\,\mathrm{k\Omega/\square}$ were calculated from two-terminal *IV* measurements of the TIT flake and local four-terminal *IV* measurements of the graphene channels, respectively, whereas the TIT flake size was determined using AFM. Since the spin diffusion length in TIT

cannot be measured in the spin-valve devices, it was estimated as $\lambda_{s,TIT} \approx 10\,\mathrm{nm}$, which is similar to reported values for WTe_2 [233, 518]. The spin resistances could then be calculated from Equation (4.4) as $R_{s,TIT} \approx 6\,\Omega$ and $R_{s,Gr} \approx 800\,\Omega$, respectively, which highlights the conductivity mismatch between TIT and graphene.

In order to further estimate the influence of the graphene/TIT interface on the charge-spin interconversion measurements, the spin signal was calculated using a drift-diffusion model with the equation

$$V_{NL} \propto 2R_{s,Gr}\mathrm{e}^{-L/\lambda_{s,Gr}} \prod_{n=TIT,FM} \left(\frac{P_{J,n}R_{i,n}}{R_{s,Gr}(1-{P_{J,n}}^2)} + \frac{p_{F,n}R_{s,n}}{R_{s,Gr}(1-{p_{F,n}}^2)} \right) \cdot \left[\prod_{n=TIT,FM} \left(1 + \frac{2R_{i,n}}{R_{s,Gr}(1-{P_{J,n}}^2)} + \frac{2R_{s,n}}{R_{s,Gr}(1-{p_{F,n}}^2)} \right) - \mathrm{e}^{-2L/\lambda_{s,Gr}} \right]^{-1}, \tag{4.5}$$

where L is the length of the graphene channel between the TIT flake and the FM contact, $R_{i,FM}$ is the interface resistance of the graphene/FM contact interface, $R_{s,FM}$ is the spin resistance of the FM contact, p_F is the current polarisation and P_J is the interfacial current polarisation, and where the indices Gr, TIT and FM correspond to graphene, TIT and the FM contact, respectively [517]. The spin resistance of Co $R_{s,FM} \approx 70\,\mathrm{m\Omega}$ was calculated analogously to Equation (4.4), with the resistivity and spin diffusion length as $\rho_{FM} = 25\,\mu\Omega\mathrm{cm}$ and $\lambda_{s,FM} = 8\,\mathrm{nm}$ [519], and the graphene/TiO_2/Co interface resistance $R_{i,FM} \approx 2-4\,\mathrm{k\Omega}$ was determined *via* three-terminal IV measurements.

Figure 4.10b shows the normalised spin signal amplitude from Equation (4.5) as a function of the interface resistance of the graphene/TIT vdW gap $R_{i,TIT}$. The spin signal is significantly enhanced by more resistive interfaces where the vdW gap acts as a tunnel barrier between graphene and TIT, whereas the spin signal amplitude is suppressed by transparent interfaces due to the conductivity mismatch problem. The two dots on the line in Figure 4.10b correspond to the $R_{i,TIT}$ values of Device TIT-1 and Device TIT-2. Although the exact quantitative values of the normalised spin signal amplitudes can vary depending on the chosen material parameters, this is nevertheless a clear indication that the relatively low graphene/TIT interface resistance in the present spin-valve devices suppresses the magnitude of the measured charge-spin interconversion signals, and that the estimated CSC polarisation in Section 4.2.3 may be significantly underestimated compared to the real spin polarisation in TIT.

Finally, the impact of the graphene/TIT interface resistance on the spin absorption from the graphene channel to the TIT flake is considered. The spin absorption rate can be calculated as

$$\Gamma = \frac{R_{\square} D_s}{\frac{\rho_{TIT}\lambda_{s,TIT}}{\tanh\left(t_{TIT}/\lambda_{s,TIT}\right)} + \frac{R_{i,TIT}A}{\tanh\left(t_{TIT}/t_{TIT,ML}\right)}}, \tag{4.6}$$

where D_s is the spin diffusion coefficient in graphene in the heterostructure, A is the area of the interface and $t_{TIT,ML}$ is the thickness of monolayer TIT [520]. Since the thickness of the TIT flakes in Device TIT-1 and Device TIT-2 is multiple tens of nanometres, Equation (4.6) can be simplified as

$$\Gamma = \frac{R_{\square} D_s}{\rho_{TIT}\lambda_{s,TIT} + R_{i,TIT}A}. \tag{4.7}$$

From this, the influence of the spin absorption on the spin lifetime in graphene in the heterostructure area can be estimated from

$$\frac{1}{\tau_s} = \frac{1}{\tau_{s,SOC}} + \frac{1}{\tau_{s,abs}}, \tag{4.8}$$

where τ_s is the total spin lifetime, $\tau_{s,SOC}$ is the contribution from SOC-induced (D'yakonov-Perel' [521] and Elliott-Yafet [522, 523]) relaxation mechanisms and $\tau_{s,abs} = \Gamma^{-1}$ is the contribution from spin absorption by the TIT [172, 391]. The relative spin absorption contribution

$$R_{abs/tot} = \tau_s/\tau_{s,abs} \tag{4.9}$$

is shown as a function of the interface resistance in Figure 4.10c, where the two coloured dots on the line correspond to the measured interface resistances of Device TIT-1 and Device TIT-2. Due to the relatively transparent graphene/TIT interfaces, both devices are expected to experience significant spin absorption by the TIT flakes. Notably, this can enhance the efficiency in the SCC measurements since spins can more easily enter TIT from graphene, but is detrimental to the spin injection efficiency in the CSC measurements due to the increased risk of spin reabsorption.

5 Magnetic phases and nonlinear transport in a magnetic topological insulator

Magnetic TIs combine the concepts of topological quantum effects and magnetism in a single material, both of which are paramount for novel condensed matter physics. Together, this combination of topology and magnetism enables a plethora of unique phenomena, including the quantum anomalous Hall effect [268, 277, 281, 283, 298, 314, 524], chiral edge states [301, 525, 526], topological magnetoelectric effects [282, 525, 527, 528] and Majorana physics [529]. The magnetic TI $MnBi_2Te_4$ (MBT) is especially interesting in this context due to its rich topology and its intrinsic and layer-dependent magnetism [275, 328, 329, 385]. Indeed, a range of exotic topological and magnetic effects are present in MBT, such as the quantum anomalous Hall effect [**Deng2021High-temperatureSuperlattice**, 317, 330], the axion insulator state [331, 332], the layer Hall effect [373] and nonlinear electronic transport [70–72].

MBT has an A-type AFM ground state at low temperatures, where its constituent vdW layers have alternating OOP magnetisations [273, 275]. However, canted AFM, FM and paramagnetic states can be induced in MBT by applied magnetic fields with different magnitudes and orientations, as well as by elevated temperatures [321, 330, 530–533]. These magnetic phases in MBT modulate its electronic and topological responses, and accurate mapping of the magnetic phases therefore provides important information about the topological quantum material. However, linear transport measurements often exhibit only weak or ambiguous signatures at the phase transitions on the boundaries between different magnetic phases in MBT, and may fail to capture some transitions entirely. This lack of sensitivity severely limits the usefulness of linear electronic transport for magnetic phase characterisation and leaves gaps in the present knowledge about the magnetic landscape of MBT.

Nonlinear electronic transport considers power-law current-voltage rela-

tionships beyond the normal constraints of Ohm's law, and can arise in topological materials with broken symmetries [248, 345, 351, 534]. It has emerged as a powerful probe of the quantum geometry in topological quantum materials, as well as of scattering mechanisms such as skew scattering and side jump [66, 73, 248, 338, 339, 345–347, 534]. Recently, nonlinear transport due to features in the quantum metric has been demonstrated in MBT, which has gathered significant attention. Second-order nonlinear electronic transport due to quantum metric dipoles was observed in thin even-layer MBT with a broken inversion symmetry [70, 71], whereas third-order nonlinear transport was found to arise due to quantum metric quadrupoles in bulk MBT with maintained inversion symmetry [72]. However, although exotic higher-order multipoles in the Berry curvature component of the quantum geometry have been theoretically predicted to give rise to higher-order nonlinear transport [342], experimental nonlinear electronic transport studies have so far been almost exclusively limited to the second and third orders in all studied materials [216, 251–254, 256–258, 260, 341].

Here, third-order nonlinear electronic transport is utilised to map out the magnetic phases in multilayer MBT under OOP, IP and oblique magnetic fields and different temperatures (*Paper V*). The third-order nonlinear transport signals consistently show a higher sensitivity and more clearly resolved signatures at the magnetic phase transitions compared to the linear transport, and enables the construction of complete magnetic phase diagrams for MBT across all magnetic field orientations. Then, higher-order nonlinear transport up to the seventh order is demonstrated in multilayer MBT (*Paper VI*). An even-odd behaviour is observed, where the odd-order components of the nonlinear transport persist whereas the even-order ones are suppressed. The microscopic origin of the nonlinear transport is identified as a combination of quantum metric multipoles and Drude-like nonlinear conductivities. These findings provide so-far missing characterisation and contribute towards a deeper understanding of the magnetic landscape and quantum geometry in MBT, utilising nonlinear transport as a powerful and versatile probe of both magnetism and topology in the magnetic TI.

5.1 Magnetic phase characterisation in magnetic topological insulator $MnBi_2Te_4$

The characteristic band structure, crystal structure and magnetic ordering of MBT are visualised in Figure 5.1a,b. The magnetic TI has gapped Dirac cones with SML and topologically protected edge states, as well as a crystal structure consisting of SLs with alternating OOP magnetisations between adjacent layers in the ground state [273, 275]. Figure 5.1c outlines the magnetic phase landscape of how the magnetisation in MBT evolves with OOP and IP magnetic fields, whereas the corresponding field-driven spin reorientation is illustrated in Figure 5.1d,e. When MBT is exposed to a moderate OOP magnetic field B_z along its easy axis, it undergoes a spin-flop transition from the AFM ground state to a canted AFM (cAFM) magnetic phase, which has a net OOP magnetisation and where the canted magnetisation of adjacent SLs have alternating IP components [330, 530]. The OOP magnetisation of MBT grows continuously for increasing B_z as the canted magnetisation of the SLs gradually align towards the magnetic field orientation, until they become fully aligned in the FM phase [330, 530]. In contrast, application of an IP magnetic field B_{xy} results in a softer magnetic behaviour where the magnetisation is pulled gradually from the OOP AFM ordering towards a fully IP polarisation [321, 533]. This smooth reorientation passes through a canted AFM phase where adjacent SLs have opposite OOP magnetisations but a continuously increasing IP polarisation, which is distinctly different from the cAFM above with a net OOP magnetisation [321, 533]. In the following, the canted AFM phase with a net IP magnetisation is referred to as the cAFM' phase for clarity.

5.1.1 Spectroscopic characterisation of $MnBi_2Te_4$

First, the bulk MBT material was characterised using ARPES. The measured spectrum in Figure 5.2a shows a well-resolved band structure with a 132 meV bulk band gap. Notably, surface-state Dirac cones can be seen in a slightly faded red colour in the bulk band gap. The clearly resolved bulk and surface states indicate a good single-crystalline quality of the MBT sample. The second derivative of the ARPES spectrum around the bulk band gap is shown in Figure 5.2b, which offers an enhanced visual contrast. This allows a small exchange gap in the surface states of about $10 - 15$ meV (indicated with dashed lines) to be observed, which confirms the ferromagnetic character of the surface of the MBT crystal. To be noted, although the size and

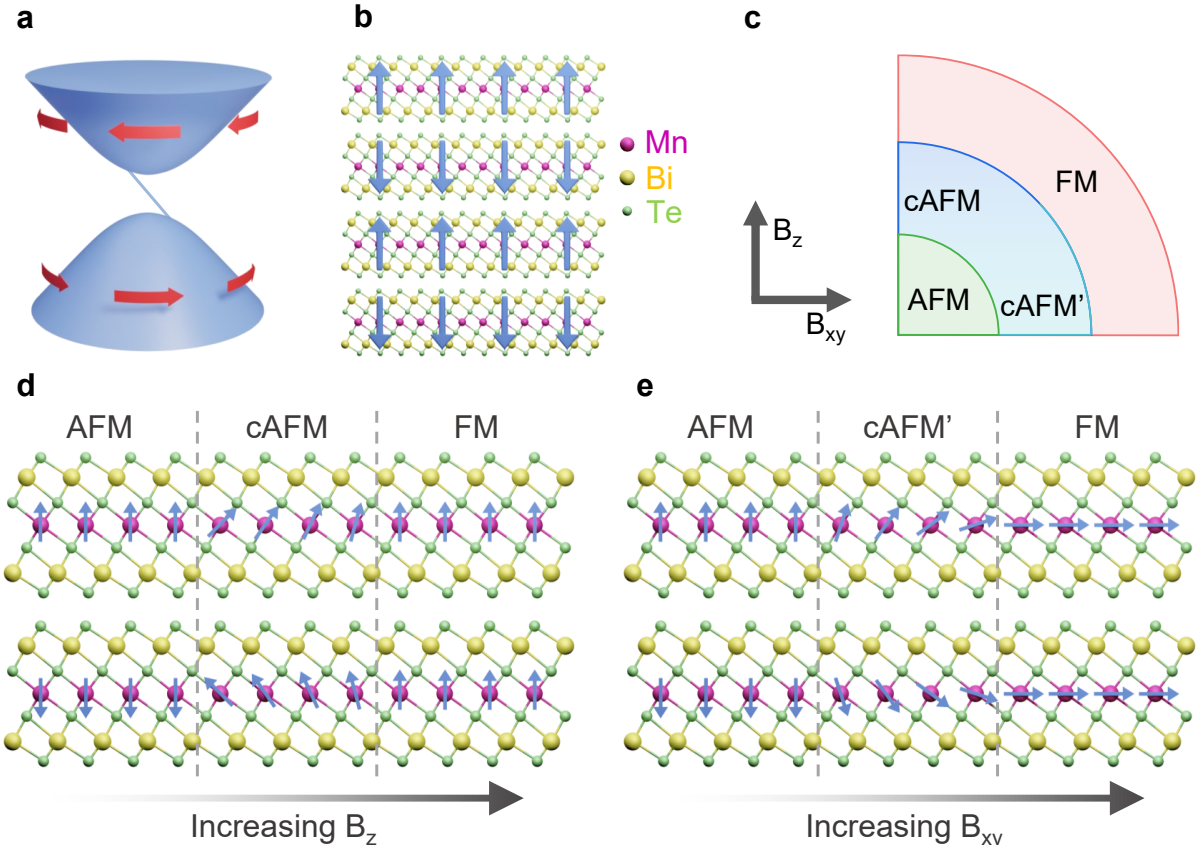


Figure 5.1: The magnetic landscape of $MnBi_2Te_4$. (a,b) Schematic band structure (a) and side-view of the crystal structure (b) of $MnBi_2Te_4$. The red arrows in (a) indicate the SML of the Dirac cones, and the blue arrows in (b) indicate the magnetisation of the SLs. **(c)** Outlined magnetic phase diagram of MBT for OOP (B_z) and IP (B_{xy}) magnetic fields. Adapted from *Paper V*. **(d,e)** Illustrations of the field-induced spin reorientation in MBT under OOP (d) and IP (e) magnetic fields, showcasing the evolution of AFM, cAFM/cAFM' and FM spin orientations under increasing magnetic field strengths. The blue arrows in (d,e) indicate the spin direction of the respective Mn atoms.

even the presence of surface state gaps in MBT are known to differ between samples depending on their defect concentration [323, 324], the results in Figure 5.2a,b nevertheless agree well with previous reports [273, 275, 320, 323, 324].

Next, x-ray magnetic circular dichroism (XMCD) spectroscopy was used to study the magnetisation of MBT under OOP magnetic fields. X-ray absorption spectroscopy (XAS) signals were measured using both the bulk-sensitive total fluorescence yield mode and the surface-sensitive total electron yield mode [535]. The top panel of Figure 5.2c,d show representative

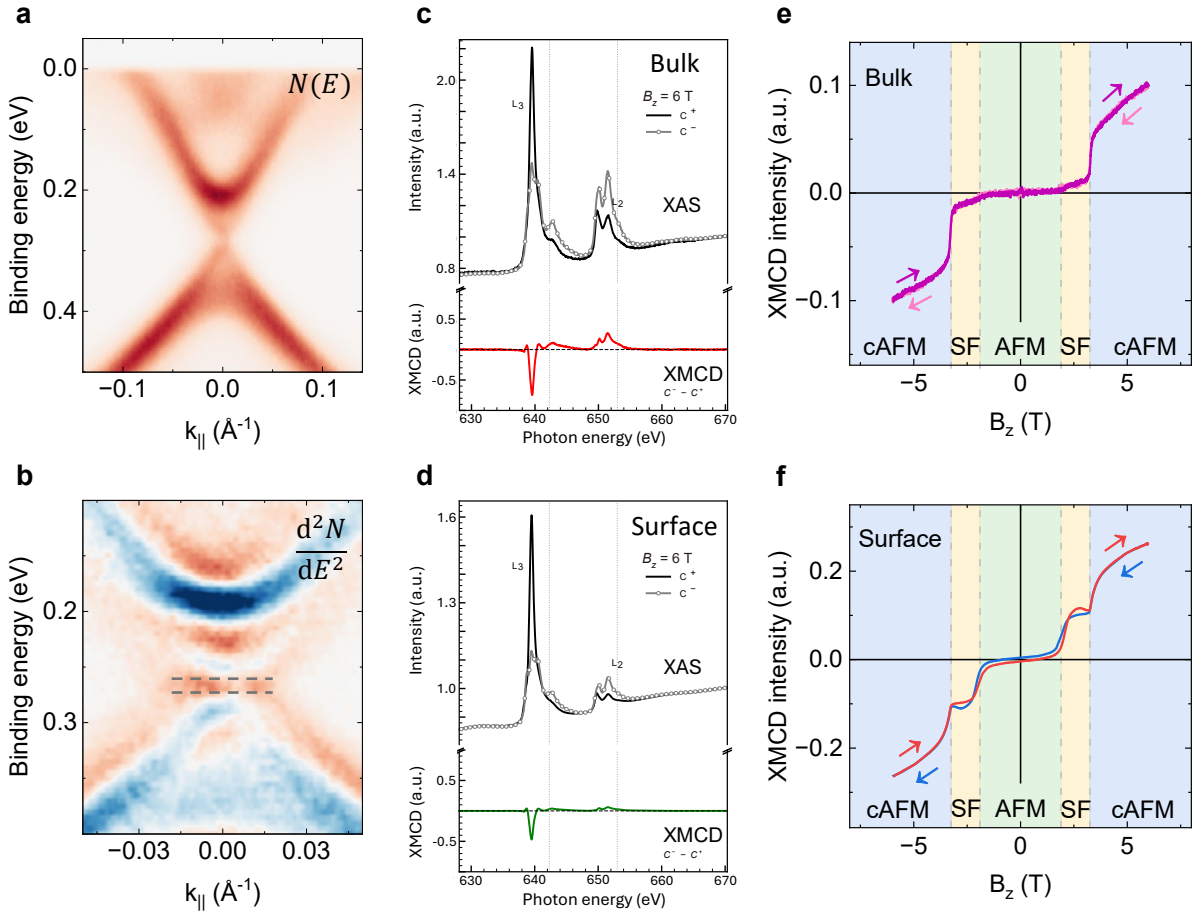


Figure 5.2: Spectroscopic characterisation of MBT. (a) ARPES spectrum measured along the $\overline{M}-\overline{\Gamma}-\overline{M}$ direction in MBT. The measurement was performed at $T = 20\,\mathrm{K}$ with a photon energy of 14 eV. **(b)** Second derivative $\mathrm{d}^2N(E)/\mathrm{d}E^2$ of the ARPES spectrum in (a), for a zoomed-in area around the bulk band gap. An exchange gap in the surface states is indicated with dashed lines. **(c,d)** Bulk- (c) and surface-sensitive (d) XAS spectra for circularly polarised light with opposite chiralities (C^+ and C^-, respectively) under a magnetic field $B_z = 6\,\mathrm{T}$ (top), and corresponding bulk- (c) and surface-sensitive (d) XMCD spectra ($C^- - C^+$) (bottom). **(e,f)** Bulk- (e) and surface-sensitive (f) XMCD intensities as a function of OOP magnetic fields. The coloured arrows indicate the magnetic field sweep directions, and magnetic phase transitions are indicated with dashed lines. The measurements were performed at $T = 4\,\mathrm{K}$ using a total fluorescence yield mode (c,e) and a total electron yield mode (d,f), respectively. Adapted from *Paper V*.

bulk- and surface-sensitive XAS spectra, respectively, under the application of an OOP magnetic field $B_z = 6\,\mathrm{T}$ and with opposite chiralities of the circularly polarised light (C^+ and C^-, respectively). XMCD spectra were

subsequently obtained as the difference in XAS intensity between the opposite light polarisations ($C^- - C^+$), and is shown in the bottom panel of Figure 5.2c,d. Importantly, the XAS spectra in Figure 5.2c,d have a strong dependence on the light polarisation, resulting in clear dips in the XMCD intensities. This translates to a notable net magnetisation both in the bulk and at the surface of MBT under large magnetic fields ($B_z = 6\,\mathrm{T}$). Interestingly, similar measurements in the absence of external magnetic fields yield no XMCD signal from the bulk but a noticeable dip in the surface-sensitive signal, which indicates that MBT is fully AFM in the bulk but has a remanent surface magnetisation.

In order to investigate the magnetic behaviour of MBT in more detail, XMCD measurements were repeated for different magnetic fields within $\pm 6\,\mathrm{T}$. By extracting the amplitude of each measured XMCD spectrum, the bulk- and surface-sensitive XMCD intensities could be obtained as a function of magnetic field, which is presented in Figure 5.2e,f. Here, the XMCD intensities are proportional to the bulk and surface magnetisation of MBT, respectively [535–537]. Three distinct magnetic phases can be identified. Under small magnetic fields, the zero-intensity bulk signal in Figure 5.2e indicates a fully AFM phase with no net bulk magnetisation. The slowly increasing XMCD signal from $B_z \approx \pm 1.9\,\mathrm{T}$ can be understood as a spin-flop transition with a small OOP net magnetisation, before the onset of a cAFM phase with a sharp increase in XMCD intensity at $B_z = \pm 3.3\,\mathrm{T}$. The continuously increasing XMCD intensity with magnetic fields beyond this point signifies a gradual realignment of the canted magnetic moments in MBT towards the z axis. Notably, no fully FM phase was observed in the XMCD measurements, since this requires the application of even stronger magnetic fields.

Whereas the bulk-sensitive XMCD signal in Figure 5.2e is non-hysteretic, the surface-sensitive signal in Figure 5.2f contains a hysteresis loop as well as a nonzero XMCD intensity in the AFM phase. This behaviour originates from a magnetic remanence due to the FM character of the individual SLs, which do not cancel perfectly at the MBT surface. Furthermore, the strong response of the surface-sensitive XMCD signal in the spin-flop transition region, compared to that of the bulk-sensitive signal, indicates that the gradual spin reorientation of the spin-flop transition predominately takes place at the surface of MBT. Conversely, the spin reorientation in the bulk happens more suddenly at the onset of the cAFM phase [530]. Interestingly and somewhat unexpectedly, a switchover point in the surface-sensitive XMCD signal is observed during the spin-flop transition, where the signals for the

forward and backward sweeps of the magnetic field cross. This may appear due to a weakened magnetic exchange coupling of the SLs at the surface, compared to the exchange coupling between those in the bulk [538].

5.1.2 Electronic transport and magnetic phase transitions in $MnBi_2Te_4$

The magnetic phase transitions in MBT were probed using linear and nonlinear transport measurements under the application of OOP, IP and oblique magnetic fields as well as different temperatures in a multilayer MBT Hall bar device, which is illustrated in the inset of Figure 5.3a. The multilayer MBT was exfoliated mechanically from a bulk MBT crystal in a glovebox with inert N_2 atmosphere, and was then shaped into a Hall bar through EBL and Ar milling. The whole Hall bar device was then covered by Al_2O_3 to prevent oxidation of MBT, and Ti/Au electrodes were deposited through electron-beam evaporation after opening the capping layer through brief *in situ* Ar milling. The linear and nonlinear electronic transport was measured with a lock-in technique. While applying an AC current I^ω with a frequency ω across the device, lock-in amplifiers were used to measure the linear first-harmonic signal (with the same frequency ω as the applied AC current) and the nonlinear third-harmonic signal (with three times the frequency 3ω) [248]. The third-harmonic component of the nonlinear transport signal was measured since the second-harmonic component is suppressed by the $\mathcal{P}$ symmetry in multilayer MBT, which leaves the third harmonic as the leading order of the nonlinear transport signal [72].

Figure 5.3a,b shows the temperature and OOP magnetic field dependence of the linear longitudinal resistance R_{xx}^ω in MBT. It has a metallic behaviour with temperature (Figure 5.3a), containing an evenly decreasing resistance from room temperature down to the Néel temperature $T_N = 23.8\,\mathrm{K}$, where MBT transitions from the paramagnetic (PM) to the AFM phase. This phase transition is seen as a kink in the linear resistance. Similarly, kinks are also observed in the linear resistance signal at the AFM-cAFM phase transition under the application of a magnetic field in Figure 5.3b. However, these features in the linear resistance are relatively small, and the cAFM-FM transition in Figure 5.3b is not resolved at all. In contrast, the nonlinear transport is closely connected to the magnetisation of MBT and responds strongly with magnetic phase transitions. This sensitivity of the nonlinear transport is showcased in Figure 5.3c,d, where the first- (V_x^ω) and third-harmonic ($V_x^{3\omega}$) longitudinal voltages are presented side-by-side as functions

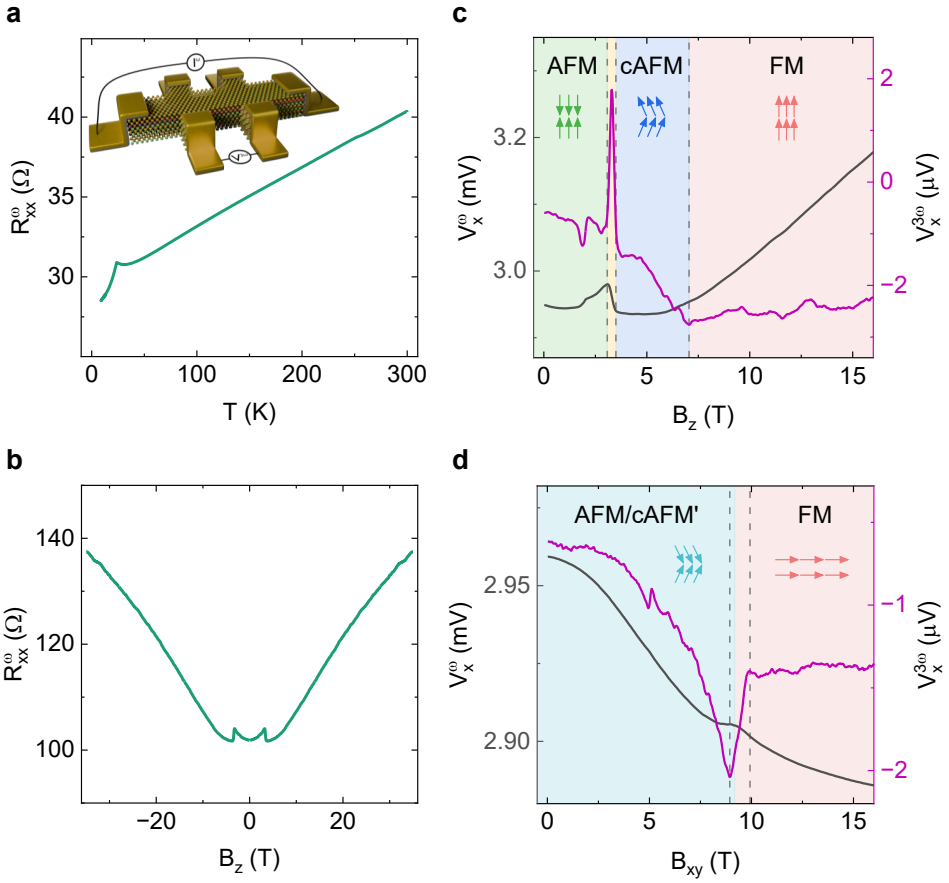


Figure 5.3: Electronic transport and magnetic phase transitions in MBT. (a,b) Temperature (a) and OOP magnetic field (b) dependencies, respectively, of the first-harmonic longitudinal resistance R^{ω}_{xx}. Inset of (a): Schematic of a representative MBT Hall bar device. **(c,d)** First- (V^{ω}_{x}) and third-harmonic ($V^{3\omega}_{x}$) longitudinal voltages as functions of OOP (c) and IP (d) magnetic fields, respectively, with magnetic phase transitions indicated with dashed lines. The coloured arrows indicate the magnetic ordering of MBT in each phase. The measurements were performed with $B_z = 0\,\mathrm{T}$ in Device MBT-3 (a) and at $T = 0.5\,\mathrm{K}$ (b) and $T \approx 4\,\mathrm{K}$ (c,d) in Device MBT-1, respectively. Adapted from *Paper V*.

of OOP and IP magnetic fields, and where magnetic phase transitions are indicated with dashed lines.

5.1.3 Out-of-plane magnetic phase diagram of $MnBi_2Te_4$

The OOP magnetic field dependence of the first-harmonic signal at different temperatures is shown in Figure 5.4a. The kinks in the signals near $B_z = \pm 3\,\mathrm{T}$ can be identified as the spin-flop phase transition between the

AFM and the cAFM phases of MBT [330, 530], as mentioned above for the case of Figure 5.3b. However, no indication of the cAFM-FM phase transition could be resolved in the linear transport signal. Meanwhile, the third-harmonic voltage signal in Figure 5.4b responds strongly to changes in the magnetisation in MBT and contains clear signatures for both phase transitions. By correlating the first- and third-harmonic signals at the same temperature in the same device, the sharp peak near $B_z = \pm 3\,\mathrm{T}$ in $V_x^{3\omega}$ was identified to appear in the middle of the spin-flop transition region. Similarly, by comparing Figure 5.4b to Figure 5.11c in Section 5.2, it was concluded that the following slope in the third-harmonic voltage corresponds to the evolution of the cAFM phase, and that the cAFM-FM phase transition is seen as a shoulder point near $B_z = \pm 6.5\,\mathrm{T}$ in the $T = 4.2\,\mathrm{K}$ signal (which takes the shape of a kink for higher temperatures before becoming completely smooth above the Néel temperature).

Temperature-dependent measurements of the first- and third-harmonic transport signals at zero magnetic field are shown in Figure 5.4c. The linear transport signal shows a relatively small kink with a local maximum at the Néel temperature $T_N = 24.2\,\mathrm{K}$, whereas the third-harmonic signal contains a more well-resolved kink at the same temperature. The small difference in T_N between Figure 5.3a (Device MBT-3) and Figure 5.4c (Device MBT-1) most likely appears due to a difference in thickness between the two multilayer MBT devices [328].

The magnetic phase transitions in Figure 5.4a-c (outlined by dashed lines) were used to construct the phase diagram in Figure 5.4d. Here, the magnetic phase of MBT is shown as a function of the temperature and the OOP magnetic field. The AFM, cAFM, FM and PM phases and the spin-flop transition region are all well-resolved thanks to the sensitivity and clear signatures of the third-harmonic nonlinear transport signals.

5.1.4 In-plane magnetic phase diagram of $MnBi_2Te_4$

Next, the IP magnetic field dependence of the linear and nonlinear transport was measured. Both the first- and third-harmonic signals gain significantly different shapes under IP magnetic fields compared to the OOP situation, as can be seen in Figure 5.5a,b. As mentioned above, MBT has a perpendicular magnetic anisotropy and an OOP magnetic easy axis, which causes the hard magnetic behaviour in Figure 5.4, whereas the signals in Figure 5.5 correspond to the softer magnetic behaviour with a gradual reorientation of the magnetisation under IP fields [321, 533]. Because of the smooth

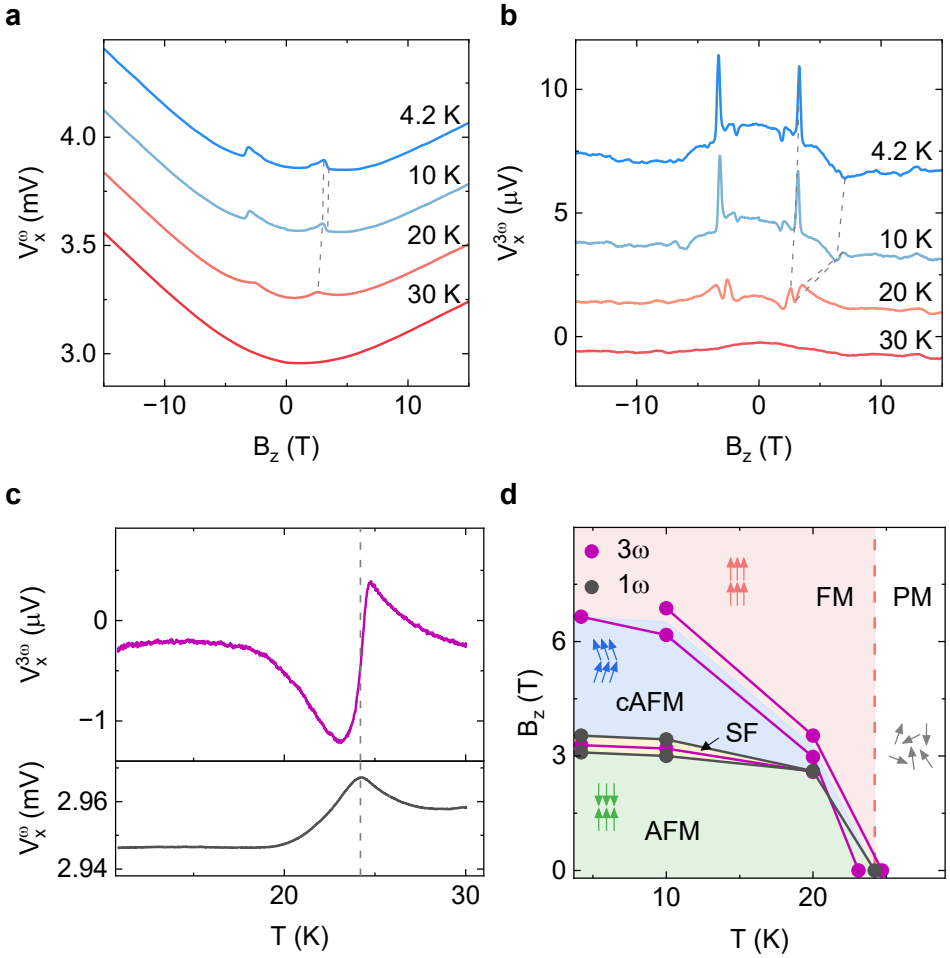


Figure 5.4: Magnetic phase diagram of MBT for out-of-plane magnetic fields. (a,b) OOP magnetic field dependence of the first- (a) and third-harmonic (b) longitudinal voltages at different temperatures. The data has been shifted vertically for clarity. **(c)** Temperature dependence of the first- (bottom) and third-harmonic (top) longitudinal voltages for zero magnetic field. Magnetic phase transitions are outlined with dashed lines. The measurements were performed in Device MBT-1. **(d)** T *vs* B_z magnetic phase diagram of MBT, containing AFM, cAFM, FM and PM phases as well as a spin-flop (SF) transition region. The magnetic ordering in each phase is indicated by coloured arrows. Adapted from *Paper V* (a,b,d) and *Paper VI* (c), respectively.

transition between the AFM and cAFM' phases, both the first- and the third-harmonic signals are smooth in the low-field range, and the two phases cannot be distinguished. Small kinks are observed in V_x^{ω} near $B_{xy} = \pm 9\,\mathrm{T}$ at $T = 4.3\,\mathrm{K}$ (which shift towards smaller fields with increasing temperatures), which correlates with the cAFM'-FM phase transition where MBT is fully magnetised IP. In contrast, the same cAFM'-FM transition is clearly visible

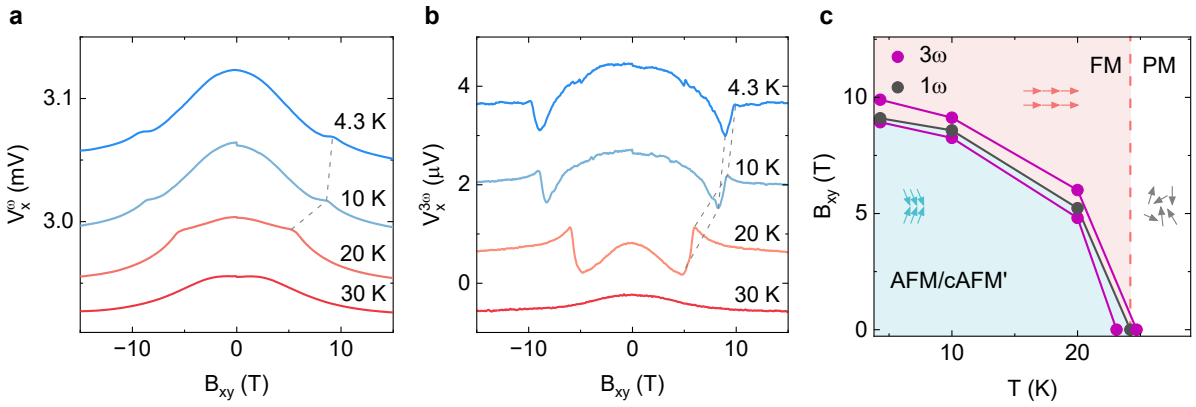


Figure 5.5: Magnetic phase diagram of MBT for in-plane magnetic fields. (a,b) IP magnetic field dependence of the first- (a) and third-harmonic (b) longitudinal voltages at different temperatures. Magnetic phase transitions are outlined with dashed lines. The data has been shifted vertically for clarity. The measurements were performed in Device MBT-1. **(d)** *T vs* B_{xy} magnetic phase diagram of MBT, containing AFM, cAFM', FM and PM phases. The magnetic ordering in each phase is indicated by coloured arrows. Adapted from *Paper V*.

in the third-harmonic signals with sharp kinks in Figure 5.5b, due to the strong correlation between the magnetisation of MBT and the nonlinear transport.

Using the phase transitions in Figure 5.5a,b (and Figure 5.4c), the phase diagram in Figure 5.5c could be constructed. As can be seen, the phase diagram displays the AFM/cAFM', FM and PM phases in MBT as a function of temperature and IP magnetic field. To be noted, the AFM and cAFM' phases are shown together in the phase diagram, since the smooth transition between them is not well-defined.

5.1.5 Oblique magnetic phase diagram of $MnBi_2Te_4$

Finally, an oblique magnetic field B_θ applied at a polar angle θ (*i.e.* with $\theta = 0\,^\circ$ corresponding to fully OOP and $\theta = 90\,^\circ$ corresponding to fully IP) was used to fully investigate the directional dependence of the magnetic phases of MBT. The evolution of the first-harmonic signal with the orientation of the applied magnetic field is shown in Figure 5.6a,b. The signals develop continuously between the respective behaviours for OOP and IP magnetic fields that are seen in Figure 5.4a and Figure 5.5a. A similar continuous evolution is observed for the third-harmonic signals, as shown in Figure 5.6c, although with consistently sharper features that allow for

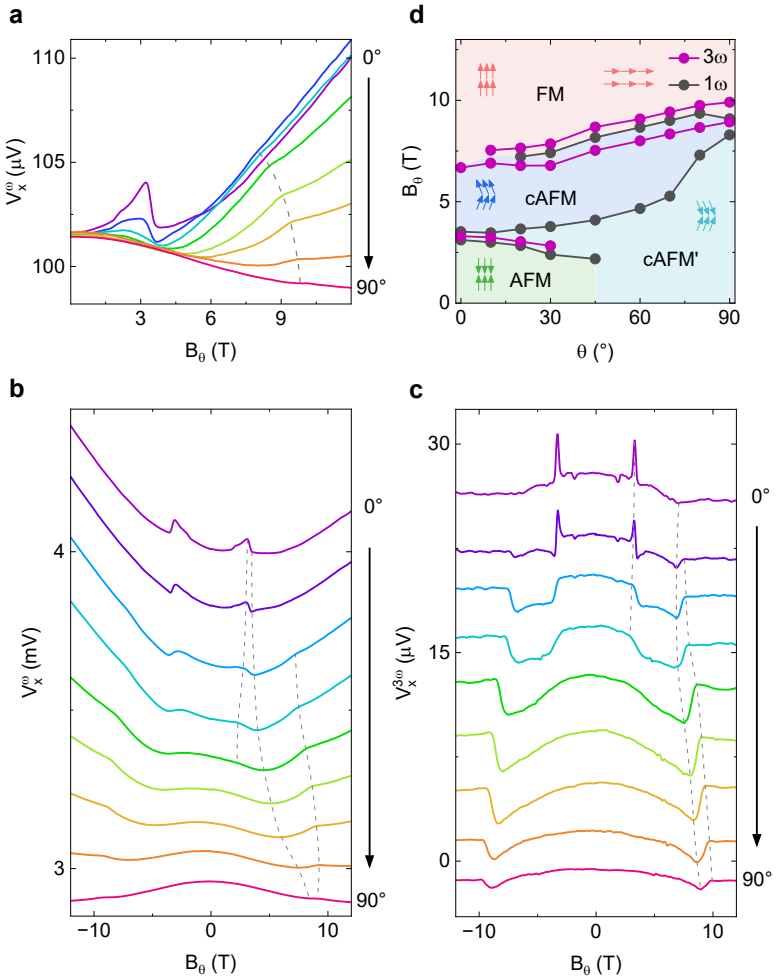


Figure 5.6: Magnetic phase diagram of MBT for oblique magnetic fields. (a-c) Oblique magnetic field dependence of the first- (a,b) and third-harmonic (c) longitudinal voltages for different magnetic field orientations. Magnetic phase transitions are outlined with dashed lines. The data in (b,c) has been shifted vertically for clarity. The measurements were performed in Device MBT-1. **(d)** θ *vs* B_θ magnetic phase diagram of MBT, containing AFM, cAFM, cAFM' and FM phases. The magnetic ordering in each phase is indicated by coloured arrows. Adapted from *Paper V*.

easier identification of the magnetic phase transitions.

The phase diagram in Figure 5.6d was constructed from the magnetic phase transitions in Figure 5.6b,c, and contains the AFM, cAFM, cAFM' and FM phases of MBT as functions of the orientation and magnitude of the oblique magnetic field. Here, the FM phase includes both the fully OOP and the fully IP polarisations of MBT, depending on the direction of B_θ. Since the spin-flop transition region cannot be clearly distinguished from

the cAFM' phase, it is not explicitly indicated in the phase diagram, but it can nevertheless be inferred to exist between the AFM and cAFM phases when the magnetic field has a predominant OOP orientation.

Interestingly, all of the magnetic phases of MBT have a strong dependence on θ. As discussed above, OOP magnetic fields cause MBT to transition from the AFM to the cAFM phase *via* a distinct spin-flop transition, whereas IP fields induce a smooth AFM-CAFM' transition. While varying the orientation of B_θ, the well-resolved transition from the AFM phase is maintained up to $\theta \approx 45\,^\circ$. This can be understood as MBT having an OOP-dominated AFM state up to this point, before favouring an IP magnetisation for larger values of θ. Meanwhile, both the cAFM and the FM phases are shifted towards larger magnetic fields when B_θ is oriented towards the IP direction. This happens because the net magnetisation of MBT is pulled away from its OOP easy axis, so that a stronger magnetic field is required for a partial (full) polarisation of MBT to transition into the cAFM (FM) phase.

5.2 Higher-order nonlinear transport in magnetic topological insulator $MnBi_2Te_4$

Whereas dipoles and quadrupoles in the quantum metric in MBT can generate second- and third-order nonlinear electronic transport [70–72], higher-order nonlinear transport can arise due to higher-order multipoles in the quantum geometry. A schematic band diagram with the quantum metric septupole as a colour plot, which corresponds to a seventh-order nonlinear conductivity, is illustrated in Figure 5.7a as an example of such multipoles. The nonlinear transport was measured in multilayer MBT Hall bar devices, as described in Section 5.1. A microscopy image of a representative device is shown in Figure 5.7b. The n^{th}-harmonic components of the nonlinear transport signals were extracted using a lock-in technique by measuring the voltage response at a higher frequency $n\omega$ compared to the frequency ω of the applied AC current.

5.2.1 Observation of higher-harmonic transport signals in $MnBi_2Te_4$

The third- (3ω), fifth- (5ω) and seventh-harmonic (7ω) longitudinal voltage signals $V_x^{n\omega}$ of the nonlinear transport are shown in Figure 5.7c. All three voltage responses clearly follow a nonlinear current-voltage relationship. In contrast, the even-order harmonic signals (*i.e.* the second- [2ω], fourth- [4ω] and sixth-harmonic [6ω] signals) are suppressed in the same current range, as can be seen in Figure 5.7d. In addition to this even-odd behaviour, the signal amplitude is found to be significantly larger for the lower harmonic orders than for the higher orders. This kind of decreasing amplitude with increasing harmonic order is generally expected for nonlinear transport, where the lower-harmonic signals normally dominate if they are not suppressed by symmetry [342]. The amplitude of the nonlinear transport signals are summarised in Figure 5.8a, where both the even-odd behaviour and the overall decreasing trend are visualised.

The scaling of the odd-order harmonic voltage responses with respect to the applied AC current was examined analytically and through fitting of the experimental data. For an AC current $I^{\omega}(t) = I_0 \sin(\omega t)$, the voltage response up to the seventh order can be expanded as

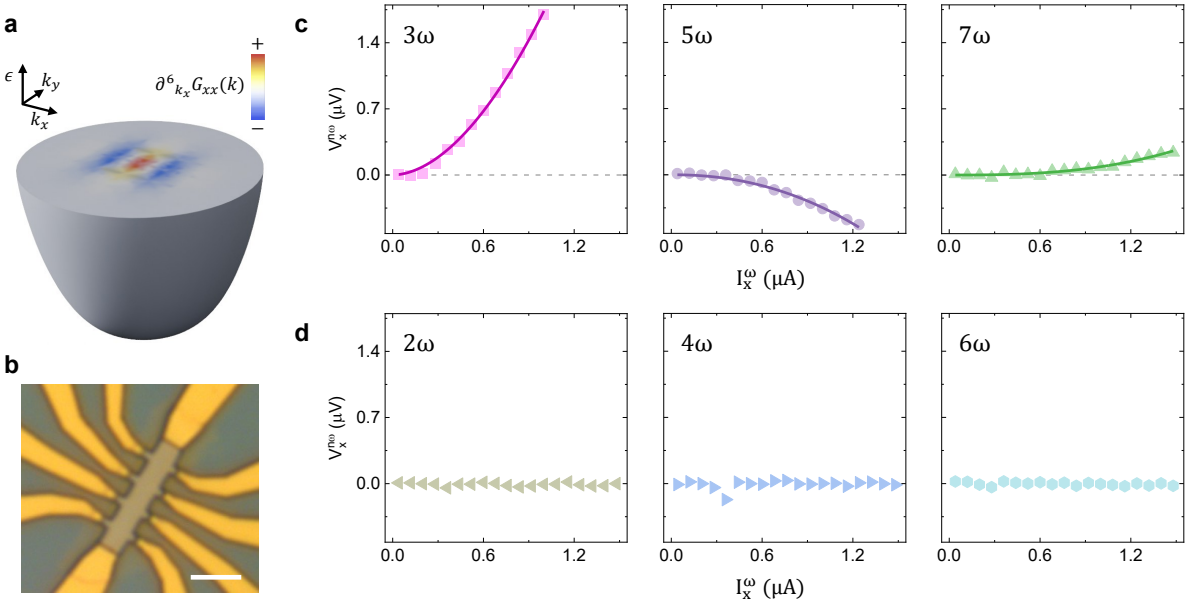


Figure 5.7: Higher-harmonic nonlinear transport in multilayer MBT. **(a)** Schematic band diagram with the quantum metric septupole as a colour plot, which correlates to seventh-order nonlinear transport. **(b)** Optical microscope image of a representative multilayer MBT Hall bar device. The scale bar is 3 μm. **(c)** Nonlinear IV characteristics of the third- (3ω), fifth- (5ω) and seventh-harmonic (7ω) voltage responses. The solid lines are power-law fits as guides to the eye. **(d)** Nonlinear IV characteristics of the second- (2ω), fourth- (4ω) and sixth-harmonic (6ω) voltage responses. The measurements were performed in Device MBT-2 at $T = 2$ K. Adapted from *Paper VI*.

$$\begin{aligned} V(t) &= a_1 I + a_2 I^2 + a_3 I^3 + a_4 I^4 + a_5 I^5 + a_6 I^6 + a_7 I^7 \\ &= a_1 I_0 \sin(\omega t) + a_2 I_0^2 \sin^2(\omega t) + a_3 I_0^3 \sin^3(\omega t) + a_4 I_0^4 \sin^4(\omega t) \\ &\quad + a_5 I_0^5 \sin^5(\omega t) + a_6 I_0^6 \sin^6(\omega t) + a_7 I_0^7 \sin^7(\omega t), \end{aligned} \tag{5.1}$$

where a_n are time-independent coefficients. This can be rearranged as

$$\begin{aligned} V(t) = V^0 &+ V^{1\omega} \sin(\omega t) \\ &+ V^{2\omega} \sin\left(2\omega t + \frac{\pi}{2}\right) + V^{3\omega} \sin(3\omega t + \pi) \\ &+ V^{4\omega} \sin\left(4\omega t + \frac{3\pi}{2}\right) + V^{5\omega} \sin(5\omega t + 2\pi) \\ &+ V^{6\omega} \sin\left(6\omega t + \frac{5\pi}{2}\right) + V^{7\omega} \sin(7\omega t + 3\pi), \end{aligned} \tag{5.2}$$

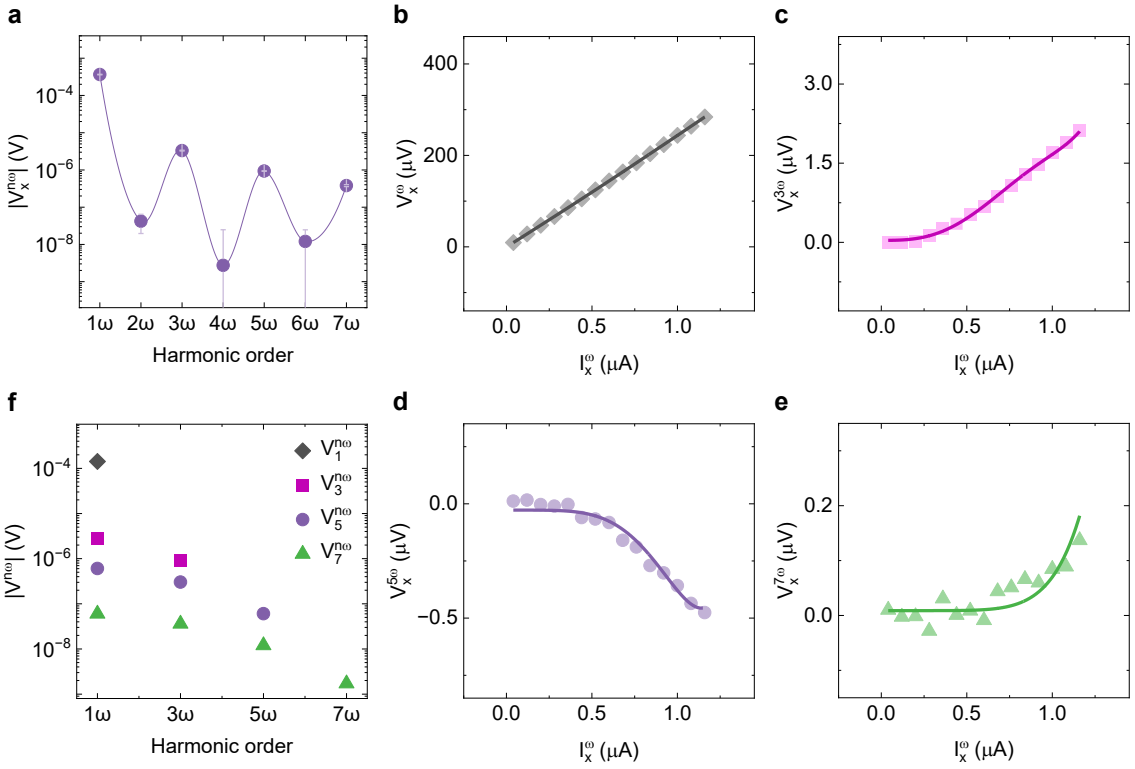


Figure 5.8: Even-odd behaviour and current scaling of nonlinear transport in MBT. (a) The nonlinear voltage signals of different harmonic orders, showing an even-odd behaviour and a decreasing amplitude with increasing harmonic orders. **(b-e)** Odd-harmonic IV characteristics with polynomial fits to the signals using Equation (5.3) (solid lines). The experimental signals in (c-e) are the same data as in Figure 5.7c. **(f)** The respective terms from the fits in (b-e), where $V_m^{n\omega}$ is the I_0^m-order contribution to the n^{th}-harmonic signal in Equation (5.3). Adapted from *Paper VI*.

where

$$\begin{cases} V^0 = \frac{a_2}{2} I_0^2 + \frac{3a_4}{8} I_0^4 + \frac{5a_6}{16} I_0^6 \\ V^{1\omega} = a_1 I_0 + \frac{3a_3}{4} I_0^3 + \frac{5a_5}{8} I_0^5 + \frac{35a_7}{64} I_0^7 \\ V^{2\omega} = -\frac{a_2}{2} I_0^2 - \frac{a_4}{2} I_0^4 - \frac{15a_6}{32} I_0^6 \\ V^{3\omega} = \frac{a_3}{4} I_0^3 + \frac{5a_5}{16} I_0^5 + \frac{21a_7}{64} I_0^7 \\ V^{4\omega} = -\frac{a_4}{8} I_0^4 - \frac{3a_6}{16} I_0^6 \\ V^{5\omega} = \frac{a_5}{16} I_0^5 + \frac{7a_7}{64} I_0^7 \\ V^{6\omega} = -\frac{a_6}{32} I_0^6 \\ V^{7\omega} = \frac{a_7}{64} I_0^7. \end{cases} \tag{5.3}$$

Interestingly, Equation (5.2) and Equation (5.3) demonstrate a harmonic mixing where higher-power current dependencies contribute to lower-order harmonic signals. However, this mixing occurs only from higher power dependencies to lower harmonics and not the other way around, which importantly rules out contributions from lower-order nonlinear transport components to higher-harmonic signals.

The polynomial current-voltage dependency in Equation (5.3) holds generally for lock-in measurements in any system with higher-order voltage responses. Figure 5.8b-e shows the odd-order harmonic IV characteristics and corresponding polynomial fits with joint coefficients a_n. The contributions from the respective voltage responses and the significance of the harmonic mixing are estimated quantitatively in Figure 5.8f, where $V_m^{n\omega}$ is the I_0^m-order contribution to the n^{th}-harmonic voltage signal. As can be seen, the lower-order contributions dominate so that all odd-order harmonic signals follow a $V^{n\omega} \propto (I^{\omega})^n$ power-law behaviour in the leading term.

5.2.2 Spurious effects and control measurements

Before continuing the investigation of the nonlinear transport in MBT, spurious effects that can lead to higher-harmonic signals were considered and control measurements were performed. First, thermoelectric effects can be present in MBT due to its high electrical conductivity and low thermal conductivity [539, 540], which can generate nonlinear transport. However, although thermoelectric effects may have a minor contribution to the observed higher-harmonic signals, they are not expected to be significant in the present devices. The Seebeck effect in MBT is expected to be elevated at high temperatures, with only a minute response to the Néel temperature [533, 540, 541], which is in complete contrast to the measured higher-harmonic signals that appear only below the Néel temperature, as shown in Section 5.2.3. Furthermore, longitudinal voltages from the anomalous Nernst effect require a net magnetisation and a transverse thermal gradient in the device [539, 542], neither of which is expected in the highly symmetric Hall bar devices with AFM multilayer MBT. Still, the contribution from thermoelectric effects were estimated through control measurements. To indicate the overall Joule heating in the device, linear magnetoresistance measurements were performed with different currents. As can be seen in Figure 5.9a, the harmonic signals are almost identical and the kinks corresponding to the AFM-cAFM phase transition near $B_z = \pm 3\,\text{T}$ are shifted only very slightly towards smaller magnetic fields when the applied current

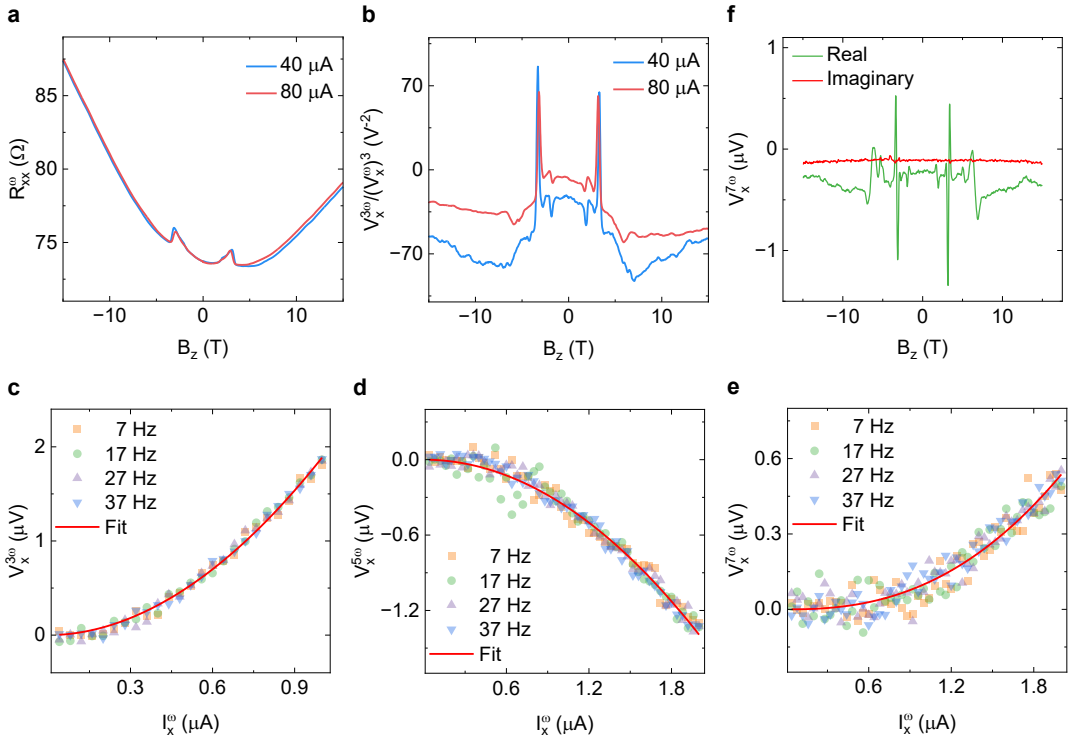


Figure 5.9: Control measurements to rule out spurious effects. **(a)** First-harmonic magnetoresistance for different AC currents. **(b)** The normalised third-harmonic signal $V_x^{3\omega}/\left(V_x^{\omega}\right)^3$ as a function of the OOP magnetic field for different AC currents. **(c-e)** Third- (c), fifth- (d) and seventh-harmonic (e) *IV* characteristics for different frequencies of the AC current. The red lines are power-law fits as guides to the eye. **(f)** The real and imaginary signal components of the longitudinal seventh-harmonic signal as a function of the OOP magnetic field. The real signal component is the raw data corresponding to the seventh-harmonic signal in Figure 5.11a. The measurements were performed in Device MBT-1 (a,b,f) and in Device MBT-2 (c-e), respectively. Adapted from *Paper VI*.

is doubled, indicating negligible thermal effects and only a minor increase in temperature. Additionally, Figure 5.9b shows the magnetic field dependence of the third-harmonic voltage normalised by the cube of the first-harmonic voltage ($V_x^{3\omega}/\left(V_x^{\omega}\right)^3$), which decreases in amplitude when a larger current is applied. In contrast, the expected behaviour of thermoelectrically induced nonlinear voltage signals is for the $V_x^{3\omega}/\left(V_x^{\omega}\right)^3$ ratio to grow with increasing currents due to the enhanced heating effects [72]. Thermoelectric effects are therefore strongly indicated not to be the main mechanism behind the higher-harmonic signals.

Second, the higher-harmonic signals were measured for different frequen-

cies of the applied AC current I_x^ω. The absence of a frequency dependence of the measured signals (which can be seen in Figure 5.9c-e) in the low-frequency quasi-DC range excludes artificial contributions which could otherwise arise from capacitive coupling effects [251, 254, 258, 543]. This also acts as a further indication against thermoelectric effects, since nonlinear transport due to Joule heating can have a frequency dependence with a cut-off frequency due to thermal relaxation [544], which is not observed in the present devices.

Third, the ohmic behaviour of the voltage probe contacts was confirmed by first-harmonic IV characteristics, which were measured in a two-terminal geometry and showed a linear current-voltage relationship with no visible indication of a diodic behaviour. Moreover, artificial contributions to the nonlinear transport signals from contact junctions are expected to be insensitive to the Néel temperature [70], different from the observed behaviour in Section 5.2.3 below.

Fourth, it is noted that electron scattering against the edges in asymmetrically shaped MBT flakes can give rise to transverse nonlinear voltage signals [70]. However, the higher-order nonlinear transport measurements were performed in symmetrically shaped Hall bar devices that are patterned through EBL and subsequent Ar milling, with a representative device being shown in Figure 5.7b. Additionally, asymmetric edge scattering effects are expected to be temperature independent [70], which does not align with the experimental observations.

Fifth, harmonic signals which can appear due to unavoidable nonlinearities of the integrated circuits in the lock-in amplifiers were examined [545]. Control measurements were performed where the nonlinear transport across a gold lead without MBT was measured, which did not result in an observable nonlinear voltage response for any harmonic order.

Finally, the lock-in phase of the measured higher-harmonic signals was considered. As is shown in Equation (5.2), the harmonic voltages follow a $\sin\left(n\omega t + \frac{(n-1)\pi}{2}\right)$ time dependence. Consequently, the odd-order signals appear in-phase or with a π phase shift with respect to the applied AC current, whereas the even-order signals have a phase shift of $\pm\pi/2$. Therefore, the odd-order and even-order harmonic voltages are obtained as the real and imaginary parts of the measured lock-in signal, respectively. In order to further rule out artificial contributions, the real and imaginary signal components were measured for all harmonic orders, and the imaginary (real) components of the odd-order (even-order) harmonic signals were confirmed to be negligible. This is exemplified with the seventh-harmonic signal under

an external magnetic field in Figure 5.9f.

5.2.3 Temperature dependence and conductivity scaling analysis in $MnBi_2Te_4$

The temperature dependence of the first- to seventh-harmonic voltage signals is presented in Figure 5.10a. The third-harmonic signal is below the noise level at higher temperatures but grows drastically below the Néel temperature $T_N = 23.8\,\mathrm{K}$. The fifth- and seventh-harmonic signals follow a similar behaviour, albeit with significantly lower amplitudes. The even-order harmonic signals, however, remain suppressed at all temperatures. The onset of the odd-order higher-harmonic signals below T_N signifies a strong correlation between the nonlinear transport and the magnetisation of MBT, in agreement with the results in Section 5.1.

In order to identify the microscopic mechanism behind the nonlinear transport, conductivity scaling analysis of the third-harmonic signal was utilised. Both the quantum metric and Drude-like (*i.e.* extrinsic scattering-induced [248, 351]) contributions to the nonlinear transport were considered. Nonlinear transport can generally also arise due to Berry curvature multipoles, but such contributions to the longitudinal voltage are forbidden by the C_3 crystal symmetry of MBT [72, 248, 338, 339]. Since the third-order nonlinear transport contribution from the quantum metric is independent of the scattering time τ whereas the Drude-like contribution scales as τ^2 [72, 248, 338–340, 546, 547], the respective contributions from the two mechanisms could be evaluated comparatively based on the dependence of the third-harmonic signal with respect to the linear conductivity of MBT. Figure 5.10b shows the third-harmonic voltage normalised by the cube of the first-harmonic voltage as a function of the square of the linear longitudinal conductivity σ_{xx}, which vary with temperature and are extracted from Figure 5.10a in the low-temperature regime. Here, the conductivity is calculated as $\sigma_{xx} = I_x^\omega L / V_x^\omega wt$, where L, w and t are the dimensions of the MBT channel between the two voltage probes in the device. The data in Figure 5.10b was fitted linearly by the scaling formula

$$\frac{V_x^{3\omega}}{(V_x^\omega)^3} = \alpha {\sigma_{xx}}^2 + \beta, \tag{5.4}$$

where the slope α and the intercept β correspond to the Drude-like and the quantum metric contributions to the third-harmonic signal, respectively [72]. From this, nearly equal contributions were obtained of $\alpha {\sigma_{xx}}^2 \approx 1.0 \cdot 10^6\,\mathrm{V}^{-2}$

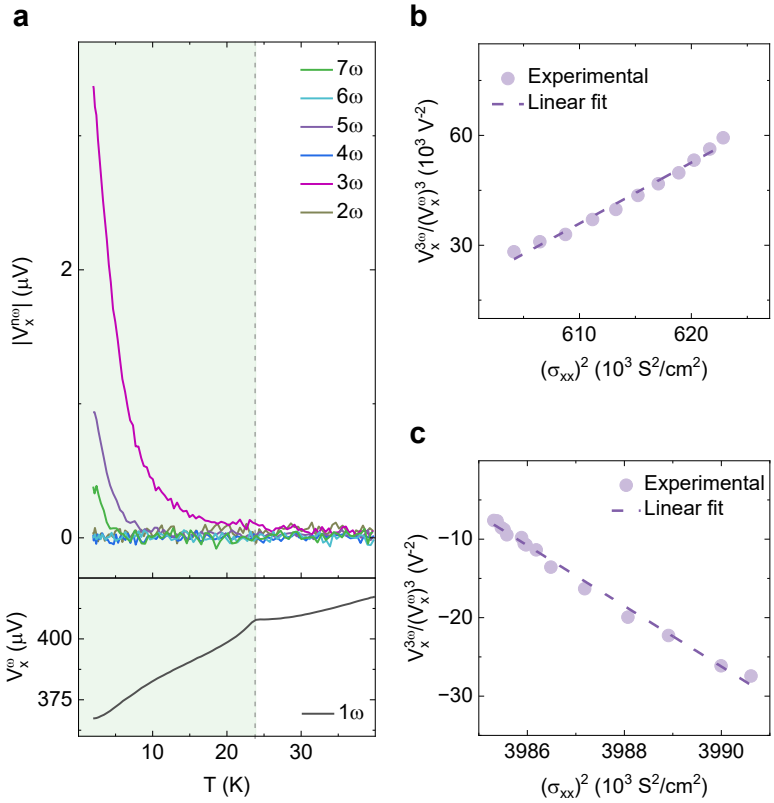


Figure 5.10: Temperature-dependent higher-harmonic nonlinear transport and conductivity scaling analysis. **(a)** Nonlinear voltages of the second to seventh harmonic orders (top) and first-harmonic linear voltage (bottom) as functions of temperature. The Néel temperature $T_N = 23.8\,\mathrm{K}$ is indicated by a dashed line. **(b)** The third-harmonic voltage in (a) normalised by the cube of the first-harmonic voltage as a function of the square of the longitudinal conductivity of MBT in the low-temperature range. **(c)** Normalised third-harmonic voltage of a separate device as a function of the square of the longitudinal conductivity of MBT (extracted from the low-temperature range of Figure 5.4c). The dashed lines in (b,c) are linear fits to the data using Equation (5.4), and both devices have very similar relationships between $\alpha{\sigma_{xx}}^2$ and β. The measurements were performed in Device MBT-2 (a,b) and in Device MBT-1 (c), respectively. Adapted from *Paper VI*.

(for an average value of the conductivity ${\sigma_{xx}}^2 = 615 \cdot 10^3\,\mathrm{S}^2/\mathrm{cm}^2$) and $\beta \approx -9.8 \cdot 10^5\,\mathrm{V}^{-2}$, respectively. Almost equal Drude-like and quantum metric contributions were similarly reproduced in additional devices, as exemplified with a second device in Figure 5.10c. Since theoretical expressions for nonlinear conductivities from the quantum metric have not yet been derived beyond the third order [345], no scaling analysis could be conducted for the fifth- and seventh-harmonic signals. Based on the results for the

third-harmonic signals above, contributions from both quantum metric and Drude-like conductivities are however expected.

5.2.4 Magnetic field dependence and magnetic phase correlation in $MnBi_2Te_4$

The evolution of the higher-order nonlinear longitudinal transport under OOP magnetic fields is displayed in Figure 5.11a. All odd-harmonic signals up to the seventh order are clearly observable and dominated by the lower harmonic orders for all magnetic fields, whereas the even-harmonic signals are suppressed. Notably, the harmonic signals exhibit sharp features near $B_z = \pm 3\,\mathrm{T}$ and $\pm 6\,\mathrm{T}$, which can be correlated with the magnetic phases of MBT. The phase diagram in Figure 5.11c was constructed from temperature- and field-dependent first-harmonic measurements, similarly to in Section 5.1, with the AFM, cAFM, FM and PM phases as well as the spin-flop transition region identified accordingly [321, 330, 371, 530]. The features in all higher-harmonic signals align well with the magnetic phase transitions, as indicated with dashed lines in Figure 5.11a. Under moderate magnetic fields, the AFM-cAFM phase transition causes the kinks near $B_z = \pm 3\,\mathrm{T}$. Interestingly, even the otherwise suppressed second-harmonic signal gains a small but noticeable response at these field values. This is likely generated by a dipole in the Berry curvature, which is normally forbidden but can be allowed by the reduced symmetry in MBT during the spin-flop transition [250]. For larger magnetic fields, the cAFM-FM phase transition at $B_z = \pm 6\,\mathrm{T}$ is seen as another kink in the odd-order higher-harmonic signals due to the close correlation between the nonlinear transport and magnetisation of MBT. Figure 5.11b shows a similar behaviour of the nonlinear transverse transport, where the odd-order higher-harmonic voltages have a clear response mainly at the AFM-cAFM transition, and where the second-harmonic signal grows in the fully polarised FM phase.

In addition to the kinks in the longitudinal transport signals at the magnetic phase transitions, significant shifts in the harmonic signals are observed during the gradual magnetisation of MBT in the cAFM phase. The difference in harmonic voltage between the FM and the AFM phases $|V_x^{n\omega,FM} - V_x^{n\omega,AFM}|$ is summarised for all harmonic orders in Figure 5.11d. Similar to the trends in Figure 5.8a, the difference in nonlinear voltage amplitude is orders of magnitude larger for the odd-harmonic signals than for the even-harmonic ones, and the overall response decreases rapidly with increasing harmonic orders. Since the nonlinear Drude-like conductivities are insensi-

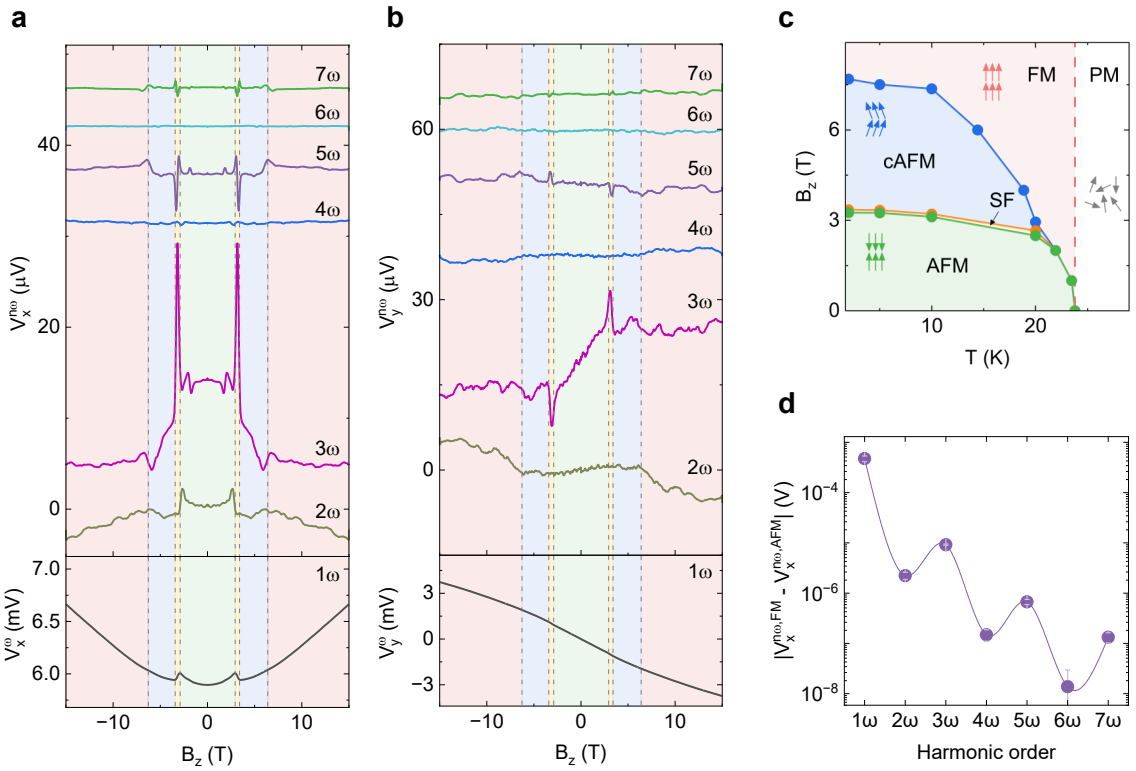


Figure 5.11: Magnetic-field-dependent higher-order nonlinear transport. (a,b) Longitudinal (a) and transverse (b) nonlinear voltages of the second to seventh harmonic orders (top) and first-harmonic linear voltage (bottom) as functions of OOP magnetic fields. The data is symmetrised (a) and antisymmetrised (b), respectively, and has been shifted vertically for clarity. Magnetic phase transitions are indicated by dashed lines. **(c)** *T vs* B_z magnetic phase diagram. The borders of the AFM, cAFM, FM and PM phases as well as a spin flop (SF) transition region were mapped out from linear first-harmonic transport measurements. The magnetic ordering in each magnetic phase is indicated by coloured arrows. **(d)** Shifts in the harmonic voltages between the AFM and the FM phases in (a), as a function of harmonic order. The measurements were performed in Device MBT-1 (a,b) and Device MBT-3 (c), respectively. Adapted from *Paper VI*.

tive to magnetic phase transitions in MBT [72], these shifts in the nonlinear transport signals are concluded to originate from changes in the nonlinear transport contributions from the quantum metric during the AFM-cAFM-FM phase transitions.

5.2.5 Theoretical calculations of the higher-order nonlinear transport in $MnBi_2Te_4$

In order to properly understand the experimental results, the microscopic origin of the higher-order nonlinear transport was investigated through theoretical calculations. The band structure of multilayer MBT was modelled by an $k.p$ model which has been fitted to first-principles calculations and allows the inclusion of perturbations to address the effects of finite magnetic fields [72]. Here, an even number of SLs was assumed, since the net magnetisation of a possible uncompensated SL is negligible in the experimental devices with more than 40 SLs.

First, the Drude-like contributions to the nonlinear transport were considered, where the nonlinear longitudinal conductivities were calculated from higher-order differentiation of the modelled dispersion relation of MBT [342]. The calculated derivatives $\partial_{k_x}^{n+1}\epsilon(k)$, which correspond to the n^{th}-order nonlinear transport, are summarised qualitatively in Figure 5.12a. The corresponding nonlinear conductivities can be evaluated from integration over reciprocal space. Importantly, the higher-order derivatives of the dispersion relation in Figure 5.12a can clearly be seen to be symmetric with respect to k_x for the odd harmonic orders and antisymmetric for the even orders, respectively. After integration, this leads to persisting odd-order nonlinear conductivities while the even-order contributions vanish, which agrees well with the behaviour of the experimental nonlinear transport signals. Quantitative values of the calculated nonlinear transport contributions furthermore replicate the experimentally observed dominance of the lower-order odd-harmonic signals over the higher-order ones.

Next, the contributions to the nonlinear transport from the quantum metric were considered. Since these nonlinear conductivities are expected to correspond to changes in the nonlinear transport under magnetic fields, their field dependence allows the quantum metric contributions to be examined in comparison to the field-insensitive Drude-like contributions [72]. Quantum metric multipoles were calculated through differentiation of the band-energy normalised quantum metric tensor G_{ab} under a finite magnetic field, where $\partial_{k_x}^{n-1}G_{xx}(k)$ corresponds to the n^{th}-order nonlinear transport, as summarised qualitatively in Figure 5.12b. Interestingly and importantly, the calculated quantum metric multipoles exhibit similar symmetries with respect to k_x as the higher-order derivatives of the dispersion relation above, and integration over the multipoles in reciprocal space consequently yields a similar even-odd behaviour where the even-order harmonic signals are

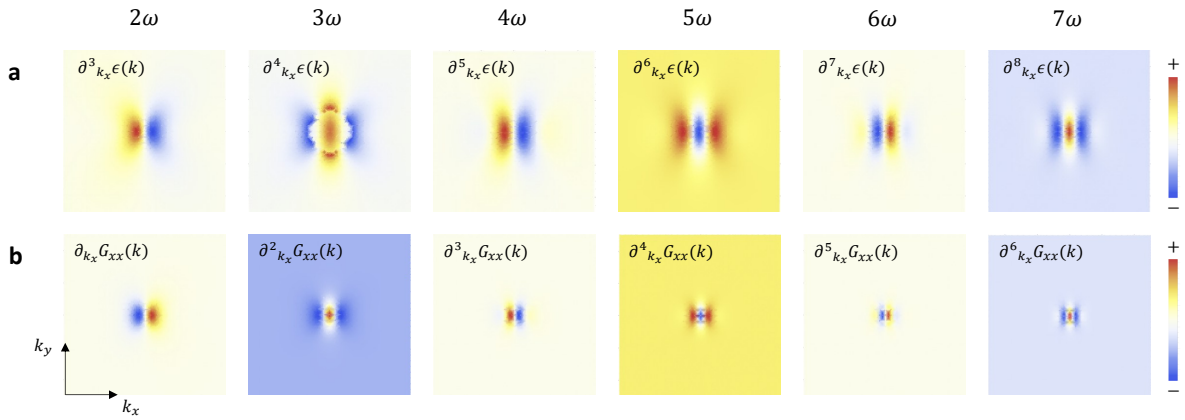


Figure 5.12: Theoretical calculations of higher-order Drude and quantum metric contributions. (a,b) Qualitative overview of calculated contributions to the higher-order nonlinear transport from Drude-like terms (a) and quantum metric multipoles (b), respectively. Adapted from *Paper VI*.

suppressed. Both the quantum metric and the Drude-like contributions to the nonlinear transport can hence give rise to the experimentally measured signals with an even-odd behaviour. Unfortunately, the magnitude of their respective contributions cannot be compared directly in the calculations, since longitudinal conductivities from quantum metric multipoles have not yet been derived beyond the third order [345]. Still, both mechanisms are nevertheless expected to contribute to the higher-order nonlinear transport in MBT from the theory results, which importantly aligns well with the scaling analysis in Section 5.2.3.

6 Summary and outlook

6.1 Summary

In this thesis and the included works, significant effort has been invested in exploring spin and topological effects in topological quantum materials through spin and electronic transport measurements in microscopic devices. First, pure spin-polarised currents in graphene were employed to electrically sense spin textures in cobalt and the van der Waals ferromagnet Fe_5GeTe_2 with designed geometrical shapes. Next, spin polarisation was generated and detected *via* charge-spin interconversion effects in the topological insulator $Bi_{1.5}Sb_{0.5}Te_{1.7}Se_{1.3}$ and the Weyl semimetal $TaIrTe_4$. Finally, the magnetic phases and the quantum geometry in the magnetic topological insulator $MnBi_2Te_4$ were probed through nonlinear transport measurements.

The all-electrical spin sensing was performed in lateral graphene spin-valve devices. Designed shapes with different geometrical constrictions were used to induce spin textures including multi-domain and chiral vortex textures in Co and Fe_5GeTe_2 at room temperature. By injecting the spin textures into the graphene channel and detecting them nonlocally with a ferromagnetic reference electrode, the polarisation of the spin textures and their evolution under magnetic fields could be traced. Distinctive multi-level spin-valve switching patterns and Hanle spin precession signals allowed the identification of the diverse spin textures corresponding to different geometric shapes, which were also corroborated with magnetic force microscopy and micromagnetic simulations of the Co electrodes. These results open a new route for all-electrical sensing of spin textures and magnetic domains in both conventional and van der Waals magnets, using pure spin currents in potentiometric measurements.

Charge-spin interconversion in $Bi_{1.5}Sb_{0.5}Te_{1.7}Se_{1.3}$ (BSTS) and in $TaIrTe_4$ (TIT) was realised and observed directly through spin transport measurements in hybrid graphene spin-valve devices with van der Waals heterostructures at room temperature. Reversible charge-to-spin and spin-to-charge conversion was demonstrated with reliable nonlocal spin-valve and Hanle spin precession measurements, with both generation and detection of po-

larised spin in the topological insulator and in the Weyl semimetal, respectively. The measured charge-spin interconversion effects were found to be robust under varying bias charge currents and magnetic fields in different in-plane and out-of-plane orientations, as well as under different gate voltages in the case of the topological insulator. These findings prove room-temperature charge-spin interconversion in BSTS and TIT, which is enabled by the strong spin-orbit coupling of their topological band structures, and build towards the use of topological quantum materials for all-electrical spin generation and sensing in next-generation energy-efficient spintronic devices.

The nonlinear transport measurements were conducted in Hall bar devices of multilayer $MnBi_2Te_4$ (MBT). The third-order nonlinear longitudinal voltage signal was founds to respond strongly with a higher sensitivity to magnetic phase transitions in MBT, compared to conventional linear transport signals. By probing the third-order transport signal against varying temperatures and magnetic fields in different in-plane and out-of-plane directions, detailed magnetic phase diagrams could be mapped out. Higher-order nonlinear transport with an even-odd behaviour could furthermore be observed, where odd-order nonlinear transport was detected up to the seventh order whereas all even-order transport components were suppressed. Through conductivity scaling analysis and theoretical calculations, the microscopic origin of the nonlinear transport was identified as a combination of quantum metric multipoles and Drude-like terms. These results establish nonlinear transport measurements as an all-electrical tool for detailed characterisation of magnetic and quantum geometric features in MBT and other related materials.

In summary, this dissertation demonstrates the rich physics and interplay of spin and topology in van der Waals topological quantum materials, including spin transport and sensing, charge-spin interconversion effects and quantum-geometry-induced nonlinear transport. Utilising their unique properties unlocks deeper and more comprehensive insights into condensed matter and quantum physics, and leads towards a new generation of technological applications.

6.2 Outlook

Looking into the future, many exciting and promising avenues can be envisioned. Spin sensing with pure spin currents in graphene can be used for characterising complex spin textures in exotic magnetic materials with or without geometric constrictions, especially in the 2D limit, and can de-

velop as a complement to conventional microscopy techniques. With the major advantage of all-electrical detection without a requirement for microscopic access, the technique can become particularly useful for integrated read-out of spin textures and magnetic states in spintronic devices. This includes novel and innovative technologies such as racetrack and multi-level magnetic memories, compute-in-memory devices, spin logic and magnetologic devices as well as Heisenberg, domain-wall and other neuromorphic computing architectures.

Charge-spin interconversion in topological insulators and Weyl semimetals at room temperature can provide efficient generation and detection of polarised spin, which can become paramount in next-generation spin-orbit-torque magnetic memories and spin-based computing technologies. By utilising the strong spin-orbit coupling of nonmagnetic topological quantum materials, such devices can be realised with a complete absence of magnetic stray fields and with a natural robustness against external magnetic fields, while simultaneously achieving a higher energy efficiency than what is possible with the spin-orbit coupling of conventional heavy metals. The broken crystal symmetries of Weyl semimetals furthermore allow the generation of unconventional out-of-plane spin polarisations, which can be used for field-free spin-orbit-torque switching of magnets with perpendicular magnetic anisotropies. Meanwhile, topological insulators have an enticing potential beyond pure spintronics, such as for dissipationless transport through their topologically protected surface states.

In a more specific perspective, the charge-spin interconversion in BSTS was concluded to originate from the topological insulator itself, which leaves the spin Hall effect, the Rashba-Edelstein effect and the spin-momentum locking of the topological surface states as the possible microscopic mechanisms. In order to narrow it down further, charge-spin interconversion measurements at different temperatures could be employed. At low temperatures, the spin Hall effect and the Rashba-Edelstein effect from the bulk bands are expected to be hampered due to freeze-out whereas the spin-momentum locking of the the metallic surface states should be unhindered, which would make it possible to distinguish the contributions from the bulk and surface states.

Concerning TIT, the charge-spin interconversion was observed through spin-valve and Hanle spin precession measurements with in-plane and out-of-plane magnetic fields in the y and z directions, respectively. By complementing this with xHanle spin precession measurements with the magnetic field along the in-plane x direction in the same device, the full x-y-z ori-

entation of the generated spin polarisation could be determined. Detailed information about out-of-plane spin components, which are allowed due to the broken crystal symmetry of TIT, would be especially important for spin-orbit-torque memory applications, as mentioned above. Moreover, gate-dependent measurements of the charge-spin interconversion, with graphene being tuned between its p- and n-doped regimes, could be used to investigate the possible contribution from proximity-induced spin-orbit coupling in graphene.

Nonlinear electronic transport as a sensitive probe of magnetic phase transitions is not limited to MBT, and can be used for characterising the magnetic order and complex magnetic landscapes of other magnetic materials as well. In addition to material characterisation, the technique is well-suited for all-electrical read-out of antiferromagnetic and ferromagnetic states without a need for optical or magnetometric access, such as in nonvolatile memories and other novel spintronic and quantum device applications.

Besides magnetic phase information, nonlinear transport in MBT is particularly interesting for investigating the quantum metric. Until recently, the quantum metric part of the quantum geometry has often been overlooked in favour of the more readily available Berry curvature, and experimental measurements of the quantum metric are still in their infancy. In order to better understand the quantum metric in topological quantum materials and its contribution to higher-order nonlinear transport, further experimental and theoretical works are necessary. Specifically, a complete theoretical model for quantum-metric-induced higher-order nonlinear transport would provide quantitative details and allow for a disentanglement of the different possible contributions to such nonlinear transport. This could also lead to predictions and experimental realisations of material systems where novel higher-than-third-order nonlinear transport components are dominant due to particular crystal symmetries. Ultimately, a comprehensive understanding of the full quantum geometry, including the quantum metric, and its interaction with electronic transport is expected to become a pillar of quantum and topological physics in solid-state matter, and can give central insights in everything from nonlinear transport to flat-band superconductivity and beyond.

Finally, although this is not the focus of this thesis, it ought to be mentioned that challenges regarding the industry integration of van der Waals and topological quantum materials must be overcome in order for commercially relevant applications to be realised. This includes growth of high-quality materials using industry-compatible techniques such as magnetron

sputtering or chemical vapour deposition, as well as the preparation of atomically clean interfaces and improvements in material stability under ambient conditions. However, this research direction is actively being pursued [512, 548–557], and these concerns may well be properly addressed in time.

References

[1] W. Heisenberg, "Über quantentheoretische Umdeutung kinematischer und mechanischer Beziehungen", Zeitschrift für Physik **33**, 879–893 (1925) (cit. on p. 1).

[2] E. Schrödinger, "An undulatory theory of the mechanics of atoms and molecules", Physical Review **28**, 1049–1070 (1926) (cit. on p. 1).

[3] W. Heisenberg, "Über den anschaulichen Inhalt der quantentheoretischen Kinematik und Mechanik", Zeitschrift für Physik **43**, 172–198 (1927) (cit. on p. 1).

[4] P. Dirac, "The Quantum Theory of the Electron", Proceedings of the Royal Society of London. Series A **117**, 610–624 (1928) (cit. on pp. 1, 10).

[5] A. Einstein, B. Podolsky, and N. Rosen, "Can quantum-mechanical description of physical reality be considered complete?", Physical Review **47**, 777–780 (1935) (cit. on p. 1).

[6] J. S. Bell, "On the Einstein Podolsky Rosen Paradox", Physics Physique Fizika **1**, 195–200 (1964) (cit. on p. 1).

[7] A. Aspect, J. Dalibard, and G. Roger, "Experimental test of Bell's inequalities using time-varying analyzers", Physical Review Letters **49**, 1804–1807 (1982) (cit. on p. 1).

[8] R. P. Feynman, "Space-time approach to quantum electrodynamics", Physical Review **76**, 769–789 (1949) (cit. on p. 1).

[9] J. Bardeen, L. N. Cooper, and J. R. Schrieffer, "Theory of superconductivity", Theory of Superconductivity **108**, 1175–1204 (1957) (cit. on p. 1).

[10] J. S. Kilby, "Invention of the Integrated Circuit", IEEE Transactions on Electron Devices **23**, 648–654 (1976) (cit. on p. 1).

[11] T. H. Maiman, "Stimulated Optical Radiation in Ruby", Nature **187**, 493–494 (1960) (cit. on p. 1).

[12] P. Benioff, "The computer as a physical system: A microscopic quantum mechanical Hamiltonian model of computers as represented by Turing machines", Journal of Statistical Physics **22**, 563–591 (1980) (cit. on p. 1).

[13] R. P. Feynman, "Simulating Physics with Computers", International Journal of Theoretical Physics **21**, 467–488 (1982) (cit. on p. 1).

[14] International Energy Agency, *Energy and AI*, tech. rep. (International Energy Agency, Paris, France, 2025) (cit. on p. 1).

[15] S. Chen, "Data centres will use twice as much energy by 2030 - driven by AI", Nature, https://doi.org/10.1038/d41586-025-01113-z (2025) (cit. on p. 1).

[16] N. Jones, "How to stop data centres from gobbling up the world's electricity", Nature **561**, 163–166 (2018) (cit. on p. 1).

[17] Y. Zhai, Z. Feng, Y. Zhou, and S. T. Han, "Energy-efficient transistors: suppressing the subthreshold swing below the physical limit", Materials Horizons **8**, 1601–1617 (2021) (cit. on p. 1).

[18] A. H. Kelechi, M. H. Alsharif, O. J. Bameyi, P. J. Ezra, I. K. Joseph, A. A. Atayero, Z. W. Geem, and J. Hong, "Artificial intelligence: An energy efficiency tool for enhanced high performance computing", Symmetry **12**, 1029 (2020) (cit. on p. 1).

[19] L. Ye, Z. Wang, Y. Liu, P. Chen, H. Li, H. Zhang, M. Wu, W. He, L. Shen, Y. Zhang, Z. Tan, Y. Wang, and R. Huang, "The Challenges and Emerging Technologies for Low-Power Artificial Intelligence IoT Systems", IEEE Transactions on Circuits and Systems I: Regular Papers **68**, 4821–4834 (2021) (cit. on p. 1).

[20] A. Andrae and T. Edler, "On Global Electricity Usage of Communication Technology: Trends to 2030", Challenges **6**, 117–157 (2015) (cit. on p. 1).

[21] A. Shehabi, S. J. Smith, E. Masanet, and J. Koomey, "Data center growth in the United States: Decoupling the demand for services from electricity use", Environmental Research Letters **13**, 124030 (2018) (cit. on p. 1).

[22] E. Masanet, A. Shehabi, N. Lei, S. Smith, and J. Koomey, "Recalibrating global data center energy-use estimates", Science **367**, 984–986 (2020) (cit. on p. 1).

[23] G. E. Uhlenbeck and S. Goudsmit, "Ersetzung der Hypothese vom unmechanischen Zwang durch eine Forderung bezüglich des inneren Verhaltens jedes einzelnen Elektrons", Die Naturwissenschaften **13**, 953–954 (1925) (cit. on pp. 2, 7).

[24] D. J. Griffiths and D. F. Schroeter, *Introduction to Quantum Mechanics*, 3rd ed. (Cambridge University Press, Cambridge, 2018) (cit. on pp. 2, 8).

[25] S. Bandyopadhyay and M. Cahay, *Introduction to Spintronics*, 2nd ed. (CRC Press, Boca Raton, Florida, 2016) (cit. on pp. 2, 10).

[26] P. Atkins, L. Jones, and L. Laverman, *Chemical Principles*, 6th ed. (W.H.Freeman & Co Ltd, London, 2012) (cit. on p. 2).

[27] L. Euler, "Solutio problematis ad geometriam situs pertinentis", Commentarii Academiae Scientiarum Petropolitanae **8**, 128–140 (1741) (cit. on p. 2).

[28] S. H. Simon, *Topological Quantum* (Oxford University Press, Oxford, UK, 2023) (cit. on p. 3).

[29] B. Keimer and J. E. Moore, "The physics of quantum materials", Nature Physics **13**, 1045–1055 (2017) (cit. on pp. 3, 10, 17, 19).

[30] I. Žutić, J. Fabian, and S. D. Sarma, "Spintronics: Fundamentals and applications", Reviews of Modern Physics **76**, 323–410 (2004) (cit. on pp. 3, 15, 36).

[31] B. Dieny et al., "Opportunities and challenges for spintronics in the microelectronics industry", Nature Electronics **3**, 446–459 (2020) (cit. on p. 3).

[32] X. Lin, W. Yang, K. L. Wang, and W. Zhao, "Two-dimensional spintronics for low-power electronics", Nature Electronics **2**, 274–283 (2019) (cit. on p. 3).

[33] H. Yang, S. O. Valenzuela, M. Chshiev, S. Couet, B. Dieny, B. Dlubak, A. Fert, K. Garello, M. Jamet, D.-E. Jeong, K. Lee, T. Lee, M.-B. Martin, G. S. Kar, P. Sénéor, H.-J. Shin, and S. Roche, "Two-dimensional materials prospects for non-volatile spintronic memories", Nature **606**, 663–673 (2022) (cit. on pp. 3, 20).

[34] M. Pinarbasi and A. D. Kent, "Perspectives on spintronics technology development: Giant magnetoresistance to spin transfer torque magnetic random access memory", APL Materials **10**, 020901 (2022) (cit. on p. 3).

[35] G. D. Fuchs, N. C. Emley, I. N. Krivorotov, P. M. Braganca, E. M. Ryan, S. I. Kiselev, J. C. Sankey, D. C. Ralph, R. A. Buhrman, and J. A. Katine, "Spin-transfer effects in nanoscale magnetic tunnel junctions", Applied Physics Letters **85**, 1205–1207 (2004) (cit. on p. 3).

[36] Everspin Technologies Inc, *Everspin Announces MRAM Solution Designed into Lucid Air Luxury Electric Vehicles [Press release]*, 2021 (cit. on p. 3).

[37] S. S. Parkin, M. Hayashi, and L. Thomas, "Magnetic Domain-Wall Racetrack Memory", Science **320**, 190–194 (2008) (cit. on pp. 3, 15, 29, 42).

[38] K. Gu, Y. Guan, B. K. Hazra, H. Deniz, A. Migliorini, W. Zhang, and S. S. Parkin, "Three-dimensional racetrack memory devices designed from freestanding magnetic heterostructures", Nature Nanotechnology **17**, 1065–1071 (2022) (cit. on pp. 3, 29).

[39] S. Chen, J. Lourembam, P. Ho, A. K. J. Toh, J. Huang, X. Chen, H. K. Tan, S. L. K. Yap, R. J. J. Lim, H. R. Tan, T. S. Suraj, M. I. Sim, Y. T. Toh, I. Lim, N. C. B. Lim, J. Zhou, H. J. Chung, S. T. Lim, and A. Soumyanarayanan, "All-electrical skyrmionic magnetic tunnel junction", Nature **627**, 522–527 (2024) (cit. on pp. 3, 29, 30).

[40] B. Behin-Aein, D. Datta, S. Salahuddin, and S. Datta, "Proposal for an all-spin logic device with built-in memory", Nature Nanotechnology **5**, 266–270 (2010) (cit. on pp. 3, 29).

[41] D. Khokhriakov, S. Sayed, A. M. Hoque, B. Karpiak, B. Zhao, S. Datta, and S. P. Dash, "Multifunctional Spin Logic Operations in Graphene Spin Circuits", Physical Review Applied **18**, 064063 (2022) (cit. on pp. 3, 29, 39).

[42] Z. Luo, A. Hrabec, T. P. Dao, G. Sala, S. Finizio, J. Feng, S. Mayr, J. Raabe, P. Gambardella, and L. J. Heyderman, "Current-driven magnetic domain-wall logic", Nature **579**, 214–218 (2020) (cit. on pp. 3, 29).

[43] C. Safranski, J. Kaiser, P. Trouilloud, P. Hashemi, G. Hu, and J. Z. Sun, "Demonstration of Nanosecond Operation in Stochastic Magnetic Tunnel Junctions", Nano Letters **21**, 2040–2045 (2021) (cit. on pp. 3, 29).

[44] R. V. Ababei, M. O. Ellis, I. T. Vidamour, D. S. Devadasan, D. A. Allwood, E. Vasilaki, and T. J. Hayward, "Neuromorphic computation with a single magnetic domain wall", Scientific Reports **11**, 15587 (2021) (cit. on pp. 3, 29).

[45] S. Bunaiyan, S. Datta, and K. Y. Camsari, "Heisenberg machines with programmable spin circuits", Physical Review Applied **22**, 014014 (2024) (cit. on pp. 3, 29, 41).

[46] M. König, S. Wiedmann, C. Brüne, A. Roth, H. Buhmann, L. W. Molenkamp, X.-l. Qi, and S.-C. Zhang, "Quantum Spin Hall Insulator State in HgTe Quantum Wells", Science **318**, 766–771 (2007) (cit. on pp. 7, 11–13, 22).

[47] D. Hsieh, D. Qian, L. Wray, Y. Xia, Y. S. Hor, R. J. Cava, and M. Z. Hasan, "A topological Dirac insulator in a quantum spin Hall phase", Nature **452**, 970–974 (2008) (cit. on pp. 7, 12, 13).

[48] B. Bradlyn, L. Elcoro, J. Cano, M. G. Vergniory, Z. Wang, C. Felser, M. I. Aroyo, and B. A. Bernevig, "Topological quantum chemistry", Nature **547**, 298–305 (2017) (cit. on pp. 7, 10).

[49] M. G. Vergniory, B. J. Wieder, L. Elcoro, S. S. Parkin, C. Felser, B. A. Bernevig, and N. Regnault, "All topological bands of all nonmagnetic stoichiometric materials", Science **376**, eabg9094 (2022) (cit. on p. 7).

[50] U. Petralanda, Y. Jiang, B. A. Bernevig, N. Regnault, and L. Elcoro, "Two-dimensional Topological Quantum Chemistry and Catalog of Topological Materials", Science **393**, 1317–1322 (2026) (cit. on p. 7).

[51] The Royal Swedish Academy of Science, *Nobelpriset i fysik 2016 [Press release]*, 2016 (cit. on p. 7).

[52] J. J. Sakurai and J. Napolitano, *Modern Quantum Mechanics*, 3rd ed. (Cambridge University Press, Cambridge, UK, 2021) (cit. on p. 8).

[53] L. Liang, T. I. Vanhala, S. Peotta, T. Siro, A. Harju, and P. Törmä, "Band geometry, Berry curvature, and superfluid weight", Physical Review B **95**, 024515 (2017) (cit. on pp. 8, 9).

[54] P. Törmä, "Essay: Where Can Quantum Geometry Lead Us", Physical Review Letters **131**, 240001 (2023) (cit. on p. 8).

[55] J. Yu, B. A. Bernevig, R. Queiroz, E. Rossi, P. Törmä, and B.-J. Yang, "Quantum geometry in quantum materials", npj Quantum Materials **10**, 101 (2025) (cit. on p. 8).

[56] M. V. Berry, "The Quantum Phase, Five Years After", in *Geometric Phases in Physics*, edited by A. Shapere and F. Wilczek (World Scientific, Singapore, Singapore, 1989), pp. 7–28 (cit. on p. 9).

[57] M. V. Berry, "Quantal phase factors accompanying adiabatic changes", Proceedings of the Royal Society of London **392**, 45–57 (1984) (cit. on p. 9).

[58] B. Simon, "Holonomy, the quantum adiabatic theorem, and Berry's phase", Physical Review Letters **51**, 2167–2170 (1983) (cit. on p. 9).

[59] L. Fu and C. L. Kane, "Topological insulators with inversion symmetry", Physical Review B **76**, 045302 (2007) (cit. on pp. 9, 12).

[60] M.-C. Chang and Q. Niu, "Berry curvature, orbital moment, and effective quantum theory of electrons in electromagnetic fields", Journal of Physics Condensed Matter **20**, 193202 (2008) (cit. on p. 9).

[61] D. Xiao, M. C. Chang, and Q. Niu, "Berry phase effects on electronic properties", Reviews of Modern Physics **82**, 1959–2007 (2010) (cit. on pp. 9, 17).

[62] L. Šmejkal, Y. Mokrousov, B. Yan, and A. H. MacDonald, "Topological antiferromagnetic spintronics", Nature Physics **14**, 242–251 (2018) (cit. on p. 9).

[63] Z. Z. Du, H. Z. Lu, and X. C. Xie, "Nonlinear Hall effects", Nature Reviews Physics **3**, 744–752 (2021) (cit. on pp. 9, 26).

[64] M. Kang, S. Kim, Y. Qian, P. M. Neves, L. Ye, J. Jung, D. Puntel, F. Mazzola, S. Fang, C. Jozwiak, A. Bostwick, E. Rotenberg, J. Fuji, I. Vobornik, J. H. Park, J. G. Checkelsky, B. J. Yang, and R. Comin, "Measurements of the quantum geometric tensor in solids", Nature Physics **21**, 110–117 (2025) (cit. on p. 9).

[65] J. P. Provost and G Vallee, "Riemannian Structure on Manifolds of Quantum States", Communications in Mathematical Physics **76**, 289–301 (1980) (cit. on p. 9).

[66] N. Verma, P. J. W. Moll, T. Holder, and R. Queiroz, "Quantum geometry and the hidden scales in materials", Nature Reviews Physics **8**, 226–239 (2026) (cit. on pp. 9, 86).

[67] S. Kim, Y. Chung, Y. Qian, S. Park, C. Jozwiak, E. Rotenberg, A. Bostwick, K. S. Kim, and B.-J. Yang, "Direct measurement of the quantum metric tensor in solids", Science **388**, 1050–1054 (2025) (cit. on p. 9).

[68] C. Jin, S. Park, Y. Jeung, Y. Chung, and K. S. Kim, "Experimental measurements of the quantum metric", Nature Reviews Physics **8**, 192–194 (2026) (cit. on p. 9).

[69] A. Arora, J. I.-J. Wang, and T.-M. Chen, "Quantum geometry in condensed matter: Fundamentals and applications", Applied Physics Letters **129**, 130401 (2026) (cit. on p. 9).

[70] A. Gao et al., "Quantum metric nonlinear Hall effect in a topological antiferromagnetic heterostructure", Science **381**, 181–186 (2023) (cit. on pp. 9, 26, 85, 86, 98, 103).

[71] N. Wang, D. Kaplan, Z. Zhang, T. Holder, N. Cao, A. Wang, X. Zhou, F. Zhou, Z. Jiang, C. Zhang, S. Ru, H. Cai, K. Watanabe, T. Taniguchi, B. Yan, and W. Gao, "Quantum-metric-induced nonlinear transport in a topological antiferromagnet", Nature **621**, 487–492 (2023) (cit. on pp. 9, 26, 27, 85, 86, 98).

[72] H. Li, C. Zhang, C. Zhou, C. Ma, X. Lei, Z. Jin, H. He, B. Li, K. T. Law, and J. Wang, "Quantum geometry quadrupole-induced third-order nonlinear transport in antiferromagnetic topological insulator MnBi2Te4", Nature Communications **15**, 7779 (2024) (cit. on pp. 9, 26, 85, 86, 91, 98, 102, 104, 107, 108).

[73] P. Törmä, S. Peotta, and B. A. Bernevig, "Superconductivity, superfluidity and quantum geometry in twisted multilayer systems", Nature Reviews Physics **4**, 528–542 (2022) (cit. on pp. 9, 86).

[74] K. E. Huhtinen, J. Herzog-Arbeitman, A. Chew, B. A. Bernevig, and P. Törmä, "Revisiting flat band superconductivity: Dependence on minimal quantum metric and band touchings", Physical Review B **106**, 014518 (2022) (cit. on p. 9).

[75] J. W. Rhim, K. Kim, and B. J. Yang, "Quantum distance and anomalous Landau levels of flat bands", Nature **584**, 59–63 (2020) (cit. on p. 9).

[76] J. Han, T. Uchimura, Y. Araki, J. Y. Yoon, Y. Takeuchi, Y. Yamane, S. Kanai, J. Ieda, H. Ohno, and S. Fukami, "Room-temperature flexible manipulation of the quantum-metric structure in a topological chiral antiferromagnet", Nature Physics **20**, 1110–1117 (2024) (cit. on pp. 9, 26).

[77] J. Xiao and B. Yan, "First-principles calculations for topological quantum materials", Nature Reviews Physics **3**, 283–297 (2021) (cit. on pp. 10, 17, 64).

[78] N. Kumar, S. N. Guin, K. Manna, C. Shekhar, and C. Felser, "Topological Quantum Materials from the Viewpoint of Chemistry", Chemical Reviews **121**, 2780–2815 (2020) (cit. on pp. 10, 17).

[79] A. Anirban, "15 Years of Topological Insulators", Nature Reviews Physics **5**, 267 (2023) (cit. on p. 10).

[80] J. E. Moore, "The birth of topological insulators", Nature **464**, 194–198 (2010) (cit. on pp. 10–13).

[81] W. Shockley, "On the surface states associated with a periodic potential", Physical Review **56**, 317–323 (1939) (cit. on p. 10).

[82] B. J. Wieder, B. Bradlyn, J. Cano, Z. Wang, M. G. Vergniory, L. Elcoro, A. A. Soluyanov, C. Felser, T. Neupert, N. Regnault, and B. A. Bernevig, "Topological materials discovery from crystal symmetry", Nature Reviews Materials **7**, 196–216 (2022) (cit. on pp. 10, 12, 22).

[83] M. Z. Hasan and C. L. Kane, "Colloquium: Topological insulators", Reviews of Modern Physics **82**, 3045–3067 (2010) (cit. on pp. 10, 63).

[84] C. L. Kane and E. J. Mele, "Quantum spin Hall effect in graphene", Physical Review Letters **95**, 226801 (2005) (cit. on pp. 10–13).

[85] L. Fu, C. L. Kane, and E. J. Mele, "Topological insulators in three dimensions", Physical Review Letters **98**, 106803 (2007) (cit. on pp. 11, 12).

[86] Z. Ringel, Y. E. Kraus, and A. Stern, "Strong side of weak topological insulators", Physical Review B **86**, 045102 (2012) (cit. on p. 11).

[87] C. L. Kane and E. J. Mele, "Z2 topological order and the quantum spin Hall effect", Physical Review Letters **95**, 146802 (2005) (cit. on p. 11).

[88] Y. Yao, F. Ye, X. L. Qi, S. C. Zhang, and Z. Fang, "Spin-orbit gap of graphene: First-principles calculations", Physical Review B **75**, 041401(R) (2007) (cit. on p. 11).

[89] S. Konschuh, M. Gmitra, and J. Fabian, "Tight-binding theory of the spin-orbit coupling in graphene", Physical Review B **82**, 245412 (2010) (cit. on p. 11).

[90] B. A. Bernevig, T. L. Hughes, and S.-C. Zhang, "Quantum Spin Hall Effect and Topological Phase Transition in HgTe Quantum Wells", Science **314**, 1757–1761 (2006) (cit. on p. 11).

[91] K. von Klitzing, G. Dorda, and M. Pepper, "New method for high-accuracy determination of the fine-structure constant based on quantized hall resistance", Physical Review Letters **45**, 494–497 (1980) (cit. on pp. 11, 22).

[92] B. A. Bernevig and S. C. Zhang, "Quantum spin Hall effect", Physical Review Letters **96**, 106802 (2006) (cit. on p. 12).

[93] D. Culcer, A. Cem Keser, Y. Li, and G. Tkachov, "Transport in two-dimensional topological materials: recent developments in experiment and theory", 2D Materials **7**, 022007 (2020) (cit. on p. 13).

[94] Y. L. Chen, J. G. Analytis, J.-H. Chu, Z. K. Liu, S.-K. Mo, X. L. Qi, H. J. Zhang, D. H. Lu, X Dai, Z Fang, S. C. Zhang, I. R. Fisher, Z Hussain, and Z.-X. Shen, "Experimental Realization of a Three-Dimensional Topological Insulator, Bi2Te3", Science **325**, 5937 (2009) (cit. on pp. 12, 13).

[95] Y. Xia, D. Qian, D. Hsieh, L. Wray, A. Pal, H. Lin, A. Bansil, D. Grauer, Y. S. Hor, R. J. Cava, and M. Z. Hasan, "Observation of a large-gap topological-insulator class with a single Dirac cone on the surface", Nature Physics **5**, 398–402 (2009) (cit. on pp. 12, 13).

[96] D. Hsieh, Y. Xia, D. Qian, L. Wray, J. H. Dil, F. Meier, J. Osterwalder, L. Patthey, J. G. Checkelsky, N. P. Ong, A. V. Fedorov, H. Lin, A. Bansil, D. Grauer, Y. S. Hor, R. J. Cava, and M. Z. Hasan, "A tunable topological insulator in the spin helical Dirac transport regime", Nature **460**, 1101–1105 (2009) (cit. on pp. 12, 13).

[97] J. E. Moore and L. Balents, "Topological invariants of time-reversal-invariant band structures", Physical Review B **75**, 121306(R) (2007) (cit. on p. 12).

[98] S. Murakami, "Phase transition between the quantum spin Hall and insulator phases in 3D: emergence of a topological gapless phase", New Journal of Physics **9**, 356 (2007) (cit. on p. 12).

[99] X.-L. Qi, T. L. Hughes, and S.-C. Zhang, "Topological field theory of time-reversal invariant insulators", Physical Review B **78**, 195424 (2008) (cit. on pp. 12, 23).

[100] R. Roy, "Topological phases and the quantum spin Hall effect in three dimensions", Physical Review B **79**, 195322 (2009) (cit. on p. 12).

[101] D. Hsieh, Y. Xia, L. Wray, D. Qian, A. Pal, J. H. Dil, J. Osterwalder, F. Meier, G. Bihlmayer, C. L. Kane, Y. S. Hor, R. J. Cava, and M. Z. Hasan, "Observation of unconventional quantum spin textures in topological insulators", Science **323**, 919–922 (2009) (cit. on p. 12).

[102] H. Zhang, C. X. Liu, X. L. Qi, X. Dai, Z. Fang, and S.-C. Zhang, "Topological insulators in Bi2Se3, Bi2Te3 and Sb2Te3 with a single Dirac cone on the surface", Nature Physics **5**, 438–442 (2009) (cit. on p. 12).

[103] D. Hsieh, Y. Xia, D. Qian, L. Wray, F. Meier, J. H. Dil, J. Osterwalder, L. Patthey, A. V. Fedorov, H. Lin, A. Bansil, D. Grauer, Y. S. Hor, R. J. Cava, and M. Z. Hasan, "Observation of time-reversal-protected single-Dirac-cone topological-insulator states in Bi2Te3 and Sb2Te3", Physical Review Letters **103**, 146401 (2009) (cit. on p. 12).

[104] Z. Ren, A. A. Taskin, S. Sasaki, K. Segawa, and Y. Ando, "Optimizing Bi2-xSbxTe3-ySey solid solutions to approach the intrinsic topological insulator regime", Physical Review B **84**, 165311 (2011) (cit. on pp. 12, 65).

[105] B. Xia, P. Ren, A. Sulaev, P. Liu, S. Q. Shen, and L. Wang, "Indications of surface-dominated transport in single crystalline nanoflake devices of topological insulator Bi1.5Sb0.5Te1.8Se1.2", Physical Review B **87**, 085442 (2013) (cit. on pp. 12, 65).

[106] Y. Pan, D. Wu, J. R. Angevaare, H. Luigjes, E. Frantzeskakis, N. De Jong, E. Van Heumen, T. V. Bay, B. Zwartsenberg, Y. K. Huang, M. Snelder, A. Brinkman, M. S. Golden, and A. de Visser, "Low carrier concentration crystals of the topological insulator Bi2-xSbxTe3-ySey: A magnetotransport study", New Journal of Physics **16**, 123035 (2014) (cit. on pp. 12, 65).

[107] K. B. Han, S. K. Chong, A. O. Oliynyk, A. Nagaoka, S. Petryk, M. A. Scarpulla, V. V. Deshpande, and T. D. Sparks, "Enhancement in surface mobility and quantum transport of Bi2-xSbxTe3-ySey topological insulator by controlling the crystal growth conditions", Scientific Reports **8**, 17290 (2018) (cit. on pp. 12, 65).

[108] S. Cai, J. Guo, V. A. Sidorov, Y. Zhou, H. Wang, G. Lin, X. Li, Y. Li, K. Yang, A. Li, Q. Wu, J. Hu, S. K. Kushwaha, R. J. Cava, and L. Sun, "Independence of topological surface state and bulk conductance in three-dimensional topological insulators", npj Quantum Materials **3**, 62 (2018) (cit. on pp. 12, 65).

[109] B. Irfan, A. Dankert, P. Bhasker, D. Khokhriakov, S. P. Dash, and R. Chatterjee, "Surface dominated magnetotransport in Bi2Te2.15Se0.85 topological insulator", Journal of Applied Physics **124**, 214302 (2018) (cit. on pp. 12, 65).

[110] G. M. Stephen, O. A. Vail, J. Lu, W. A. Beck, P. J. Taylor, and A. L. Friedman, "Weak Antilocalization and Anisotropic Magnetoresistance as a Probe of Surface States in Topological Bi2TexSe3-x Thin Films", Scientific Reports **10**, 4845 (2020) (cit. on pp. 12, 65).

[111] A. Johansson, "Theory of spin and orbital Edelstein effects", Journal of Physics: Condensed Matter **36**, 423002 (2024) (cit. on pp. 13, 14, 20).

[112] V. M. Edelstein, "Spin polarization of conduction electrons induced by electric current in two-dimensional asymmetric electron systems", Solid State Communications **73**, 233–235 (1990) (cit. on p. 13).

[113] L. Onsager, "Reciprocal Relations in Irreversible Processes. I.", Physical Review **37**, 405–426 (1931) (cit. on pp. 14, 73, 78).

[114] F Bottegoni, C Zucchetti, G Isella, M Bollani, M Finazzi, and F Ciccacci, "Spin-charge interconversion in heterostructures based on group-IV semiconductors", La Rivista del Nuovo Cimento **43**, 45–96 (2020) (cit. on p. 14).

[115] J. C. Rojas-Sánchez, S. Oyarzún, Y. Fu, A. Marty, C. Vergnaud, S. Gambarelli, L. Vila, M. Jamet, Y. Ohtsubo, A. Taleb-Ibrahimi, P. Le Fèvre, F. Bertran, N. Reyren, J. M. George, and A. Fert, "Spin to Charge Conversion at Room Temperature by Spin Pumping into a New Type of Topological Insulator: α-Sn Films", Physical Review Letters **116**, 096602 (2016) (cit. on p. 14).

[116] W. Chen, "Edelstein and inverse Edelstein effects caused by the pristine surface states of topological insulators", Journal of Physics: Condensed Matter **32**, 035809 (2020) (cit. on p. 14).

[117] A. Manchon, H. C. Koo, J. Nitta, S. M. Frolov, and R. A. Duine, "New perspectives for Rashba spin-orbit coupling", Nature Materials **14**, 871–882 (2015) (cit. on pp. 14, 15).

[118] Y. A. Bychkov and E. I. Rashba, "Properties of a 2D electron gas with lifted spectral degeneracy", JETP Letters **39**, 66–69 (1984) (cit. on p. 14).

[119] S. D. Ganichev, E. L. Ivchenko, V. V. Bel'kov, S. A. Tarasenko, M Sollinger, D Weiss, W Wegscheider, and W Prettl, "Spin-galvanic effect", Nature **417**, 153–156 (2002) (cit. on p. 14).

[120] A. Johansson, J. Henk, and I. Mertig, "Theoretical aspects of the Edelstein effect for anisotropic two-dimensional electron gas and topological insulators", Physical Review B **93**, 195440 (2016) (cit. on p. 15).

[121] E. H. Hall, "On a New Action of the Magnet on Electric Currents", American Journal of Mathematics **2**, 287–292 (1879) (cit. on pp. 15, 22).

[122] J. Sinova, S. O. Valenzuela, J. Wunderlich, C. H. Back, and T. Jungwirth, "Spin Hall effects", Reviews of Modern Physics **87**, 1213–1260 (2015) (cit. on pp. 15, 65, 69, 75).

[123] N. F. Mott, "The Scattering of Fast Electrons by Atomic Nuclei", Proceedings of the Royal Society A **124**, 425–442 (1929) (cit. on p. 15).

[124] M. I. D'yakonov and V. I. Perel', "Possibility of Orienting Electron Spins with Current", Soviet Physics JETP Letters **13**, 467–469 (1971) (cit. on p. 15).

[125] Y. K. Kato, R. C. Myers, A. C. Gossard, and D. D. Awschalom, "Observation of the spin Hall effect in semiconductors", Science **306**, 1910–1913 (2004) (cit. on pp. 15, 22).

[126] S. Murakami, N. Nagaosa, and S.-c. Zhang, "Dissipationless Quantum Spin Current at Room Temperature", Science **301**, 1348–1351 (2003) (cit. on p. 15).

[127] J. Sinova, D. Culcer, Q. Niu, N. A. Sinitsyn, T. Jungwirth, and A. H. MacDonald, "Universal intrinsic spin Hall effect", Physical Review Letters **92**, 126603 (2004) (cit. on p. 15).

[128] J. Wunderlich, B. Kaestner, J. Sinova, and T. Jungwirth, "Experimental observation of the spin-Hall effect in a two-dimensional spin-orbit coupled semiconductor system", Physical Review Letters **94**, 047204 (2005) (cit. on p. 15).

[129] T. Fujita, M. B. Jalil, and S. G. Tan, "Unified description of intrinsic spin-Hall effect mechanisms", New Journal of Physics **12**, 013016 (2010) (cit. on p. 15).

[130] J. E. Hirsch, "Spin Hall effect", Physical Review Letters **83**, 1834–1837 (1999) (cit. on p. 15).

[131] M. G. Samant and S. S. Parkin, "Magnetic tunnel junctions - principles and applications", Vacuum **74**, 705–709 (2004) (cit. on p. 15).

[132] M. Julliere, "Tunneling between ferromagnetic films", Physics Letters A **54**, 225–226 (1975) (cit. on p. 15).

[133] J. S. Moodera, L. R. Kinder, T. M. Wong, and R. Meservey, "Large magnetoresistance at room temperature in ferromagnetic thin film tunnel junctions", Physical Review Letters **74**, 3273–3276 (1995) (cit. on p. 15).

[134] T. Miyazaki and N. Tezuka, "Giant magnetic tunneling effect in Fe/Al2O3/Fe junction", Journal of Magnetism and Magnetic Materials **139**, L231–L234 (1995) (cit. on p. 15).

[135] D. C. Ralph and M. D. Stiles, "Spin transfer torques", Journal of Magnetism and Magnetic Materials **320**, 1190–1216 (2008) (cit. on p. 15).

[136] J. C. Slonczewski, "Current-driven excitation of magnetic multilayers", Journal of Magnetism and Magnetic Materials **159**, L1–L7 (1996) (cit. on p. 15).

[137] L Berger, "Emission of spin waves by a magnetic multilayer traversed by a current", Physical Review B **54**, 9353–9358 (1996) (cit. on p. 15).

[138] X. Qiu, Z. Shi, W. Fan, S. Zhou, and H. Yang, "Characterization and Manipulation of Spin Orbit Torque in Magnetic Heterostructures", Advanced Materials **30**, 1705699 (2018) (cit. on p. 15).

[139] Y. Wang and H. Yang, "Spin-Orbit Torques Based on Topological Materials", Accounts of Materials Research **3**, 1061–1072 (2022) (cit. on pp. 15, 16, 20).

[140] M. Bibes, O. Gomonay, T. Kuschel, J. Sinova, M. Weiler, S. Fukami, and M. Kläui, "Applied spintronics: From spin transport to spin-charge interconversion and emerging devices", Science Advances **12**, eaeh2967 (2026) (cit. on pp. 15, 20).

[141] R. Ramaswamy, J. M. Lee, K. Cai, and H. Yang, "Recent advances in spin-orbit torques: Moving towards device applications", Applied Physics Reviews **5**, 031107 (2018) (cit. on p. 15).

[142] X. Han, C. Wan, and G. Yu, "Materials, physics, and devices of spin-orbit torque effect", Applied Physics Letters **118**, 180401 (2021) (cit. on p. 15).

[143] Q. Shao, P. Li, L. Liu, H. Yang, S. Fukami, A. Razavi, H. Wu, K. Wang, F. Freimuth, Y. Mokrousov, M. D. Stiles, S. Emori, A. Hoffmann, J. Åkerman, K. Roy, J.-P. Wang, S.-H. Yang, K. Garello, and W. Zhang, "Roadmap of spin-orbit torques", IEEE Transactions on Magnetics **57**, 800439 (2021) (cit. on pp. 15, 16, 20).

[144] G. Ji, Y. Zhang, Y. Chai, and T. Nan, "Recent progress on controlling spin-orbit torques by materials design", npj Spintronics **2**, 56 (2024) (cit. on p. 15).

[145] J. C. Jeon, A. Migliorini, J. Yoon, J. Jeong, and S. S. Parkin, "Multicore memristor from electrically readable nanoscopic racetracks", Science **386**, 315–322 (2024) (cit. on pp. 15, 29, 30).

[146] S. Jiang, L. Yao, S. Wang, D. Wang, L. Liu, A. Kumar, A. A. Awad, A. Litvinenko, M. Ahlberg, R. Khymyn, S. Chung, G. Xing, and J. Åkerman, "Spin-torque nano-oscillators and their applications", Applied Physics Reviews **11**, 041309 (2024) (cit. on p. 15).

[147] M. Khademi, A. Kumar, M. Rajabali, S. P. Dash, and J. Åkerman, "Large Non-Volatile Frequency Tuning of Spin Hall Nano-Oscillators Using Circular Memristive Nano-Gates", IEEE Electron Device Letters **45**, 268–271 (2024) (cit. on p. 15).

[148] J. Grollier, D. Querlioz, K. Y. Camsari, K. Everschor-Sitte, S. Fukami, and M. D. Stiles, "Neuromorphic spintronics", Nature Electronics **3**, 360–370 (2020) (cit. on p. 16).

[149] J. Zhou and J. Chen, "Prospect of Spintronics in Neuromorphic Computing", Advanced Electronic Materials **7**, 2100465 (2021) (cit. on p. 16).

[150] M. A. Khan, J. Sun, B. Li, A. Przybysz, and J. Kosel, "Magnetic sensors - A review and recent technologies", Engineering Research Express **3**, 022005 (2021) (cit. on p. 16).

[151] R. Li, S. Zhang, S. Luo, Z. Guo, Y. Xu, J. Ouyang, M. Song, Q. Zou, L. Xi, X. Yang, J. Hong, and L. You, "A spin-orbit torque device for sensing three-dimensional magnetic fields", Nature Electronics **4**, 179–184 (2021) (cit. on p. 16).

[152] J. Han and L. Liu, "Topological insulators for efficient spin-orbit torques", APL Materials **9**, 060901 (2021) (cit. on pp. 16, 27).

[153] A. Hoffmann and S. D. Bader, "Opportunities at the frontiers of spintronics", Physical Review Applied **4**, 047001 (2015) (cit. on p. 16).

[154] F. Bonell, M. Goto, G. Sauthier, J. F. Sierra, A. I. Figueroa, M. V. Costache, S. Miwa, Y. Suzuki, and S. O. Valenzuela, "Control of Spin-Orbit Torques by Interface Engineering in Topological Insulator Heterostructures", Nano Letters **20**, 5893–5899 (2020) (cit. on p. 16).

[155] T. Guillet, R. Galceran, J. F. Sierra, F. J. Belarre, B. Ballesteros, M. V. Costache, D. Dosenovic, H. Okuno, A. Marty, M. Jamet, F. Bonell, and S. O. Valenzuela, "Spin-Orbit Torques and Magnetization Switching in (Bi,Sb)2Te3/Fe3GeTe2 Heterostructures Grown by Molecular Beam Epitaxy", Nano Letters **24**, 822–828 (2024) (cit. on p. 16).

[156] A. R. Mellnik, J. S. Lee, A. Richardella, J. L. Grab, P. J. Mintun, M. H. Fischer, A. Vaezi, A. Manchon, E. A. Kim, N. Samarth, and D. C. Ralph, "Spin-transfer torque generated by a topological insulator", Nature **511**, 449–451 (2014) (cit. on pp. 16, 63).

[157] Y. Fan, P. Upadhyaya, X. Kou, M. Lang, S. Takei, Z. Wang, J. Tang, L. He, L. T. Chang, M. Montazeri, G. Yu, W. Jiang, T. Nie, R. N. Schwartz, Y. Tserkovnyak, and K. L. Wang, "Magnetization switching through giant spin-orbit torque in a magnetically doped topological insulator heterostructure", Nature Materials **13**, 699–704 (2014) (cit. on pp. 16, 27).

[158] N. H. D. Khang, Y. Ueda, and P. N. Hai, "A conductive topological insulator with large spin Hall effect for ultralow power spin-orbit torque switching", Nature Materials **17**, 808–813 (2018) (cit. on pp. 16, 63).

[159] M. DC, R. Grassi, J. Y. Chen, M. Jamali, D. Reifsnyder Hickey, D. Zhang, Z. Zhao, H. Li, P. Quarterman, Y. Lv, M. Li, A. Manchon, K. A. Mkhoyan, T. Low, and J. P. Wang, "Room-temperature high spin–orbit torque due to quantum confinement in sputtered BixSe(1-x) films", Nature Materials **17**, 800–807 (2018) (cit. on pp. 16, 63).

[160] H. Wu, P. Zhang, P. Deng, Q. Lan, Q. Pan, S. A. Razavi, X. Che, L. Huang, B. Dai, K. Wong, X. Han, and K. L. Wang, "Room-Temperature Spin-Orbit Torque from Topological Surface States", Physical Review Letters **123**, 207205 (2019) (cit. on p. 16).

[161] M. Mogi, K. Yasuda, R. Fujimura, R. Yoshimi, N. Ogawa, A. Tsukazaki, M. Kawamura, K. S. Takahashi, M. Kawasaki, and Y. Tokura, "Current-induced switching of proximity-induced ferromagnetic surface states in a topological insulator", Nature Communications **12**, 1404 (2021) (cit. on p. 16).

[162] H. Wu, A. Chen, P. Zhang, H. He, J. Nance, C. Guo, J. Sasaki, T. Shirokura, P. N. Hai, B. Fang, S. A. Razavi, K. Wong, Y. Wen, Y. Ma, G. Yu, G. P. Carman, X. Han, X. Zhang, and K. L. Wang, "Magnetic memory driven by topological insulators", Nature Communications **12**, 6251 (2021) (cit. on pp. 16, 63).

[163] M. Lohmann, D. Wickramaratne, J. Moon, M. Noyan, H.-J. Chuang, B. T. Jonker, and C. H. Li, "Highly Efficient Spin-Orbit Torque Switching in Bi2Se3/Fe3GeTe2 van der Waals Heterostructures", ACS Nano **18**, 680–690 (2024) (cit. on p. 16).

[164] C. H. Li, O. M. van't Erve, J. T. Robinson, Y. Liu, L. Li, and B. T. Jonker, "Electrical detection of charge-current-induced spin polarization due to spin-momentum locking in Bi2Se3", Nature Nanotechnology **9**, 218–224 (2014) (cit. on pp. 16, 63).

[165] J. Tang, L.-t. Chang, X. Kou, K. Murata, E. S. Choi, M. Lang, Y. Fan, Y. Jiang, M. Montazeri, W. Jiang, Y. Wang, L. He, and K. L. Wang, "Electrical Detection of Spin-Polarized Conduction in (Bi0.53Sb0.47)2Te3 Topological Insulator", Nano Letters **14**, 5423–5429 (2014) (cit. on pp. 16, 63).

[166] Y. Ando, T. Hamasaki, T. Kurokawa, K. Ichiba, F. Yang, M. Novak, S. Sasaki, K. Segawa, Y. Ando, and M. Shiraishi, "Electrical Detection of the Spin Polarization Due to Charge Flow in the Surface State of the Topological Insulator Bi1.5Sb0.5Te1.7Se1.3", Nano Letters **14**, 6226–6230 (2014) (cit. on pp. 16, 63).

[167] C. H. Li, O. M. van't Erve, Y. Y. Li, L. Li, and B. T. Jonker, "Electrical Detection of the Helical Spin Texture in a p-type Topological Insulator Sb2 Te3", Scientific Reports **6**, 29533 (2016) (cit. on p. 16).

[168] C. H. Li, O. M. Vant Erve, S. Rajput, L. Li, and B. T. Jonker, "Direct comparison of current-induced spin polarization in topological insulator Bi2Se3 and InAs Rashba states", Nature Communications **7**, 13518 (2016) (cit. on pp. 16, 63).

[169] A. Dankert, P. Bhaskar, D. Khokhriakov, I. H. Rodrigues, B. Karpiak, M Venkata Kamalakar, S. Charpentier, I. Garate, and S. P. Dash, "Origin and evolution of surface spin current in topological insulators", Physical Review B **97**, 125414 (2018) (cit. on pp. 16, 29, 63, 65, 73).

[170] J. A. Voerman, C. Li, Y. Huang, and A. Brinkman, "Spin-Momentum Locking in the Gate Tunable Topological Insulator BiSbTeSe2 in Non-Local Transport Measurements", Advanced Electronic Materials **5**, 1900334 (2019) (cit. on pp. 16, 63).

[171] A. Dankert, J. Geurs, M. V. Kamalakar, S. Charpentier, and S. P. Dash, "Room temperature electrical detection of spin polarized currents in topological insulators", Nano Letters **15**, 7976–7981 (2015) (cit. on pp. 16, 29, 63).

[172] D. Khokhriakov, A. W. Cummings, K. Song, M. Vila, B. Karpiak, A. Dankert, S. Roche, and S. P. Dash, "Tailoring emergent spin phenomena in Dirac material heterostructures", Science Advances **4**, 9349 (2018) (cit. on pp. 16, 29, 71, 72, 83).

[173] D. Khokhriakov, A. M. Hoque, B. Karpiak, and S. P. Dash, "Gate-tunable spin-galvanic effect in graphene-topological insulator van der Waals heterostructures at room temperature", Nature Communications **11**, 3657 (2020) (cit. on pp. 16, 29, 69, 71–73).

[174] K. Vaklinova, A. Hoyer, M. Burghard, and K. Kern, "Current-Induced Spin Polarization in Topological Insulator-Graphene Heterostructures", Nano Letters **16**, 2595–2602 (2016) (cit. on pp. 16, 63, 68).

[175] S. Rao, "Weyl Semi-Metals: A Short Review", Journal of the Indian Institute of Science **96**, 145–156 (2016) (cit. on p. 17).

[176] H. Weyl, "Elektron und Gravitation. I.", Zeitschrift für Physik **56**, 330–352 (1929) (cit. on p. 17).

[177] Y. Sun, S.-C. Wu, and B. Yan, "Topological surface states and Fermi arcs of the noncentrosymmetric Weyl semimetals TaAs, TaP, NbAs, and NbP", Physical Review B **92**, 115428 (2015) (cit. on p. 17).

[178] B. Singh, H. Lin, and A. Bansil, "Topology and Symmetry in Quantum Materials", Advanced Materials **35**, 2201058 (2023) (cit. on p. 17).

[179] P. Hosur and X. Qi, "Recent developments in transport phenomena in Weyl semimetals", Comptes Rendus Physique **14**, 857–870 (2013) (cit. on pp. 17, 19, 64).

[180] H. B. Nielsen and M. Ninomiya, "A no-go theorem for regularizing chiral fermions", Physics Letters B **105**, 219–223 (1981) (cit. on p. 17).

[181] H. Gao, J. W. Venderbos, Y. Kim, and A. M. Rappe, "Topological Semimetals from First Principles", Annual Review of Materials Research **49**, 153–183 (2019) (cit. on pp. 17, 18).

[182] H. Inoue, "Observation of Surface Fermi Arcs in Weyl Semimetal via Scanning Tunneling Microscopy", Vacuum and Surface Science **61**, 669–674 (2018) (cit. on p. 18).

[183] X. Wan, A. M. Turner, A. Vishwanath, and S. Y. Savrasov, "Topological semimetal and Fermi-arc surface states in the electronic structure of pyrochlore iridates", Physical Review B **83**, 205101 (2011) (cit. on pp. 17, 18).

[184] O. Vafek and A. Vishwanath, "Dirac fermions in solids: From high-Tc cuprates and graphene to topological insulators and Weyl semimetals", Annual Review of Condensed Matter Physics **5**, 83–112 (2014) (cit. on pp. 17, 19, 20, 75).

[185] S.-Y. Xu, C. Liu, S. K. Kushwaha, R. Sankar, J. W. Krizan, I. Belopolski, M. Neupane, G. Bian, N. Alidoust, T.-R. Chang, H.-T. Jeng, C.-Y. Huang, W.-F. Tsai, H. Lin, P. P. Shibayev, F.-C. Chou, R. J. Cava, and M. Z. Hasan, "Observation of Fermi arc surface states in a topological metal", Science **347**, 294–299 (2015) (cit. on p. 17).

[186] P. Li, W. Wu, Y. Wen, C. Zhang, J. Zhang, S. Zhang, Z. Yu, S. A. Yang, A. Manchon, and X. x. Zhang, "Spin-momentum locking and spin-orbit torques in magnetic nano-heterojunctions composed of Weyl semimetal WTe2", Nature Communications **9**, 3990 (2018) (cit. on pp. 17, 20, 64).

[187] B. C. Lin, S. Wang, A. Q. Wang, Y. Li, R. R. Li, K. Xia, D. Yu, and Z. M. Liao, "Electric Control of Fermi Arc Spin Transport in Individual Topological Semimetal Nanowires", Physical Review Letters **124**, 116802 (2020) (cit. on p. 17).

[188] B. Yan and C. Felser, "Topological materials: Weyl semimetals", Annual Review of Condensed Matter Physics **8**, 337–354 (2017) (cit. on pp. 17, 18, 20).

[189] A. A. Soluyanov, D. Gresch, Z. Wang, Q. Wu, M. Troyer, X. Dai, and B. A. Bernevig, "Type-II Weyl semimetals", Nature **527**, 495–498 (2015) (cit. on p. 18).

[190] Z. Z. Alisultanov, "The induced by an electromagnetic field coexistence of types I and II spectra in Weyl semimetals", Scientific Reports **8**, 13707 (2018) (cit. on p. 18).

[191] G. Xu, H. Weng, Z. Wang, X. Dai, and Z. Fang, "Chern semimetal and the quantized anomalous Hall effect in HgCr2Se4", Physical Review Letters **107**, 186806 (2011) (cit. on p. 18).

[192] A. A. Burkov and L. Balents, "Weyl semimetal in a topological insulator multilayer", Physical Review Letters **107**, 127205 (2011) (cit. on p. 18).

[193] B. Q. Lv, H. M. Weng, B. B. Fu, X. P. Wang, H. Miao, J. Ma, P. Richard, X. C. Huang, L. X. Zhao, G. F. Chen, Z. Fang, X. Dai, T. Qian, and H. Ding, "Experimental discovery of Weyl semimetal TaAs", Physical Review X **5**, 031013 (2015) (cit. on p. 18).

[194] S.-Y. Xu et al., "Discovery of a Weyl fermion semimetal and topological Fermi arcs", Science **349**, 613–617 (2015) (cit. on pp. 18, 19).

[195] L. X. Yang, Z. K. Liu, Y. Sun, H. Peng, H. F. Yang, T. Zhang, B. Zhou, Y. Zhang, Y. F. Guo, M. Rahn, D. Prabhakaran, Z. Hussain, S. K. Mo, C. Felser, B. Yan, and Y. L. Chen, "Weyl semimetal phase in the non-centrosymmetric compound TaAs", Nature Physics **11**, 728–732 (2015) (cit. on p. 18).

[196] H. Weng, C. Fang, Z. Fang, B. Andrei Bernevig, and X. Dai, "Weyl semimetal phase in noncentrosymmetric transition-metal monophosphides", Physical Review X **5**, 011029 (2015) (cit. on p. 18).

[197] S.-M. Huang, S.-Y. Xu, I. Belopolski, C.-C. Lee, G. Chang, B. Wang, N. Alidoust, G. Bian, M. Neupane, C. Zhang, S. Jia, A. Bansil, H. Lin, and M. Z. Hasan, "A Weyl Fermion semimetal with surface Fermi arcs in the transition metal monopnictide TaAs class", Nature Communications **6**, 7373 (2015) (cit. on p. 18).

[198] S.-Y. Xu et al., "Experimental discovery of a topological Weyl semimetal state in TaP", Science Advances **1**, e1501092 (2015) (cit. on p. 18).

[199] D.-F. Xu, Y.-P. Du, Z. Wang, Y.-P. Li, X.-H. Niu, Q. Yao, D. Pavel, Z.-A. Xu, X.-G. Wan, and D.-L. Feng, "Observation of Fermi Arcs in Non-Centrosymmetric Weyl Semi-Metal Candidate NbP", Chinese Physics Letters **32**, 107101 (2015) (cit. on p. 18).

[200] Y. Sun, S.-C. Wu, M. N. Ali, C. Felser, and B. Yan, "Prediction of Weyl semimetal in orthorhombic MoTe2", Physical Review B **92**, 161107(R) (2015) (cit. on p. 18).

[201] Y. Wu, D. Mou, N. H. Jo, K. Sun, L. Huang, S. L. Bud'Ko, P. C. Canfield, and A. Kaminski, "Observation of Fermi arcs in the type-II Weyl semimetal candidate WTe2", Physical Review B **94**, 121113(R) (2016) (cit. on p. 18).

[202] C. Wang et al., "Observation of Fermi arc and its connection with bulk states in the candidate type-II Weyl semimetal WTe2", Physical Review B **94**, 241119(R) (2016) (cit. on p. 18).

[203] L. Huang, T. M. McCormick, M. Ochi, Z. Zhao, M. T. Suzuki, R. Arita, Y. Wu, D. Mou, H. Cao, J. Yan, N. Trivedi, and A. Kaminski, "Spectroscopic evidence for a type II Weyl semimetallic state in MoTe2", Nature Materials **15**, 1155–1160 (2016) (cit. on p. 18).

[204] K. Deng, G. Wan, P. Deng, K. Zhang, S. Ding, E. Wang, M. Yan, H. Huang, H. Zhang, Z. Xu, J. Denlinger, A. Fedorov, H. Yang, W. Duan, H. Yao, Y. Wu, S. Fan, H. Zhang, X. Chen, and S. Zhou, "Experimental observation of topological Fermi arcs in type-II Weyl semimetal MoTe2", Nature Physics **12**, 1105–1110 (2016) (cit. on p. 18).

[205] J. Jiang, Z. K. Liu, Y. Sun, H. F. Yang, C. R. Rajamathi, Y. P. Qi, L. X. Yang, C. Chen, H. Peng, C. C. Hwang, S. Z. Sun, S. K. Mo, I. Vobornik, J. Fujii, S. S. Parkin, C. Felser, B. H. Yan, and Y. L. Chen, "Signature of type-II Weyl semimetal phase in MoTe2", Nature Communications **8**, 13973 (2017) (cit. on p. 18).

[206] K. Koepernik, D. Kasinathan, D. V. Efremov, S. Khim, S. Borisenko, B. Büchner, and J. van den Brink, "TaIrTe4: A ternary type-II Weyl semimetal", Physical Review B **93**, 201101(R) (2016) (cit. on pp. 18, 64).

[207] E. Haubold, K. Koepernik, D. Efremov, S. Khim, A. Fedorov, Y. Kushnirenko, J. Van Den Brink, S. Wurmehl, B. Büchner, T. K. Kim, M. Hoesch, K. Sumida, K. Taguchi, T. Yoshikawa, A. Kimura, T. Okuda, and S. V. Borisenko, "Experimental realization of type-II Weyl state in noncentrosymmetric TaIrTe4", Physical Review B **95**, 241108(R) (2017) (cit. on pp. 18, 64, 75).

[208] E. H. da Silva Neto, ""Weyl"ing away time-reversal symmetry", Science **365**, 1248–1249 (2019) (cit. on p. 18).

[209] I. Belopolski et al., "Discovery of topological Weyl fermion lines and drumhead surface states in a room temperature magnet", Science **365**, 1278–1281 (2019) (cit. on p. 18).

[210] D. F. Liu, A. J. Liang, E. K. Liu, Q. N. Xu, Y. W. Li, C. Chen, D. Pei, W. J. Shi, S. K. Mo, P. Dudin, T. Kim, C. Cacho, G. Li, Y. Sun, L. X. Yang, Z. K. Liu, S. S. Parkin, C. Felser, and Y. L. Chen, "Magnetic Weyl semimetal phase in a Kagomé crystal", Science **365**, 1282–1285 (2019) (cit. on p. 18).

[211] N. Morali, R. Batabyal, P. Kumar Nag, E. Liu, Q. Xu, Y. Sun, B. Yan, C. Felser, N. Avraham, and H. Beidenkopf, "Fermi-arc diversity on surface terminations of the magnetic Weyl semimetal Co3Sn2S2", Science **365**, 1286–1291 (2019) (cit. on p. 18).

[212] M. Z. Hasan, S. Y. Xu, I. Belopolski, and S. M. Huang, "Discovery of Weyl fermion semimetals and topological Fermi arc states", Annual Review of Condensed Matter Physics **8**, 289–309 (2017) (cit. on p. 19).

[213] A. C. Niemann, J. Gooth, S. C. Wu, S. Bäßler, P. Sergelius, R. Hühne, B. Rellinghaus, C. Shekhar, V. Süß, M. Schmidt, C. Felser, B. Yan, and K. Nielsch, "Chiral magnetoresistance in the Weyl semimetal NbP", Scientific Reports **7**, 43394 (2017) (cit. on pp. 19, 20).

[214] L. Bainsla, B. Zhao, N. Behera, A. M. Hoque, L. Sjöström, A. Martinelli, M. Abdel-Hafiez, J. Åkerman, and S. P. Dash, "Large out-of-plane spin-orbit torque in topological Weyl semimetal TaIrTe4", Nature Communications **15**, 4649 (2024) (cit. on pp. 19, 20, 29, 64).

[215] L. Pandey, B. Zhao, K. Tenzin, R. Ngaloy, V. Lamparská, H. Bangar, A. Ali, M. Abdel-Hafiez, G. Zhang, H. Wu, H. Chang, L. Sjöström, P. Rout, J. Sławińska, and S. P. Dash, "Tunable unconventional spin orbit torque magnetization dynamics in van der Waals heterostructures", Nature Communications **16**, 8722 (2025) (cit. on pp. 19, 20, 29, 64).

[216] Q. Ma et al., "Observation of the nonlinear Hall effect under time-reversal-symmetric conditions", Nature **565**, 337–342 (2019) (cit. on pp. 19, 20, 86).

[217] N. Nagaosa, T. Morimoto, and Y. Tokura, "Transport, magnetic and optical properties of Weyl materials", Nature Reviews Materials **5**, 621–636 (2020) (cit. on pp. 19–21).

[218] S. Kar and A. M. Jayannavar, "A Primer on Weyl Semimetals: Down the Discovery of Topological Phases", Asian Journal of Research and Reviews in Physics **4**, 34–45 (2021) (cit. on p. 19).

[219] D. T. Son and B. Z. Spivak, "Chiral anomaly and classical negative magnetoresistance of Weyl metals", Physical Review B **88**, 104412 (2013) (cit. on p. 20).

[220] N. P. Armitage, E. J. Mele, and A. Vishwanath, "Weyl and Dirac semimetals in three-dimensional solids", Reviews of Modern Physics **90**, 015001 (2018) (cit. on p. 20).

[221] X. Huang, L. Zhao, Y. Long, P. Wang, D. Chen, Z. Yang, H. Liang, M. Xue, H. Weng, Z. Fang, X. Dai, and G. Chen, "Observation of the chiral-anomaly-induced negative magnetoresistance: In 3D Weyl semimetal TaAs", Physical Review X **5**, 031023 (2015) (cit. on p. 20).

[222] C.-L. Zhang et al., "Signatures of the Adler-Bell-Jackiw chiral anomaly in a Weyl fermion semimetal", Nature Communications **7**, 10735 (2016) (cit. on p. 20).

[223] M. Hirschberger, S. Kushwaha, Z. Wang, Q. Gibson, S. Liang, C. A. Belvin, B. A. Bernevig, R. J. Cava, and N. P. Ong, "The chiral anomaly and thermopower of Weyl fermions in the half-Heusler GdPtBi", Nature Materials **15**, 1161–1165 (2016) (cit. on p. 20).

[224] Y. Li, Z. Wang, P. Li, X. Yang, Z. Shen, F. Sheng, X. Li, Y. Lu, Y. Zheng, and Z.-A. Xu, "Negative magnetoresistance in Weyl semimetals NbAs and NbP: Intrinsic chiral anomaly and extrinsic effects", Frontiers of Physics **12**, 127205 (2017) (cit. on p. 20).

[225] B. Zhang, J. Liao, Z. Huang, Y. Shangguan, S. Cheng, H. Xu, Z. Song, S. Dong, S. Bao, R. Wang, and J. Wen, "Significant chiral magnetotransport magnified by multiple Weyl nodes", Physical Review B **111**, 045163 (2025) (cit. on p. 20).

[226] E. Liu et al., "Giant anomalous Hall effect in a ferromagnetic kagome-lattice semimetal", Nature Physics **14**, 1125–1131 (2018) (cit. on p. 20).

[227] P. Li, J. Koo, W. Ning, J. Li, L. Miao, L. Min, Y. Zhu, Y. Wang, N. Alem, C. X. Liu, Z. Mao, and B. Yan, "Giant room temperature anomalous Hall effect and tunable topology in a ferromagnetic topological semimetal Co2MnAl", Nature Communications **11**, 3476 (2020) (cit. on p. 20).

[228] S. Nandy, G. Sharma, A. Taraphder, and S. Tewari, "Chiral Anomaly as the Origin of the Planar Hall Effect in Weyl Semimetals", Physical Review Letters **119**, 176804 (2017) (cit. on p. 20).

[229] Shama, R. K. Gopal, and Y. Singh, "Observation of planar Hall effect in the ferromagnetic Weyl semimetal Co3Sn2S2", Journal of Magnetism and Magnetic Materials **502**, 166547 (2020) (cit. on p. 20).

[230] P. Li, Y. Wen, X. He, Q. Zhang, C. Xia, Z. M. Yu, S. A. Yang, Z. Zhu, H. N. Alshareef, and X. X. Zhang, "Evidence for topological type-II Weyl semimetal WTe2", Nature Communications **8**, 2150 (2017) (cit. on p. 20).

[231] Y. Sun, Y. Zhang, C. Felser, and B. Yan, "Strong Intrinsic Spin Hall Effect in the TaAs Family of Weyl Semimetals", Physical Review Letters **117**, 146403 (2016) (cit. on p. 20).

[232] A. Johansson, J. Henk, and I. Mertig, "Edelstein effect in Weyl semimetals", Physical Review B **97**, 085417 (2018) (cit. on p. 20).

[233] B. Zhao, D. Khokhriakov, Y. Zhang, H. Fu, B. Karpiak, A. M. Hoque, X. Xu, Y. Jiang, B. Yan, and S. P. Dash, "Observation of charge to spin conversion in Weyl semimetal WTe2 at room temperature", Physical Review Research **2**, 013286 (2020) (cit. on pp. 20, 29, 64, 82).

[234] B. Zhao, A. M. Hoque, D. Khokhriakov, B. Karpiak, and S. P. Dash, "Charge-spin conversion signal in WTe2 van der Waals hybrid devices with a geometrical design", Applied Physics Letters **117**, 242401 (2020) (cit. on pp. 20, 29, 36, 37, 64, 67).

[235] A. M. Hoque, D. Khokhriakov, K. Zollner, B. Zhao, B. Karpiak, J. Fabian, and S. P. Dash, "All-electrical creation and control of spin-galvanic signal in graphene and molybdenum ditelluride heterostructures at room temperature", Communications Physics **4**, 124 (2021) (cit. on pp. 20, 29, 64, 71, 73).

[236] D. MacNeill, G. M. Stiehl, M. H. Guimaraes, R. A. Buhrman, J. Park, and D. C. Ralph, "Control of spin-orbit torques through crystal symmetry in WTe2/ferromagnet bilayers", Nature Physics **13**, 300–305 (2017) (cit. on pp. 20, 64).

[237] D. MacNeill, G. M. Stiehl, M. H. Guimarães, N. D. Reynolds, R. A. Buhrman, and D. C. Ralph, "Thickness dependence of spin-orbit torques generated by WTe2", Physical Review B **96**, 054450 (2017) (cit. on pp. 20, 64).

[238] S. Shi, S. Liang, Z. Zhu, K. Cai, S. D. Pollard, Y. Wang, J. Wang, Q. Wang, P. He, J. Yu, G. Eda, G. Liang, and H. Yang, "All-electric magnetization switching and Dzyaloshinskii–Moriya interaction in WTe2/ferromagnet heterostructures", Nature Nanotechnology **14**, 945–949 (2019) (cit. on pp. 20, 64).

[239] C. K. Safeer, N. Ontoso, J. Ingla-Aynés, F. Herling, V. T. Pham, A. Kurzmann, K. Ensslin, A. Chuvilin, I. Robredo, M. G. Vergniory, F. De Juan, L. E. Hueso, M. R. Calvo, and F. Casanova, "Large Multidirectional Spin-to-Charge Conversion in Low-Symmetry Semimetal

MoTe2 at Room Temperature", Nano Letters **19**, 8758–8766 (2019) (cit. on pp. 20, 36, 64).

[240] S. Liang, S. Shi, C. H. Hsu, K. Cai, Y. Wang, P. He, Y. Wu, V. M. Pereira, and H. Yang, "Spin-Orbit Torque Magnetization Switching in MoTe2/Permalloy Heterostructures", Advanced Materials **32**, 2002799 (2020) (cit. on pp. 20, 64).

[241] B. Zhao, B. Karpiak, D. Khokhriakov, A. Johansson, A. M. Hoque, X. Xu, Y. Jiang, I. Mertig, and S. P. Dash, "Unconventional Charge–Spin Conversion in Weyl-Semimetal WTe2", Advanced Materials **32**, 2000818 (2020) (cit. on pp. 20, 29, 64).

[242] K. Ohnishi, M. Aoki, R. Ohshima, E. Shigematsu, Y. Ando, T. Takenobu, and M. Shiraishi, "All-Electric Spin Device Operation Using the Weyl Semimetal, WTe2, at Room Temperature", Advanced Electronic Materials **9**, 2200647 (2023) (cit. on pp. 20, 64).

[243] S. N. Kajale, T. Nguyen, N. T. Hung, M. Li, and D. Sarkar, "Field-free deterministic switching of all–van der Waals spin-orbit torque system above room temperature", Science Advances **10**, eadk8669 (2024) (cit. on pp. 20, 64).

[244] X. Fan, H. Zhu, J. Mi, J. Li, Y. Ji, and L. Li, "Crystallographic-Orientation-Independent Field-Free Deterministic Magnetization Switching in Perpendicularly Aligned WTe2/Fe3GeTe2/WTe2 Heterostructures", Small Structures **7**, e202500607 (2026) (cit. on pp. 20, 64).

[245] M. N. H. Shazon, P. Kumar, L. Liu, D. C. Ralph, and A. Naeemi, "Modeling and optimization of two-terminal spin-orbit-torque MRAM", arXiv, 2512.06215 (2025) (cit. on p. 20).

[246] Z. Zhao, Y. Lin, and A. Avsar, "Novel spintronic effects in two- dimensional van der Waals heterostructures", npj 2D Materials and Applications **9**, 30 (2025) (cit. on p. 20).

[247] Y. Liu, G. Shi, D. Kumar, T. Kim, S. Shi, D. Yang, J. Zhang, C. Zhang, F. Wang, S. Yang, Y. Pu, P. Yu, K. Cai, and H. Yang, "Field-free switching of perpendicular magnetization at room temperature using out-of-plane spins from TaIrTe4", Nature Electronics **6**, 732–738 (2023) (cit. on pp. 20, 64).

[248] M. Suárez-Rodríguez, F. de Juan, I. Souza, M. Gobbi, F. Casanova, and L. E. Hueso, "Nonlinear transport in non-centrosymmetric systems", Nature Materials **24**, 1005–1018 (2025) (cit. on pp. 20, 26, 86, 91, 104).

[249] G. S. Ohm, *Die galvanische Kette* (Bei T. H. Riemann, Berlin, 1827) (cit. on p. 20).

[250] I. Sodemann and L. Fu, "Quantum Nonlinear Hall Effect Induced by Berry Curvature Dipole in Time-Reversal Invariant Materials", Physical Review Letters **115**, 216806 (2015) (cit. on pp. 20, 21, 106).

[251] K. Kang, T. Li, E. Sohn, J. Shan, and K. F. Mak, "Nonlinear anomalous Hall effect in few-layer WTe2", Nature Materials **18**, 324–328 (2019) (cit. on pp. 20, 86, 103).

[252] D. Kumar, C. H. Hsu, R. Sharma, T. R. Chang, P. Yu, J. Wang, G. Eda, G. Liang, and H. Yang, "Room-temperature nonlinear Hall effect and wireless radiofrequency rectification in Weyl semimetal TaIrTe4", Nature Nanotechnology **16**, 421–425 (2021) (cit. on pp. 20, 21, 86).

[253] T. Ma, H. Chen, K. Yananose, X. Zhou, L. Wang, R. Li, Z. Zhu, Z. Wu, Q. H. Xu, J. Yu, C. W. Qiu, A. Stroppa, and K. P. Loh, "Growth of bilayer MoTe2 single crystals with strong non-linear Hall effect", Nature Communications **13**, 5465 (2022) (cit. on pp. 20, 86).

[254] J. E. Lee, A. Wang, S. Chen, M. Kwon, J. Hwang, M. Cho, K. H. Son, D.-S. Han, J. W. Choi, Y. D. Kim, S. K. Mo, C. Petrovic, C. Hwang, S. Y. Park, C. Jang, and H. Ryu, "Spin-orbit-splitting-driven nonlinear Hall effect in NbIrTe4", Nature Communications **15**, 3971 (2024) (cit. on pp. 20, 86, 103).

[255] A. Q. Wang, D. Li, T. Y. Zhao, X. Y. Liu, J. Zhang, X. Liao, Q. Yin, Z. C. Pan, P. Yu, and Z. M. Liao, "Orbital anomalous Hall effect in the few-layer Weyl semimetal TaIrTe4", Physical Review B **110**, 155434 (2024) (cit. on p. 20).

[256] T. Xi, H. Jiang, J. Li, Y. He, Y. Gu, C. Fox, L. Primeau, Y. Mao, J. Rollins, T. Taniguchi, K. Watanabe, D. van der Weide, D. Rhodes, Y. Zhang, Y. Wang, and J. Xiao, "Terahertz sensing based on the nonlinear electrodynamics of the two-dimensional correlated topological semimetal TaIrTe4", Nature Electronics **8**, 578–586 (2025) (cit. on pp. 20, 21, 86).

[257] H. Jiang, T. Xi, J. Li, Y. He, H. Ma, Y. Mao, T. Taniguchi, K. Watanabe, D. A. Rhodes, Y. Zhang, J. Xiao, and Y. Wang, "Probing interplay of topological properties and electron correlation in TaIrTe4 via nonlinear Hall effect", Nature Communications **16**, 6351 (2025) (cit. on pp. 20, 86).

[258] S. Lai, H. Liu, Z. Zhang, J. Zhao, X. Feng, N. Wang, C. Tang, Y. Liu, K. S. Novoselov, S. A. Yang, and W.-b. Gao, "Third-order nonlinear Hall effect induced by the Berry-connection polarizability tensor", Nature Nanotechnology **16**, 869–873 (2021) (cit. on pp. 20, 21, 86, 103).

[259] X. G. Ye, P. F. Zhu, W. Z. Xu, Z. Zang, Y. Ye, and Z. M. Liao, "Orbital polarization and third-order anomalous Hall effect in WTe2", Physical Review B **106**, 045414 (2022) (cit. on p. 20).

[260] C. Wang, R.-C. Xiao, H. Liu, Z. Zhang, S. Lai, C. Zhu, H. Cai, N. Wang, S. Chen, Y. Deng, Z. Liu, S. A. Yang, and W.-B. Gao, "Room-temperature third-order nonlinear Hall effect in Weyl semimetal TaIrTe4", National Science Review **9**, nwac020 (2022) (cit. on pp. 20, 86).

[261] Y. Zhang, J. van den Brink, C. Felser, and B. Yan, "Electrically tuneable nonlinear anomalous Hall effect in two-dimensional transition-metal dichalcogenides WTe2 and MoTe2", 2D Materials **5**, 044001 (2018) (cit. on p. 21).

[262] F. Zhang, C. L. Kane, and E. J. Mele, "Surface state magnetization and chiral edge states on topological insulators", Physical Review Letters **110**, 046404 (2013) (cit. on p. 22).

[263] R. Yu, W. Zhang, H.-J. Zhang, S.-C. Zhang, X. Dai, and Z. Fang, "Quantized Anomalous Hall Effect in Magnetic Topological Insulators", Science **329**, 61–64 (2010) (cit. on pp. 22, 23).

[264] Y. L. Chen, J. H. Chu, J. G. Analytis, Z. K. Liu, K. Igarashi, H. H. Kuo, X. L. Qi, S. K. Mo, R. G. Moore, D. H. Lu, M. Hashimoto, T. Sasagawa, S. C. Zhang, I. R. Fisher, Z. Hussain, and Z. X. Shen, "Massive Dirac fermion on the surface of a magnetically doped topological insulator", Science **329**, 659–662 (2010) (cit. on pp. 22, 24, 25).

[265] J. M. Zhang, W. Zhu, Y. Zhang, D. Xiao, and Y. Yao, "Tailoring magnetic doping in the topological insulator Bi2Se3", Physical Review Letters **109**, 266405 (2012) (cit. on p. 22).

[266] F. Ortmann, S. Roche, and S. O. Valenzuela, eds., *Topological Insulators: Fundamentals and Perspectives* (Wiley-VCH Verlag GmbH & Co. KGaA, Weinheim, Germany, 2015) (cit. on pp. 22, 23).

[267] M. Mogi, R. Yoshimi, A. Tsukazaki, K. Yasuda, Y. Kozuka, K. S. Takahashi, M. Kawasaki, and Y. Tokura, "Magnetic modulation doping in topological insulators toward higher-temperature quantum anomalous Hall effect", Applied Physics Letters **107**, 182401 (2015) (cit. on pp. 22, 24).

[268] H. Chi and J. S. Moodera, "Progress and prospects in the quantum anomalous Hall effect", APL Materials **10**, 090903 (2022) (cit. on pp. 22, 24, 85).

[269] W. Luo and X.-L. Qi, "Massive Dirac surface states in topological insulator/magnetic insulator heterostructures", Physical Review B **87**, 085431 (2013) (cit. on pp. 22, 24).

[270] P. Wei, F. Katmis, B. A. Assaf, H. Steinberg, P. Jarillo-Herrero, D. Heiman, and J. S. Moodera, "Exchange-coupling-induced symmetry breaking in topological insulators", Physical Review Letters **110**, 186807 (2013) (cit. on pp. 22, 24).

[271] P. Li, J. Yu, J. Xu, L. Zhang, and K. Huang, "Topological-magnetic proximity effect in Sb2Te3/CrI3 heterostructures", Physica B: Condensed Matter **573**, 77–80 (2019) (cit. on p. 22).

[272] D. Zhang, M. Shi, T. Zhu, D. Xing, H. Zhang, and J. Wang, "Topological Axion States in the Magnetic Insulator MnBi2Te4 with the Quantized Magnetoelectric Effect", Physical Review Letters **122**, 206401 (2019) (cit. on pp. 22, 24).

[273] M. M. Otrokov et al., "Prediction and observation of an antiferromagnetic topological insulator", Nature **576**, 416–422 (2019) (cit. on pp. 22, 24, 25, 85, 87, 88).

[274] B. A. Bernevig, C. Felser, and H. Beidenkopf, "Progress and prospects in magnetic topological materials", Nature **603**, 41–51 (2022) (cit. on pp. 22–24).

[275] S. Li, T. Liu, C. Liu, Y. Wang, H.-Z. Lu, and X. C. Xie, "Progress on the antiferromagnetic topological insulator MnBi2Te4", National Science Review **11**, nwac296 (2024) (cit. on pp. 22, 24, 85, 87, 88).

[276] E. Hall, " XVIII. On the "Rotational Coefficient" in nickel and cobalt ", The London, Edinburgh, and Dublin Philosophical Magazine and Journal of Science **12**, 157–172 (1881) (cit. on p. 22).

[277] C. Z. Chang et al., "Experimental observation of the quantum anomalous Hall effect in a magnetic topological insulator", Science **340**, 167–170 (2013) (cit. on pp. 22, 24, 25, 85).

[278] J. Wang, B. Lian, and S.-C. Zhang, "Quantum anomalous Hall effect in magnetic topological insulators", Physica Scripta **2015**, 014003 (2015) (cit. on p. 23).

[279] L. K. Rodenbach, J. M. Underwood, N. T. M. Tran, A. R. Panna, M. P. Andersen, Z. S. Barcikowski, S. U. Payagala, P. Zhang, L. Tai, K. L. Wang, D. G. Jarrett, R. E. Elmquist, D. B. Newell, A. F. Rigosi, and D. Goldhaber-Gordon, "A unified realization of electrical quantities from the quantum International System of Units", Nature Electronics **8**, 663–671 (2025) (cit. on p. 23).

[280] H. Jiang, Z. Qiao, H. Liu, and Q. Niu, "Quantum anomalous Hall effect with tunable Chern number in magnetic topological insulator film", Physical Review B **85**, 045445 (2012) (cit. on p. 23).

[281] Y. F. Zhao, R. Zhang, R. Mei, L. J. Zhou, H. Yi, Y. Q. Zhang, J. Yu, R. Xiao, K. Wang, N. Samarth, M. H. Chan, C. X. Liu, and C. Z. Chang, "Tuning the Chern number in quantum anomalous Hall insulators", Nature **588**, 419–423 (2020) (cit. on pp. 23, 24, 85).

[282] R. S. Mong, A. M. Essin, and J. E. Moore, "Antiferromagnetic topological insulators", Physical Review B - Condensed Matter and Materials Physics **81**, 245209 (2010) (cit. on pp. 23, 85).

[283] C. Z. Chang, C. X. Liu, and A. H. Macdonald, "Colloquium: Quantum anomalous Hall effect", Reviews of Modern Physics **95**, 11002 (2023) (cit. on pp. 23, 24, 85).

[284] M. Franz, "High-energy physics in a new guise", Physics **1**, 10.1103/physics.1.36 (2008) (cit. on p. 23).

[285] M. Mogi, M. Kawamura, R. Yoshimi, A. Tsukazaki, Y. Kozuka, N. Shirakawa, K. S. Takahashi, M. Kawasaki, and Y. Tokura, "A magnetic heterostructure of topological insulators as a candidate for an axion insulator", Nature Materials **16**, 516–521 (2017) (cit. on pp. 23, 24).

[286] F. D. Haldane, "Model for a quantum Hall effect without Landau levels: Condensed-matter realization of the "parity anomaly"", Physical Review Letters **61**, 2015–2018 (1988) (cit. on p. 23).

[287] Y. S. Hor, P. Roushan, H. Beidenkopf, J. Seo, D. Qu, J. G. Checkelsky, L. A. Wray, D. Hsieh, Y. Xia, S. Y. Xu, D. Qian, M. Z. Hasan, N. P. Ong, A. Yazdani, and R. J. Cava, "Development of ferromagnetism in the doped topological insulator Bi2-xMnxTe3", Physical Review B **81**, 195203 (2010) (cit. on p. 24).

[288] J. Zhang, C.-Z. Chang, P. Tang, Z. Zhang, X. Feng, K. Li, L.-l. Wang, X. Chen, C. Liu, W. Duan, K. He, Q.-K. Xue, X. Ma, and Y. Wang, "Topology-Driven Magnetic Quantum Phase Transition in Topological Insulators", Science **339**, 1582–1586 (2013) (cit. on p. 24).

[289] C.-Z. Chang, J. Zhang, M. Liu, Z. Zhang, X. Feng, K. Li, L. L. Wang, X. Chen, X. Dai, Z. Fang, X. L. Qi, S.-C. Zhang, Y. Wang, K. He, X.-C. Ma, and Q.-K. Xue, "Thin films of magnetically doped topological insulator with carrier-independent long-range ferromagnetic order", Advanced Materials **25**, 1065–1070 (2013) (cit. on p. 24).

[290] C. Chang, M. Liu, Z. Zhang, Y. Wang, K. He, and Q. Xue, "Field-effect modulation of anomalous Hall effect in diluted ferromagnetic topological insulator epitaxial films", Science China Physics, Mechanics & Astronomy **59**, 637501 (2016) (cit. on p. 24).

[291] M. Lang, M. Montazeri, M. C. Onbasli, X. Kou, Y. Fan, P. Upadhyaya, K. Yao, F. Liu, Y. Jiang, W. Jiang, K. L. Wong, G. Yu, J. Tang, T. Nie, L. He, R. N. Schwartz, Y. Wang, C. A. Ross, and K. L. Wang, "Proximity induced high-temperature magnetic order in topological insulator - ferrimagnetic insulator heterostructure", Nano Letters **14**, 3459–3465 (2014) (cit. on p. 24).

[292] L. D. Alegria, H. Ji, N. Yao, J. J. Clarke, R. J. Cava, and J. R. Petta, "Large anomalous Hall effect in ferromagnetic insulator-topological insulator heterostructures", Applied Physics Letters **105**, 053512 (2014) (cit. on p. 24).

[293] F. Katmis, V. Lauter, F. S. Nogueira, B. A. Assaf, M. E. Jamer, P. Wei, B. Satpati, J. W. Freeland, I. Eremin, D. Heiman, P. Jarillo-Herrero, and J. S. Moodera, "A higherature ferromagnetic topological insulating phase by proximity coupling", Nature **533**, 513–516 (2016) (cit. on p. 24).

[294] T. Hirahara, S. V. Eremeev, T. Shirasawa, Y. Okuyama, T. Kubo, R. Nakanishi, R. Akiyama, A. Takayama, T. Hajiri, S. I. Ideta, M. Matsunami, K. Sumida, K. Miyamoto, Y. Takagi, K. Tanaka, T. Okuda, T. Yokoyama, S. I. Kimura, S. Hasegawa, and E. V. Chulkov, "Large-Gap Magnetic Topological Heterostructure Formed by Subsurface Incorporation of a Ferromagnetic Layer", Nano Letters **17**, 3493–3500 (2017) (cit. on p. 24).

[295] M. Mogi, T. Nakajima, V. Ukleev, A. Tsukazaki, R. Yoshimi, M. Kawamura, K. S. Takahashi, T. Hanashima, K. Kakurai, T. H. Arima, M. Kawasaki, and Y. Tokura, "Large Anomalous Hall Effect in Topological Insulators with Proximitized Ferromagnetic Insulators", Physical Review Letters **123**, 016804 (2019) (cit. on p. 24).

[296] J. G. Checkelsky, R. Yoshimi, A. Tsukazaki, K. S. Takahashi, Y. Kozuka, J. Falson, M. Kawasaki, and Y. Tokura, "Trajectory of the anomalous Hall effect towards the quantized state in a ferromagnetic topological insulator", Nature Physics **10**, 731–736 (2014) (cit. on p. 24).

[297] X. Kou, S. T. Guo, Y. Fan, L. Pan, M. Lang, Y. Jiang, Q. Shao, T. Nie, K. Murata, J. Tang, Y. Wang, L. He, T. K. Lee, W. L. Lee, and K. L. Wang, "Scale-invariant quantum anomalous hall effect in magnetic topological insulators beyond the two-dimensional limit", Physical Review Letters **113**, 137201 (2014) (cit. on p. 24).

[298] C. Z. Chang, W. Zhao, D. Y. Kim, H. Zhang, B. A. Assaf, D. Heiman, S. C. Zhang, C. Liu, M. H. Chan, and J. S. Moodera, "High-precision realization of robust quantum anomalous Hall state in a hard ferromagnetic topological insulator", Nature Materials **14**, 473–477 (2015) (cit. on pp. 24, 85).

[299] A. J. Bestwick, E. J. Fox, X. Kou, L. Pan, K. L. Wang, and D. Goldhaber-Gordon, "Precise quantization of the anomalous Hall effect near zero magnetic field", Physical Review Letters **114**, 187201 (2015) (cit. on p. 24).

[300] A. Kandala, A. Richardella, S. Kempinger, C. X. Liu, and N. Samarth, "Giant anisotropic magnetoresistance in a quantum anomalous Hall insulator", Nature Communications **6**, 7434 (2015) (cit. on p. 24).

[301] C. Z. Chang, W. Zhao, D. Y. Kim, P. Wei, J. K. Jain, C. Liu, M. H. Chan, and J. S. Moodera, "Zero-Field Dissipationless Chiral Edge Transport and the Nature of Dissipation in the Quantum Anomalous Hall State", Physical Review Letters **115**, 057206 (2015) (cit. on pp. 24, 85).

[302] Y. Feng, X. Feng, Y. Ou, J. Wang, C. Liu, L. Zhang, D. Zhao, G. Jiang, S. C. Zhang, K. He, X. Ma, Q. K. Xue, and Y. Wang, "Observation of the Zero Hall Plateau in a Quantum Anomalous Hall Insulator", Physical Review Letters **115**, 126801 (2015) (cit. on p. 24).

[303] X. Kou, L. Pan, J. Wang, Y. Fan, E. S. Choi, W. L. Lee, T. Nie, K. Murata, Q. Shao, S. C. Zhang, and K. L. Wang, "Metal-to-insulator switching in quantum anomalous Hall states", Nature Communications **6**, 8474 (2015) (cit. on p. 24).

[304] E. O. Lachman, A. F. Young, A. Richardella, J. Cuppens, H. R. Naren, Y. Anahory, A. Y. Meltzer, A. Kandala, S. Kempinger, Y. Myasoedov, M. E. Huber, N. Samarth, and E. Zeldov, "Visualization of superparamagnetic dynamics in magnetic topological insulators", Science Advances **1**, e1500740 (2015) (cit. on p. 24).

[305] S. Grauer, S. Schreyeck, M. Winnerlein, K. Brunner, C. Gould, and L. W. Molenkamp, "Coincidence of superparamagnetism and perfect quantization in the quantum anomalous Hall state", Physical Review B **92**, 201304(R) (2015) (cit. on p. 24).

[306] X. Feng, Y. Feng, J. Wang, Y. Ou, Z. Hao, C. Liu, Z. Zhang, L. Zhang, C. Lin, J. Liao, Y. Li, L. L. Wang, S. H. Ji, X. Chen, X. Ma, S.-C. Zhang, Y. Wang, K. He, and Q.-K. Xue, "Thickness Dependence of the Quantum Anomalous Hall Effect in Magnetic Topological Insulator Films", Advanced Materials **28**, 6386–6390 (2016) (cit. on p. 24).

[307] M. Liu, W. Wang, A. R. Richardella, A. Kandala, J. Li, A. Yazdani, N. Samarth, and N. Phuan Ong, "Large discrete jumps observed in the transition between Chern states in a ferromagnetic topological insulator", Science Advances **2**, e1600167 (2016) (cit. on p. 24).

[308] S. Grauer, K. M. Fijalkowski, S. Schreyeck, M. Winnerlein, K. Brunner, R. Thomale, C. Gould, and L. W. Molenkamp, "Scaling of the Quantum Anomalous Hall Effect as an Indicator of Axion Electrodynamics", Physical Review Letters **118**, 246801 (2017) (cit. on p. 24).

[309] M. Kawamura, R. Yoshimi, A. Tsukazaki, K. S. Takahashi, M. Kawasaki, and Y. Tokura, "Current-Driven Instability of the Quantum Anomalous Hall Effect in Ferromagnetic Topological Insulators", Physical Review Letters **119**, 016803 (2017) (cit. on p. 24).

[310] Y. Ou, C. Liu, G. Jiang, Y. Feng, D. Zhao, W. Wu, X.-X. Wang, W. Li, C. Song, L. L. Wang, W. Wang, W. Wu, Y. Wang, K. He, X.-C. Ma, and Q.-K. Xue, "Enhancing the Quantum Anomalous Hall Effect by Magnetic Codoping in a Topological Insulator", Advanced Materials **30**, 1703062 (2018) (cit. on p. 24).

[311] G. Lippertz, A. Bliesener, A. Uday, L. M. Pereira, A. A. Taskin, and Y. Ando, "Current-induced breakdown of the quantum anomalous Hall effect", Physical Review B **106**, 045419 (2022) (cit. on p. 24).

[312] M. Mogi, M. Kawamura, A. Tsukazaki, R. Yoshimi, K. S. Takahashi, M. Kawasaki, and Y. Tokura, "Tailoring tricolor structure of magnetic topological insulator for robust axion insulator", Science Advances **3**, eaao1669 (2017) (cit. on p. 24).

[313] D. Xiao, J. Jiang, J.-H. Shin, W. Wang, F. Wang, Y. F. Zhao, C. Liu, W. Wu, M. H. Chan, N. Samarth, and C.-Z. Chang, "Realization of the Axion Insulator State in Quantum Anomalous Hall Sandwich Heterostructures", Physical Review Letters **120**, 056801 (2018) (cit. on p. 24).

[314] R. Watanabe, R. Yoshimi, M. Kawamura, M. Mogi, A. Tsukazaki, X. Z. Yu, K. Nakajima, K. S. Takahashi, M. Kawasaki, and Y. Tokura, "Quantum anomalous Hall effect driven by magnetic proximity coupling in all-telluride based heterostructure", Applied Physics Letters **115**, 102403 (2019) (cit. on pp. 24, 85).

[315] G. Jiang, Y. Feng, W. Wu, S. Li, Y. Bai, Y. Li, Q. Zhang, L. Gu, X. Feng, D. Zhang, C. Song, L. Wang, W. Li, X. C. Ma, Q. K. Xue, Y. Wang, and K. He, "Quantum Anomalous Hall Multilayers Grown by Molecular Beam Epitaxy", Chinese Physics Letters **35**, 076802 (2018) (cit. on p. 24).

[316] Y.-F. Zhao, R. Zhang, L.-J. Zhou, R. Mei, Z.-J. Yan, M. H. Chan, C.-X. Liu, and C.-Z. Chang, "Zero Magnetic Field Plateau Phase Transition in Higher Chern Number Quantum Anomalous Hall Insulators", Physical Review Letters **128**, 216801 (2022) (cit. on p. 24).

[317] Y. Deng, Y. Yu, M. Z. Shi, Z. Guo, Z. Xu, J. Wang, X. H. Chen, and Y. Zhang, "Quantum anomalous Hall effect in intrinsic magnetic topological insulator MnBi2Te4", Science **367**, 895–900 (2020) (cit. on pp. 24, 25, 85).

[318] Y. Gong et al., "Experimental Realization of an Intrinsic Magnetic Topological Insulator", Chinese Physics Letters **36**, 076801 (2019) (cit. on p. 24).

[319] D. S. Lee, T. H. Kim, C. H. Park, C. Y. Chung, Y. S. Lim, W. S. Seo, and H. H. Park, "Crystal structure, properties and nanostructuring of a new layered chalcogenide semiconductor, Bi2MnTe4", CrystEngComm **15**, 5532–5538 (2013) (cit. on p. 24).

[320] R. C. Vidal et al., "Surface states and Rashba-type spin polarization in antiferromagnetic MnBi2Te4 (0001)", Physical Review B **100**, 121104(R) (2019) (cit. on pp. 24, 88).

[321] S. H. Lee, Y. Zhu, Y. Wang, L. Miao, T. Pillsbury, H. Yi, S. Kempinger, J. Hu, C. A. Heikes, P. Quarterman, W. Ratcliff, J. A. Borchers, H. Zhang, X. Ke, D. Graf, N. Alem, C. Z. Chang, N. Samarth, and Z. Mao, "Spin scattering and noncollinear spin structure-induced intrinsic anomalous Hall effect in antiferromagnetic topological insulator MnBi2Te4", Physical Review Research **1**, 012011(R) (2019) (cit. on pp. 24, 85, 87, 93, 106).

[322] B. Chen et al., "Intrinsic magnetic topological insulator phases in the Sb doped MnBi2Te4 bulks and thin flakes", Nature Communications **10**, 4469 (2019) (cit. on p. 24).

[323] A. M. Shikin, D. A. Estyunin, N. L. Zaitsev, D. Glazkova, I. I. Klimovskikh, S. O. Filnov, A. G. Rybkin, E. F. Schwier, S. Kumar, A. Kimura, N. Mamedov, Z. Aliev, M. B. Babanly, K. Kokh, O. E. Tereshchenko, M. M. Otrokov, E. V. Chulkov, K. A. Zvezdin, and A. K. Zvezdin, "Sample-dependent Dirac-point gap in and its response to applied surface charge: A combined photoemission and ab initio study", Physical Review B **104**, 115168 (2021) (cit. on pp. 24, 88).

[324] M. Garnica, M. M. Otrokov, P. C. Aguilar, I. I. Klimovskikh, D. Estyunin, Z. S. Aliev, I. R. Amiraslanov, N. A. Abdullayev, V. N. Zverev, M. B. Babanly, N. T. Mamedov, A. M. Shikin, A. Arnau, A. L. de Parga, E. V. Chulkov, and R. Miranda, "Native point defects and their implications for the Dirac point gap at MnBi2Te4(0001)", npj Quantum Materials **7**, 7 (2022) (cit. on pp. 24, 88).

[325] Z. Jiang, J. Liu, Z. Liu, and D. Shen, "A review of angle-resolved photoemission spectroscopy study on topological magnetic material family of MnBi2Te4", Electronic Structure **4**, 043002 (2022) (cit. on p. 24).

[326] H. Padmanabhan et al., "Large Exchange Coupling Between Localized Spins and Topological Bands in MnBi2Te4", Advanced Materials **34**, 2202841 (2022) (cit. on p. 24).

[327] M. M. Otrokov, I. P. Rusinov, M. Blanco-Rey, M. Hoffmann, A. Y. Vyazovskaya, S. V. Eremeev, A. Ernst, P. M. Echenique, A. Arnau, and E. V. Chulkov, "Unique Thickness-Dependent Properties of the

van der Waals Interlayer Antiferromagnet MnBi2Te4 Films", Physical Review Letters **122**, 107202 (2019) (cit. on p. 24).

[328] S. Yang, X. Xu, Y. Zhu, R. Niu, C. Xu, Y. Peng, X. Cheng, X. Jia, Y. Huang, X. Xu, J. Lu, and Y. Ye, "Odd-Even Layer-Number Effect and Layer-Dependent Magnetic Phase Diagrams in MnBi2Te4", Physical Review X **11**, 011003 (2021) (cit. on pp. 24, 85, 93).

[329] D. Ovchinnikov, X. Huang, Z. Lin, Z. Fei, J. Cai, T. Song, M. He, Q. Jiang, C. Wang, H. Li, Y. Wang, Y. Wu, D. Xiao, J. H. Chu, J. Yan, C. Z. Chang, Y. T. Cui, and X. Xu, "Intertwined Topological and Magnetic Orders in Atomically Thin Chern Insulator MnBi2Te4", Nano Letters **21**, 2544–2550 (2021) (cit. on pp. 24, 85).

[330] Z. Lian, Y. Wang, Y. Wang, W.-H. Dong, Y. Feng, Z. Dong, M. Ma, S. Yang, L. Xu, Y. Li, B. Fu, Y. Li, W. Jiang, Y. Xu, C. Liu, J. Zhang, and Y. Wang, "Antiferromagnetic quantum anomalous Hall effect under spin flips and flops", Nature **641**, 70–75 (2025) (cit. on pp. 24, 85, 87, 93, 106).

[331] C. Liu, Y. Wang, H. Li, Y. Wu, Y. Li, J. Li, K. He, Y. Xu, J. Zhang, and Y. Wang, "Robust axion insulator and Chern insulator phases in a two-dimensional antiferromagnetic topological insulator", Nature Materials **19**, 522–527 (2020) (cit. on pp. 24, 85).

[332] J.-X. Qiu et al., "Observation of the axion quasiparticle in 2D MnBi2Te4", Nature **641**, 62–69 (2025) (cit. on pp. 24, 85).

[333] H. Deng, Z. Chen, A. Wołoś, M. Konczykowski, K. Sobczak, J. Sitnicka, I. V. Fedorchenko, J. Borysiuk, T. Heider, L. Pluciński, K. Park, A. B. Georgescu, J. Cano, and L. Krusin-Elbaum, "High-temperature quantum anomalous Hall regime in a MnBi2Te4/Bi2Te3 superlattice", Nature Physics **17**, 36–42 (2021) (cit. on p. 25).

[334] R. Yang, X. Man, J. Peng, J. Zhang, F. Wang, F. Wang, H. Zhang, and X. Xu, "Septuple XBi2Te4 (X=Ge, Sn, Pb) intercalated MnBi2Te4 for realizing interlayer ferromagnetism and quantum anomalous hall effect", npj Quantum Materials **10**, 3 (2025) (cit. on p. 25).

[335] M. U. Muzaffar, K. Z. Bai, W. Qin, G. Cao, Y. Yang, S. Zhang, P. Cui, S. Q. Shen, and Z. Zhang, "Prediction of high-temperature half-quantum anomalous Hall effect in the semimagnetic topological insulator MnBi2Te4/Sb2Te3", Physical Review B **112**, 045405 (2025) (cit. on p. 25).

[336] C. Ortix, "Nonlinear Hall Effect with Time-Reversal Symmetry: Theory and Material Realizations", Advanced Quantum Technologies **4**, 2100056 (2021) (cit. on p. 26).

[337] Y. Gao, S. A. Yang, and Q. Niu, "Field induced positional shift of bloch electrons and its dynamical implications", Physical Review Letters **112**, 166601 (2014) (cit. on p. 26).

[338] H. Liu, J. Zhao, Y. X. Huang, W. Wu, X. L. Sheng, C. Xiao, and S. A. Yang, "Intrinsic Second-Order Anomalous Hall Effect and Its Application in Compensated Antiferromagnets", Physical Review Letters **127**, 277202 (2021) (cit. on pp. 26, 86, 104).

[339] C. Wang, Y. Gao, and D. Xiao, "Intrinsic Nonlinear Hall Effect in Antiferromagnetic Tetragonal CuMnAs", Physical Review Letters **127**, 277201 (2021) (cit. on pp. 26, 86, 104).

[340] K. Das, S. Lahiri, R. B. Atencia, D. Culcer, and A. Agarwal, "Intrinsic nonlinear conductivities induced by the quantum metric", Physical Review B **108**, L201405 (2023) (cit. on pp. 26, 104).

[341] X. Li, Z. Dai, S. Zhang, H. Zhang, C. Li, B. Wei, F. Guo, C. Li, F. Fei, M. Zhang, X. Wang, H. Wang, and F. Song, "Higher odd-order nonlinear Hall effect in magnetic topological insulator Mn(Bi1-xSbx)2Te4", Nature Communications **17**, 6652 (2026) (cit. on pp. 26, 86).

[342] C. P. Zhang, X. J. Gao, Y. M. Xie, H. C. Po, and K. T. Law, "Higher-order nonlinear anomalous Hall effects induced by Berry curvature multipoles", Physical Review B **107**, 115142 (2023) (cit. on pp. 26, 86, 98, 108).

[343] S. Nandy and I. Sodemann, "Symmetry and quantum kinetics of the nonlinear Hall effect", Physical Review B **100**, 195117 (2019) (cit. on p. 26).

[344] Z. Z. Du, C. M. Wang, S. Li, H. Z. Lu, and X. C. Xie, "Disorder-induced nonlinear Hall effect with time-reversal symmetry", Nature Communications **10**, 3047 (2019) (cit. on p. 26).

[345] H. Liu, J. Zhao, Y. X. Huang, X. Feng, C. Xiao, W. Wu, S. Lai, W. B. Gao, and S. A. Yang, "Berry connection polarizability tensor and third-order Hall effect", Physical Review B **105**, 045118 (2022) (cit. on pp. 26, 86, 105, 109).

[346] D. Ma, A. Arora, G. Vignale, and J. C. Song, "Anomalous Skew-Scattering Nonlinear Hall Effect and Chiral Photocurrents in PT - Symmetric Antiferromagnets", Physical Review Letters **131**, 076601 (2023) (cit. on pp. 26, 86).

[347] Y. Fang, J. Cano, and S. A. A. Ghorashi, "Quantum Geometry Induced Nonlinear Transport in Altermagnets", Physical Review Letters **133**, 106701 (2024) (cit. on pp. 26, 86).

[348] A. Bhattacharya and A. M. Black-Schaffer, "Electric field induced second-order anomalous Hall transport in unconventional Rashba systems", Physical Review B **111**, L041202 (2025) (cit. on p. 26).

[349] M. T. Mercaldo, M. Cuoco, and C. Ortix, "Nonlinear planar magnetotransport as a probe of the topology of surface states", Physical Review B **111**, 155442 (2025) (cit. on p. 26).

[350] K. Das, Y. Zhao, and B. Yan, "Surface-Dominated Quantum-Metric-Induced Nonlinear Transport in the Layered Antiferromagnet CrSBr", Nano Letters **25**, 9189–9196 (2025) (cit. on p. 26).

[351] Z. H. Gong, Z. Z. Du, H. P. Sun, H. Z. Lu, and X. C. Xie, "Scaling analysis of quantum geometry in second-order nonlinear transport", Science Bulletin **71**, 4422–4428 (2026) (cit. on pp. 26, 86, 104).

[352] J. Godinho, H. Reichlová, D. Kriegner, V. Novák, K. Olejník, Z. Kašpar, Z. Šobáň, P. Wadley, R. P. Campion, R. M. Otxoa, P. E. Roy, J. Železný, T. Jungwirth, and J. Wunderlich, "Electrically induced and detected Néel vector reversal in a collinear antiferromagnet", Nature Communications **9**, 4686 (2018) (cit. on p. 26).

[353] J. Wang, H. Zeng, W. Duan, and H. Huang, "Intrinsic Nonlinear Hall Detection of the Néel Vector for Two-Dimensional Antiferromagnetic Spintronics", Physical Review Letters **131**, 056401 (2023) (cit. on p. 26).

[354] J. Jo, M. Suárez-Rodríguez, S. Mañas-Valero, E. Coronado, I. Souza, F. de Juan, F. Casanova, M. Gobbi, and L. E. Hueso, "Anomalous Nonlinear Magnetoconductivity in van der Waals Magnet CrSBr", Advanced Materials **37**, 2419283 (2025) (cit. on p. 26).

[355] S. Sinha, P. C. Adak, A. Chakraborty, K. Das, K. Debnath, L. D. Sangani, K. Watanabe, T. Taniguchi, U. V. Waghmare, A. Agarwal, and M. M. Deshmukh, "Berry curvature dipole senses topological transition in a moiré superlattice", Nature Physics **18**, 765–770 (2022) (cit. on p. 26).

[356] A. Chakraborty, K. Das, S. Sinha, P. C. Adak, M. M. Deshmukh, and A. Agarwal, "Nonlinear anomalous Hall effects probe topological phase-transitions in twisted double bilayer graphene", 2D Materials **9**, 045020 (2022) (cit. on p. 26).

[357] T. Nishijima, T. Watanabe, H. Sekiguchi, Y. Ando, E. Shigematsu, R. Ohshima, S. Kuroda, and M. Shiraishi, "Ferroic Berry Curvature Dipole in a Topological Crystalline Insulator at Room Temperature", Nano Letters **23**, 2247–2252 (2023) (cit. on p. 26).

[358] K. Yasuda, A. Tsukazaki, R. Yoshimi, K. Kondou, K. S. Takahashi, Y. Otani, M. Kawasaki, and Y. Tokura, "Current-Nonlinear Hall Effect and Spin-Orbit Torque Magnetization Switching in a Magnetic Topological Insulator", Physical Review Letters **119**, 137204 (2017) (cit. on p. 27).

[359] X. Che, Q. Pan, B. Vareskic, J. Zou, L. Pan, P. Zhang, G. Yin, H. Wu, Q. Shao, P. Deng, and K. L. Wang, "Strongly Surface State Carrier-Dependent Spin-Orbit Torque in Magnetic Topological Insulators", Advanced Materials **32**, 1907661 (2020) (cit. on p. 27).

[360] L.-J. Zhou, D. Zhuo, H. Tay, Z.-J. Yan, P. Xiao, X. Liu, B. Zhang, and C.-Z. Chang, "Designing Magnetic Topological Insulator Trilayers for Highly Efficient Spin-Orbit Torque Switching", Nano Letters **26**, 7833–7840 (2026) (cit. on p. 27).

[361] Y. Fan, X. Kou, P. Upadhyaya, Q. Shao, L. Pan, M. Lang, X. Che, J. Tang, M. Montazeri, K. Murata, L. T. Chang, M. Akyol, G. Yu, T. Nie, K. L. Wong, J. Liu, Y. Wang, Y. Tserkovnyak, and K. L. Wang, "Electric-field control of spin-orbit torque in a magnetically doped topological insulator", Nature Nanotechnology **11**, 352–359 (2016) (cit. on p. 27).

[362] Y. Liu, A. Lee, K. Qian, P. Zhang, Z. Xiao, H. He, Z. Ren, S. K. Cheung, R. Liu, Y. Li, X. Zhang, Z. Ma, J. Zhao, W. Zhao, G. Yu, X. Wang, J. Liu, Z. Wang, K. L. Wang, and Q. Shao, "Cryogenic in-memory computing using magnetic topological insulators", Nature Materials **24**, 559–564 (2025) (cit. on p. 27).

[363] Z. Li, S. Pan, S. Liu, Y. Zhang, A. Li, L. Ai, X. Xie, X. Cao, Z. Jia, X. Han, J. Yu, and F. Xiu, "Magnetization switching by asymmetric topological surfaces", National Science Review **12**, nwaf178 (2025) (cit. on p. 27).

[364] V. Baltz, A. Manchon, M. Tsoi, T. Moriyama, T. Ono, and Y. Tserkovnyak, "Antiferromagnetic spintronics", Reviews of Modern Physics **90**, 015005 (2018) (cit. on p. 27).

[365] P. Khalili Amiri, C. Phatak, and G. Finocchio, "Prospects for Antiferromagnetic Spintronic Devices", Annual Review of Materials Research **54**, 117–142 (2024) (cit. on p. 27).

[366] K. Olejník, T. Seifert, Z. Kašpar, V. Novák, P. Wadley, R. P. Campion, M. Baumgartner, P. Gambardella, P. Nemec, J. Wunderlich, J. Sinova, P. Kužel, M. Müller, T. Kampfrath, and T. Jungwirth, "Terahertz electrical writing speed in an antiferromagnetic memory", Science Advances **4**, eaar3566 (2018) (cit. on p. 27).

[367] Y. Takeuchi, Y. Sato, Y. Yamane, J. Y. Yoon, Y. Kanno, T. Uchimura, K. V. De Zoysa, J. Han, S. Kanai, J. Ieda, H. Ohno, and S. Fukami, "Electrical coherent driving of chiral antiferromagnet", Science **389**, 830–834 (2025) (cit. on p. 27).

[368] K. Ogawa, H. Tsai, N. Yoshikawa, T. Matsuo, Y. Tsushima, M. Asakura, H. Peng, T. Matsuda, T. Higo, S. Nakatsuji, and R. Shimano, "Ultrafast time-resolved observation of non-thermal current-induced switching in an antiferromagnetic Weyl semimetal", Nature Materials **25**, 434–439 (2026) (cit. on p. 27).

[369] I. T. Rosen, E. J. Fox, X. Kou, L. Pan, K. L. Wang, and D. Goldhaber-Gordon, "Chiral transport along magnetic domain walls in the quantum anomalous Hall effect", npj Quantum Materials **2**, 69 (2017) (cit. on p. 27).

[370] P. M. Perez-Piskunow and S. Roche, "Hinge Spin Polarization in Magnetic Topological Insulators Revealed by Resistance Switch", Physical Review Letters **126**, 167701 (2021) (cit. on p. 27).

[371] C. Ye, X. Xie, W. Lv, K. Huang, A. J. Yang, S. Jiang, X. Liu, D. Zhu, X. Qiu, M. Tong, T. Zhou, C. H. Hsu, G. Chang, H. Lin, P. Li, K. Yang, Z. Wang, T. Jiang, and X. Renshaw Wang, "Nonreciprocal Transport in a Bilayer of MnBi2Te4 and Pt", Nano Letters **22**, 1366–1373 (2022) (cit. on pp. 27, 106).

[372] Z. Zhang, N. Wang, N. Cao, A. Wang, X. Zhou, K. Watanabe, T. Taniguchi, B. Yan, and W.-b. Gao, "Controlled large non-reciprocal charge transport in an intrinsic magnetic topological insulator MnBi2Te4", Nature Communications **13**, 6191 (2022) (cit. on p. 27).

[373] A. Gao et al., “Layer Hall effect in a 2D topological axion antiferromagnet”, Nature **595**, 521–525 (2021) (cit. on pp. 27, 85).

[374] A. Gao et al., “An antiferromagnetic diode effect in even-layered MnBi2Te4”, Nature Electronics **7**, 751–759 (2024) (cit. on p. 27).

[375] R. Mei, Y. F. Zhao, C. Wang, Y. Ren, D. Xiao, C. Z. Chang, and C. X. Liu, “Electrically Controlled Anomalous Hall Effect and Orbital Magnetization in Topological Magnet MnBi2Te4”, Physical Review Letters **132**, 066604 (2024) (cit. on p. 27).

[376] W.-Z. Xu, C.-G. Chu, Z.-C. Pan, J.-J. Chen, A.-Q. Wang, Z.-B. Tan, P.-F. Zhu, X.-G. Ye, D.-P. Yu, and Z.-M. Liao, “Proximity-induced superconducting gap in the intrinsic magnetic topological insulator MnBi2Te4”, Physical Review B **105**, 184515 (2022) (cit. on p. 27).

[377] Y. H. Li and R. Cheng, “Quantum interference in a superconductor-MnBi2Te4-superconductor Josephson junction”, Physical Review Research **4**, 033227 (2022) (cit. on p. 27).

[378] Z. S. Aliev, I. R. Amiraslanov, D. I. Nasonova, A. V. Shevelkov, N. A. Abdullayev, Z. A. Jahangirli, E. N. Orujlu, M. M. Otrokov, N. T. Mamedov, M. B. Babanly, and E. V. Chulkov, “Novel ternary layered manganese bismuth tellurides of the MnTe-Bi2Te3 system: Synthesis and crystal structure”, Journal of Alloys and Compounds **789**, 443–450 (2019) (cit. on p. 27).

[379] E. D. Rienks et al., “Large magnetic gap at the Dirac point in Bi2Te3/MnBi2Te4 heterostructures”, Nature **576**, 423–428 (2019) (cit. on p. 27).

[380] R. X. Zhang, F. Wu, and S. Das Sarma, “Möbius Insulator and Higher-Order Topology in MnBi2nTe3n+1”, Physical Review Letters **124**, 136407 (2020) (cit. on p. 27).

[381] I. I. Klimovskikh et al., “Tunable 3D/2D magnetism in the (MnBi2Te4)(Bi2Te3)m topological insulators family”, npj Quantum Materials **5**, 54 (2020) (cit. on p. 27).

[382] C. Yan, Y. Zhu, S. Fernandez-Mulligan, E. Green, R. Mei, B. Yan, C. Liu, Z. Mao, and S. Yang, “Delicate Ferromagnetism in MnBi6Te10”, Nano Letters **22**, 9815–9822 (2022) (cit. on p. 27).

[383] X. Xu, S. Yang, H. Wang, R. Guzman, Y. Gao, Y. Zhu, Y. Peng, Z. Zang, M. Xi, S. Tian, Y. Li, H. Lei, Z. Luo, J. Yang, Y. Wang, T. Xia, W. Zhou, Y. Huang, and Y. Ye, "Ferromagnetic-antiferromagnetic coexisting ground state and exchange bias effects in MnBi4Te7 and MnBi6Te10", Nature Communications **13**, 7646 (2022) (cit. on p. 27).

[384] A. V. Tcakaev et al., "Intermixing-Driven Surface and Bulk Ferromagnetism in the Quantum Anomalous Hall Candidate MnBi6Te10", Advanced Science **10**, 2203239 (2023) (cit. on p. 27).

[385] J. Li, Y. Li, S. Du, Z. Wang, B. L. Gu, S. C. Zhang, K. He, W. Duan, and Y. Xu, "Intrinsic magnetic topological insulators in van der Waals layered MnBi2Te4-family materials", Science Advances **5**, eaaw5685 (2019) (cit. on pp. 27, 85).

[386] L. Zhou, Z. Tan, D. Yan, Z. Fang, Y. Shi, and H. Weng, "Topological phase transition in the layered magnetic compound MnSb2Te4: Spin-orbit coupling and interlayer coupling dependence", Physical Review B **102**, 085114 (2020) (cit. on p. 27).

[387] P. Li, J. Yu, Y. Wang, and W. Luo, "Electronic structure and topological phases of the magnetic layered materials MnBi2Te4, MnBi2Se4, and MnSb2Te4", Physical Review B **103**, 155118 (2021) (cit. on p. 27).

[388] Q. Jiang, C. Wang, P. Malinowski, Z. Liu, Y. Shi, Z. Lin, Z. Fei, T. Song, D. Graf, S. Chikara, X. Xu, J. Yan, D. Xiao, and J. H. Chu, "Quantum oscillations in the field-induced ferromagnetic state of MnBi2-xSbxTe4", Physical Review B **103**, 205111 (2021) (cit. on p. 27).

[389] S. Chowdhury, K. F. Garrity, and F. Tavazza, "Prediction of Weyl semimetal and antiferromagnetic topological insulator phases in Bi2MnSe4", npj Computational Materials **5**, 33 (2019) (cit. on p. 27).

[390] B. Karpiak, A. W. Cummings, K. Zollner, M. Vila, D. Khokhriakov, A. M. Hoque, A. Dankert, P. Svedlindh, J. Fabian, S. Roche, and S. P. Dash, "Magnetic proximity in a van der Waals heterostructure of magnetic insulator and graphene", 2D Materials **7**, 015026 (2020) (cit. on p. 29).

[391] B. Zhao, R. Ngaloy, S. Ghosh, S. Ershadrad, R. Gupta, K. Ali, A. M. Hoque, B. Karpiak, D. Khokhriakov, C. Polley, B. Thiagarajan, A. Kalaboukhov, P. Svedlindh, B. Sanyal, and S. P. Dash, "A Room-Temperature Spin-Valve with van der Waals Ferromagnet Fe5GeTe2/ Graphene Heterostructure", Advanced Materials **35**, 2209113 (2023) (cit. on pp. 29, 36, 37, 52, 54, 60, 81, 83).

[392] B. Zhao, B. Karpiak, A. M. Hoque, P. Dhagat, and S. P. Dash, "Strong perpendicular anisotropic ferromagnet Fe3GeTe2/graphene van der Waals heterostructure", Journal of Physics D: Applied Physics **56**, 094001 (2023) (cit. on p. 29).

[393] R. Ngaloy, B. Zhao, S. Ershadrad, R. Gupta, M. Davoudiniya, L. Bainsla, L. Sjöström, M. A. Hoque, A. Kalaboukhov, P. Svedlindh, B. Sanyal, and S. P. Dash, "Strong In-Plane Magnetization and Spin Polarization in (Co0.15Fe0.85)5GeTe2/Graphene van der Waals Heterostructure Spin-Valve at Room Temperature", ACS Nano **18**, 5240–5248 (2024) (cit. on p. 29).

[394] B. Zhao, L. Pandey, K. Ali, E. Wang, C. M. Polley, B. Thiagarajan, P. Makk, M. H. D. Guimarães, and S. P. Dash, "Field-Free Spin-Orbit Torque Switching of Canted van der Waals Magnets", ACS Nano **19**, 13817–13824 (2025) (cit. on pp. 29, 59).

[395] B. Zhao, L. Bainsla, S. Ershadrad, L. Zeng, R. Ngaloy, P. Svedlindh, E. Olsson, B. Sanyal, and S. P. Dash, "Coexisting Non-Trivial Van der Waals Magnetic Orders Enable Field-Free Spin-Orbit Torque Magnetization Dynamics", Advanced Materials **37**, 2502822 (2025) (cit. on p. 29).

[396] R. Ngaloy, N. Yamashita, B. Zhao, S. Kim, K. Yamashita, I. P. C. Cools, M. N. Agusutrisno, S. Lee, Y. Kurokawa, C.-Y. You, H. Yuasa, and S. P. Dash, "Deterministic spin-orbit torque switching of epitaxial ferrimagnetic insulator with perpendicular magnetic anisotropy fabricated by on-axis magnetron sputtering", npj Spintronics **3**, 40 (2025) (cit. on p. 29).

[397] S. Parkin and S. H. Yang, "Memory on the racetrack", Nature Nanotechnology **10**, 195–198 (2015) (cit. on p. 29).

[398] M. Zhao, A. Chen, P. Y. Huang, C. Liu, L. Shen, J. Liu, L. Zhao, B. Fang, W. C. Yue, D. Zheng, L. Wang, H. Bai, K. Shen, Y. Zhou, S. Wang, E. Liu, S. He, Y. L. Wang, X. Zhang, and W. Jiang, "Electrical detection of mobile skyrmions with 100% tunneling magnetoresistance

in a racetrack-like device", npj Quantum Materials **9**, 50 (2024) (cit. on p. 29).

[399] Q. Shao, "Magnetic whirlpools offer improved data storage", Nature **627**, 494–495 (2024) (cit. on p. 29).

[400] M. Al Bahri and R. Sbiaa, "Geometrically pinned magnetic domain wall for multi-bit per cell storage memory", Scientific Reports **6**, 28590 (2016) (cit. on p. 29).

[401] M. Al Bahri, B. Borie, T. L. Jin, R. Sbiaa, M. Kläui, and S. N. Piramanayagam, "Staggered Magnetic Nanowire Devices for Effective Domain-Wall Pinning in Racetrack Memory", Physical Review Applied **11**, 024023 (2019) (cit. on pp. 29, 42).

[402] A. Sarkar, S. Srinivasan, B. Behin-Aein, and S. Datta, "Modeling all spin logic: Multi-magnet networks interacting via spin currents", in 2011 International Electron Devices Meeting (2011), p. 11.1 (cit. on pp. 29, 41).

[403] C. H. Marrows, J. Barker, T. A. Moore, and T. Moorsom, "Neuromorphic computing with spintronics", npj Spintronics **2**, 12 (2024) (cit. on p. 29).

[404] K. A. Omari, T. J. Broomhall, R. W. Dawidek, D. A. Allwood, R. C. Bradley, J. M. Wood, P. W. Fry, M. C. Rosamond, E. H. Linfield, M. Y. Im, P. J. Fischer, and T. J. Hayward, "Toward Chirality-Encoded Domain Wall Logic", Advanced Functional Materials **29**, 1807282 (2019) (cit. on p. 29).

[405] Q. Wang, M. Kewenig, M. Schneider, R. Verba, F. Kohl, B. Heinz, M. Geilen, M. Mohseni, B. Lägel, F. Ciubotaru, C. Adelmann, C. Dubs, S. D. Cotofana, O. V. Dobrovolskiy, T. Brächer, P. Pirro, and A. V. Chumak, "A magnonic directional coupler for integrated magnonic half-adders", Nature Electronics **3**, 765–774 (2020) (cit. on p. 29).

[406] S. Datta and B. Das, "Electronic analog of the electro-optic modulator", Applied Physics Letters **56**, 665–667 (1990) (cit. on p. 29).

[407] M. Zeng, L. Shen, M. Zhou, C. Zhang, and Y. Feng, "Graphene-based bipolar spin diode and spin transistor: Rectification and amplification of spin-polarized current", Physical Review B **83**, 115427 (2011) (cit. on p. 29).

[408] H. Wen, H. Dery, W. Amamou, T. Zhu, Z. Lin, J. Shi, I. Žutić, I. Krivorotov, L. J. Sham, and R. K. Kawakami, "Experimental Demonstration of XOR Operation in Graphene Magnetologic Gates at Room Temperature", Physical Review Applied **5**, 044003 (2016) (cit. on p. 29).

[409] R. P. Cowburn, A. O. Adeyeye, and M. E. Welland, "Configurational anisotropy in nanomagnets", Physical Review Letters **81**, 5414–5417 (1998) (cit. on pp. 29, 48).

[410] Y.-S. Shin, H.-J. Lee, J. Kim, J. Park, and K. Char, "Magnetic domain configuration in cobalt and permalloy micro-structures", Journal of the Korean Physical Society **44**, 904–907 (2004) (cit. on pp. 29, 48).

[411] A. Himeno, S. Kasai, and T. Ono, "Current-driven domain-wall motion in magnetic wires with asymmetric notches", Applied Physics Letters **87**, 243108 (2005) (cit. on pp. 29, 42).

[412] A. Wachowiak, J. Wiebe, M. Bode, O. Pietzsch, M. Morgenstern, and R. Wiesendanger, "Direct observation of internal spin structure of magnetic vortex cores", Science **298**, 577–580 (2002) (cit. on p. 29).

[413] M. Schneider, H. Hoffmann, S. Otto, T. Haug, and J. Zweck, "Stability of magnetic vortices in flat submicron permalloy cylinders", Journal of Applied Physics **92**, 1466–1472 (2002) (cit. on pp. 29, 46).

[414] F. Casola, T. van der Sar, and A. Yacoby, "Probing condensed matter physics with magnetometry based on nitrogen-vacancy centres in diamond", Nature Reviews Materials **3**, 17088 (2018) (cit. on p. 29).

[415] M. Kläui, C. A. Vaz, J. A. Bland, W. Wernsdorfer, G. Faini, E. Cambril, L. J. Heyderman, F. Nolting, and U. Rüdiger, "Controlled and reproducible domain wall displacement by current pulses injected into ferromagnetic ring structures", Physical Review Letters **94**, 106601 (2005) (cit. on pp. 29, 42).

[416] N. Trong Hai, Z. T. Chen, I. Kindiak, R. C. Bhatt, L. X. Ye, T.-h. Wu, K. A. Zvezdin, L. Horng, and J. C. Wu, "Electrical characterization of magnetic domain wall via distinctive hysteresis and magnetoresistance", Journal of Magnetism and Magnetic Materials **546**, 168776 (2022) (cit. on p. 29).

[417] V. T. Pham, G. Zahnd, A. Marty, W. Savero Torres, M. Jamet, P. Noël, L. Vila, and J. P. Attané, "Electrical detection of magnetic domain walls by inverse and direct spin Hall effect", Applied Physics Letters **109**, 192401 (2016) (cit. on p. 29).

[418] N. E. Penthorn, X. Hao, Z. Wang, Y. Huai, and H. W. Jiang, "Experimental Observation of Single Skyrmion Signatures in a Magnetic Tunnel Junction", Physical Review Letters **122**, 257201 (2019) (cit. on p. 29).

[419] E. Raymenants, O. Bultynck, D. Wan, T. Devolder, K. Garello, L. Souriau, A. Thiam, D. Tsvetanova, Y. Canvel, D. E. Nikonov, I. A. Young, M. Heyns, B. Soree, I. Asselberghs, I. Radu, S. Couet, and V. D. Nguyen, "Nanoscale domain wall devices with magnetic tunnel junction read and write", Nature Electronics **4**, 392–398 (2021) (cit. on p. 29).

[420] T. Kimura, Y. Otani, and J. Hamrle, "Determination of magnetic vortex chirality using lateral spin-valve geometry", Applied Physics Letters **87**, 172506 (2005) (cit. on pp. 29, 30, 50).

[421] T. Kimura and Y. Otani, "Magnetization process of a single magnetic ring detected by nonlocal spin valve measurement", Journal of Applied Physics **101**, 126102 (2007) (cit. on pp. 29, 30).

[422] D. Ilgaz, J. Nievendick, L. Heyne, D. Backes, J. Rhensius, T. A. Moore, M. A. Niño, A. Locatelli, T. O. Menteş, A. V. Schmidsfeld, A. V. Bieren, S. Krzyk, L. J. Heyderman, and M. Kläui, "Domain-wall depinning assisted by pure spin currents", Physical Review Letters **105**, 076601 (2010) (cit. on pp. 29, 30).

[423] N. Motzko, B. Burkhardt, N. Richter, R. Reeve, P. Laczkowski, W. Savero Torres, L. Vila, J. P. Attané, and M. Kläui, "Pure spin current-induced domain wall motion probed by localized spin signal detection", Physical Review B **88**, 214405 (2013) (cit. on pp. 29, 30).

[424] A. Avsar, H. Ochoa, F. Guinea, B. Zyilmaz, B. J. Van Wees, and I. J. Vera-Marun, "Colloquium: Spintronics in graphene and other two-dimensional materials", Reviews of Modern Physics **92**, 021003 (2020) (cit. on pp. 30, 63).

[425] J. F. Sierra, J. Fabian, R. K. Kawakami, S. Roche, and S. O. Valenzuela, "Van der Waals heterostructures for spintronics and opto-spintronics", Nature Nanotechnology **16**, 856–868 (2021) (cit. on p. 30).

[426] S. Roche, J. Åkerman, B. Beschoten, J. C. Charlier, M. Chshiev, S. P. Dash, B. Dlubak, J. Fabian, A. Fert, M. Guimarães, F. Guinea, I. Grigorieva, C. Schönenberger, P. Seneor, C. Stampfer, S. O. Valenzuela, X. Waintal, and B. Van Wees, "Graphene spintronics: The Eu-

ropean Flagship perspective", 2D Materials **2**, 030202 (2015) (cit. on p. 30).

[427] N. Tombros, C. Jozsa, M. Popinciuc, H. T. Jonkman, and B. J. Van Wees, "Electronic spin transport and spin precession in single graphene layers at room temperature", Nature **448**, 571–574 (2007) (cit. on pp. 30, 38, 57, 67).

[428] M. V. Kamalakar, C. Groenveld, A. Dankert, and S. P. Dash, "Long distance spin communication in chemical vapour deposited graphene", Nature Communications **6**, 6766 (2015) (cit. on pp. 30, 39, 71).

[429] D. Khokhriakov, B. Karpiak, A. M. Hoque, and S. P. Dash, "Two-dimensional spintronic circuit architectures on large scale graphene", Carbon **161**, 892–899 (2020) (cit. on pp. 30, 36–39, 41).

[430] J. Panda, M. Ramu, O. Karis, T. Sarkar, and M. V. Kamalakar, "Ultimate spin currents in commercial chemical vapor deposited graphene", ACS Nano **14**, 12771–12780 (2020) (cit. on pp. 30, 39).

[431] T. Bisswanger, Z. Winter, A. Schmidt, F. Volmer, K. Watanabe, T. Taniguchi, C. Stampfer, and B. Beschoten, "CVD Bilayer Graphene Spin Valves with 26 μm Spin Diffusion Length at Room Temperature", Nano Letters **22**, 4949–4955 (2022) (cit. on pp. 30, 39).

[432] K. S. Novoselov, A. K. Geim, S. V. Morozov, D. Jiang, Y. Zhang, S. V. Dubonos, I. V. Grigorieva, and A. A. Firsov, "Electric Field Effect in Atomically Thin Carbon Films", Science **306**, 666–669 (2004) (cit. on p. 32).

[433] The Royal Swedish Academy of Science, *Nobelpriset i fysik 2010 [Press release]*, 2010 (cit. on p. 32).

[434] C. Lee, X. Wei, J. W. Kysar, and J. Hone, "Measurement of the Elastic Properties and Intrinsic Strength of Monolayer Graphene", Science **321**, 385–388 (2008) (cit. on p. 32).

[435] R. R. Nair, P. Blake, A. N. Grigorenko, K. S. Novoselov, T. J. Booth, T. Stauber, N. M. Peres, and A. K. Geim, "Fine structure constant defines visual transparency of graphene", Science **320**, 1308 (2008) (cit. on p. 32).

[436] K. S. Novoselov, A. K. Geim, S. V. Morozov, D. Jiang, M. I. Katsnelson, I. V. Grigorieva, S. V. Dubonos, and A. A. Firsov, "Two-dimensional gas of massless Dirac fermions in graphene", Nature **438**, 197–200 (2005) (cit. on p. 32).

[437] M. S. Dresselhaus and G. Dresselhaus, "Intercalation compounds of graphite", Advances in Physics **51**, 1–186 (2002) (cit. on p. 32).

[438] N. Brandt, S. Chudinov, and Y. Ponomarev, *Semimetals 1: Graphite and Its Compounds*, edited by V. Agranovich and A. Maradudin (North-Holland, Amsterdam, 1988) (cit. on p. 32).

[439] S. V. Morozov, K. S. Novoselov, M. I. Katsnelson, F. Schedin, D. C. Elias, J. A. Jaszczak, and A. K. Geim, "Giant intrinsic carrier mobilities in graphene and its bilayer", Physical Review Letters **100**, 016602 (2008) (cit. on p. 32).

[440] J. H. Chen, C. Jang, S. Xiao, M. Ishigami, and M. S. Fuhrer, "Intrinsic and extrinsic performance limits of graphene devices on SiO2", Nature Nanotechnology **3**, 206–209 (2008) (cit. on p. 32).

[441] X. Du, I. Skachko, A. Barker, and E. Y. Andrei, "Approaching ballistic transport in suspended graphene", Nature Nanotechnology **3**, 491–495 (2008) (cit. on p. 32).

[442] K. I. Bolotin, K. J. Sikes, Z. Jiang, M. Klima, G. Fudenberg, J. Hone, P. Kim, and H. L. Stormer, "Ultrahigh electron mobility in suspended graphene", Solid State Communications **146**, 351–355 (2008) (cit. on p. 32).

[443] D. Pesin and A. H. MacDonald, "Spintronics and pseudospintronics in graphene and topological insulators", Nature Materials **11**, 409–416 (2012) (cit. on p. 32).

[444] D. A. Neamen, *Semiconductor Physics and Devices*, 4th ed. (McGraw-Hill, New York, NY, 2012) (cit. on p. 32).

[445] T. Ando, "The electronic properties of graphene and carbon nanotubes", NPG Asia Materials **1**, 17–21 (2009) (cit. on p. 33).

[446] Y. Zhang, Y. W. Tan, H. L. Stormer, and P. Kim, "Experimental observation of the quantum Hall effect and Berry's phase in graphene", Nature **438**, 201–204 (2005) (cit. on p. 32).

[447] K. S. Novoselov, Z. Jiang, Y. Zhang, S. V. Morozov, H. L. Stormer, U. Zeitler, J. C. Maan, G. S. Boebinger, P. Kim, and A. K. Geim, "Room-temperature quantum hall effect in graphene", Science **315**, 1379 (2007) (cit. on p. 32).

[448] H. He, K. Cedergren, N. Shetty, S. Lara-Avila, S. Kubatkin, T. Bergsten, and G. Eklund, "Accurate graphene quantum Hall arrays for the new International System of Units", Nature Communications **13**, 6933 (2022) (cit. on p. 32).

[449] A. A. Balandin, S. Ghosh, W. Bao, I. Calizo, D. Teweldebrhan, F. Miao, and C. N. Lau, "Superior thermal conductivity of single-layer graphene", Nano Letters **8**, 902–907 (2008) (cit. on p. 32).

[450] A. Kaidarova, M. A. Khan, M. Marengo, L. Swanepoel, A. Przybysz, C. Muller, A. Fahlman, U. Buttner, N. R. Geraldi, R. P. Wilson, C. M. Duarte, and J. Kosel, "Wearable multifunctional printed graphene sensors", npj Flexible Electronics **3**, 15 (2019) (cit. on p. 32).

[451] E. O. Polat, G. Mercier, I. Nikitskiy, E. Puma, T. Galan, S. Gupta, M. Montagut, J. J. Piqueras, M. Bouwens, T. Durduran, G. Konstantatos, S. Goossens, and F. Koppens, "Flexible graphene photodetectors for wearable fitness monitoring", Science Advances **5**, eaaw7846 (2019) (cit. on p. 32).

[452] N. Alzate-Carvajal and A. Luican-Mayer, "Functionalized Graphene Surfaces for Selective Gas Sensing", ACS Omega **5**, 21320–21329 (2020) (cit. on p. 33).

[453] Z. Chen, Q. Lei, Y. Ma, J. Wang, Y. Yan, J. Yin, J. Li, J. Shen, G. Li, T. Pan, X. Dong, B. Davaasuren, Y. Zhang, J. Z. Liu, J. Tao, and Y. Han, "Highly sensitive, responsive, and selective iodine gas sensor fabricated using AgI-functionalized graphene", Nature Communications **16**, 1169 (2025) (cit. on p. 33).

[454] A. Hasnain, H. Heilmann, A. Pohl, C. Weber, B. Bufe, and A. Tarasov, "Cross-Platform Biosensing of Immune Receptors Using Peptide- Functionalized Graphene", Advanced Science **13**, e19436 (2025) (cit. on p. 33).

[455] M. Khan, I. Mijakovic, S. Pandit, and A. Yurgens, "A complementary impedance spectroscopy biosensing method with graphene", Biosensors and Bioelectronics **305**, 118679 (2026) (cit. on p. 33).

[456] Y. Cao, V. Fatemi, S. Fang, K. Watanabe, T. Taniguchi, E. Kaxiras, and P. Jarillo-Herrero, "Unconventional superconductivity in magic-angle graphene superlattices", Nature **556**, 43–50 (2018) (cit. on p. 33).

[457] E. Y. Tsymbal, S. Yuasa, W. Wang, P. Khalili Amiri, C. Gong, and D.-F. Shao, "Magnetic tunnel junctions", Nature Review Methods Primers **6**, 38 (2026) (cit. on p. 34).

[458] F. J. Jedema, H. B. Heersche, A. T. Filip, J. J. A. Baselmans, and B. J. van Wees, "Electrical detection of spin precession in a metallic mesoscopic spin valve", Nature **416**, 713–716 (2002) (cit. on pp. 34, 36).

[459] M. Z. Iqbal, N. A. Qureshi, and G. Hussain, "Recent advancements in 2D-materials interface based magnetic junctions for spintronics", Journal of Magnetism and Magnetic Materials **457**, 110–125 (2018) (cit. on p. 34).

[460] J. Tang and K. L. Wang, "Electrical spin injection and transport in semiconductor nanowires: Challenges, progress and perspectives", Nanoscale **7**, 4325–4337 (2015) (cit. on p. 34).

[461] W. Han, R. K. Kawakami, M. Gmitra, and J. Fabian, "Graphene spintronics", Nature Nanotechnology **9**, 794–807 (2014) (cit. on pp. 36, 63).

[462] E. W. Hill, A. K. Geim, K. Novoselov, F. Schedin, and P. Blake, "Graphene spin valve devices", IEEE Transactions on Magnetics **42**, 2694–2696 (2006) (cit. on p. 38).

[463] M. Choi, J. Baek, H. Zeng, S. Jin, and S. Jeon, "Toward high-quality graphene film growth by chemical vapor deposition system", Current Opinion in Solid State and Materials Science **31**, 101176 (2024) (cit. on p. 38).

[464] A. Fert and H. Jaffrès, "Conditions for efficient spin injection from a ferromagnetic metal into a semiconductor", Physical Review B - Condensed Matter and Materials Physics **64**, 184420 (2001) (cit. on pp. 39, 80).

[465] W. Han, K. Pi, K. M. McCreary, Y. Li, J. J. Wong, A. G. Swartz, and R. K. Kawakami, "Tunneling spin injection into single layer graphene", Physical Review Letters **105**, 167202 (2010) (cit. on pp. 39, 67, 71, 80).

[466] Z. M. Gebeyehu, S. Parui, J. F. Sierra, M. Timmermans, M. J. Esplandiu, S. Brems, C. Huyghebaert, K. Garello, M. V. Costache, and S. O. Valenzuela, "Spin communication over 30 μm long channels of chemical vapor deposited graphene on SiO2", 2D Materials **6**, 034003 (2019) (cit. on p. 39).

[467] M. V. Kamalakar, A. Dankert, J. Bergsten, T. Ive, and S. P. Dash, "Enhanced tunnel spin injection into graphene using chemical vapor deposited hexagonal boron nitride", Scientific Reports **4**, 6146 (2014) (cit. on pp. 41, 43, 71).

[468] M. V. Kamalakar, A. Dankert, J. Bergsten, T. Ive, and S. P. Dash, "Spintronics with graphene-hexagonal boron nitride van der Waals heterostructures", Applied Physics Letters **105**, 212405 (2014) (cit. on p. 41).

[469] A. Dankert, M. Venkata Kamalakar, A. Wajid, R. S. Patel, and S. P. Dash, "Tunnel magnetoresistance with atomically thin two-dimensional hexagonal boron nitride barriers", Nano Research **8**, 1357–1364 (2015) (cit. on pp. 41, 43).

[470] M. Drögeler, C. Franzen, F. Volmer, T. Pohlmann, L. Banszerus, M. Wolter, K. Watanabe, T. Taniguchi, C. Stampfer, and B. Beschoten, "Spin Lifetimes Exceeding 12 ns in Graphene Nonlocal Spin Valve Devices", Nano Letters **16**, 3533–3539 (2016) (cit. on p. 41).

[471] J. Wang, F. Ma, and M. Sun, "Graphene, hexagonal boron nitride, and their heterostructures: properties and applications", RSC Advances **7**, 16801–16822 (2017) (cit. on p. 41).

[472] M. Kläui, C. A. Vaz, J. Rothman, J. A. Bland, W. Wernsdorfer, G. Faini, and E. Cambril, "Domain Wall Pinning in Narrow Ferromagnetic Ring Structures Probed by Magnetoresistance Measurements", Physical Review Letters **90**, 097202 (2003) (cit. on p. 42).

[473] H. Y. Yuan and X. R. Wang, "Domain wall pinning in notched nanowires", Physical Review B **89**, 054423 (2014) (cit. on p. 42).

[474] M. V. Kamalakar, A. Dankert, P. J. Kelly, and S. P. Dash, "Inversion of Spin Signal and Spin Filtering in Ferromagnet|Hexagonal Boron Nitride-Graphene van der Waals Heterostructures", Scientific Reports **6**, 21168 (2016) (cit. on p. 43).

[475] A. Vansteenkiste, J. Leliaert, M. Dvornik, M. Helsen, F. Garcia-Sanchez, and B. van Waeyenberge, "The design and verification of MuMax3", AIP Advances **4**, 107133 (2014) (cit. on p. 43).

[476] L. Exl, S. Bance, F. Reichel, T. Schrefl, H. Peter Stimming, and N. J. Mauser, "LaBonte's method revisited: An effective steepest descent method for micromagnetic energy minimization", Journal of Applied Physics **115**, 17D118 (2014) (cit. on p. 43).

[477] J. Leliaert, B. Van de Wiele, A. Vansteenkiste, L. Laurson, G. Durin, L. Dupré, and B. Van Waeyenberge, "Current-driven domain wall mobility in polycrystalline Permalloy nanowires: A numerical study", Journal of Applied Physics **115**, 233903 (2014) (cit. on p. 43).

[478] R. P. Cowburn, D. K. Koltsov, A. O. Adeyeye, M. E. Welland, and D. M. Tricker, "Single-domain circular nanomagnets", Physical Review Letters **83**, 1042–1045 (1999) (cit. on pp. 46, 48, 50).

[479] R. Antos, Y. Otani, and J. Shibata, "Magnetic vortex dynamics", Journal of the Physical Society of Japan **77**, 031004 (2008) (cit. on p. 46).

[480] B. Van Waeyenberge, A. Puzic, H. Stoll, K. W. Chou, T. Tyliszczak, R. Hertel, M. Fähnle, H. Brückl, K. Rott, G. Reiss, I. Neudecker, D. Weiss, C. H. Back, and G. Schütz, "Magnetic vortex core reversal by excitation with short bursts of an alternating field", Nature **444**, 461–464 (2006) (cit. on pp. 48, 50).

[481] K. S. Burch, D. Mandrus, and J.-G. Park, "Magnetism in two-dimensional van der Waals materials", Nature **563**, 47–52 (2018) (cit. on p. 52).

[482] M.-C. Wang, C.-C. Huang, C.-H. Cheung, C.-Y. Chen, S. G. Tan, T.-W. Huang, Y. Zhao, Y. Zhao, G. Wu, Y.-P. Feng, H.-C. Wu, and C.-R. Chang, "Prospects and Opportunities of 2D van der Waals Magnetic Systems", Annalen der Physik **532**, 1900452 (2020) (cit. on p. 52).

[483] Y. Wu, S. Zhang, J. Zhang, W. Wang, Y. L. Zhu, J. Hu, G. Yin, K. Wong, C. Fang, C. Wan, X. Han, Q. Shao, T. Taniguchi, K. Watanabe, J. Zang, Z. Mao, X. Zhang, and K. L. Wang, "Néel-type skyrmion in WTe2/Fe3GeTe2 van der Waals heterostructure", Nature Communications **11**, 3860 (2020) (cit. on p. 52).

[484] H. Zhang, D. Raftrey, Y.-T. Chan, Y.-T. Shao, R. Chen, X. Chen, X. Huang, J. T. Reichanadter, K. Dong, S. Susarla, L. Caretta, Z. Chen, J. Yao, P. Fischer, J. B. Neaton, W. Wu, D. A. Muller, R. J. Birgeneau, and R. Ramesh, "Room-temperature skyrmion lattice in a layered magnet (Fe0.5Co0.5)5GeTe2", Science Advances **8**, eabm7103 (2022) (cit. on p. 52).

[485] M. Schmitt, T. Denneulin, A. Kovács, T. G. Saunderson, P. Rüßmann, A. Shahee, T. Scholz, A. H. Tavabi, M. Gradhand, P. Mavropoulos, B. V. Lotsch, R. E. Dunin-Borkowski, Y. Mokrousov, S. Blügel, and M. Kläui, "Skyrmionic spin structures in layered Fe5GeTe2 up to room temperature", Communications Physics **5**, 254 (2022) (cit. on p. 52).

[486] S. Grebenchuk, C. McKeever, M. Grzeszczyk, Z. Chen, M. Šiškins, A. R. McCray, Y. Li, A. K. Petford-Long, C. M. Phatak, D. Ruihuan, L. Zheng, K. S. Novoselov, E. J. Santos, and M. Koperski, "Topological Spin Textures in an Insulating van der Waals Ferromagnet", Advanced Materials **36**, 2311949 (2024) (cit. on p. 52).

[487] M.-G. Han, J. D. Thomsen, J. P. Philbin, J. Mun, E. Park, F. Camino, L. Děkanovský, C. Liu, Z. Sofer, P. Narang, F. M. Ross, and Y. Zhu, "Electric Field Control of Magnetic Skyrmion Helicity in a Centrosymmetric 2D van der Waals Magnet", Nano Letters **25**, 5174–5180 (2025) (cit. on p. 52).

[488] T. T. Ly, J. Park, K. Kim, H.-B. Ahn, N. J. Lee, K. Kim, T. E. Park, G. Duvjir, N. H. Lam, K. Jang, C. Y. You, Y. Jo, S. K. Kim, C. Lee, S. Kim, and J. Kim, "Direct Observation of Fe-Ge Ordering in Fe5-xGeTe2 Crystals and Resultant Helimagnetism", Advanced Functional Materials **31**, 2009758 (2021) (cit. on p. 52).

[489] R. Fujita, P. Bassirian, Z. Li, Y. Guo, M. A. Mawass, F. Kronast, G. Van Der Laan, and T. Hesjedal, "Layer-Dependent Magnetic Domains in Atomically Thin Fe5GeTe2", ACS Nano **16**, 10545–10553 (2022) (cit. on p. 52).

[490] M. Kläui, C. A. Vaz, A. Lapicki, T. Suzuki, Z. Cui, and J. A. Bland, "Domain wall pinning in ferromagnetic structures fabricated by focused ion beam", Microelectronic Engineering **73-74**, 785–789 (2004) (cit. on p. 52).

[491] F. Büttner, I. Lemesh, M. Schneider, B. Pfau, C. M. Günther, P. Hessing, J. Geilhufe, L. Caretta, D. Engel, B. Krüger, J. Viefhaus, S. Eisebitt, and G. S. Beach, "Field-free deterministic ultrafast creation of magnetic skyrmions by spin-orbit torques", Nature Nanotechnology **12**, 1040–1044 (2017) (cit. on p. 52).

[492] H. Vakili, W. Zhou, C. T. Ma, S. J. Poon, M. G. Morshed, M. N. Sakib, S. Ganguly, M. Stan, T. Q. Hartnett, P. Balachandran, J. W. Xu, Y. Quessab, A. D. Kent, K. Litzius, G. S. Beach, and A. W. Ghosh, "Skyrmionics-Computing and memory technologies based on topological excitations in magnets", Journal of Applied Physics **130**, 070908 (2021) (cit. on p. 52).

[493] L.-M. Kern, B. Pfau, V. Deinhart, M. Schneider, C. Klose, K. Gerlinger, S. Wittrock, D. Engel, I. Will, C. M. Günther, R. Liefferink, J. H. Mentink, S. Wintz, M. Weigand, M. J. Huang, R. Battistelli, D. Metternich, F. Büttner, K. Höflich, and S. Eisebitt, "Deterministic Generation and Guided Motion of Magnetic Skyrmions by Focused He+-Ion Irradiation", Nano Letters **22**, 4028–4035 (2022) (cit. on p. 52).

[494] X. Lv, K. Pei, C. Yang, G. Qin, M. Liu, J. Zhang, and R. Che, "Controllable Topological Magnetic Transformations in the Thickness-Tunable van der Waals Ferromagnet Fe5GeTe2", ACS Nano **16**, 19319–19327 (2022) (cit. on p. 54).

[495] X.-L. Qi and S.-C. Zhang, "Topological insulators and superconductors", Reviews of Modern Physics **83**, 1057–1110 (2011) (cit. on p. 63).

[496] Y. Tokura, M. Kawasaki, and N. Nagaosa, "Emergent functions of quantum materials", Nature Physics **13**, 1056–1068 (2017) (cit. on p. 63).

[497] A. Manchon, J. Železný, I. M. Miron, T. Jungwirth, J. Sinova, A. Thiaville, K. Garello, and P. Gambardella, "Current-induced spin-orbit torques in ferromagnetic and antiferromagnetic systems", Reviews of Modern Physics **91**, 035004 (2019) (cit. on p. 63).

[498] Y. Lei et al., "Graphene and Beyond: Recent Advances in Two-Dimensional Materials Synthesis, Properties, and Devices", ACS Nanoscience Au **2**, 450–485 (2022) (cit. on p. 63).

[499] S. K. Chakraborty, B. Kundu, B. Nayak, S. P. Dash, and P. K. Sahoo, "Challenges and opportunities in 2D heterostructures for electronic and optoelectronic devices", iScience **25**, 103942 (2022) (cit. on p. 63).

[500] J. Han, A. Richardella, S. A. Siddiqui, J. Finley, N. Samarth, and L. Liu, "Room-Temperature Spin-Orbit Torque Switching Induced by a Topological Insulator", Physical Review Letters **119**, 077702 (2017) (cit. on p. 63).

[501] L. Liu, A. Richardella, I. Garate, Y. Zhu, N. Samarth, and C. T. Chen, "Spin-polarized tunneling study of spin-momentum locking in topological insulators", Physical Review B **91**, 235437 (2015) (cit. on p. 63).

[502] J. Tian, I. Miotkowski, S. Hong, and Y. P. Chen, "Electrical injection and detection of spin-polarized currents in topological insulator Bi2Te2Se", Scientific Reports **5**, 14293 (2015) (cit. on p. 63).

[503] J. Tian, S. Hong, I. Miotkowski, S. Datta, and Y. P. Chen, "Observation of current-induced, long-lived persistent spin polarization in a topological insulator: A rechargeable spin battery", Science Advances **3**, e1602531 (2017) (cit. on p. 63).

[504] C. K. Safeer, F. Herling, W. Y. Choi, N. Ontoso, J. Ingla-Aynés, L. E. Hueso, and F. Casanova, "Reliability of spin-to-charge conversion measurements in graphene-based lateral spin valves", 2D Materials **9**, 015024 (2022) (cit. on p. 63).

[505] I. Belopolski, P. Yu, D. S. Sanchez, Y. Ishida, T. R. Chang, S. S. Zhang, S. Y. Xu, H. Zheng, G. Chang, G. Bian, H. T. Jeng, T. Kondo, H. Lin, Z. Liu, S. Shin, and M. Z. Hasan, "Signatures of a time-reversal symmetric Weyl semimetal with only four Weyl points", Nature Communications **8**, 942 (2017) (cit. on p. 64).

[506] R. Sun, S. Yang, X. Yang, E. Vetter, D. Sun, N. Li, L. Su, Y. Li, Y. Li, Z. Z. Gong, Z. K. Xie, K. Y. Hou, Q. Gul, W. He, X. Q. Zhang, and Z. H. Cheng, "Large Tunable Spin-to-Charge Conversion Induced by Hybrid Rashba and Dirac Surface States in Topological Insulator Heterostructures", Nano Letters **19**, 4420–4426 (2019) (cit. on pp. 65, 69, 75).

[507] Z. Kovács-Krausz, A. M. Hoque, P. Makk, B. Szentpéteri, M. Kocsis, B. Fülöp, M. V. Yakushev, T. V. Kuznetsova, O. E. Tereshchenko, K. A. Kokh, I. E. Lukács, T. Taniguchi, K. Watanabe, S. P. Dash, and S. Csonka, "Electrically Controlled Spin Injection from Giant Rashba Spin-Orbit Conductor BiTeBr", Nano Letters **20**, 4782–4791 (2020) (cit. on p. 67).

[508] D. Khokhriakov, B. Karpiak, A. M. Hoque, B. Zhao, S. Parui, and S. P. Dash, "Robust spin interconnect with isotropic spin dynamics in chemical vapor deposited graphene layers and boundaries", ACS Nano **14**, 15864–15873 (2020) (cit. on p. 67).

[509] B. Zhao, B. Karpiak, D. Khokhriakov, A. Johansson, A. M. Hoque, X. Xu, Y. Jiang, I. Mertig, and S. P. Dash, "Unconventional Charge–Spin Conversion in Weyl-Semimetal WTe2", Advanced Materials **32**, 2000818 (2020) (cit. on p. 69).

[510] C. J. Lee, H. Park, J. Kang, J. Lee, M. Choi, and H. Park, "Extraction of intrinsic field-effect mobility of graphene considering effects of gate-bias-induced contact modulation", Journal of Applied Physics **127**, 185105 (2020) (cit. on p. 71).

[511] A. M. Hoque, D. Khokhriakov, B. Karpiak, and S. P. Dash, "Charge-spin conversion in layered semimetal TaTe2 and spin injection in van der Waals heterostructures", Physical Review Research **2**, 033204 (2020) (cit. on p. 71).

[512] A. M. Hoque, V. Ramachandra, A. George, E. Najafidehaghani, Z. Gan, R. Mitra, B. Zhao, D. Khokhriakov, A. Turchanin, S. Lara-Avila, S. Kubatkin, and S. P. Dash, "Spin-valley coupling and spin-relaxation anisotropy in all-CVD Graphene-MoS2 van der Waals heterostructure", Physical Review Materials **7**, 044005 (2023) (cit. on pp. 71, 115).

[513] L. A. Benítez, W. Savero Torres, J. F. Sierra, M. Timmermans, J. H. Garcia, S. Roche, M. V. Costache, and S. O. Valenzuela, "Tunable room-temperature spin galvanic and spin Hall effects in van der Waals heterostructures", Nature Materials **19**, 170–175 (2020) (cit. on p. 72).

[514] F. Herling, C. K. Safeer, J. Ingla-Aynés, N. Ontoso, L. E. Hueso, and F. Casanova, "Gate tunability of highly efficient spin-to-charge conversion by spin Hall effect in graphene proximitized with WSe2", APL Materials **8**, 071103 (2020) (cit. on p. 72).

[515] L. Li, J. Zhang, G. Myeong, W. Shin, H. Lim, B. Kim, S. Kim, T. Jin, S. Cavill, B. S. Kim, C. Kim, J. Lischner, A. Ferreira, and S. Cho, "Gate-Tunable Reversible Rashba-Edelstein Effect in a Few-Layer Graphene/2H-TaS2 Heterostructure at Room Temperature", ACS Nano **14**, 5251–5259 (2020) (cit. on p. 72).

[516] B. Karpiak, A. Dankert, A. W. Cummings, S. R. Power, S. Roche, and S. P. Dash, "1D ferromagnetic edge contacts to 2D graphene/h-BN heterostructures", 2D Materials **5**, 014001 (2018) (cit. on p. 72).

[517] S. Takahashi and S. Maekawa, "Spin injection and detection in magnetic nanostructures", Physical Review B **67**, 052409 (2003) (cit. on pp. 81, 82).

[518] M. Zheng, W. Zhang, Y. Lv, Y. Liu, R. Xiong, Z. Zhang, and Z. Lu, "Observation of Thickness-Modulated Out-of-Plane Spin-Orbit Torque in Polycrystalline Few-Layer Td-WTe2 Film", Nanomaterials **15**, 762 (2025) (cit. on p. 82).

[519] G. Zahnd, L. Vila, V. T. Pham, M. Cosset-Cheneau, W. Lim, A. Brenac, P. Laczkowski, A. Marty, and J. P. Attané, "Spin diffusion length and polarization of ferromagnetic metals measured by the spin-absorption technique in lateral spin valves", Physical Review B **98**, 174414 (2018) (cit. on p. 82).

[520] W. Amamou, G. Stecklein, S. J. Koester, P. A. Crowell, and R. K. Kawakami, "Spin Absorption by In Situ Deposited Nanoscale Magnets on Graphene Spin Valves", Physical Review Applied **10**, 044050 (2018) (cit. on p. 83).

[521] M. I. D'yakonov and V. I. Perel', "Spin relaxation of conduction electrons in noncentrosymmetric semiconductors", Soviet Physics - Solid State **13**, 3023–3026 (1972) (cit. on p. 83).

[522] R. J. Elliott, "Theory of the effect of spin-orbit coupling on magnetic resonance in some semiconductors", Physical Review **96**, 266–279 (1954) (cit. on p. 83).

[523] Y. Yafet, "g Factors and Spin-Lattice Relaxation of Conduction Electrons", Solid State Physics **14**, 1–98 (1963) (cit. on p. 83).

[524] Y. Okazaki, T. Oe, M. Kawamura, R. Yoshimi, S. Nakamura, S. Takada, M. Mogi, K. S. Takahashi, A. Tsukazaki, M. Kawasaki, Y. Tokura, and N. H. Kaneko, "Quantum anomalous Hall effect with a permanent magnet defines a quantum resistance standard", Nature Physics **18**, 25–29 (2022) (cit. on p. 85).

[525] Y. Tokura, K. Yasuda, and A. Tsukazaki, "Magnetic topological insulators", Nature Reviews Physics **1**, 126–143 (2019) (cit. on p. 85).

[526] K. Yasuda, M. Mogi, R. Yoshimi, A. Tsukazaki, K. S. Takahashi, M. Kawasaki, F. Kagawa, and Y. Tokura, "Quantized chiral edge conduction on domain walls of a magnetic topological insulator", Science **358**, 1311–1314 (2017) (cit. on p. 85).

[527] J. Wang, B. Lian, X. L. Qi, and S. C. Zhang, "Quantized topological magnetoelectric effect of the zero-plateau quantum anomalous Hall state", Physical Review B - Condensed Matter and Materials Physics **92**, 081107(R) (2015) (cit. on p. 85).

[528] Y. Wan, J. Li, and Q. Liu, "Topological magnetoelectric response in ferromagnetic axion insulators", National Science Review **11**, nwac138 (2024) (cit. on p. 85).

[529] Y. Peng and Y. Xu, "Proximity-induced Majorana hinge modes in antiferromagnetic topological insulators", Physical Review B **99**, 195431 (2019) (cit. on p. 85).

[530] S.-K. Bac, K. Koller, F. Lux, J. Wang, L. Riney, K. Borisiak, W. Powers, M. Zhukovskyi, T. Orlova, M. Dobrowolska, J. K. Furdyna, N. R. Dilley, L. P. Rokhinson, Y. Mokrousov, R. J. McQueeney, O. Heinonen, X. Liu, and B. A. Assaf, "Topological response of the anomalous Hall effect in MnBi2Te4 due to magnetic canting", npj Quantum Materials **7**, 46 (2022) (cit. on pp. 85, 87, 90, 93, 106).

[531] H. Padmanabhan, M. Poore, P. K. Kim, N. Z. Koocher, V. A. Stoica, D. Puggioni, H. H. Wang, X. Shen, A. H. Reid, M. Gu, M. Wetherington, S. H. Lee, R. D. Schaller, Z. Mao, A. M. Lindenberg, X. Wang, J. M. Rondinelli, R. D. Averitt, and V. Gopalan, "Interlayer magnetophononic coupling in MnBi2Te4", Nature Communications **13**, 1929 (2022) (cit. on p. 85).

[532] Y Xu, D Kurebayashi, D Zhang, P Schoenherr, L Li, Z Yue, W. J. Ren, M.-G. Han, Y Zhu, Z Cheng, X Wang, O. A. Tretiakov, and J Seidel, "Antiferromagnetic Chiral Bobber Formation and Topological Proximity Effect in MnBi2Te4", arXiv, 2504.07747 (2025) (cit. on p. 85).

[533] J. Q. Yan, Q. Zhang, T. Heitmann, Z. Huang, K. Y. Chen, J. G. Cheng, W. Wu, D. Vaknin, B. C. Sales, and R. J. McQueeney, "Crystal growth and magnetic structure of MnBi2Te4", Physical Review Materials **3**, 064202 (2019) (cit. on pp. 85, 87, 93, 101).

[534] H. Zhu, J. Li, X. Chen, Y. Yu, and Q. Liu, "Magnetic geometry induced quantum geometry and nonlinear transports", Nature Communications **16**, 4882 (2025) (cit. on p. 86).

[535] C. A. Vaz, G. van der Laan, S. A. Cavill, H. A. Dürr, A. Fraile Rodríguez, F. Kronast, W. Kuch, P. Sainctavit, G. Schütz, H. Wende, E. Weschke, and F. Wilhelm, "X-ray magnetic circular dichroism", Nature Reviews Methods Primers **5**, 27 (2025) (cit. on pp. 88, 90).

[536] J. Stöhr and Y. Wu, "X-Ray Magnetic Circular Dichroism: Basic Concepts and Theory for 3D Transition Metal Atoms", in *New Directions in Research with Third-Generation Soft X-Ray Synchrotron Radiation Sources*, Vol. 254, edited by A. S. Schlachter and F. J. Wuilleumier (Springer, Dordrecht, the Netherlands, 1994), pp. 221–250 (cit. on p. 90).

[537] J. Stöhr, "Exploring the microscopic origin of magnetic anisotropies with X-ray magnetic circular dichroism (XMCD) spectroscopy", Journal of Magnetism and Magnetic Materials **200**, 470–497 (1999) (cit. on p. 90).

[538] S. F. Weber and V. Sunko, "Deterministic domain selection of antiferromagnets via magnetic fields", arXiv, 2601.06646 (2026) (cit. on p. 91).

[539] Y. Morishima, N. Yamaguchi, H. Sawahata, and F. Ishii, "Seebeck-induced anomalous Nernst effect in van der Waals MnBi2Te4 layers", Applied Physics Express **16**, 043003 (2023) (cit. on p. 101).

[540] L. Chai, F. Zhang, Y. Bai, and B. Dong, "Thermoelectric properties of monolayered MnBi2Te4", Journal of the American Ceramic Society **107**, 7331–7340 (2024) (cit. on p. 101).

[541] H. H. Wang, X. G. Luo, M. Z. Shi, K. L. Peng, B. Lei, J. H. Cui, D. H. Ma, W. Z. Zhuo, J. J. Ying, Z. Y. Wang, and X. H. Chen, "Possible bipolar effect inducing anomalous transport behavior in the magnetic topological insulator Mn(Bi1-x Sbx)2 Te4", Physical Review B **103**, 085126 (2021) (cit. on p. 101).

[542] M. Ceccardi, A. Zeugner, L. C. Folkers, C. Hess, B. Büchner, D. Marré, A. Isaeva, and F. Caglieris, "Anomalous Nernst effect in the topological and magnetic material MnBi4Te7", npj Quantum Materials **8**, 76 (2023) (cit. on p. 101).

[543] J. Yang, L. Wei, Y. Li, L. Chen, W. Niu, S. Wang, F. Li, P. Liu, S. Zhou, and Y. Pu, "Electric field control of nonlinear Hall effect in the type-II Weyl semimetal TaIrTe4", Applied Physics Letters **127**, 033102 (2025) (cit. on p. 103).

[544] S. Furuta, W. Koshibae, K. Matsuura, N. Abe, F. Wang, S. Zhou, T.-h. Arima, and F. Kagawa, "Reconsidering nonlinear emergent inductance: Time-varying Joule heating and its impact on AC electrical response", Physical Review B **110**, 174402 (2024) (cit. on p. 103).

[545] C. Thibierge, D. L'Hôte, F. Ladieu, and R. Tourbot, "A method for measuring the nonlinear response in dielectric spectroscopy through third harmonics detection", Review of Scientific Instruments **79**, 103905 (2008) (cit. on p. 103).

[546] D. Kaplan, T. Holder, and B. Yan, "Unification of Nonlinear Anomalous Hall Effect and Nonreciprocal Magnetoresistance in Metals by the Quantum Geometry", Physical Review Letters **132**, 26301 (2024) (cit. on p. 104).

[547] Y. X. Huang, Y. Wang, H. Wang, C. Xiao, X. Li, and S. A. Yang, "Nonlinear current response of two-dimensional systems under in-plane magnetic field", Physical Review B **108**, 075155 (2023) (cit. on p. 104).

[548] S. Bae, H. Kim, Y. Lee, X. Xu, J. S. Park, Y. Zheng, J. Balakrishnan, T. Lei, H. Ri Kim, Y. I. Song, Y. J. Kim, K. S. Kim, B. Özyilmaz, J. H. Ahn, B. H. Hong, and S. Iijima, "Roll-to-roll production of 30-inch graphene films for transparent electrodes", Nature Nanotechnology **5**, 574–578 (2010) (cit. on p. 115).

[549] J.-i. Fujita, T. Hiyama, A. Hirukawa, T. Kondo, J. Nakamura, S. I. Ito, R. Araki, Y. Ito, M. Takeguchi, and W. W. Pai, "Near room temperature chemical vapor deposition of graphene with diluted methane and molten gallium catalyst", Scientific Reports **7**, 12371 (2017) (cit. on p. 115).

[550] R. Ramaswamy, T. Dutta, S. Liang, G. Yang, M. S. Saifullah, and H. Yang, "Spin orbit torque driven magnetization switching with sputtered Bi2Se3 spin current source", Journal of Physics D: Applied Physics **52**, 224001 (2019) (cit. on p. 115).

[551] Q. Guo et al., "Electrically Tunable Wafer-Sized Three-Dimensional Topological Insulator Thin Films Grown by Magnetron Sputtering", Chinese Physics Letters **37**, 057301 (2020) (cit. on p. 115).

[552] X. Li, P. Li, V. D. Hou, M. DC, C.-H. Nien, F. Xue, D. Yi, C. Bi, C.-M. Lee, S.-J. Lin, W. Tsai, Y. Suzuki, and S. X. Wang, "Large and robust charge-to-spin conversion in sputtered conductive WTex with disorder", Matter **4**, 1639–1653 (2021) (cit. on p. 115).

[553] S. Shi, J. Li, C.-H. Hsu, K. Lee, Y. Wang, L. Yang, J. Wang, Q. Wang, H. Wu, W. Zhang, G. Eda, G. Liang, H. Chang, and H. Yang, "Observation of the Out-of-Plane Polarized Spin Current from CVD Grown WTe2", Advanced Quantum Technologies **4**, 2100038 (2021) (cit. on p. 115).

[554] T. Fan, N. H. D. Khang, S. Nakano, and P. N. Hai, "Ultrahigh efficient spin orbit torque magnetization switching in fully sputtered topological insulator and ferromagnet multilayers", Scientific Reports **12**, 2998 (2022) (cit. on p. 115).

[555] D. Akinwande, C. Huyghebaert, C. H. Wang, M. I. Serna, S. Goossens, L. J. Li, H. S. Wong, and F. H. Koppens, "Graphene and two-dimensional materials for silicon technology", Nature **573**, 507–518 (2019) (cit. on p. 115).

[556] Z. Ahmed, A. Afzalian, T. Schram, D. Jang, D. Verreck, Q. Smets, P. Schuddinck, B. Chehab, S. Sutar, G. Arutchelvan, A. Soussou, I. Asselberghs, A. Spessot, I. P. Radu, B. Parvais, J. Ryckaert, and M. H. Na, "Introducing 2D-FETs in device scaling roadmap using DTCO", 2020 IEEE International Electron Devices Meeting **22**, 5 (2020) (cit. on p. 115).

[557] K. S. Kim et al., "Growth-based monolithic 3D integration of single-crystal 2D semiconductors", Nature **636**, 615–621 (2024) (cit. on p. 115).

[558] W. Miller, "Death of a Genius: His fourth dimension, time, overtakes Einstein", LIFE, 61–64 (1955).

[559] C. Paolini, *To Sleep in a Sea of Stars* (Tor Books, London, UK, 2021).